INFLUENCE OF DIFFERENT PARAMETERS ON SHEAR STRENGTH OF FRP REINFORCED CONCRETE BEAMS WITHOUT WEB REINFORCEMENT

MD. SHAH ALAM


CENTRE FOR NFLD. STUDIES
MEMORIAL UNIVERSITY
OF NEWFOUNDLAND

Influence of Different Parameters on Shear Strength of FRP Reinforced Concrete Beams without Web Reinforcement

by

© Md. Shah Alam, B. Sc. (Eng.), M. Eng.

A thesis submitted to the School of Graduate

Studies in partial fulfillment of the

requirements for the degree of

Doctor of Philosophy

Faculty of Engineering and Applied Science

Memorial University of Newfoundland

June 28, 2010

St. John's Newfoundland Canada

Abstract

This research focuses on the shear behaviour of FRP reinforced concrete members without web reinforcement. The investigation was carried out in three phases, viz., experimental, analytical, and numerical simulation. The experimental investigation was carried out to investigate the effect of different parameters on the behaviour and concrete contribution to the shear strength. A new test set-up was designed and constructed for testing the beams. A total of thirty-six beams reinforced with GFRP, CFRP, and steel bars were tested. The test parameters were shear span-to-depth ratio (a/d), depth of beam (d), longitudinal reinforcement ratio (ρ), concrete compressive strength (f'_c), and reinforcement type. Each of the parameters was varied while keeping all other parameters constant. The structural behaviour of the tested beams with regard to the deflections, strains, modes of failure, and ultimate capacity was examined. The test results revealed that there is an effect of the parameters on the shear strength of the beams.

The experimental results were compared to the predictions of some of the available design codes, manuals, and guidelines for calculating the concrete contribution to the shear strength. It was observed that the predicted results did not match well with some of the experimental results. The experimental investigation revealed that there is a relationship between the cracking load and the shear strength of the beams. This relationship was further verified using the test results of 101 FRP reinforced beams that were available in the literature. Based on this relationship, a simple yet robust shear design method was proposed to calculate the concrete contribution to the shear strength

of FRP reinforced rectangular beams without transverse reinforcement. The proposed method was validated against the experimental results of the current investigation as well the test results obtained from the literature. The predicted results using the proposed method were compared with the predicted results of some of the available design codes, manuals, and guidelines. The proposed method was found to be more consistent and reliable in predicting the shear strength of FRP reinforced concrete members than the other methods. The method is simple to apply and is suitable for use in design codes.

Finally, finite element analysis was carried out to simulate the behaviour of shear critical FRP reinforced concrete beams with a wide range of design parameters such as shear span-to-depth ratio, depth of beam, reinforcement ratio, concrete strength, and reinforcement type. For this purpose, two concrete material models were used. The models were a concrete damage plasticity model (Model-1) and a hypoelastic concrete model (Model-2). An idealized tension-stiffening model was proposed based on the reinforcement type and varies as a function of the member strain. The models were implemented in general purpose finite element programs ABAQUS and ADINA, respectively. The models were used to simulate the experimental results of some of the beams tested in this investigation and to examine how well these models simulate the behaviour of shear critical FRP reinforced concrete members. The models predicted results are in a reasonable agreement with the experimental results. It was observed that a better prediction can be achieved using a proper tension-stiffening idealization.

Acknowledgments

I want to take this opportunity to express my sincere thanks to my Supervisor Dr. Amgad Hussein, Associate Professor, Faculty of Engineering and Applied Science for his constant supervision, continuous guidance, helpful criticism, suggestions and encouragement given throughout the course of this research.

My special thanks to Dr. Hesham Marzouk and Dr. Shawn Kenny for their comments and suggestions on this research as a member of the supervisory committee. Thanks are due to Dr. Stephen Butt, Associate Dean of Graduate Studies and Mrs. Moya Crocker, Secretary of Associate Dean's office for their smooth administrative works in my graduate program.

I wish to express my thanks to Shawn Organ and Matt Curtis of the Concrete and Structural Laboratory of Memorial University for their assistance during fabrication and testing of the specimens. Thanks are also extended to my colleagues Yahia Ibrahim, Emad Rizk, Nabil Dawood for their help during the experimental phase of this study. Thanks are also due to the technical service staff especially Billy bidGood and Mark for their services in manufacturing the testing frame and formwork preparation.

The financial assistance provided by the School of Graduate Studies and the Natural Sciences and Engineering Research Council of Canada (NSERC) are gratefully acknowledged. The cooperation of the Concrete Products for providing concrete for this research is also gratefully acknowledged.

Finally, my deepest appreciation goes to my parents, late Md. Mizanur Rahman and Mrs. Samsunnahar for their continual encouragement to pursue my goal even if it

was hurtful for them. I would like to thank my brothers and sister for their support in different aspects of my life. Last but not the least; special thanks are due to my wife Dr. Mist Sabina Jesmin for her continuous inspiration, and sacrificing lots of time so that I could finish this thesis in time.

Table of Contents

List of Figures

List of Tables

List of Symbols and Abbreviations

A_f	=	Area of FRP bars
A_p	=	Area of tendons
A_s	=	Area of steel bars
C	=	Compressive force
E	=	Modulus of elasticity
E_c	=	Modulus of elasticity of concrete
E_s	=	Modulus of elasticity of steel bars
E_f	=	Modulus of elasticity of FRP bars
E_{long}	=	Modulus of elasticity of longitudinal bars
E_o	=	Initial undamaged elastic modulus
E_p	=	Modulus of elasticity of tendons
G_f	=	Fracture energy
I	=	Moment of inertia
I_T	=	Moment of inertia of transformed section
I_g	=	Gross section moment of inertia
L	=	Clear span
M	=	Moment
M_f	=	Factored moment
M_{cr}	=	Cracking moment
M_o	=	Decompression moment
M_d	=	Design bending moment
N'_d	=	Design axial compressive force
N_f	=	Factored axial load

P	=	Applied load
P_{cr}	=	Cracking load
R	=	Reaction
T	=	Tensile force
V	=	Shear force
V_a	=	Interface shear transfer between cracks (aggregate interlock)
V_{ay}	=	Vertical component of interface shear
V_c	=	Concrete contribution of shear strength
$V_{c(\min)}$	=	Minimum shear strength of a section
V_f	=	Factored shear force
V_p	=	Shear force due to pre-stressing
V_{c1}	=	Concrete contribution from un-cracked section
V_{c2}	=	Concrete contribution from aggregate interlock mechanism
V_{cr}	=	Shear load at first flexural cracking
$V_{cr-a/2}$	=	Shear load at flexural cracking of the middle of the shear span
V_{cr-obs}	=	Observed shear load at first flexural cracking
V_{cz}	=	Shear resistance of uncracked concrete compression zone
V_d	=	Dowel force of longitudinal reinforcement
V_{exp}	=	Experimental shear strength
V_{pred}	=	Predicted shear strength
V_s	=	Shear carried by stirrups
a	=	Shear span
	=	Depth of rectangular stress block
a_g	=	Maximum aggregate size
b	=	Width of beam

b_v	=	Effective web width of beam
b_w	=	Web width of beam
c	=	Cracked concrete section neutral axis depth
d	=	Effective depth of beam
d_c	=	Degradation variable for compression
d_t	=	Degradation variable for tension
d_v	=	Distance between the resultant tensile and compressive force
a/d	=	Shear span-to-depth ratio
f_{b0}	=	Initial equibiaxial compressive yield stress
f_{c0}	=	Initial uniaxial compressive yield stress
f_c	=	Compressive stress of concrete
f_{cr}	=	Cracking stress of concrete
f'_c	=	Compressive strength of concrete
f_{mcd}	=	Design compressive strength of concrete
f_{po}	=	Stress in tendons when the stress in surrounding concrete is zero
f_r	=	Modulus of rupture
f_t	=	Tensile stress of concrete
f'_t	=	Tensile strength of concrete
$f_{tp}{}'$	=	Uniaxial cut-off tensile stress
f_u	=	Ultimate strength of FRP bars
f_y	=	Yield strength of steel
h	=	Height of beam
l	=	Element length
j	=	Ratio of the distance between the internal resultant forces in concrete and reinforcement and the effective depth of beam, d

k	=	Ratio of the neutral axis depth to the effective depth of beam, d
	=	Stress decay factor
k_1, k_2, k_3	=	Coefficients
k_a	=	Represent the effect of arch action
k_m	=	Represents the effect of interaction between the factored moment and the factored shear at a section on its shear strength
k_r	=	Represents the effect of reinforcement rigidity
k_s	=	Represent the effect of beam size
κ	=	Scalar hardening parameter
l_{cr}	=	Horizontal distance of the failure crack location at the bottom of the beam from the loading point
n	=	Modular ratio
	=	Curve fitting factor
n_f	=	Modular ratio for FRP bar
$\overline{p}$	=	Effective hydrostatic pressure stress
$\overline{q}$	=	Mises equivalent effective stress
y_t	=	Distance from neutral axis to the extreme tension fibre
s_{ze}	=	Equivalent crack spacing factor
s_z	=	Crack spacing parameter
σ_1	=	Maximum principal stress
σ_2	=	Minimum principal stress
ρ	=	Longitudinal reinforcement ratio
ρ_f	=	Longitudinal reinforcement ratio of FRP bar
$\rho_f E_f$	=	Axial stiffness of longitudinal FRP reinforcement
ρ_b	=	Balanced reinforcement ratio
ρ_{eff}	=	Effective reinforcement ratio = $\rho_f E_f / E_s$

β	=	Ability of concrete to transmit tensile stress
	=	Dimensionless coefficient
α	=	Dimensionless coefficient
α_1, β_1	=	Stress block factor
ε_x	=	Longitudinal strain at mid-depth
ε	=	Strain
ε_c	=	Compression strain in concrete
ε_o	=	Concrete strain at f_c'
ε_{cr}	=	Cracking strain
ε_m	=	Mean strain
ε_t	=	Tensile strain in steel
$\tilde{\varepsilon}_t^{pl}$	=	Equivalent plastic strain in tension
$\tilde{\varepsilon}_c^{pl}$	=	Equivalent plastic strain in compression
$\tilde{\varepsilon}_t^{ck}$	=	Cracking strain
$\tilde{\varepsilon}_c^{in}$	=	Inelastic strain
ε_{ot}^{el}, ε_{oc}^{el}	=	Elastic strain in tension and compression, respectively
ε_u	=	Ultimate strain
ε_y	=	Yield strain
ξ	=	Dimensionless coefficient
γ_b	=	Member safety factor
λ	=	Concrete density factor
ϕ_c	=	Concrete resistance factor
ψ	=	Dilation angle

ACI	=	American Concrete Institute
ASCE	=	American Society of Civil Engineers
ASTM	=	American Society for Testing and Materials
CFRP	=	Carbon Fibre Reinforced Polymer
CHBDC	=	Canadian Highway Bridge Design Code
CSA	=	Canadian Standard Association
FEA	=	Finite Element Analysis
FRP	=	Fibre Reinforced Polymer
GFRP	=	Glass Fibre Reinforced Polymer
HSC	=	High Strength Concrete
ISIS	=	Intelligent Sensing for Innovative Structures
JSCE	=	Japan Society of Civil Engineers
LVDT	=	Linear Variable Differential Transformer
MCFT	=	Modified Compression Field Theory
NSC	=	Normal Strength Concrete

Chapter 1 Introduction

1.1 General

The use of fibre reinforced plastic (FRP) bars, as an alternative to steel reinforcement for reinforced concrete members, is gaining acceptance among the structural engineers. These bars have some favourable properties than conventional steel bars; such as: corrosion resistance, high strength to weight ratio, longer durability, and magnetic neutrality. On the other hand, GFRP bars are less expensive than CFRP bars. Where serviceability is not a concern, GFRP bars can be used instead of CFRP bars. There is a wide range of applications of FRP reinforcements that covers new construction as well as the strengthening and rehabilitation of existing structures. Apart from structural use, where corrosion is the main concern, these bars are also used in structures requiring magnetic neutrality and members' susceptible to chemical attack. However, the low modulus of elasticity and low ductility of FRP bars, especially GFRP bars, have limited their use considering the serviceability of the structures, where deflection and crack width are a primary concern.

There has been extensive research on the flexural behaviour of FRP reinforced concrete members, and it has been well established that the flexural capacity of concrete members reinforced with FRP bars can be predicted by traditional beam theory (Faza and Gangarao 1993, Nanni 1993, ISIS 2001). In contrast, the shear behaviour of FRP reinforced concrete members is different from that of steel-reinforced concrete members due to their different properties; including the modulus of elasticity, E, surface

characteristics, and bond characteristics. Several studies on the shear capacity of FRP reinforced concrete members without shear reinforcement has indicated that the shear strength is influenced by the stiffness of the tensile reinforcement (Sonobe et al.1997, Michaluk et al. 1998, Tureyen and Frosch 2002). In addition, the behaviour of FRPs is elastic-brittle with no yielding or ductility at failure and its modulus of elasticity is lower than that of steel. These characteristics make the shear behaviour of FRP reinforced concrete beams more complex. Therefore, it has been recognized that the shear behaviour of FRP reinforced concrete beams should be further investigated independently to reflect these specific material characteristics.

1.2 Nature of the Problems

After more than 100 years of research on the shear behaviour of steel reinforced concrete beams, the National Cooperative Highway Research Program (NCHRP 2005) has reported that there is a lack of understanding and consensus on how structural concrete members carry shear. The behaviour and design methods of steel reinforced concrete members in shear are still an area of concern (Bentz and Collins, 2006). The behaviour of FRP reinforced concrete beams in shear has additional complications due to its different properties. The shear design methods for FRP reinforced members are mostly empirical and designed to fit a limited set of shear test results that are available in the literature. These methods may not properly predict the shear strength for a range of parameters outside the experimental results. Some of the codes give widely scattered and conservative results (El-Sayed et al. 2006a). The degree of conservatism of the predicted

results for GFRP and CFRP reinforced beams, using ACI 440.1R (2006), CSA-S806 (2002), and JSCE (1997) shear design methods, are shown in Figures 1.1 and 1.2, respectively.

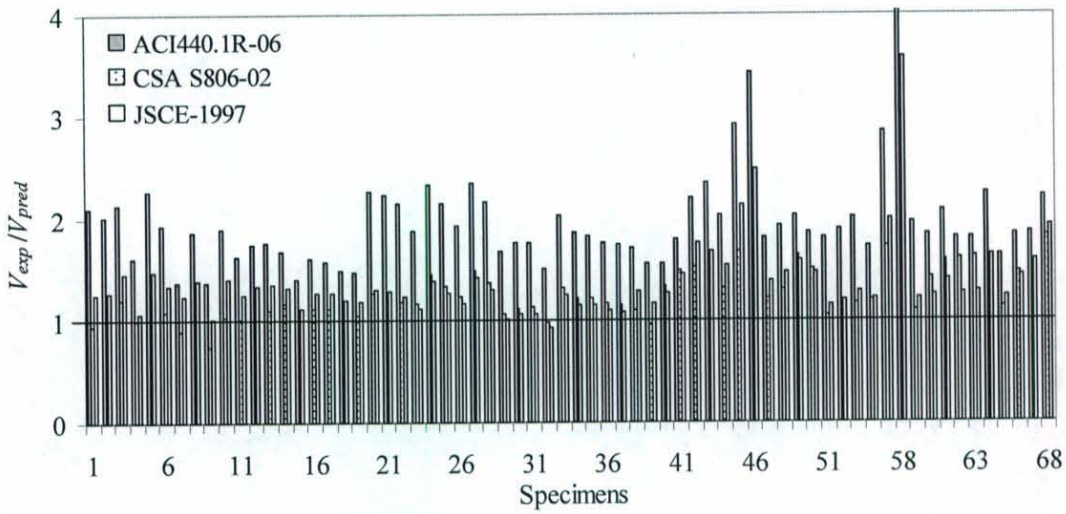

Figure 1.1: Degree of conservatism for different design guidelines for GFRP reinforced specimens

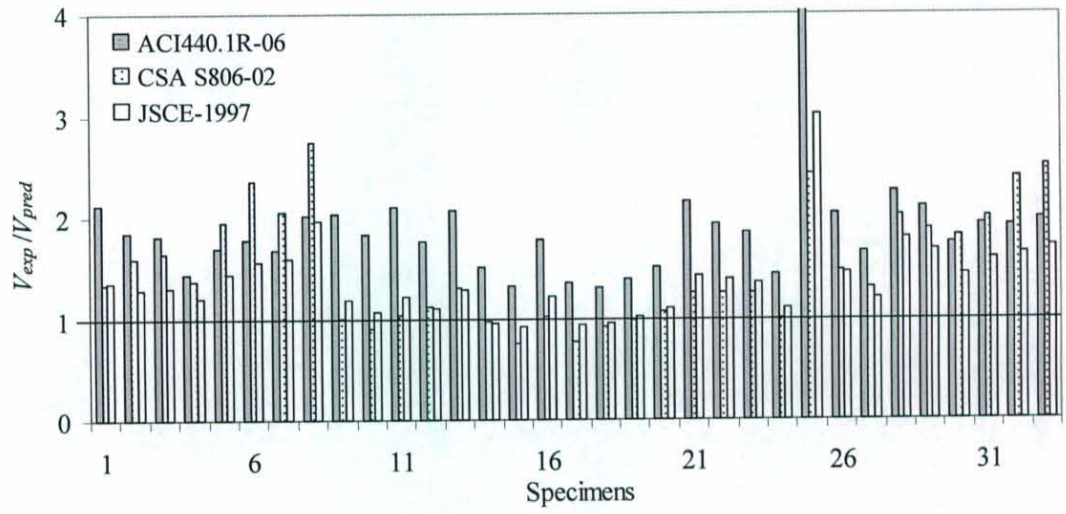

Figure 1.2: Degree of conservatism for different design guidelines for CFRP reinforced specimens

In these comparisons, 68 GFRP and 33 CFRP reinforced beams, which are included in the database in Chapter 5 of this thesis, were used. The ratios of the experimental shear strength, V_{exp}, to the predicted shear strength, V_{pred}, are plotted against the number of specimens. The average ratios of the experimental to the predicted shear strength, V_{exp}/V_{pred}, using the ACI, CSA and JSCE methods, for GFRP reinforced concrete beams, are 1.94, 1.24 and 1.35, respectively. The standard deviations (STDV) for these methods are 54, 30, and 39%, respectively. The same ratios for 33 CFRP reinforced concrete beams are 1.86, 1.50, and 1.38 with standard deviation (STDV) of 49, 56, and 29% for the three methods, respectively. For some of the specimens, the results varied by approximately 350%. These results indicate that there is a lack of suitability of these shear design methods. This could be attributed to the lack of sufficient test data to corroborate the robustness of the available design methods. A diminution in the degree of conservatism is expected with the addition of more test data (Razaqpur et al. 2004).

A database of published test results on shear strength of conventional steel reinforcement for simply supported rectangular beams without axial force was compiled by Brown et al. (2006). The database contained the test results of twelve hundreds beams failing in shear. In contrast, the results of less than one-hundred FRP reinforced concrete beams without web reinforcement are available in the literature (Sherwood et al. 2008, Hoult et al. 2008, El-Sayed et al. 2005). Therefore, more tests with different test variables are needed to check the suitability of the existing design methods, and to develop a consistent shear design method.

On the other hand, the code based design equations cannot predict the complete shear behaviour of FRP reinforced concrete members, especially the nonlinear behaviour. To model this nonlinear behaviour and other complex behaviour, such as cracking, aggregate interlock, bond, and dowel action, numerous finite element models have been developed (ASCE 1982). Some of the available finite element models can simulate the nonlinear behaviour of traditional reinforced concrete beam in a realistic way. However, the various approaches of these finite element models differ in: a) material models, b) element formulations, and c) solution procedures. It can generally be argued that a specific approach will be more suited to certain structure/loading situations and less to others; no single approach performs well over the entire range of structural details and loading conditions encountered in practice (Coronelli and Mulas, 2006).

FRP has different properties than those of steel reinforcement. Hence, the finite element modelling of shear critical FRP reinforced members may differ from that of steel reinforced members. Figure 1.3 shows the results obtained from a preliminary finite element modelling, carried out in the current research, of steel and GFRP reinforced concrete beams without web reinforcement. It was observed that the behaviour of steel reinforced concrete beam was better predicted than the GFRP reinforced concrete beam, in terms of both the cracking and ultimate loads. The difference in the predicted behaviour of the GFRP reinforced beam can be attributed to the low modulus of elasticity, different bond characteristics, and difference in tension stiffening. Bischoff and Paixao (2004) observed that GFRP reinforced concrete demonstrated greater tension stiffening than that of steel reinforced concrete. Using proper constitutive models can

improve the prediction of the behaviour of GFRP reinforced concrete beams in shear. In general, a finite element model of shear critical FRP reinforced concrete members that is capable of predicting the complete behaviour for a wide range of design parameters, load conditions, and reinforcement arrangements, is still lacking.

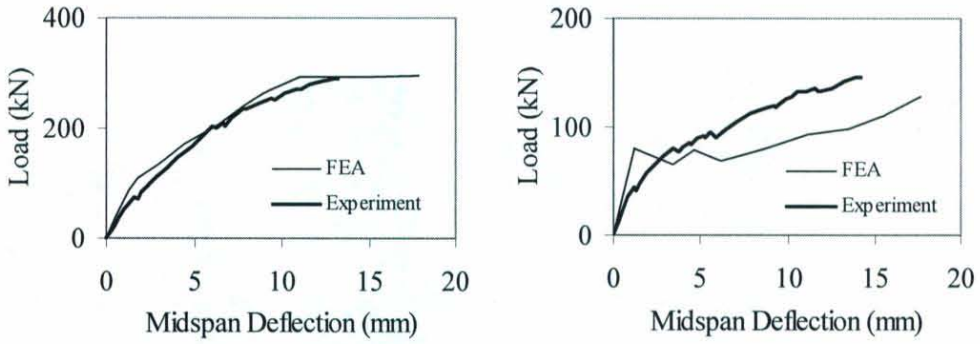

Figure 1.3: Load-deflection behaviour of reinforced concrete beam reinforced with (a) steel reinforcement, and (b) GFRP bars (preliminary simulation)

1.3 Objectives and Scope of Research

There were three objectives for the current research; to carry out a systematic experimental investigation on the shear strength and behaviour of FRP reinforced concrete beams without web reinforcement, to propose a shear design method, and to develop a finite element model for shear behaviour of FRP reinforced members. The experimental results were used to assess the applicability of some of the shear design methods, to develop a shear design method, and to validate the finite element analysis results.

The experimental investigation was carried out on concrete beams reinforced with GFRP, CFRP, and steel bars in the longitudinal direction only. The experimental program consists of a total of fourteen beams for each type the FRP reinforcement and seven beams with traditional steel bar. The test variables were shear span-to-depth ratio (a/d), depth of beam (d), longitudinal reinforcement ratio (ρ), concrete compressive strength (f'_c), and reinforcement type. Each parameter was investigated, while keeping all other parameters constant. The test specimens were designed to add to the data bank available in the literature and to attempt to cover a wider range of parameters than those available in the literature.

The finite element modelling approach was based on the material models for concrete, FRP, and the interaction between the concrete and FRP bars. The models were implemented in the general purpose finite element programs ABAQUS and ADINA and were used to simulate the behaviour of shear critical FRP reinforced concrete members. The analysis was carried out to predict the ultimate load, deflection, and structural behaviour of some of the beams tested in this investigation.

In summary, the objectives of this research were:

- To investigate the effect of different parameters on the shear strength of FRP reinforced concrete beams without web reinforcement.
- To investigate the size effect for normal and high strength FRP reinforced concrete beams.
- To examine the robustness of the current shear design provisions.
- To develop a robust shear design method.

- To develop a finite element model for shear critical FRP-reinforced concrete beams.

1.4 Organisation of the Thesis

This thesis consists of seven chapters and three appendices. Chapter 2 is devoted to studying the background and literature on shear behaviour of concrete members without web reinforcement focusing on areas most relevant to the current research. Chapter 3 describes the details of the experimental program, test specimens, materials, test set-up, and instrumentation. Chapter 4 presents the experimental results. The influence of test parameters on crack patterns, load-deflection behaviour, load-strain behaviour, and shear strength are discussed. The shear strength of the test beams are also compared with the theoretical predictions using different shear design provisions and code equations. Based on the experimental observations in Chapter 4, a relationship between the shear strength and the shear load at first flexural cracking of the beams is confirmed in Chapter 5. Based on this relationship, a shear design method for FRP reinforced concrete members is developed and proposed in this chapter. The proposed method is verified against the test results gathered from the literature as well as the experimental results in this study. In addition, the proposed method is compared with the available shear design methods and the influence of different parameters on the proposed method is presented in this chapter. Chapter 6 is devoted to the finite element modelling of shear critical FRP reinforced concrete members. This chapter focuses on the constitutive models of concrete and the idealization of tension stiffening models for FRP

reinforced concrete members. Two finite element programs were used, namely ABAQUS and ADINA. The results of the finite element modelling of some FRP reinforced concrete beams tested in this investigation are presented and discussed in this chapter. Summary and conclusions of the investigation performed in this thesis are given in Chapter 7 with some recommendations for future study.

Appendix A shows the photographs of the crack patterns at failure and failure modes of all of the test beams. The load-deflection behaviour and load-strain behaviour of reinforcement and concrete for all of the beams are given in Appendix B and C, respectively.

Chapter 2 Background and Literature Review

2.1 General

The flexural failure of steel reinforced concrete members is ductile; the members give ample warning before failure and sometimes are capable of resisting large loads. Unlike flexural failures, the shear failure of concrete members is relatively brittle and can occur without warning for members without web reinforcements. The manner in which this failure can occur varies widely depending on the dimension, geometry, loading, and properties of the materials (MacGregor and Bartlett, 2000). Furthermore, such failures tend to be less predictable than flexural failure due to their more complex failure mechanisms. This complexity arises from the non-homogeneity of the materials, nonuniformity and nonlinearity in material responses, presence of cracks, presence of reinforcement, and combined load effects. These lead to an extensive research work on shear behaviour of steel reinforced concrete members in the last century. A comprehensive review of shear in reinforced concrete members is provided by Joint ASCE-ACI Committee 426 on Shear and Torsion (1973) and Joint ASCE-ACI Committee 445 on Shear and Torsion (1998). This chapter focuses on the shear resisting mechanisms, parameters affecting the shear strength, and the literature available on the behaviour of FRP reinforced concrete beams in shear. The shear design provisions of the American Concrete Institute (ACI440.1-06), Canadian Standard Association (CSA S806-02), Japanese Society of Civil Engineers (JSCE 1987), ISIS Design Manual, (2007), and CHBDC (CSA S6-06) for FRP reinforced members are briefly reviewed.

2.2 Shear Resistance Mechanism

There are several mechanisms by which shear is transmitted between two planes in a concrete member. Joint ASCE-ACI Committee 445 (1998) reported that after the formation of diagonal cracks in members without stirrups, shear is carried by concrete as a combination of five mechanisms as shown in Figure 2.1:

(1) Shear resistance of uncracked concrete compression zone, V_{cz}

(2) Vertical component, (V_{ay}), of the interface shear, (V_a) (aggregate interlock)

(3) Dowel force of longitudinal reinforcement, V_d

(4) Arching action, and

(5) Residual tensile stress across the cracks (f_t).

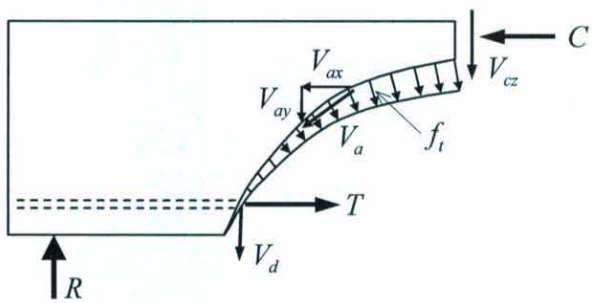

Figure 2.1: Internal forces in a cracked beam without stirrups

The total contribution to the shear resistance from the five mechanisms is termed as the concrete contribution to the shear resistance, V_c. The insights of these mechanisms are briefly discussed as follows:

(1) **Shear resistance of uncracked concrete compression zone**: In this zone, the shear force is transferred by inclined principal tensile and compressive stresses. The integration of the shear stresses over the depth of the compression zone gives a shear force component. The contribution of the uncracked concrete depends on the depth of the uncracked zone and the concrete strength. For slender members without axial compression, the shear force in the compression zone does not contribute significantly to the shear capacity, because the depth of the compression zone is relatively small (Taylor 1970, Reineck 1991). Taylor (1970) found that 20-40% of the total shear is carried by the compression zone.

(2) **Interface shear transfer (V_a)**: This shear transfer mechanism is based on the friction along the inclined crack interface, which develops when the two crack surfaces slide on each other. Depending on the concrete type and strength, crack passes though the aggregate, or between the aggregate and mortar surface. The aggregates protruding from the crack surface of normal strength concrete provide resistance against slip, which is termed as aggregate interlock. For lightweight and high strength concrete shear is transferred by friction or interface shear, because the cracks go through the aggregate. About 33-50% of the total shear is carried by the aggregate interlock (Taylor 1970).

(3) **Dowel action**: Dowel contribution is strongly dependent on the transverse rigidity and strength of the longitudinal bar. This action is not very important in members

without stirrups, because the maximum shear in a dowel is limited by the tensile strength of the concrete cover supporting the dowel. Dowel action may be noteworthy in members with large amounts of longitudinal reinforcement, particularly when the longitudinal reinforcement is distributed in more than one layer (ASCE-ACI 1998). It is very difficult to quantify the amount of dowel forces that can be activated in a particular situation. According to Fenwick and Paulay (1968), 25% of the total shear is carried by compression zone and the remainder of the shear is carried by the aggregate interlock and the dowel forces in the flexural reinforcing bars.

(4) **Arc action**: The arching action occurs in deep beams or members with shear span-to-depth ratio (a/d) less than 2.5, where the transfer of shear flow is prevented by an inclined crack extending from the load to the reaction (Figure 2.2). In such a case, the shear is transferred by arch action rather than beam action. The horizontal reinforcement serves as a tension tie to form a tied arch.

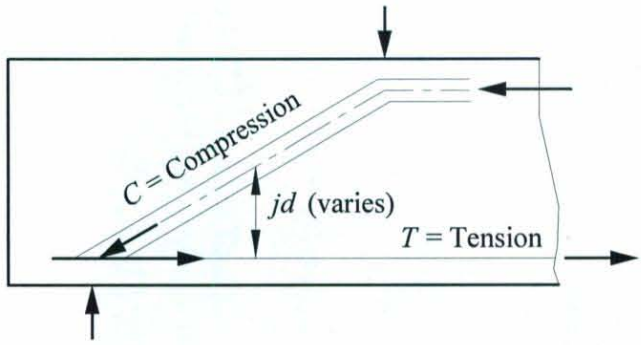

Figure 2.2: Arch action in a beam (MacGregor and Bartlett 2000)

(5) **Residual tensile stress across the cracks**: When concrete is loaded in direct tension, a significant softening branch is obtained after the peak tensile stress is reached (Gopalaratnam and Shah 1985). This softening branch is attributed to the residual tensile stress across the crack. This is explained as the small pieces of concrete bridges the crack and continues to transmit tensile force up to the crack widths in the range of 0.05-0.15 mm (ASCE-ACI 1998). Reineck's (1991) tooth model indicated that residual tensile stress provide a major portion of the shear resistance of very shallow members (for depth less than 100 mm), where the widths of flexural and diagonal cracks are small.

2.3 Factors Affecting the Shear Strength of Concrete

The concrete contribution to the shear resistance (V_c) of beams without web reinforcement is affected by five principal variables (ASCE-ACI 1998). How these variables affect the shear strength are discussed below:

2.3.1 Tensile Strength of Concrete

The shear failure of beams without web reinforcement occurs when the inclined cracks form, or shortly after the formation of inclined cracks. These cracks occur when the principal tensile stress of the concrete exceeds the tensile strength of concrete. The principal tensile stress arises from the interaction of flexural and shear stresses. The

tensile strength of concrete is considered as a function of the compressive strength of concrete (f_c') and is usually taken to be proportional to $\sqrt{f_c'}$ or $\sqrt[3]{f_c'}$.

2.3.2 Longitudinal Reinforcement Ratio

The shear strength of beams without web reinforcement is a function of longitudinal reinforcement ratio, ρ . Figure 2.3 reveals that the shear strength decreases with a decrease in the longitudinal reinforcement ratio. This can be attributed to the fact that the low reinforcement ratio leads to the formation of wider and deeper cracks compared to beams with high reinforcement ratio. Wider cracks reduce the interface shear by reducing the residual tensile stress and aggregate interlock in the cracked surface. On the other hand, deeper cracks reduce the depth of uncracked concrete compression zone, thereby reducing the contribution of uncracked concrete to the shear strength. Furthermore, the contribution from dowel action decreases with a decrease in the reinforcement ratio due to the wider crack formation. For moderately long beams with a/d equal to 5.0 and with low amount of longitudinal reinforcement ($\rho <$ 1.0 %), flexural failure rather than shear failure will govern (ASCE-ACI 998).

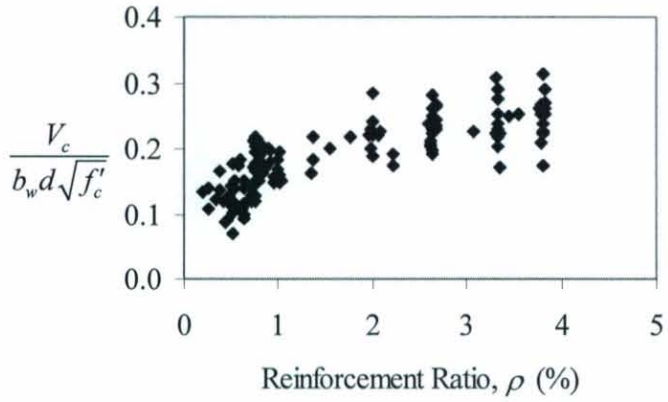

Figure 2.3: Effect of reinforcement ratio on shear capacity of beams without stirrups (ACI-ASCE Committee 326 Report 1962)

2.3.3 Shear Span-to-depth Ratio

The shear span-to-depth ratio has an effect on the shear strength of concrete beams without web reinforcement. The behaviour of beam changes from beam action to arch action as the shear span-to-depth ratio decreases below 2.5. In this type of beams, the shear is transmitted directly to the support by a compression strut (Figure 2.2) and the shear strength of these beams depends on the compressive strength of concrete instead of the tensile strength. Therefore, these beams experience an increase in shear strength. Figure 2.4 shows the relationship between shear strength and a/d ratio. For longer shear span, where the shear span-to-depth ratio is beyond 2.5, the effect of a/d ratio on the inclined cracking shear and shear strength is negligible (MacGregor and Bartlett 2000).

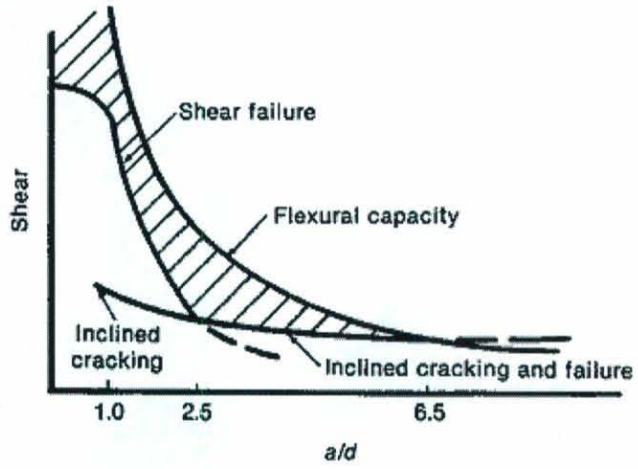

Figure 2.4: Effect of a/d ratio on shear strength of beams without stirrups (MacGregor and Bartlett 2000)

2.3.4 Size of Beam

As the overall depth of a beam increases, the shear stress at inclined cracking tends to decrease for a given f'_c, ρ, and a/d (Kani 1967). It was shown by Kani (1967) that there is a significant size effect on the shear strength of members without transverse reinforcement. Kani et al. (1979) reported that "all other factors being equal, the safety factor decreases as the depth of the beam increases". Figure 2.5 shows the size effect on shear strength of beams without web reinforcement. The test results of Shioya et al. (1989) showed that the average shear stress at failure for the beam with d equal to 3000 mm is about one-third of the beam with d equal to 200 mm. There is a general agreement that the size effect could be attributed to the larger width of diagonal cracks in larger beams (ASCE-ACI 1998). However, when the aggregate and the specimen are

scaled appropriately, the decreasing trend of shear strength with increasing beam depth was not observed (Taylor 1972).

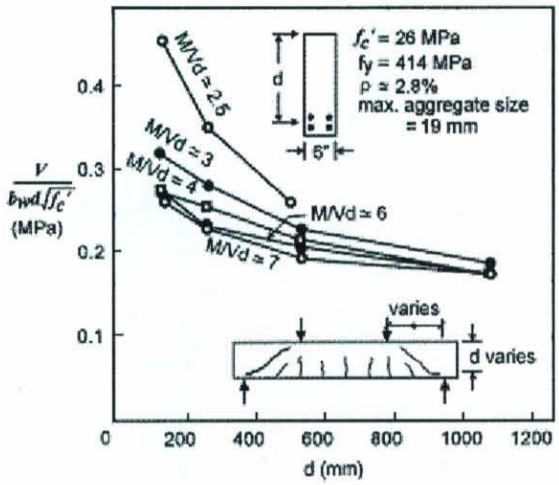

Figure 2.5: Size effect in steel reinforced concrete beams (Kani 1967)

2.3.5 Axial Force

Axial tension forces tend to decrease the shear strength of beams without web reinforcement, while axial compression forces tend to increase the shear resistance. The onset of flexural cracking is delayed due to the increase in axial compression and the flexural cracks do not penetrate deeper into the beam. However, beams without shear reinforcement subjected to large axial compression and shear may fail in a very brittle manner at the instance of first diagonal cracking (ASCE-ACI 1998). On the other hand, axial tension produces the opposite effect (Bentz and Collins 2006).

2.4 Shear Behaviour of FRP Reinforced Concrete Members

The mechanical behaviour of FRP bars differs from the behaviour of conventional steel bars. FRP bars have high tensile strength combined with low elastic modulus, and elastic brittle stress-strain relationship. When FRP bars are used as flexural reinforcement, additional complications arise due to their different behaviour, different bond, and surface characteristics. Consequently, the shear behaviour of FRP reinforced concrete members will be different than that of steel reinforced concrete members. Hence, all of the mechanisms of shear transfer discussed in Section 2.2 for conventional steel reinforced members are expected to be affected when using FRP bars. In addition, the relative contribution from these mechanisms may not be the same as in conventional steel reinforced concrete. The effect on the mechanisms is discussed in the following paragraphs.

The contribution of the uncracked concrete depends mainly on the concrete strength, f_c', and on the depth of the uncracked concrete compression zone, which is a function of the longitudinal reinforcement properties. Due to the lower elastic modulus of FRP bars, their axial rigidity would be smaller than conventional steel reinforcement. Therefore, the area of concrete under compression would be smaller than that developed in similar steel reinforced sections. Hence, it is expected that the contributions of the uncracked concrete will be reduced.

To sustain a given load, due to the higher strength of the bars, a smaller amount of FRP reinforcement is required compared to steel. This leads to higher strain in the FRP bars. This higher strain coupled with the lower stiffness of the bars reduces the total stiffness of the member and thus larger deflections and wider cracks are attained. Therefore, a smaller amount of shear force is expected to be carried by aggregate interlock in FRP-reinforced members. Wider cracks also reduce the contribution from residual tensile stresses.

Although GFRP is less stiff than steel bar, the dowel strength of GFRP bar is 8.7 percent of the ultimate tensile strength, obtained in pure dowel strength test (Grieef 1996). Experimental tests carried out by Tottori and Wakui (1993) showed that the dowel capacity of members using FRP reinforcement is about 70% of those using steel reinforcement. It has been suggested (Kotsovos and Pavlovic 1999) that the load carried by dowel action is very small in steel-reinforced members. Consequently, for FRP reinforcement, which has a low transverse stiffness and strength, an even smaller load will be carried by dowel action. Hence, the dowel contribution from FRP reinforcement could be neglected.

On the other hand, the arch action in FRP reinforced member may remain strong as conventional steel reinforcement, as long as proper anchorage is maintained. This is because the FRP reinforcement can resist high tensile force, and the shear transfer in arch action is primarily depends on shear span-to-depth ratio (a/d) and concrete strength (f_c'), neither of which depends on the reinforcement characteristics (Razaqpur et al. 2004).

The shear strength predicted using the equations developed for steel reinforced members is considerably higher than that observed from test results (Michaluk et al. 1998). Researchers have investigated the shear behaviour of FRP reinforced concrete members and developed new models to predict the shear resistance of FRP-reinforced beams. Some of those investigations and models are briefly discussed in the following sections.

2.4.1 Experimental Investigations

Michaluk et al. (1998) investigated the shear strength of eight one-way concrete slabs reinforced with GFRP, CFRP, and steel bars. Two of the slabs reinforced with GFRP bars failed in shear at a load considerably lower than the predicted values, while the others failed in flexure. The authors attributed the low shear capacity to the large width and depth of flexural cracks, and the resulting reduction in aggregate interlock and shear transfer across the concrete compression zone. Based on their observations, it was recommended that the calculated shear strength of FRP reinforced members be multiplied by the ratio of modulus of elasticity of FRP bars to that of steel bars. Similar modification to the ACI 318M-95 equations for calculating shear capacity of GFRP reinforced slab was proposed by Deitz et al. (1999). In all of these modifications, the authors only considered the ratio of modulus of elasticity (E_f/E_s) of longitudinal bar as the main variable between the shear strength of FRP and steel reinforced members.

Relative to the previous studies, a detailed experimental work were carried out by Yost et al. (2001) to provide experimental data on the shear strength of normal weight

concrete beams reinforced with longitudinal GFRP bar. The only variable considered in the test was the longitudinal reinforcement ratio (ρ), which varied between 1.53% and 2.27%. Three identical beams for each reinforcement ratio were tested. The beams were simply supported with a clear span of 2134 mm. The effective depth and shear span-to-depth ratio for all of the beams were 225 mm and 4.0, respectively. The authors concluded that the longitudinal reinforcement has no significant influence on the shear capacity of the beams. This is contrary to the findings by Alkhrdaji et al. (2001), who investigated the shear strength of GFRP RC beams and slabs. The beams were 330 mm deep and 178 mm wide with a clear span of 1.5 m. Three of the beams had no stirrups and reinforced in the longitudinal direction with 0.8, 1.3, and 2.3% reinforcement ratios. The authors reported that the shear strength of beams without stirrups increased with an increase in the amount of longitudinal GFRP reinforcement as shown in Figure 2.6.

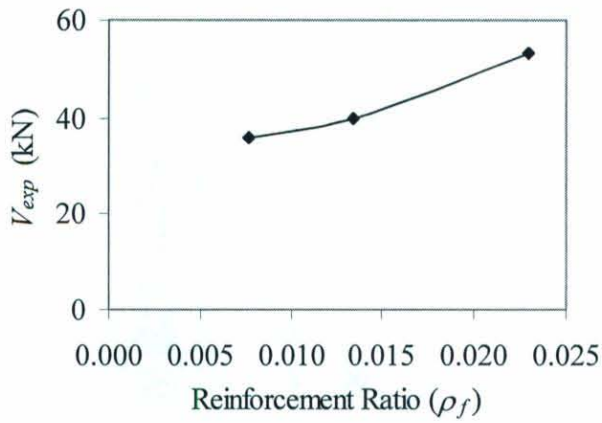

Figure 2.6: Effect of reinforcement ratio (Alkhrdaji et al. 2001)

Tureyen and Frosch (2002) conducted experiment on nine simply supported reinforced concrete beams without transverse reinforcement, to investigate the shear strength and behaviour of FRP reinforced concrete beams. The test variables were reinforcement type (GFRP, AFRP, and two types of steel) and longitudinal reinforcement ratio. The length of the beams was 3962 mm with a clear span of 2438 mm. The shear span-to-depth ratio and depth of beams were 3.4 and 360 mm, respectively. The longitudinal reinforcement ratio (ρ) was varied from approximately 0.36 to 2%. It was concluded that the shear strength increased with an increase in the longitudinal reinforcement ratio and it depended on the reinforcement type.

Tariq and Newhook (2003) tested eighteen beams reinforced with steel, GFRP, and CFRP bars to investigate the influence of longitudinal reinforcement properties on the shear strength of concrete beams with no transverse reinforcement. For each type of reinforcing materials, a total of six beams with two identical beams that had the same reinforcement ratio, three different reinforcement ratios of 0.72, 1.1, and 1.5% were used. The depths of the beams were 310, 325, and 346 mm and the widths were 130 or 160 mm. The shear span-to-depth ratios were in the range of 3.1 to 3.7, and the clear span of the beams was 2500 mm, with 250 mm overhang on each outer side of the support. From their investigations, it was concluded that the shear strength decreased with a decrease in the modulus of elasticity of longitudinal reinforcing bars.

Gross et al. (2003, 2004) evaluated the shear strength of high strength concrete beams reinforced with longitudinal GFRP and CFRP bars without transverse reinforcement. The test variable was the longitudinal reinforcement ratio only and three

identical beams were tested for each reinforcement ratio. The reinforcement ratios and concrete strength for GFRP reinforced beams were 1.25 to 2.56%, and 79.6 MPa, respectively. The same variables for CFRP reinforced beams were 0.33 to 0.76%, and 60 and 81 MPa, respectively. The authors concluded that the longitudinal reinforcement ratio had a small influence on the concrete shear strength.

The concrete contribution to the shear strength of CFRP reinforced concrete beams was investigated by Razaqpur et al. (2004). The test variables were the shear span-to-depth ratio, varying from 1.82 to 4.5, and the flexural reinforcement ratio, varying from 1.1 to 3.88 times the balanced reinforcement ratio. It was concluded that the concrete contribution to the shear strength of beams is a function of the concrete strength, the axial rigidity of the main flexural reinforcement, and the shear span-to-depth ratio.

Recently, the behaviour and shear strength of concrete slender beams reinforced with three different reinforcing materials (Steel, GFRP and CFRP) without stirrups were investigated by El-Sayed et al. (2006a). The reinforcement ratios for each type of materials varied from 0.87 to 1.72%. All of the beams were 3250 mm long with 2750 mm clear span. The shear span-to-depth ratio and effective depth of the beams were 3.1 and 326 mm, respectively. It was found that the shear strength is directly proportional with the axial stiffness ($\rho_f E_f$) of the reinforcing bars rather than the ratio of axial stiffness of the FRP bars to that of the steel bars. The relationship is shown in Figure 2.7.

The authors also investigated the shear strength of high strength concrete beams reinforced with FRP bars (2006b). The length and cross sectional dimensions of the

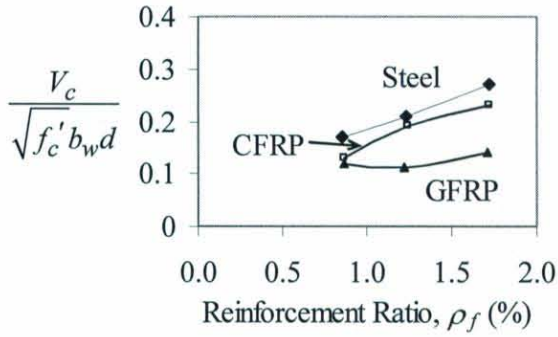

Figure 2.7: Effect of reinforcement ratio (El-Sayed et al. 2006a)

beams were the same as in the previous investigation. The concrete strength and reinforcement ratios were 43.6 and 63.0 MPa, and 1.7 and 2.2%, respectively. The conclusion made from the investigation was that the shear strength increased with an increase in the concrete strength and it was proportional to the cubic root of the axial stiffness of the longitudinal bars. This conclusion was based on the results of specimen with two different concrete strengths and two different reinforcement ratios as shown in Figure 2.8.

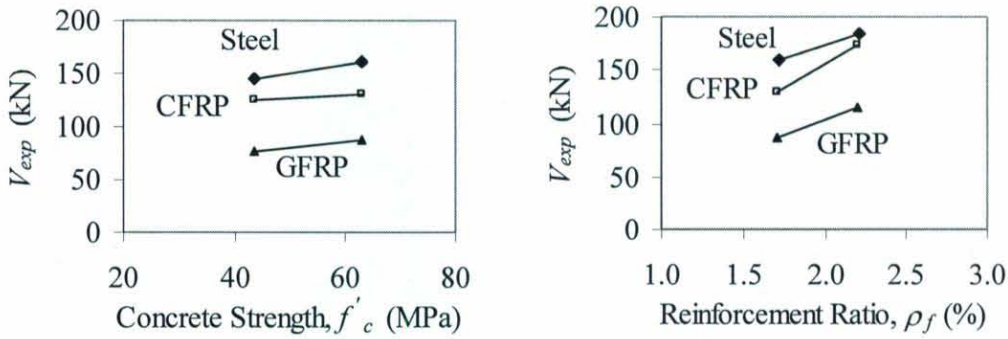

Figure 2.8: Effect of concrete strength and reinforcement ratio (El-Sayed et al. 2006b)

Steiner et al. (2008) investigated the shear strength of two large-size concrete beams reinforced with GFRP bars in longitudinal direction only. The beams were 9143 mm long, 457 mm wide, and 978 mm deep. The shear span-to-depth ratio, reinforcement ratio, and clear span of the beams were 3.1, 0.6%, and 7315 mm, respectively. In addition to the main flexural reinforcement, one of the beams had 3 layers of intermediate crack control reinforcement distributed over the depth of the beam. The author concluded that the shear stress at failure reduced for larger beams without stirrups, and this could be restored using longitudinal bars distributed over the depth of the beam.

From the previous experimental investigations on the shear behaviour of FRP reinforced concrete beams, it is evident that the shear strength varies widely for different parameters. Therefore, a systematic study is still needed to evaluate the relationship between the shear strength and the different parameters affecting the shear strength, and to consolidate the test results of several authors. Figure 2.9 shows the range of different parameters that affect the shear strength with respect to the depth of the beam for the data available in the literature. From the figure, it can be seen that few data are available in the literature for beams with a/d less than 2.5 (Figure 2.9a). The shear span-to-depth ratio (a/d) has a considerable influence on the shear strength of reinforced concrete beams. The behaviour of a beam changes from beam action to arch action for a/d ratio less than 2.5 (MacGregor and Bartlett 2000). Similarly, most of the tests were conducted on beams with concrete compressive strength less than 50 MPa (Figure 2.9b). As the shear strength of concrete depends on the concrete compressive strength, high strength concrete coupled with higher strength of FRP bars may increase the shear strength.

On the other hand, almost all of the members had reinforcement ratio greater than the balanced reinforcement ratio (Figure 2.9c). Notice that the effective depths of the beams available in the literature were less than 400 mm except one beam, which was 889 mm. These parameters will be investigated in the current study with some values that are beyond the range available in the literature.

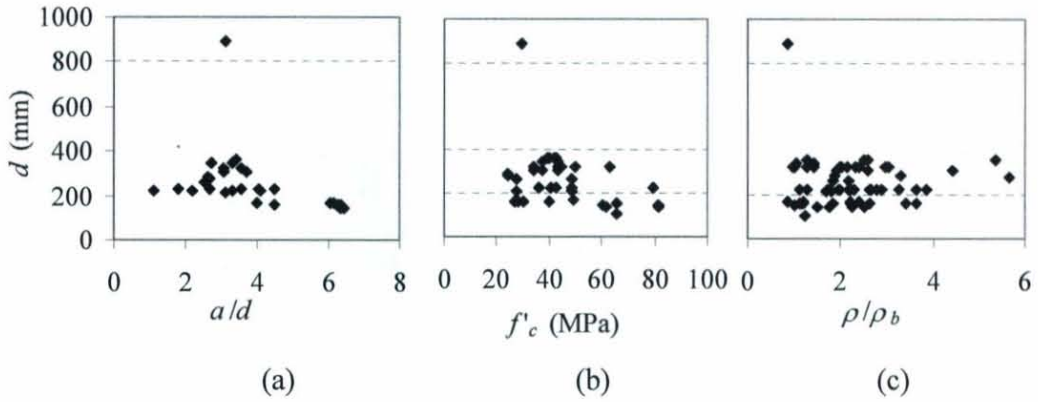

Figure 2.9: Range of parameters for FRP reinforced beams tested in the literature; (a) shear span-to-depth ratio, (b) concrete compressive strength, and (c) reinforcement ratio, versus the depth of the beams

2.4.2 Prediction Equations

In addition to the guidelines and code equations, there are several equations, proposed by different authors, for predicting the concrete contribution to the shear strength (V_c) of FRP reinforced concrete members. Tureyen and Frosch (2003) proposed a shear design method for steel and FRP reinforced members that took into account the effect of stiffness of the longitudinal reinforcement. According to this method, the

concrete shear capacity, V_c, for both steel and FRP reinforced members without transverse reinforcement can be calculated as:

$$V_c = \frac{2}{5}\sqrt{f'_c}\, b_w c \tag{2.1}$$

where b_w = width of the web, and c = cracked transformed section neutral axis depth as shown in Figure 2.10.

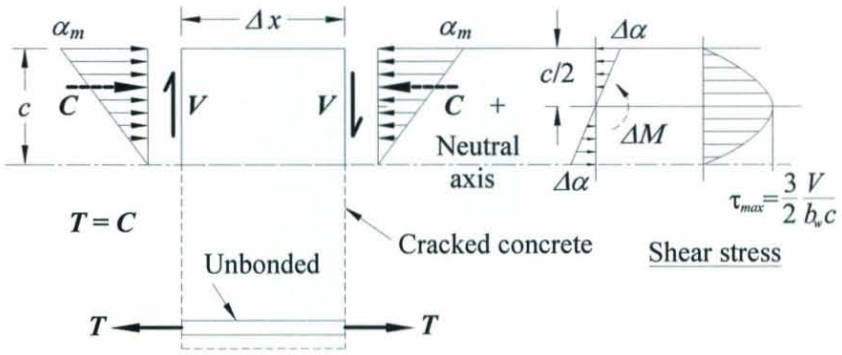

Figure 2.10: Free-body diagram in cracked region (Tureyen and Frosch 2003)

For singly-reinforced rectangular sections, the neutral axis depth, c, may be computed as:

$$c = kd \tag{2.2}$$

where,

$$k = \sqrt{2\rho_f n_f + \left(\rho_f n_f\right)^2} - \rho_f n_f$$

ρ_f = FRP reinforcement ratio = $A_f / b_w d$

n_f = modular ratio = E_f / E_c

In equation 2.2, the modulus of elasticity is included in the calculation of the uncracked neutral axis depth. The concrete compressive strength is taken into account through the correlation with concrete tensile strength as well as through its effect on the neutral axis depth. An increase in the concrete compressive strength decreases the modular ratio, and the value of k, and hence the neutral axis depth decreases. Consequently, the effect of the concrete compressive strength is less than that in the expression, $V_c = 0.17\sqrt{f_c'}b_w d$, of ACI 318.

This shear strength model may result in more conservatism than ACI 318, when used for calculating the shear strength of beams with shear reinforcement, because it assumes that only the uncracked concrete contributes to the shear strength of reinforced concrete beams, and neglects any interface shear transfer (Figure 2.10).

This method predicts negligible or zero shear strength for members with very low reinforcement or with no reinforcement at all, which contradicts with the experimental evidence. There is no upper limit on the shear resistance of concrete; it does not include the effect of moment-shear interaction, arch action, and size effect on the shear resistance of a section. The method gives the same shear strength irrespective of the amount of bending moment. The assumption used in this method that the failure shear strength is governed by the linear elastic properties of concrete was questioned by Razaqpur and Isgor (2006).

Razaqpur and Isgor (2006) proposed a shear design method for FRP reinforced concrete members in which the authors split the total shear strength attributed to the

concrete, V_c, into the concrete contribution from uncracked section (V_{c1}), and the aggregate interlock mechanism (V_{c2}) as follows:

$$V_c = V_{c1} + V_{c2} = 0.035 k_m k_s k_a \left[1 + k_r\right] \sqrt{f_c'} b_w d \le 0.2 k_s \sqrt{f_c'} b_w d \tag{2.3}$$

where k_m represents the effect of interaction between the factored moment and the factored shear at a section on its shear strength; k_r represents the effect of reinforcement rigidity $\rho_f E_f$; and k_a and k_s represent the effect of arch action and beam size, respectively. The above factors are defined as:

$$k_m = \left(\frac{V_f d}{M_f}\right)^{2/3} \tag{2.4}$$

$$k_r = \left(\rho_f E_f\right)^{1/3} \tag{2.5}$$

$$\begin{aligned} k_a &= 1.0, \text{ for } \left(\frac{M_f}{V_f d}\right) \ge 2.5 \\ k_a &= \frac{2.5}{\left(M_f / V_f d\right)}, \text{ for } \left(M_f / V_f d\right) < 2.5 \end{aligned} \tag{2.6}$$

$$\begin{aligned} k_s &= 1.0, \text{ for beams with } d \le 300 \text{ mm} \\ k_s &= \frac{750}{450 + d}, \text{ for beams with } d > 300 \text{ mm} \end{aligned} \tag{2.7}$$

The proposed design method requires the calculation of the four factors and predicts the shear strength with more consistency than some of the design methods available in the literature (Razaqpur and Isgor 2006). Although the method reflects the

effect of axial rigidity, the concrete strength, and the arch action, it does not include the effect of maximum aggregate size on the shear resistance. According to Lubell et al. (2004), this factor is important for calculating the shear strength in steel reinforced concrete beams. This should be investigated for FRP reinforced concrete members. Also, in this method, the upper limit of the shear strength includes only the depth of beams without considering other parameters.

Based on the experimental results, El-Sayed et al. (2005) proposed a modification to the ACI 440.1R-03 shear design method for the calculation of shear strength of FRP reinforced beams. El-Sayed (2006) introduced further modification to the proposed equation of El-Sayed et al. (2005), for the calculation of shear strength of deep beams. The final form of the equation to calculate the shear strength for slender and deep beams is given as follows:

$$V_c = 0.037k\left(\frac{\rho_f E_f \sqrt{f_c'}}{\beta_1}\right)^{1/3} b_w d \tag{2.8}$$

Such that,

$$\begin{aligned} &k = 1.0 \text{ and } V_c \le \frac{f_c'}{6} b_w d \qquad \text{for } M_f/V_f d \ge 2.5 \\ &k = \frac{4.0}{\left(M_f/V_f d\right)} - 0.6 \text{ and } V_c \le \frac{f_c'}{2} b_w d \qquad \text{for } M_f/V_f d < 2.5 \end{aligned} \tag{2.9}$$

where,

ρ_f = reinforcement ratio = $A_f / b_w d$

b_w = minimum efective web width within depth d, mm

d = distance from the extreme compression surface to the centroid of reinforcement, mm

E_f = modulus of elasticity of flexural FRP reinforcement, MPa

$M_f / V_f d = a/d$, and

β_1 is a function of concrete compressive strength and is given by:

$$0.85 \geq \beta_1 = 0.85 - 0.007(f_c' - 28) \geq 0.65 \tag{2.10}$$

There is no lower limit of shear strength. If the member has no reinforcement, the equation predicts zero shear strength of the member.

Recently Sherwood et al. (2008) proposed a modification to the CSA A23.3-04 general shear design method for application to FRP reinforced concrete members based on the Modified Compression Field Theory (MCFT). The CSA A23.3-04 general shear design method employs the following relationship to determine the shear resistance of a concrete section without stirrups:

$$V_c = \beta \sqrt{f_c'} b_w d_v \tag{2.11}$$

where,

$$\beta = \frac{0.40}{(1+1500\varepsilon_x)} \cdot \frac{1300}{(1000+s_{ze})} \tag{2.12}$$

ε_x is the longitudinal strain at mid-depth and is taken as one-half of the longitudinal tensile steel strain. For sections that are neither pre-stressed nor subjected to axial loads,

$$\varepsilon_x = \frac{M_f / d_v + V_f}{2E_s A_s} \tag{2.13}$$

s_{ze} is the equivalent crack spacing factor and is given by:

$$s_{ze} = \frac{35s_z}{15 + a_g} \geq 0.85s_z \tag{2.14}$$

where s_z is the crack spacing parameter, which is equal to the flexural lever arm, d_v, ($d_v = 0.9d$ or $0.72h$, whichever is greater) for members without longitudinal crack control steel, distributed along the depth of the web and a_g is the maximum aggregate size. The term s_z is set equal to 300 mm for members with at least a minimum quantity of stirrups. For high strength concrete, when the strength is greater than 70 MPa, the term a_g is equal to zero.

For FRP reinforced members, all other factors being the same, the only modification was made to β, where a second order expression was used. The proposed expression for β is given as follows:

$$\beta = \frac{0.30}{0.5 + (1000\varepsilon_x + 0.15)^{0.7}} \cdot \frac{1300}{(1000 + s_{ze})} \tag{2.15}$$

The proposed method accounts fully for the strain effect and the size effect (Sherwood et al. 2008). Nonetheless, the use of this method is not straightforward. Several factors need to be considered for using this method. Overall, the calculation of shear strength by this method is an iterative process and is difficult to perform without a spreadsheet.

2.5 Shear Design Equation in the Codes and Guidelines for FRP Reinforced Concrete Members

Most of the current design provisions for FRP-reinforced concrete beams follow the same approach as conventional steel reinforced concrete design methods; using the well-known $V_c + V_s$ format to compute the shear resistance of FRP reinforced concrete members. Although, the specific manner in which the codes specify the contribution of concrete, V_c, may differ considerably, the steel contribution, V_s, is determined using the same equations as those for conventional steel reinforcement. This section summarizes the design equations used to compute V_c as recommended by the American Concrete Institute (ACI 440.1R-06), the Japan Society of Civil Engineers (JSCE 1997), the Canadian Standard Association (CSA S806-02), the ISIS Design Manual (ISIS-07), and the Canadian Highway Bridge Design Code (CHBDC) (CSA-S6-06).

2.5.1 American Concrete Institute (ACI)

To address some issues and to find a reasonable equation for calculating the shear strength of FRP reinforced concrete beams, the American Concrete Institute has revised the shear equation in ACI 440.1R-06 for a third time based on the work of Tureyen and Frosch (2003). According to this new revision, the concrete shear capacity, V_c, for flexural members with FRP as main reinforcement is given as:

$$V_c = \frac{2}{5}\sqrt{f'_c}\, b_w c \tag{2.16}$$

The different terms used in this expression and some of the drawbacks of this method are discussed in section 2.4.2.

2.5.2 Japan Society of Civil Engineers (JSCE)

The Japan Society of Civil Engineers (JSCE 1997) recommended the following expression for shear strength (V_c) of FRP reinforced concrete members:

$$V_c = \beta_d \beta_\rho \beta_n f_{vud} b_w d / \gamma_b \tag{2.17}$$

where,

$\beta_p = \sqrt[3]{100\rho_f E_f / E_s} \leq 1.5$

$\beta_d = (1000/d)^{1/4} \leq 1.5$

$\beta_n = 1 + M_o/M_d \leq 2$ for $N'_d \geq 0$

$\beta_n = 1 + 2M_o/M_d \geq 0$ for $N'_d < 0$

$f_{vud} = 0.2 f'^{1/3}_{mcd} \leq 0.72$

where γ_b = strength reduction factor, generally equal to 1.3, M_o = decompression moment, M_d = design bending moment, N'_d = design axial compressive force, and β_n=1.0 for sections without axial force resultant. According to this code, the concrete contribution to the shear strength has a limiting value. Similar to the ACI (2006), this method does not include the effect of shear span-to-depth ratio (a/d), and if a section has no longitudinal reinforcement, the equation will give zero shear strength.

2.5.3 Canadian Standard Association (CSA)

According to the Canadian Standard Association (CSA-S806-02) Code, the shear strength of a section, having either at least the minimum amount of transverse reinforcement as specified by the CSA standard or an effective depth not exceeding 300 mm, is given by:

$$V_c = 0.035\lambda\phi_c\left(f_c'\rho_f E_f \frac{V_f}{M_f}d\right)^{1/3} b_w d \qquad (2.18)$$

where V_c need not be taken as less than $0.1\lambda\phi_c\sqrt{f_c'}b_w d$ nor shall it exceeds $0.2\lambda\phi_c\sqrt{f_c'}b_w d$, where λ reflects the concrete density factor; and ϕ_c represents the concrete material resistance factor. The quantity $V_f d/M_f$ is equivalent to d/a, and shall not be taken as greater than 1.0, where V_f and M_f are the factored shear force and bending moment at the section of interest. This equation considers the effect of axial stiffness ($E_f\rho_f$), shear span-to-depth ratio (a/d), and concrete compressive strength (f_c') for calculating the shear strength.

To account for the size effect for sections with an effective depth greater than 300 mm and with no transverse shear reinforcement or less transverse reinforcement than the minimum given by CSA standard, the value of V_c is calculated using:

$$V_c = \left(\frac{130}{1000+d}\right)\lambda\phi_c\sqrt{f_c'}b_w d \geq 0.08\lambda\phi_c\sqrt{f_c'}b_w d \qquad (2.19)$$

This equation gives the concrete contribution to the shear strength of FRP reinforced concrete members regardless of the FRP type or the FRP reinforcement ratio, which is anomalous to the findings that the shear strength increases with an increase in the reinforcement ratio. Thus, the equation gives more conservative results for the beams with high axial stiffness ($E_f \rho_f$) of the longitudinal FRP bar (El-Sayed et al. 2006a). In addition, the equation neglects the shear transfer by arch action and it is quite conservative for beams with a/d less than 2.5 (Razaqpur and Isgor 2006). The transition between the limits of shear strength is abrupt and unusual, and hence this issue should be considered in the future issues of the Code.

2.5.4 ISIS M03-07 Design Manual

ISIS M03-07 shear design method for FRP reinforced members is based on the simplified method of CSA A23.3-94 code. According to this method, the factored shear resistance of concrete, V_c, for members with effective depth not greater than 300 mm or for members in which at least the minimum stirrups are provided, is calculated as:

$$V_c = 0.2\lambda\phi_c\sqrt{f_c'}b_w d\sqrt{E_f/E_s} \tag{2.20}$$

where,

$\sqrt{E_f/E_s} \leq 1.0$

λ = concrete density factor
ϕ_c = concrete resistance factor
b_w = minimum efective web width within depth d

d = distance from the extreme compression surface to the centroid of reinforcement

E_f = modulus of elasticity of flexural FRP reinforcement

E_s = modulus of elasticity of steel taken as 200×10^3 MPa

For sections with an effective depth greater than 300 mm and not containing at least the minimum transverse reinforcement, the concrete resistance, V_c, is taken as:

$$V_c = \left(\frac{260}{1000+d}\right)\lambda\phi_c\sqrt{f_c'}b_w d\sqrt{E_f/E_s} \tag{2.21}$$

where,

$$\sqrt{E_f/E_s} \le 1.0$$

In this method, the reduction in V_c compared to the steel reinforced concrete is based on the ratio of the modulus of elasticity. This method does not consider the effect of shear span-to-depth ratio and longitudinal reinforcement ratio, which are believed to affect the shear strength. In addition, there is no upper limit of the shear strength in this method.

2.5.5 Canadian Highway Bridge Design Code (CHBDC)

According to the shear design provisions of CHBDC (CSA S6-06) for FRP-reinforced members, the concrete contribution to the shear strength (V_c) is calculated using the following equation:

$$V_c = 0.25\beta\phi_c f_{cr} b_v d_v\sqrt{E_{long}/E_s} \tag{2.22}$$

where,

β = factor that depends on the ability of concrete to transmit tensile stress

f_{cr} = cracking strength of concrete = $0.4\sqrt{f_c'} \leq 3.2$ MPa

b_v = effective width of the web

d_v = effective shear depth taken as the greater of $0.9d$ or $0.72h$

E_{long} = modulus of elasticity of longitudinal bars

The value of β is determined from the following equation:

$$\beta_c = \left(\frac{0.4}{1+1500\varepsilon_x}\right)\left(\frac{1300}{1000+s_{ze}}\right) \tag{2.23}$$

where, s_{ze} is the equivalent crack spacing factor as mention earlier.

For calculating longitudinal strain, ε_x, following equation is used:

$$\varepsilon_x = \frac{\left(M_f/d_v\right)+V_f-V_p+0.5N_f-(A_f f_{po} \text{ or } A_p f_{po})}{2\left[E_s A_s+\left(E_f A_f \text{ or } E_p A_p\right)\right]} \leq 0.003 \tag{2.24}$$

where,

V_p = shear force due to prestressing

N_f = factored axial load

f_{po} = stress in tendons when the stress in surrounding concrete is zero

A_p = area of tendons

E_p = modulus of elasticity of tendons

Similar to the ISIS method, this method multiplies the concrete contribution to the shear strength of steel reinforced beams by the ratio of the modulus of elasticity of FRP and steel to calculate the shear strength of FRP reinforced beams.

The preceding discussions of the proposed design methods and some of the codes/design guidelines reveal that there are some shortcomings in those methods. Some of the methods require comprehensive understanding of the different parameters, and

some of them do not consider all of the shear strength parameters. Therefore, a more refined shear design method which addresses some of the shortcomings in the existing equations is still lacking, and this issue will be addressed in the current study.

2.6 Review of Finite Element Analysis (FEA)

Shear failure of members without stirrups is usually sudden and brittle, and occurs without warning. There are several methods proposed for predicting the shear strength of members without stirrups as mentioned in the previous sections. Nonetheless, methods for predicting the complete load-deflection behaviour, crack patterns, and failure modes, with sufficient reliability are still lacking.

Laboratory test is one of the ways to determine the exact behaviour, and strength of structural members. However, a laboratory test is expensive, time consuming, and difficult to conduct on a complex structures due to the limitations of the testing devices. On the other hand, the assessment of strength, stiffness of existing structures and newly design structures, for all possible loading conditions, requires an advanced analytical method. Finite element analysis can be used for the evaluation of strength, stiffness, load-deflection behaviour, crack patterns, and failure modes of complex reinforced concrete members, for different loading conditions.

Extensive research has been done on the application of finite element method to model the behaviour of reinforced concrete members. A comprehensive summary by Darwin (1993) gives a wide range of options available to perform a reliable finite element analysis of steel reinforced concrete. It concluded that there are both usefulness and

limitations of finite element modeling of reinforced concrete. These limitations may be due to the nonlinear behaviour of reinforced concrete. Three major factors cause the non-linear response of reinforced concrete, namely: (a) crushing in compression, (b) cracking of concrete in tension, and (c) yielding of reinforcement. Since FRP does not yield before failure, this will not create any nonlinearity. However, the interaction of the constituents of reinforced concrete, such as bond-slip between FRP and surrounding concrete, aggregate interlock at a crack, and dowel action of the longitudinal FRP at a crack, create nonlinearities.

Most of the studies of finite element analysis of reinforced concrete structures were conducted on steel reinforced concrete members and reasonable agreement were observed between experiments and numerical results (Darwin 1993). Vecchio (2001) reported that even though great advances have been made in the finite element analysis of the complex shear behaviour of reinforced concrete structures, there are some shadows on the capability of numerical analysis to provide reliable indication for design. While there are some shadows for steel reinforced members, additional complications may arise for FRP reinforced members due to its different properties such as low modulus of elasticity, difference in surface characteristics, bond characteristics, and interaction between reinforcing bars and concrete (tension stiffening). In the early stages of finite element analysis of reinforced concrete, tension stiffening was ignored. However, it has become increasingly evident that, for rational modelling using finite element analysis, it is necessary to include tension stiffening effects to accurately predict the behaviour of concrete structures (ASCE 1982).

Bischoff and Paixao (2004) studied the tension stiffening behaviour of axial tension members reinforced with both GFRP and steel bars. The authors reported that GFRP reinforced concrete exhibited greater tension stiffening than steel reinforced concrete. The authors attributed that to the fact that the difference in tension stiffening was due to lower elastic modulus of elasticity of GFRP bars. Based on their experimental results, a model for post peak response of both steel and FRP reinforced members was proposed. According to this model, the post peak response is given as follows:

$$f_t = f_{cr}\, exp\left[-1100\left(\varepsilon_m - \varepsilon_{cr}\right)\left(\frac{E_f}{200}\right)\right] \tag{2.25}$$

This model shows that the post-peak softening branch of the cracked concrete depends mainly on the elastic modulus of the reinforcing bar.

The influence of concrete strength, reinforcement ratio, and bar diameter on the tension stiffening behaviour of GFRP reinforced concrete members were investigated experimentally by Sooriyaarachchi et al. (2005, 2007). The authors observed an increase in the tension stiffening behaviour with a decrease in the reinforcement ratio and with an increase in the concrete strength. No noticeable change in the tension stiffening was recorded with changes in bar diameter with constant reinforcement ratio. The authors proposed some modifications to the ACI 224.2R-86 and CEB-FIP (1978) model for tension stiffening behaviour of GFRP reinforced members.

Nour et al. (2007) investigated the nonlinear response of concrete members reinforced with internal and external FRP bars using finite element analysis. A 3D

hypoelastic concrete constitutive law that models the nonlinear behaviour of concrete using a scalar damage parameter was utilized in the investigation. In tension, the model adopted a macroscopic approach that was directly integrated into the concrete law. The proposed tension stiffening model was based on the nature of the reinforcement and varied as a function of the member strain. The model simulated the behaviour of internal and external FRP reinforced members, which agreed well with the experimental results. Nonetheless, the investigation was carried out for beams reinforced with both longitudinal and transverse reinforcements, and for slabs with both top and bottom reinforcement.

Abdel Baky et al. (2008) discussed the numerical aspects concerning the finite element modelling of FRP strengthened concrete beams in flexure, and carried out a finite element analysis using a hypoelastic concrete constitutive law and the microplane model to capture the debonding loads of FRP strengthened concrete beams. The aspects that were discussed were the mesh size, the discrete interface element length, the interfacial fracture energy, and the concrete fracture energy. The authors concluded that the concrete fracture energy rather than the interfacial fracture energy has a significant effect on the debonding load of the FRP-strengthened beams, and the main factors affecting the accuracy of finite element simulation of FRP-strengthened concrete beams were the tension-stiffening model and the involved concrete fracture energy. The microplane approach rather than the hypoelastic relation successfully simulated the nonlinearities of the interfacial shear behaviour for FRP-flexural strengthened reinforced concrete beams.

Despite some progresses, more research is still needed on finite element analysis of shear critical FRP reinforced members that covers a wide range of design parameters, load conditions, and reinforcement arrangements.

Chapter 3 Experimental Programs

3.1 Introduction

Razaqpur and Isgor (2006) concluded that the existing data is not sufficiently comprehensive to accurately test the effect of different parameters, which are believed to affect the shear strength of FRP reinforced beams. In the current research, a systematic experimental investigation was carried out to examine the effect of some of the parameters, discussed in Section 2.3, on the shear strength of GFRP and CFRP reinforced concrete beams without transverse reinforcement. A summary of the test program with parameters investigated is shown in Figure 3.1. Some identical steel reinforced concrete beams were also tested to investigate the effect of the type of reinforcements. The effect of axial force on the shear strength is beyond the scope of the current study.

In this chapter, the details of the test specimens, materials and procedure used in the preparation of specimens, instrumentation of the test specimens, test set-up, and testing procedure are discussed.

3.2 Detail of Test Specimens

There are several structural members, such as retaining walls, foundation, upper and lower slabs of cut-and-cover tunnel and bridge deck, where shear reinforcement is

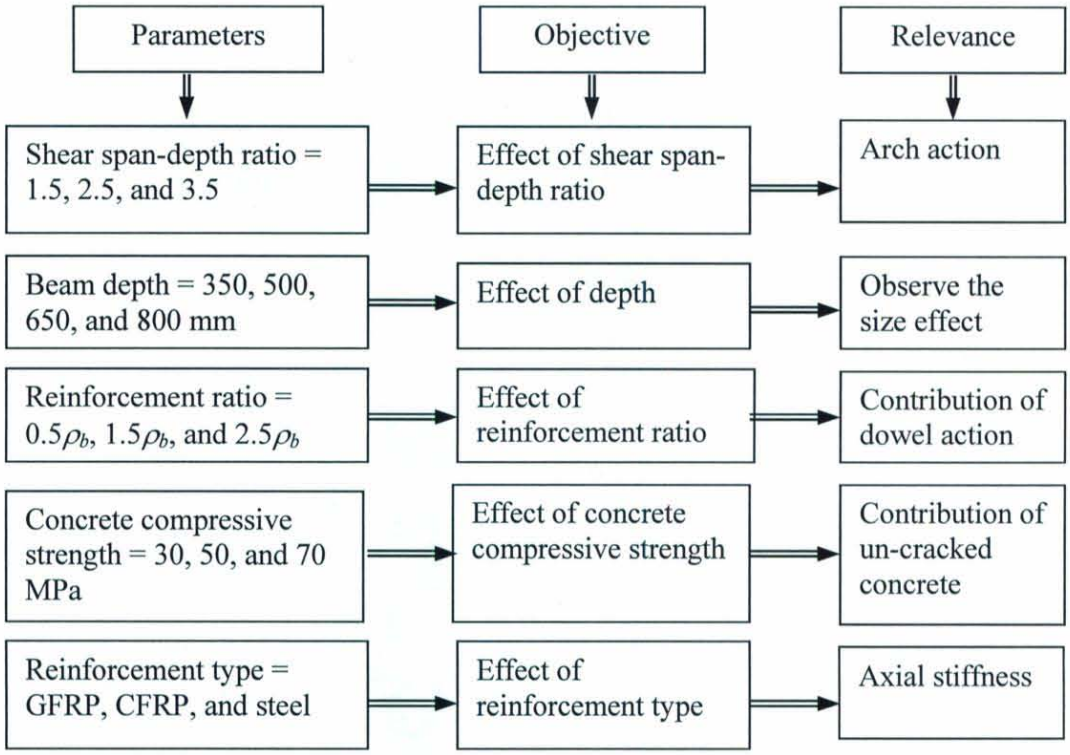

Figure 3.1: Summary of test program

not used. The specimens in the current research represent those members as well as beams and girders without transverse shear reinforcement. The main objective of the current research is to determine the concrete contribution to the shear strength. Hence, only longitudinal reinforcement was used in order to measure the shear strength provided by concrete. A total of thirty-six large scale beams with most of them to fail in shear rather than flexure were designed. The reinforcement ratio for all of the beams was chosen based on the balanced reinforcement ratio. The balanced reinforcement ratio was calculated according to CSA S806-02 as follows:

$$\rho_b = \frac{\alpha_1 \beta_1 f_c'}{f_u} \frac{0.0035}{0.0035 + f_u / E_f} \tag{3.1}$$

where, f_c' is the compressive strength of concrete (MPa), f_u and E_f are the tensile strength and modulus of elasticity of the reinforcement (MPa), respectively. The parameters α_1 and β_1 are the equivalent stress block parameters as shown in Figure 3.2. The values of these parameters are calculated as $\alpha_1 = 0.85 - 0.0015 f_c' \geq 0.67$, and $\beta_1 = 0.97 - 0.0025 f_c' \geq 0.67$ based on CSA S806-02.

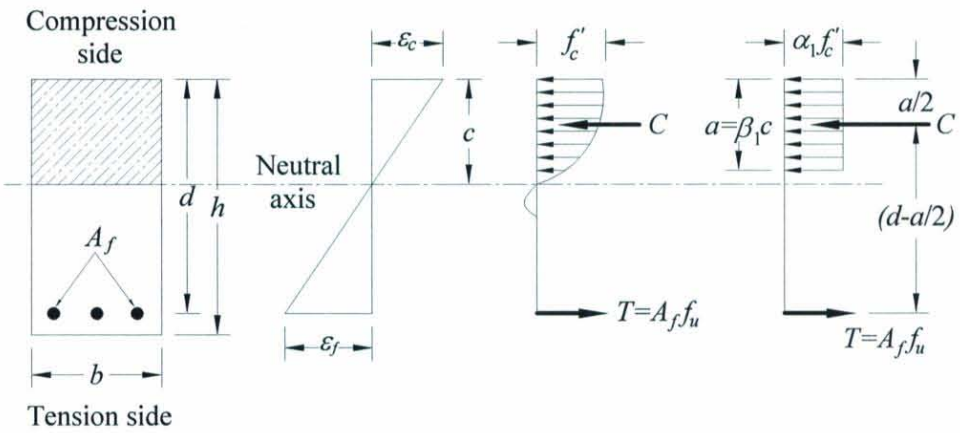

Figure 3.2: The equivalent stress block

Table 3.1 shows the details of the test specimens and the parameters that were investigated in the current study. Most of the specimens were designed to cover a range of parameters beyond the values that were commonly available in the literature (Figure

2.9). However, some of the parameters were within the available range to maintain continuity of the investigation.

The lengths of the beams varied between 2140 and 4040 mm and the widths were 250 mm and 300 mm. All beams had 220 mm overhang length beyond the support centerline, on each side, to provide adequate anchorage length and to avoid bond failures. Based on the parameters investigated (Figure 3.1), the specimens were divided into four groups for GFRP and CFRP reinforced beams. The steel reinforced concrete specimens were divided into three groups, since the effect of concrete compressive strength was not investigated for this type of reinforcement.

Few data are available in the literature for beams with a/d ratio less than 2.5 (Razaqpur and Isgor 2006). Hence, the selected a/d ratios were 1.5, 2.5, and 3.5 to investigate this parameter (Group 1). To maintain the same loading pattern, that is the loading point is approximately at the one-third of the clear span, the beam lengths were chosen as 2140, 2840, and 3540 mm, respectively. For all other beams, considering the depth of beams, space, and manageability issues, the shear span-to-depth ratio was selected to be equal to 2.5. This shear span-to-depth ratio produces a shear critical specimen (Kani 1966, 1979).

To investigate the size effect of normal and high strength concrete, five sets of beams, three for normal strength concrete and two for high strength concrete, with different heights and constant reinforcement ratio were selected in Group 2. The heights chosen for this investigation were 350, 500, 650, and 800 mm, respectively. The clear cover used for all beams was 30 mm. The effective depth of the beams varied between

305 and 758 mm. To ensure the transverse stability of the beams with 650 and 800 mm height during testing, the width of those beams was chosen as 300 mm. For high strength concrete, the size effect was investigated for beams with GFRP and CFRP reinforcement. The targeted concrete strength was 70 MPa.

The beams in Group 3 were designed to investigate the effect of the longitudinal reinforcement ratio. Two sets of beams with height of 350 and 500 mm were selected for each reinforcement type. Three reinforcement ratios, ρ_f, of 0.5, 1.5 and 2.5 times the balanced reinforcement ratio, ρ_b, were used for each beam depth. One of the beams with 350 mm height and with 2.5 times the balanced reinforcement ratio was accidentally cracked before testing and this beam was repeated. A section with a reinforcement ratio of $\rho_f/\rho_b <$ 1.0 is defined as tension-controlled failure and a section with a reinforcement ratio $\rho_f/\rho_b >$ 1.0 is defined as compression-controlled failure. The general design approach for FRP reinforced beams is to use a compression-controlled failure in the concrete. However, according to Feeser and Brown (2005), and in some cases, GFRP reinforced sections could be designed for tension-controlled failure. To observe the behaviour of tension-controlled beam in shear, the lowest reinforcement ratio of one-half the balanced reinforcement ratio was chosen. However, for all steel reinforced beams, the reinforcement ratio was less than the balanced reinforcement ratio.

The effect of concrete strength was investigated using the beams in Group 4. The targeted concrete strengths for this investigation were 30, 50, and 70 MPa. The effect of concrete strength on the beams with traditional steel reinforcement was not investigated.

The specimen identifications (IDs) were defined in the following manner. The first letter of the specimen ID was for the type of reinforcement used (G for GFRP, C for CFRP, and S for Steel). This was followed by, if only one number was used, the shear span-to-depth ratio (a/d), or the height of the beam (h), or the concrete compressive strength (f'_c). Where the type of reinforcement was followed by two numbers, the small number stood for the ratio of reinforcement used to the balanced reinforcement ratio (ρ/ρ_b), or the concrete compressive strength (f'_c), and the large number was for the height of the beam. The parameters that were used for the identifications of a specimen are highlighted in Table 3.1.

3.3 Materials

3.3.1 Reinforcement

The reinforcing materials used in this investigation were Glass and Carbon FRP bars and conventional steel bars. Two different sizes for each of the GFRP and CFRP bars were used in this study. The bars were manufactured by Pultrall Inc. Quebec, Canada. The bars were sand coated to enhance the bond between the bars and the concrete. The stress-strain behaviour of FRP bars is linear elastic up to failure. The properties of the reinforcement, as specified by the manufacturer, are given in Table 3.2. The nominal yield stress of the grade 400 steel bars was used. That is, the yield strength of the bars was assumed to be 400 MPa. The stress-strain relationships of the bars are shown in Figure 3.3.

Table 3.1: Details of test specimens and parameters investigated

	Bar type	Specimen ID	h (mm)	b (mm)	Clear span, L (mm)	a/d	Targeted f_c' (MPa)	ρ (%)	ρ/ρ_b	A_f (mm^2)	Axial stiffness, $A_f E_f$ (N×10^6)	Shear capacity* (kN)	Flexural capacity (kN)	Parameters investigated
Group 1	GFRP	G-1.5	350	250	1700	1.5	30	0.84	1.39	658	30.5	42.3	209.4	a/d
		G-2.5			2400	2.5							125.6	$a/d, d, f_c', \rho$
		G-3.5			3100	3.5							89.7	a/d
	CFRP	C-1.5	350	250	1700	1.5	30	0.42	1.54	329	47.4	42.6	263.7	a/d
		C-2.5			2400	2.5							158.2	$a/d, d, f_c', \rho$
		C-3.5			3100	3.5							113.0	a/d
	Steel	S-2.5	350	250	2400	2.5	30	0.90	0.18	700	140.0	88.1	82.2	$a/d, d, \rho$
		S-3.5			3100	3.5							58.7	a/d
Group 2	GFRP	G-500	500	250	3100	2.5	30	0.89	1.47	987	45.7	54.8	183.9	d, f_c'
		G-650	650	300	3600			0.91	1.50	1600	74.1	79.2	291.3	
		G-800	800	300	3600			0.90	1.49	2000	92.6	90.8	381.7	d
		G-500-70	500	250	3100		70	1.46	1.26	1600	74.1	83.0	366.8	d, f_c'
		G-650-70	650	300	3600			1.51	1.30	2600	120.4	118.9	586.4	
	CFRP	C-500	500	250	3100	2.5	30	0.44	1.63	516	74.3	56.5	234.4	d, f_c'
		C-650	650	300	3600			0.43	1.58	774	111.5	80.0	362.4	
		C-800	800	300	3600			0.40	1.48	903	130.0	91.6	473.9	d
		C-500-70	500	250	3100		70	0.82	1.58	916	131.9	83.7	453.9	d, f_c'
		C-650-70	650	300	3600			0.73	1.39	1290	185.8	121.3	718.3	
	Steel	S-500	500	250	3100	2.5	30	0.87	0.19	1000	200.0	108.4	120.3	d
		S-650	650	300	3600			0.88	0.19	1600	320.0	157.7	191.7	
		S-800	800	300	3600			0.88	0.19	2000	400.0	180.8	259.8	

Table 3.1 (Contd.): Details of test specimens and parameters investigated

	Bar type	Specimen ID	h (mm)	b (mm)	Clear span, L (mm)	a/d	Targeted f_c' (MPa)	ρ (%)	ρ/ρ_b	A_f (mm^2)	Axial stiffness, $A_f E_f$ (N×10^6)	Shear capacity* (kN)	Flexural capacity (kN)	Parameters investigated
Group 3	GFRP	G-0.5-350	350	250	2400	2.5	30	0.33	0.55	258	11.9	42.5	60.6	ρ
		G-2.5-350(1)						1.41	2.32	1058	49.0	51.7	146.6	
		G-2.5-350(2)												
		G-0.5-500	500		3100			0.35	0.57	400	18.5	56.3	90.5	ρ
		G-2.5-500						1.46	2.41	1600	74.1	54.3	216.1	
	CFRP	C-0.5-350	350	250	2400	2.5	30	0.18	0.66	142	20.4	42.6	68.1	ρ
		C-2.5-350						0.66	2.41	516	74.3	42.6	188.5	
		C-0.5-500	500		3100			0.22	0.82	258	37.2	56.5	98.2	ρ
		C-2.5-500						0.65	2.37	716	103.1	56.5	267.6	
	Steel	S-2.5-350	350	250	2400	2.5	30	1.43	0.28	1100	220.0	87.5	135.9	ρ
		S-2.5-500	500		3100			1.40	0.31	1600	320.0	108.4	200.5	
Group 4	GFRP	G-50	350	250	2400	2.5	50	0.87	0.95	645	29.9	50.2	157.6	f_c', d
		G-70					70	0.87	0.75	645	29.9	56.1	165.6	
	CFRP	C-50	350	250	2400	2.5	50	0.42	1.01	329	47.4	55.0	207.7	f_c', d
		C-70					70	0.42	0.80	329	47.4	65.1	212.8	

* Shear capacity was calculated using CSA S806-02 and CSA A23.3-04 for FRP and steel reinforced beams, respectively.

Table 3.2: Properties of the different types of reinforcement

Bar type	Bar #	X-section area (mm^2)	Elastic modulus (GPa)	Design tensile strength (MPa)	Yield stress (MPa)
GFRP	#4	127	46	708	-
	#5	198	48	683	-
CFRP	#3	71	120	1431	-
	#4	127	144	1765	-
Steel	10M	100	200	-	400
	20M	300	200	-	400
	25M	500	200	-	440

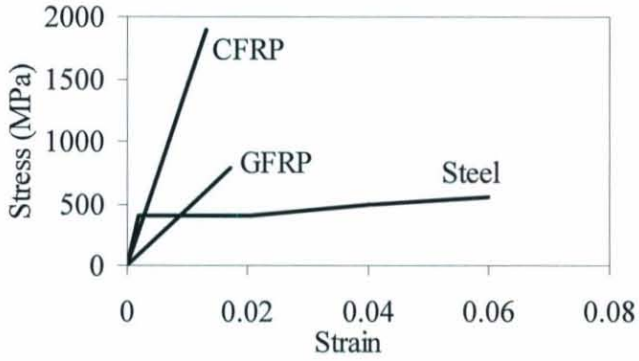

Figure 3.3: Stress-strain relationship of the different types of reinforcement

3.3.2 Concrete

The beams were cast using ready mix concrete that was delivered from a local batch plant. Both normal and high strength concrete with maximum aggregate size of 20 mm were used for all specimens. At least five 100×200 mm cylinders were cast from each concrete batch and cured under the same conditions as the beams. The cylinders were tested at the time of testing of each beam and the compressive strength was taken as the average of the five cylinders.

3.4 Fabrication and Curing Practices

3.4.1 Formwork and Reinforcement Layout

The formwork was designed and constructed using 25 mm thick plywood sheets. The sides of the formwork were cut according to the height of each beam. A sufficient number of vertical supports and top bracings were used to maintain the integrity of the formwork during casting, and to ensure that the dimensions of the beams remained unchanged. Figure 3.4 shows a typical formwork and reinforcement layout for a single formwork. The beams contained longitudinal reinforcement only that was placed at the bottom of each beam. For single layer of bars, the bars were placed on plastic chairs to maintain clear cover. The longitudinal bars were tied using several cross bars of the same dimension of the width of the beam to maintain the side cover and the spacing of the bars. For two or more layers of longitudinal bars, the required bars in each layer were tied up with 3 or 4 cross bars to make a grid. These grids were then tied up with small vertical bars to maintain the clear cover and vertical spacing of the bars (Figure 3.4).

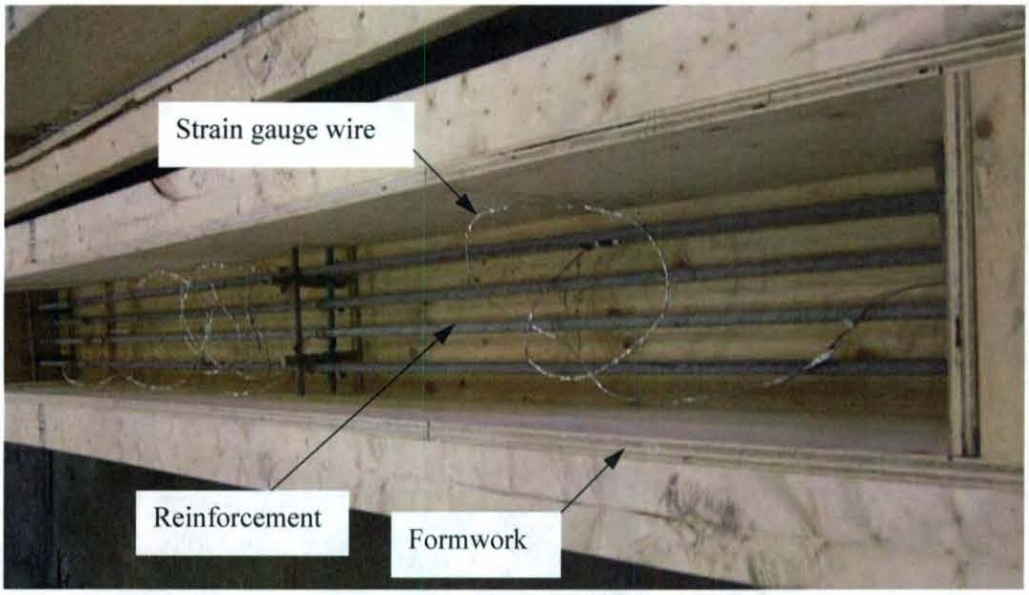

Figure 3.4: Top view of typical formwork and reinforcement layout (before placing the top cross bracing for the formwork)

3.4.2 Casting and Curing of the Specimens

Several beams were cast from each batch of concrete as shown in Table 3.3. The same casting sequence was used for all beams. First, some concrete was poured in the formwork to form a layer that extend just above the level of the reinforcement. The concrete, which poured for this layer, was spread throughout the whole length of the beam and vibrated to ensure the proper compaction of the concrete within the reinforcement area. The remaining portion of the beam was poured in layers depending on the depth of the beam. Test cylinders were prepared from the same batch of concrete according to the ASTM-C192. At the end of the pour, the surface of each beam was finished with a steel trowel. After the final set of the concrete, the beams were covered

with plastic sheets to prevent moisture loss. The specimens were watered 2-3 times a day for 7 days. After the curing process was finished, the beams were removed from the formwork and stored in the laboratory until the day of testing. Before testing, the beams were painted using white colour paint to facilitate the observation of the crack propagation. The compressive strength of the concrete for the different batches was determined at the time of testing of each beam. The recorded values of the compressive strengths are shown in Table 3.3.

The concrete used in the beams was delivered at different times of the year. As a result, and due to the weather conditions in Newfoundland, there was a difference between the targeted strength and the actual strength. The setting of the batch plant was such that it ensured a minimum value of the compressive strength, which was satisfied for almost all the beams. However, in some cases, the actual strength was higher than the targeted strength.

3.5 Instrumentation

Figure 3.5 shows a schematic diagram of a test specimen and loading, where P represents the load, L is the distance between the supports (clear span), and a is the distance from the support to the loading point (shear-span). During the test, each beam was instrumented with six electrical resistance strain gauges and three LVDTs as shown in Figure 3.6. Four strain gauges designated as RS were placed on the reinforcement. The

Table 3.3: Cylinder test results

Type of concrete	Specimen IDs	Average compressive strength, f'_c (MPa)
Normal strength concrete	G-2.5, G-3.5, G-2.5-350	39.8
	G-500	44.7
	G-1.5, C-1.5, C-2.5, C-3.5, C-2.5-350	34.5
	C-650	37.0
	G-650, G-800, G-0.5-350, G-0.5-500, G-2.5-500	37.1
	G-2.5-350, C-500, C-800, C-0.5-350, C-0.5-500, C-2.5-500	42.4
	S-500, S-650, S-800, S-2.5-500	41.8
	S-2.5, S-3.5, S-2.5-350	49.3
High strength concrete	G-50, C-50	65.3
	G-70, C-70	88.3
	G-500-70, G-650-70, C-500-70, C-650-70	74.2

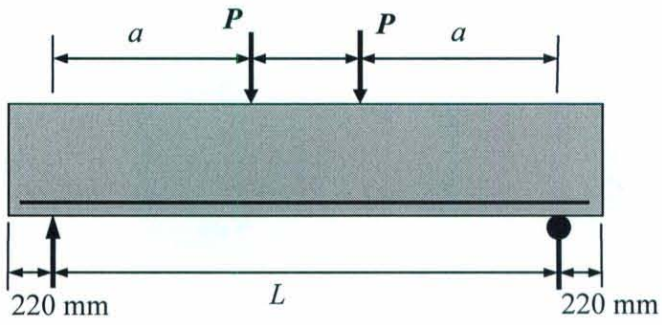

Figure 3.5: Schematic diagram of a test specimen and loading

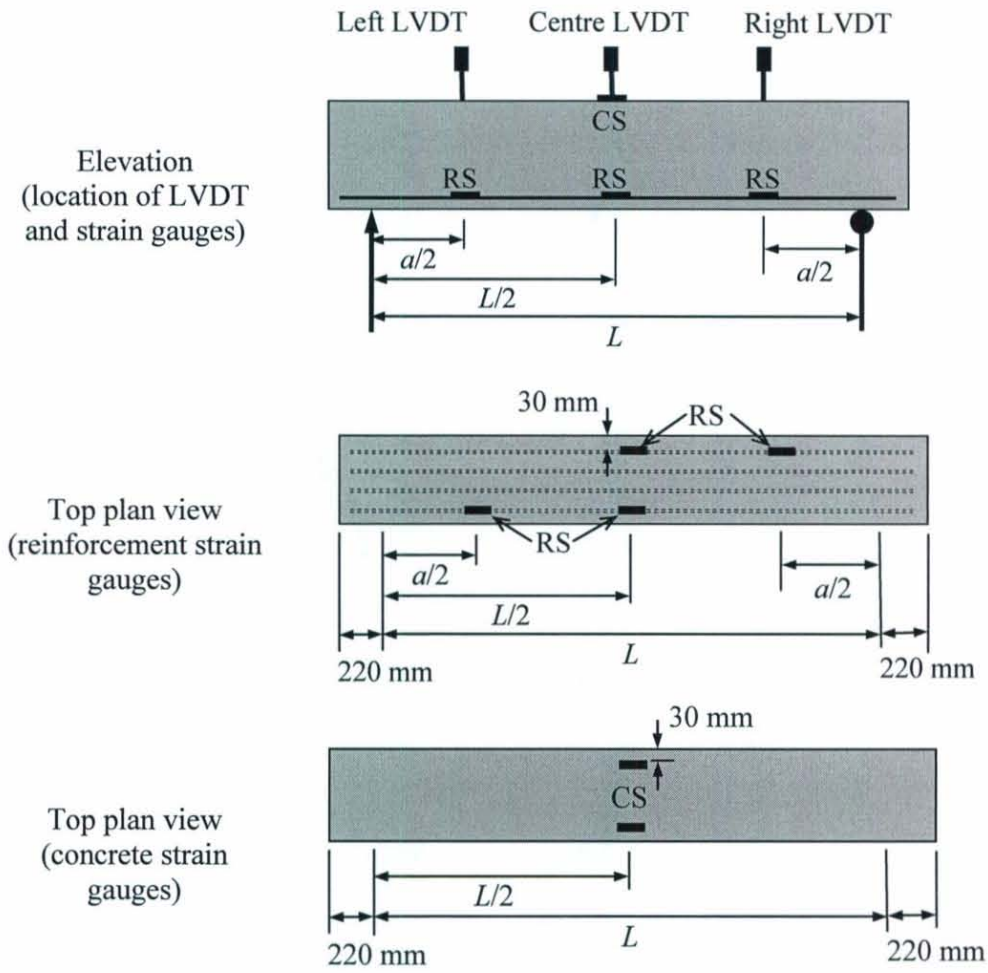

Note: CS refers concrete strain gauges and RS refers reinforcement strain gauges.

Figure 3.6: Instrumentation used during a test

strain gauges were bonded to the outside bars equally spaced from the faces of the beam. For ease of fabrication, the strain gauges were placed on the outer bars. Two of the gauges were placed at the mid span of the beam. One gauge was placed at the center of each shear span. The purpose of these strain gauges was to measure the strains at these locations and to see if there was any relation between the strain at midspan and the centre

of the shear span. Two strain gauges designated as CS were placed on the top surface of the beam at mid span to measure the concrete strain. All of the strain gauges were 10 mm long. The resistance of the strain gauges was 120 Ω with a gauge factor of 2.07 ± 0.5%. Three LVDTs were placed at the same location of the reinforcement strain gauges to measure the deflections of the beam at the centre of the beam and at the centre of each shear span. Another purpose of the two LVDTs placed at the centre of each shear span was to check the symmetry of the loading on the beam.

3.6 Test Setup and Procedure

The tests were performed in the structural engineering laboratory of Memorial University of Newfoundland. A new test setup was designed and constructed for testing the beams of the current investigation. Figure 3.7 shows the detail of the test frame. The frame consists of two vertical columns of W310×107 sections. The columns were braced using two C310×45 sections on both sides. The bottoms of the columns were stiffened using 15 mm thick plates, and the columns were supported on two 20 mm thick plates to avoid any possible bending. The columns were mounted with 1.0 m thick floor, using four ϕ40 mm bolts for each column. The front column was braced at the bottom, using two 152×152 mm angles on both sides, to spread the loads and to facilitate the use of 4 more bolts, as this column will experience tensile force. The beam supporting the actuator consists of two C460×86 sections, which were bolted to the columns. Both of the channels were stiffened using 15 mm thick plates to avoid the warping of the flange. The

channels were connected to each other using horizontal plates at both top and bottom of the channels.

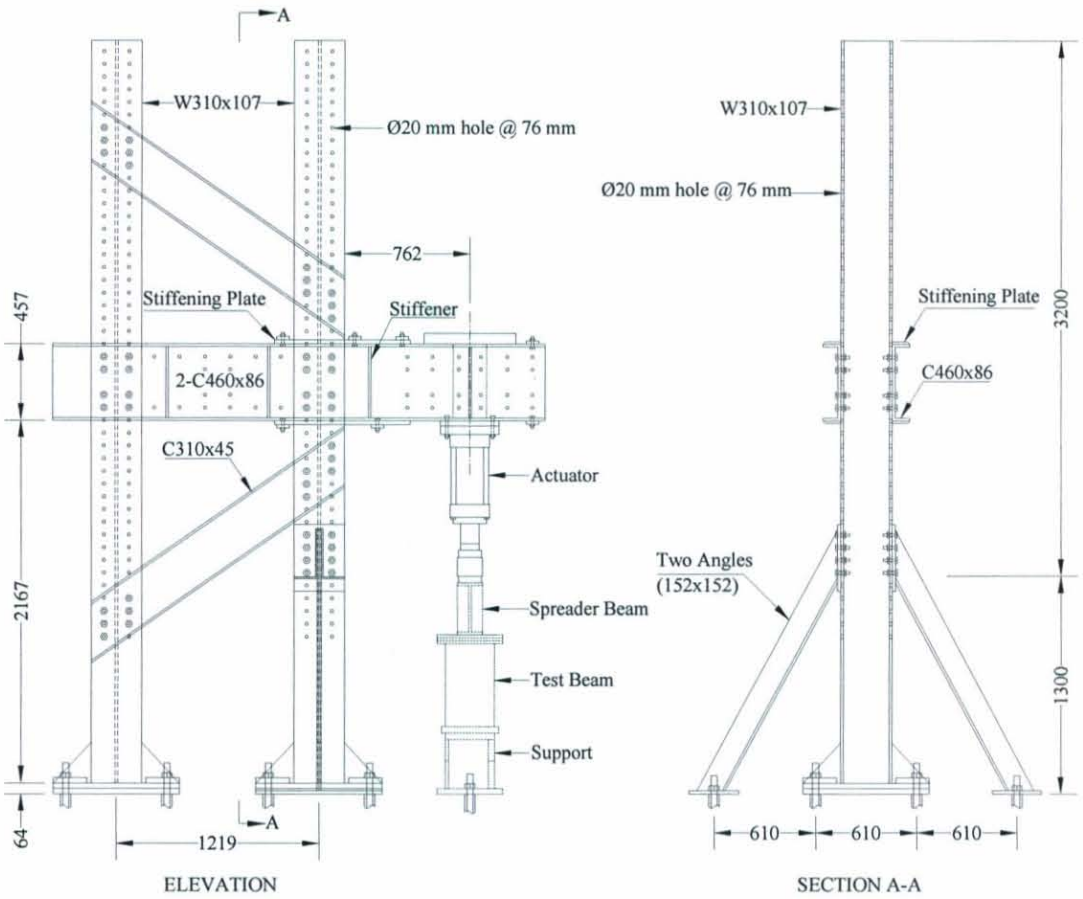

Figure 3.7: Test frame

All beams were simply supported and loaded with four-point loading as shown in Figure 3.5. The loading was applied using a 600 kN servo-hydraulic MTS actuator in displacement control. A spreader beam was used to divide the load into two points as

shown in Figure 3.8. Each beam was preloaded to approximately 10 kN to minimize the settlement of the beam. The preload was released prior to starting the test. During a test, the load was applied in increments of approximately 10 to 20 kN. The load increment was chosen depending on the beam dimensions. Smaller load increment was used at the beginning of the test to capture the load that caused the first cracking in the beam. At each load increment, the beam was inspected and the cracks were marked. The applied load, deflections, and strains from the different sensors were recorded using a high speed data acquisition system. The data was monitored by a personnel computer using LABVIEW program and stored on the hard disk of the computer. The frequency of the data sampling was 2.0 Hz. The photograph of a test set-up used in this investigation is shown in Figure 3.9.

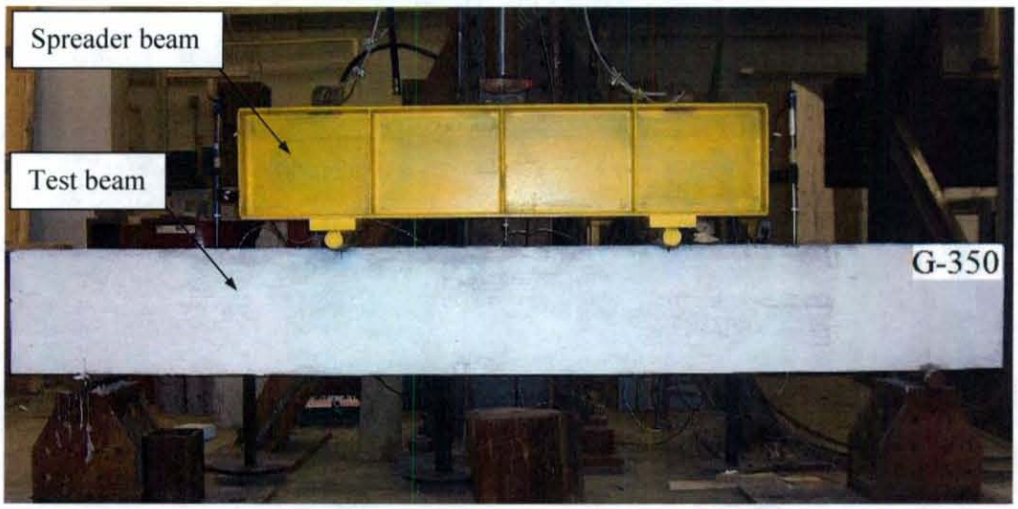

Figure 3.8: A typical beam mounted on the test-frame

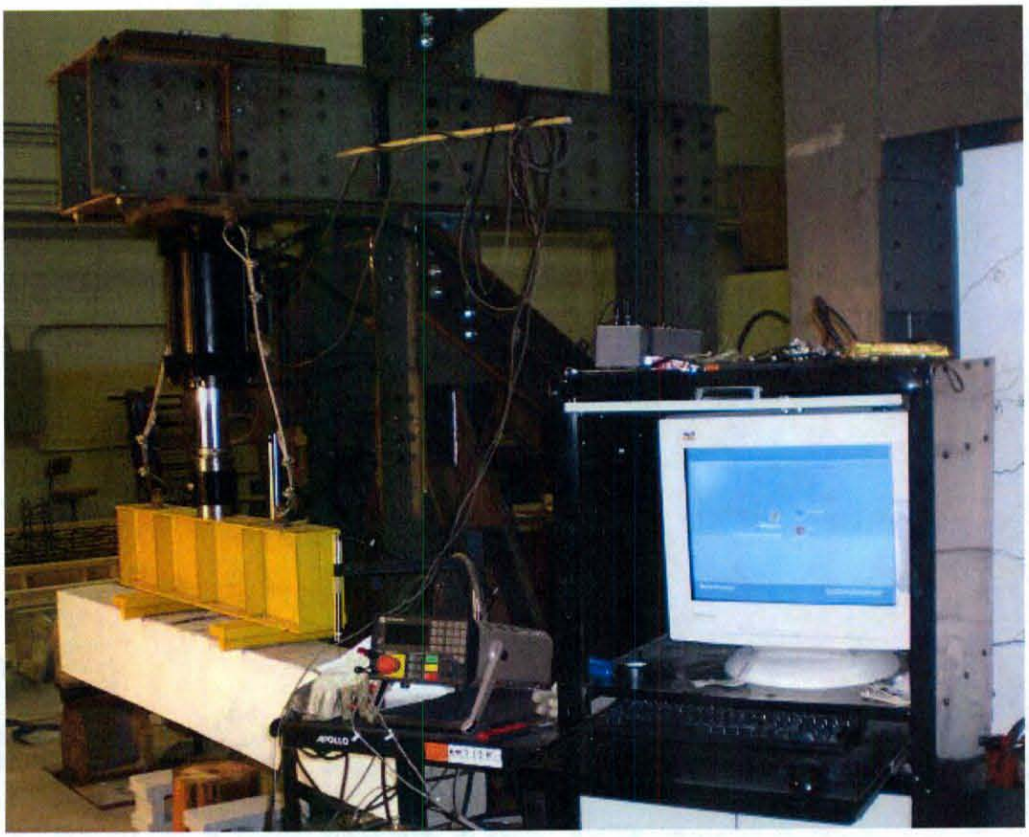

Figure 3.9: Photograph of the test setup

Chapter 4 Experimental Results and Analysis

4.1 Introduction

The experimental results of the current investigation are presented in this chapter. As mentioned earlier, a total of thirty-six beams reinforced with GFRP, CFRP, and steel bars were tested. The experimental program was undertaken to investigate the influence of five parameters on the behaviour and shear strength of concrete beams. The parameters were the shear span-to-depth ratio (a/d), depth of beam (d), longitudinal reinforcement ratio (ρ), concrete compressive strength (f_c'), and reinforcement type.

The results are presented in terms of crack patterns, load-deflection behaviour, load-strain behaviour, and failure modes. The test results are analyzed to show the effect of the different parameters on the behaviour and capacity of the test beams. Finally, the test results are compared with the theoretical prediction of some of the proposed shear design expressions and code predictions that are available in the literature.

4.2 General Behaviour

4.2.1 Crack Patterns

During the test and at the end of a load increment, the growth of cracks was marked on each beam. This was carried out to identify the direction of crack propagation and to determine the differences in crack patterns of the beams. Figure 4.1 shows the typical gradual formation of cracks in a test beam. The thick lines in the figure are used to

identify the cracks that were formed at failure. The slope of the inclined crack at failure is shown on the figures of the crack patterns. The cracks were drawn to scale as in the actual tests. The extent of a crack at the end of a load increment was marked by a short horizontal line. The loads shown at each crack tip corresponds to the actuator load in kilo-pounds (kips). This load was twice the value of the load at each loading point. For all beams, the first flexural cracks initiated at the bottom of the beam in the constant moment region, where the flexural tension stress was the highest and the shear stress was zero. The observed flexural cracks propagated vertically upward to the level of the neutral axis, which reflected the absence of shear stress. As the load was increased, additional flexural cracks were developed within the shear span. Due to the presence of shear stresses, these flexural cracks became progressively more inclined and propagated towards the load points. These types of cracks are known as flexural-shear cracks. These cracks extended rapidly through the beam leading to the so-called a diagonal-tension failure. The duration between the formation of an inclined crack and failure of a beam was small. ASCE-ACI Committee 426 (1973) reported that for beams with shear span-to-depth ratio between 2.5 and 6.0, the inclined flexural cracks extend to form a diagonal tension crack. This behaviour was observed for most of the beams in the current study. Photographs of the crack patterns for all beams at failure are shown in Appendix A.

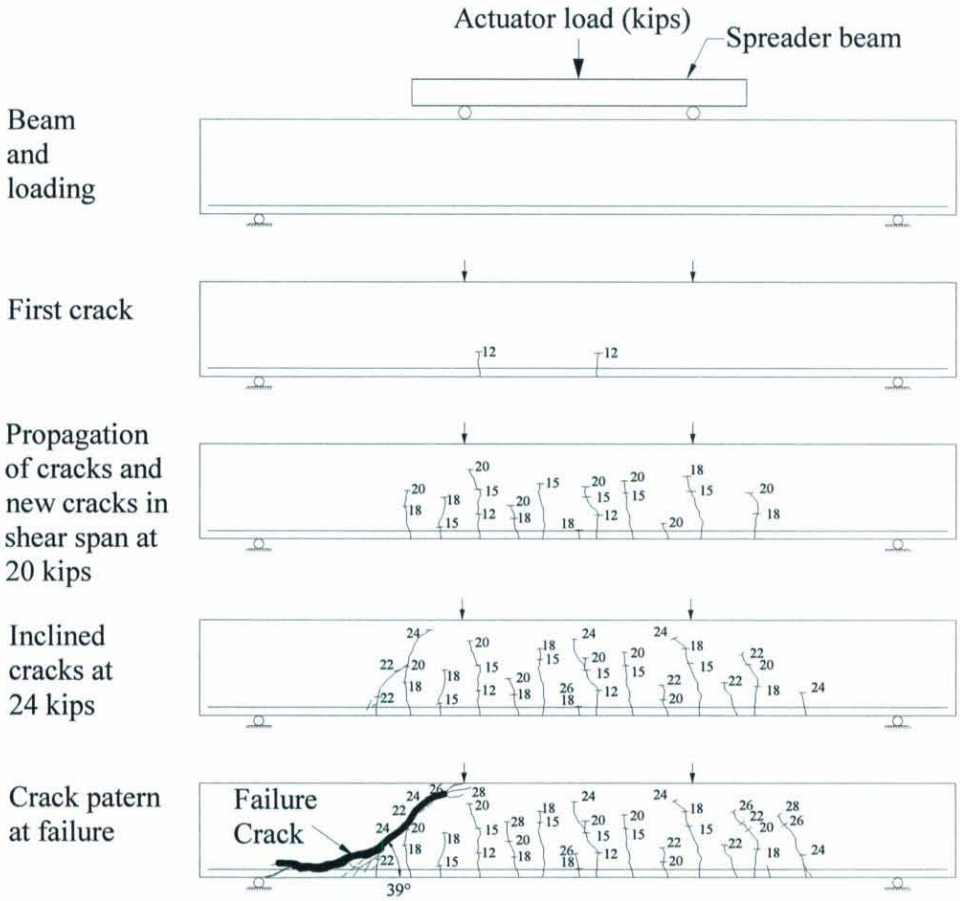

Figure 4.1: Typical formation of cracks in a beam during a test

Figure 4.2 shows the crack patterns for the beams in Group 1 with variable shear span-to-depth ratio (a/d). In general, the slope of the inclined crack decreased as the a/d ratio of the beam increased for all reinforcement types. This is because, at a certain shear load, the moment as well as flexural stress increases as the shear span to depth ratio of a beam increases. Higher flexural stress could lead to the reduction in the inclination of shear cracks. Hence, the horizontal projection of the inclined cracks increased with an

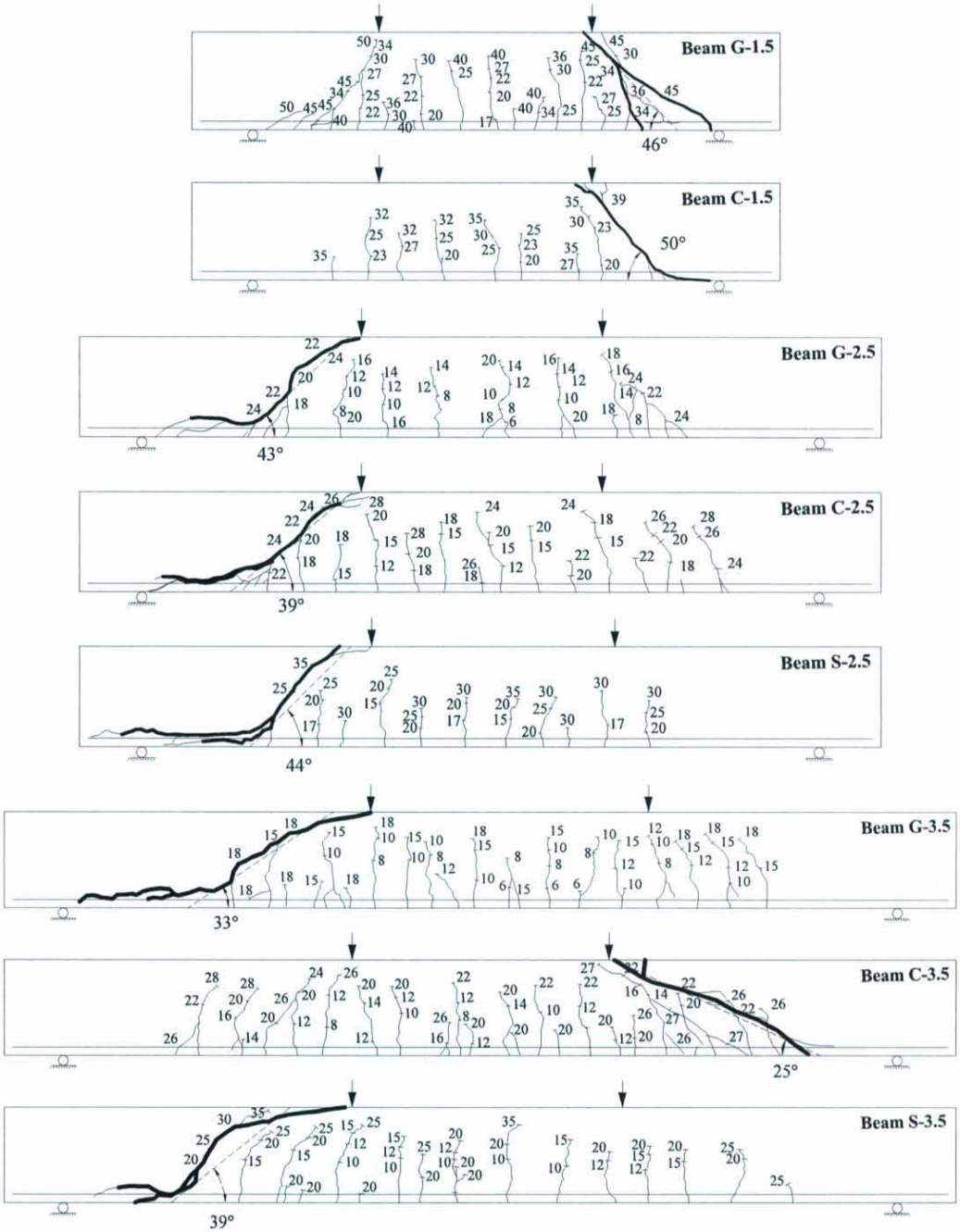

Figure 4.2: Crack patterns for beams with different shear span-to-depth ratios

increase in the shear span-to-depth ratio, for beams with the same depth. It can be seen from Figure 4.2 that the horizontal projection of the cracks for beams with a/d equal to 1.5 was less than the effective depth (d). For beams with a/d equal to 3.5, the horizontal projection was greater than d of the beams. On the other hand, for the same shear span-to-depth ratio, the slope of the inclined shear crack was almost the same for the three types of reinforcements. At a certain load level, and prior to the formation of inclined cracks, the flexural cracks penetrated deeper into the beam for GFRP reinforced beams than in CFRP reinforced beams. Similarly, the cracks penetration in CFRP reinforced beams was higher than those in the steel reinforced beams. This could be due to the higher axial stiffness of the steel reinforcement. Another observation from the test results was the number of cracks in the shear span zone, which increased with an increase in a/d ratio for all reinforcement types.

A distinct behaviour was observed for the beams tested in this group. For all of the beams with different shear span-to-depth ratio, the failure cracks intersected the reinforcement level at approximately the middle of the shear span. The distance of this location from the loading point was greater than the effective depth (d), for beams with a/d greater than 2.5.

Crack patterns for normal strength concrete (NSC) beams with different depths and different reinforcement types are shown in Figure 4.3. The beams had a constant shear span-to-depth ratio. It was noted that the slope of the inclined crack at failure for all beams was close to the 40°. This result revealed that, as the shear span-to-depth ratio of the beams remains constant, the horizontal projection of the inclined crack at failure was

almost same irrespective of the reinforcement type and depth. The number of cracks in the shear span zone during failure was found to be approximately the same for all reinforcement types and depths. At a certain load level, the flexural cracks penetrated deeper into the beam as the axial stiffness of the reinforcing bars decreased.

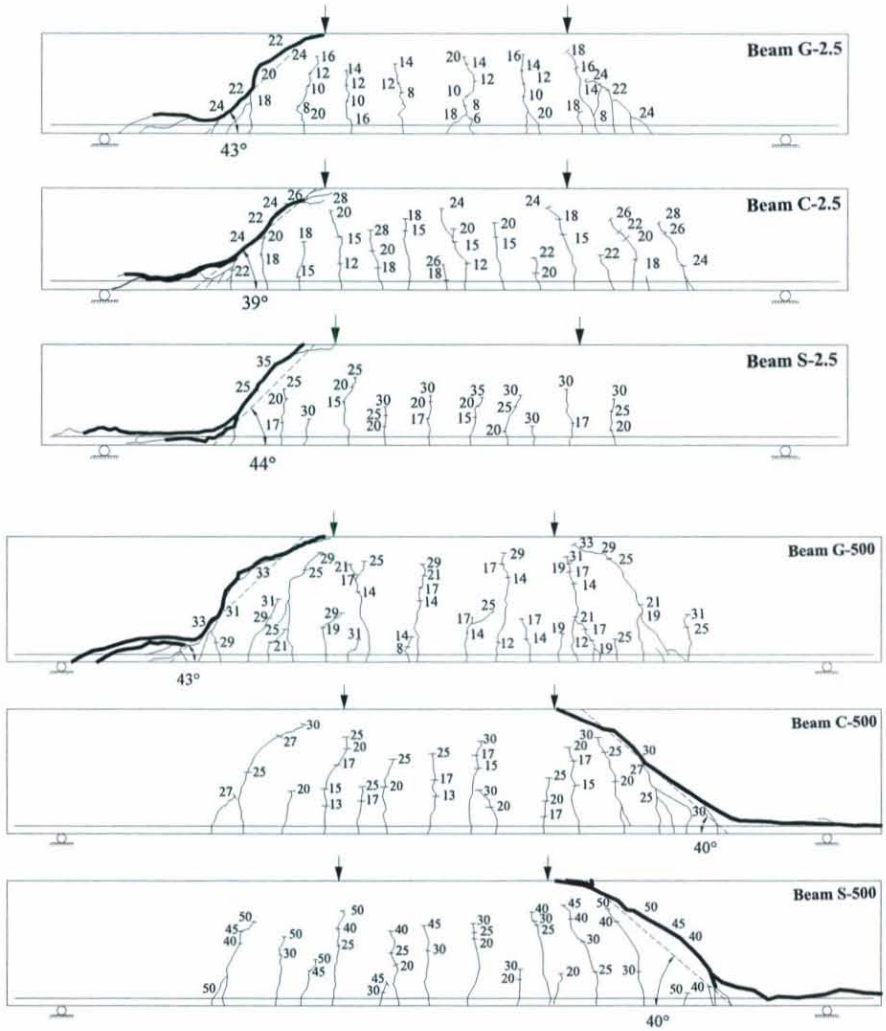

Figure 4.3: Crack patterns for NSC beams with different depths

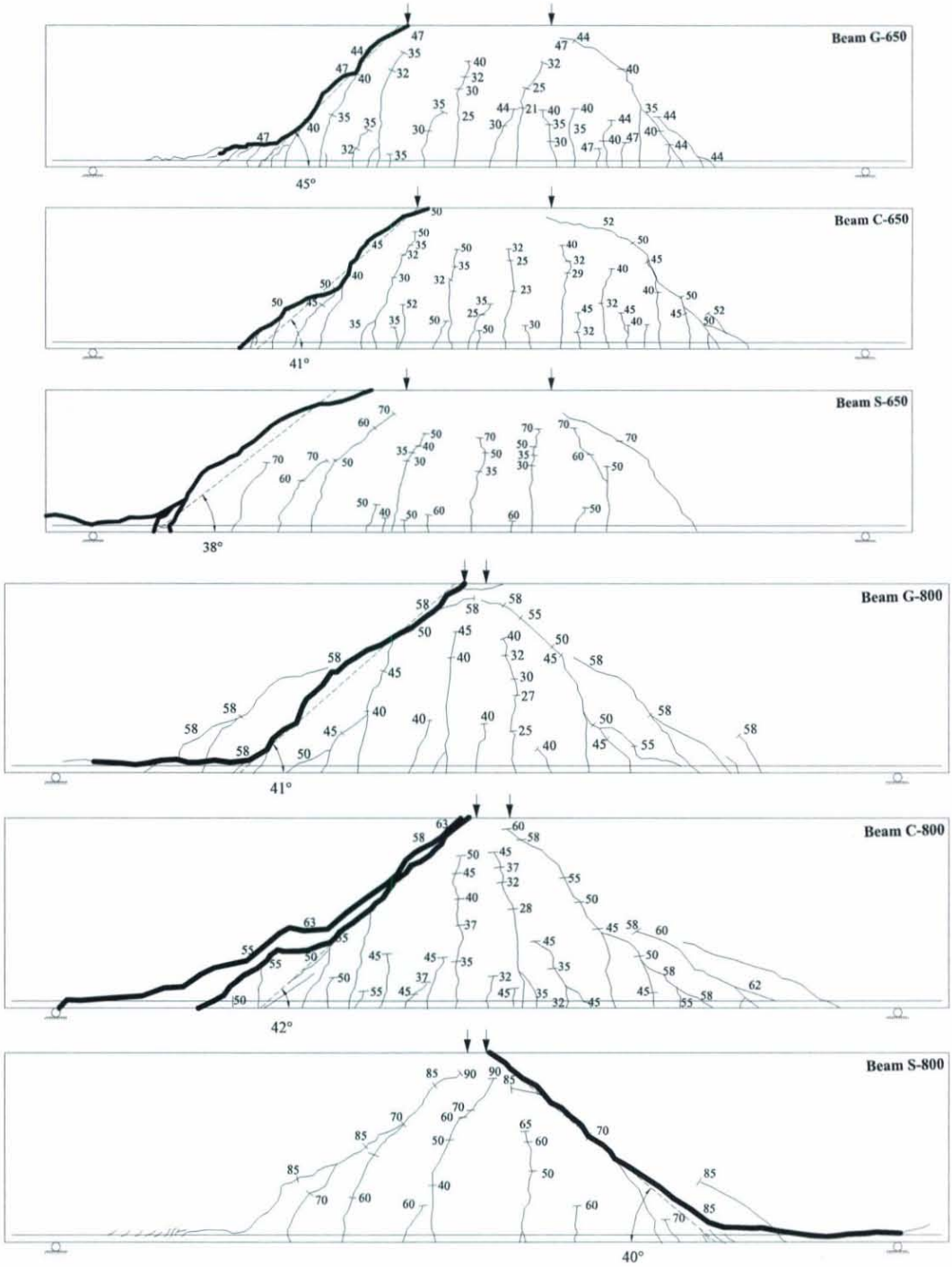

Figure 4.3 (Contd.): Crack patterns for NSC beams with different depths

Figure 4.4 shows the crack patterns of high strength concrete (HSC) beams with different heights and reinforced with GFRP and CFRP bars. The concrete strength was approximately 70 MPa. The observed crack patterns of the high strength concrete beams were approximately similar to those of the normal strength concrete beams, except for beam G-650-70. Several cracks were observed in the shear span for beam G-650-70. This could be attributed to the fact that the inclined crack, developed in one side of the beam, was arrested and the beam continued to carry load. The beam failed after a second inclined crack was formed on the other side of the beam. The slope of the inclined crack at failure for all beams was close to the 40°, which resulted in the horizontal projection of the inclined crack being slightly greater than the depth of the beams.

The effect of reinforcement ratio and type of reinforcement on the crack patterns of Group 3 beams with height equal to 350 mm is shown in Figure 4.5. The beams in this set had the same shear span-to-depth ratio. Three distinct features were observed in these beams. First, the number of flexural cracks which propagated up to the neutral axis decreased as the axial stiffness of the beams decreased. The lowest number of cracks was observed for beam G-0.5-350, where the reinforcement ratio and modulus of elasticity, i.e. the axial stiffness of the reinforcing bar was the lowest. Several cracks were developed at the bottom of the beam which did not propagate to the neutral axis. These cracks merged with previously formed flexural cracks. This can be attributed to the fact that the low axial stiffness of the bars might cause higher strain in the vicinity of the cracks, which caused some bond degradation near the cracks. This could be further

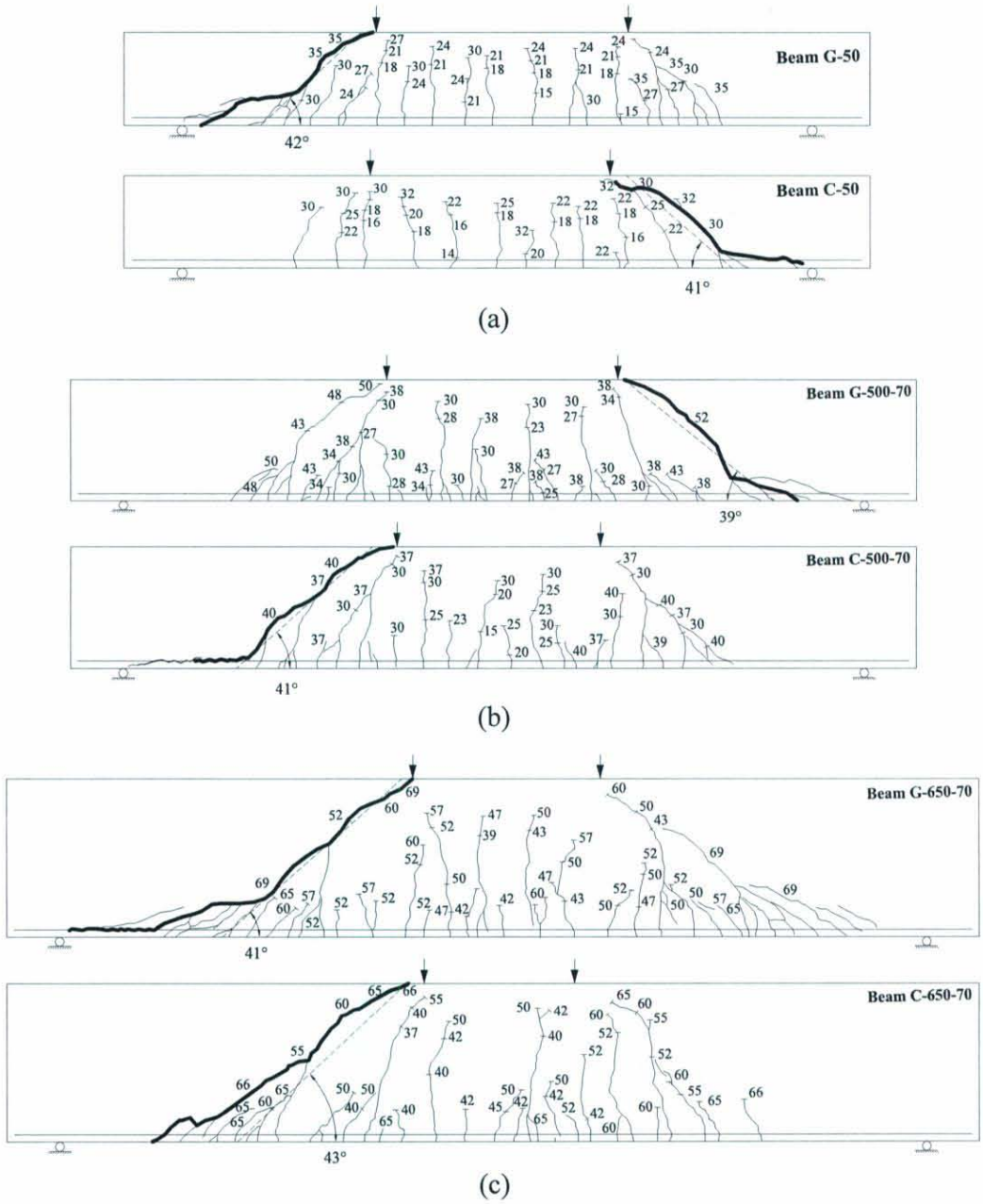

Figure 4.4: Crack patterns for HSC beams with different depths

explained by the tension stiffening effect. According to Sooriyaarachchi et al. (2005), tension stiffening effect in low reinforced members is greater than those in high

reinforced members. Due to higher tension stiffening effect and bond degradation near the cracks, the formation of additional flexural cracks to propagate up to the neutral axis was prevented. Another possible reason is that the redistribution of internal forces in this beam was limited or could not take place due to its low reinforcement ratio (Kani et al. 1979). Second, at a certain load level, the depth of the uncracked concrete compression zone increased as the axial stiffness of the bars increased. This can be explained as the axial stiffness of the bars increased, the strain and the elongation in the bars decreased, which resulted in narrower and shallower cracks in the beam. As a result, the uncracked concrete compression zone increased. This observation is in good agreement with the test results of Gross et al. (2003). The authors reported that, for doubling the reinforcement ratio, the neutral axis depth theoretically increased by 35% for linear-elastic cross section behaviour. The third observation was that the slopes of the failure cracks for all beams were approximately the same.

The crack patterns of Group 3 beams with height equal to 500 mm, for different reinforcement ratios and different reinforcement types, are shown in Figure 4.6. In general, the observed crack patterns were similar to those of the 350 mm beams, except for beam S-2.5-500. Due to anchorage failure that occurred in the beam, the crack patterns were slightly different than those of other beams. The failure crack of this beam occurred away from the loading point. Similar to the observed behaviour of beam G-0.5-350, some of the cracks in beams G-0.5-500 and C-0.5-500 did not propagate to the neutral axis. The same reasons as mentioned earlier for beam G-0.5-350 can be used to explain the behaviour of these beams.

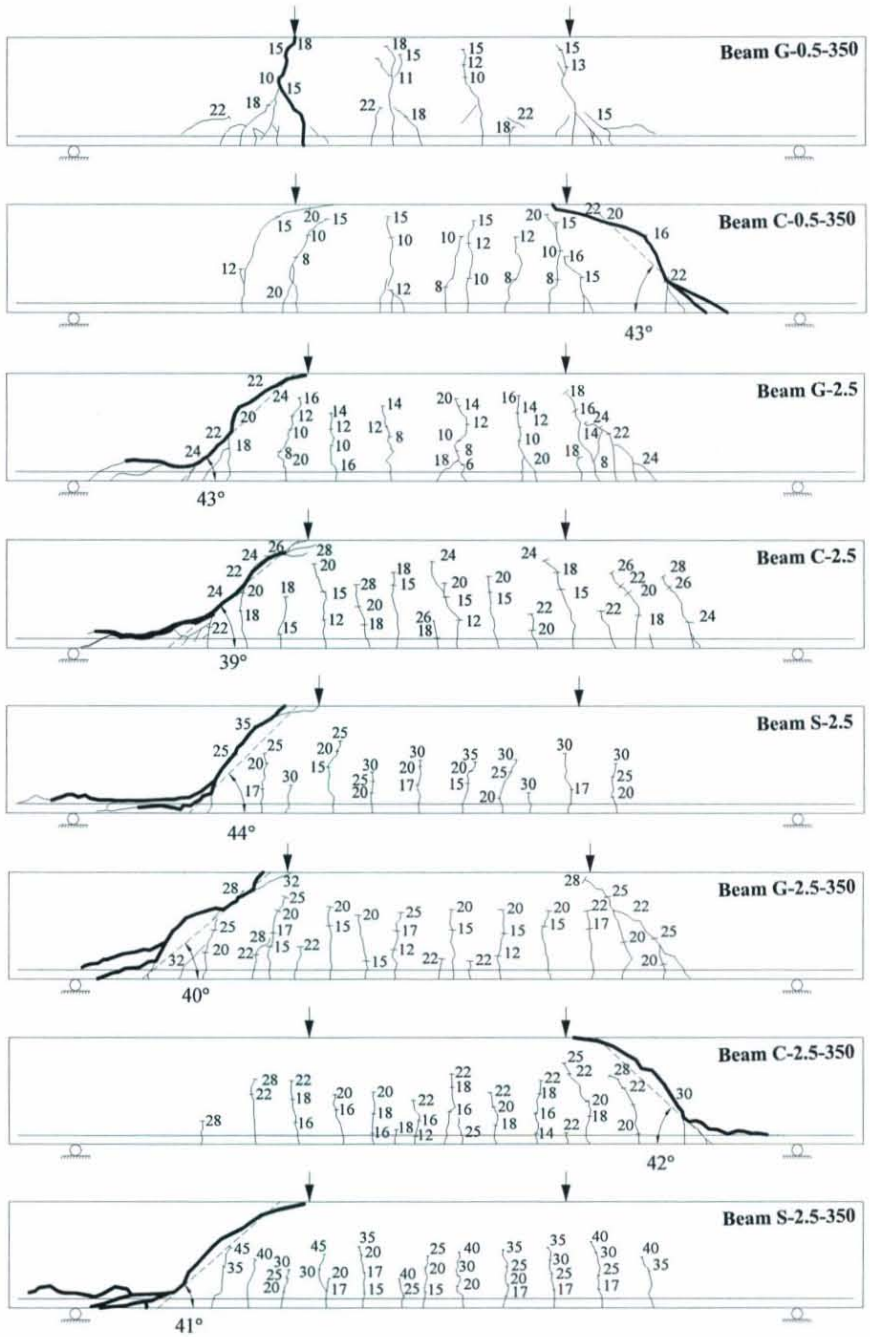

Figure 4.5: Crack patterns for beams with height equal to 350 mm

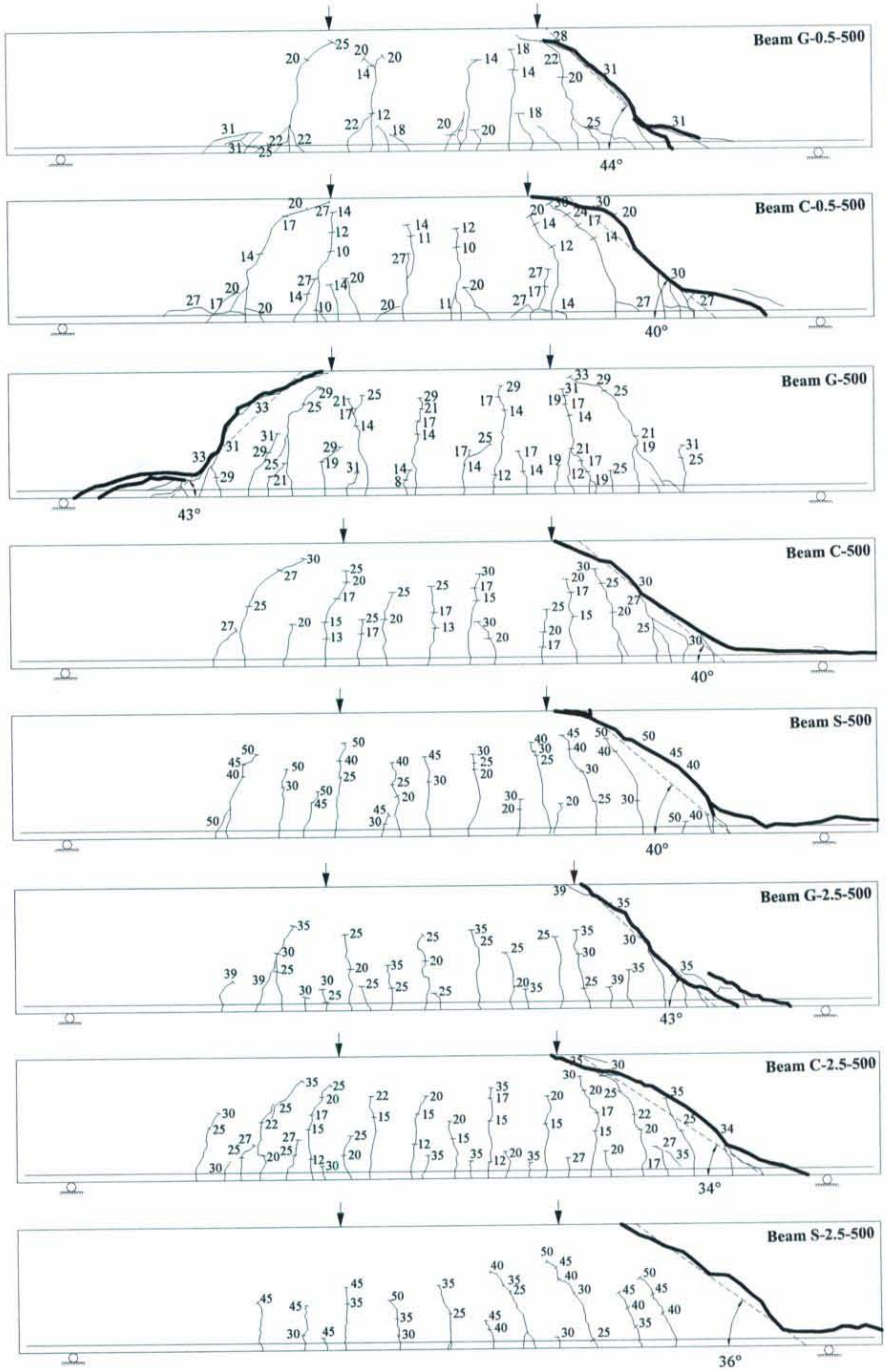

Figure 4.6: Crack patterns for beams with height equal to 500 mm

The crack patterns of Group 4 beams with different compressive strengths are shown in Figure 4.7. The concrete strengths of the beams were approximately 40, 65, and 88 MPa. It was reported by different authors that the depth of uncracked concrete compression zone in high strength concrete beams was smaller than that in normal strength concrete beams (Khuntia and Stojadinovic 2001, Gross et al. 2003, El-Sayed et al. 2006b). This could be attributed to the higher modulus of elasticity of high strength concrete compared to that of normal strength concrete. As a result, the modular ratio ($n = E_f / E_c$) can be expected to decrease for high strength concrete. Consequently, the neutral axis depth, from the extreme compression fibre, and for elastic section behaviour would be smaller for high strength concrete beams than in normal strength concrete beams. For the beams in this group, a decreasing trend in the neutral axis depth, after the first flexural cracking occurred, was observed as the concrete strength was increased. The neutral axis depths for the GFRP reinforced beams were approximately 85, 65, and 72% of the beam height for the three different compressive strengths, respectively. For the CFRP reinforced beams, the neutral axes depths were 74, 89, and 50% of the beam height, respectively. The small discrepancy in the result could be due to human error in visualizing the exact cracking depths. Beam C-70 failed by bond failure between the bars and the sand coating, which resulted in pulling off the bars from one end of the beam. This will be discussed in section 4.2.5. On the other hand, beam G-70 failed by diagonal tension. In beam G-70, many cracks developed in the shear span zone at the bottom of the beam. These cracks propagated towards the loading point and met with the diagonal crack. This can be explained by Kani's (1967) comb model. Due to the flexural action,

the forces in the longitudinal bars were high enough to pull and break the teeth at the root, causing the cracks to merge in one diagonal crack.

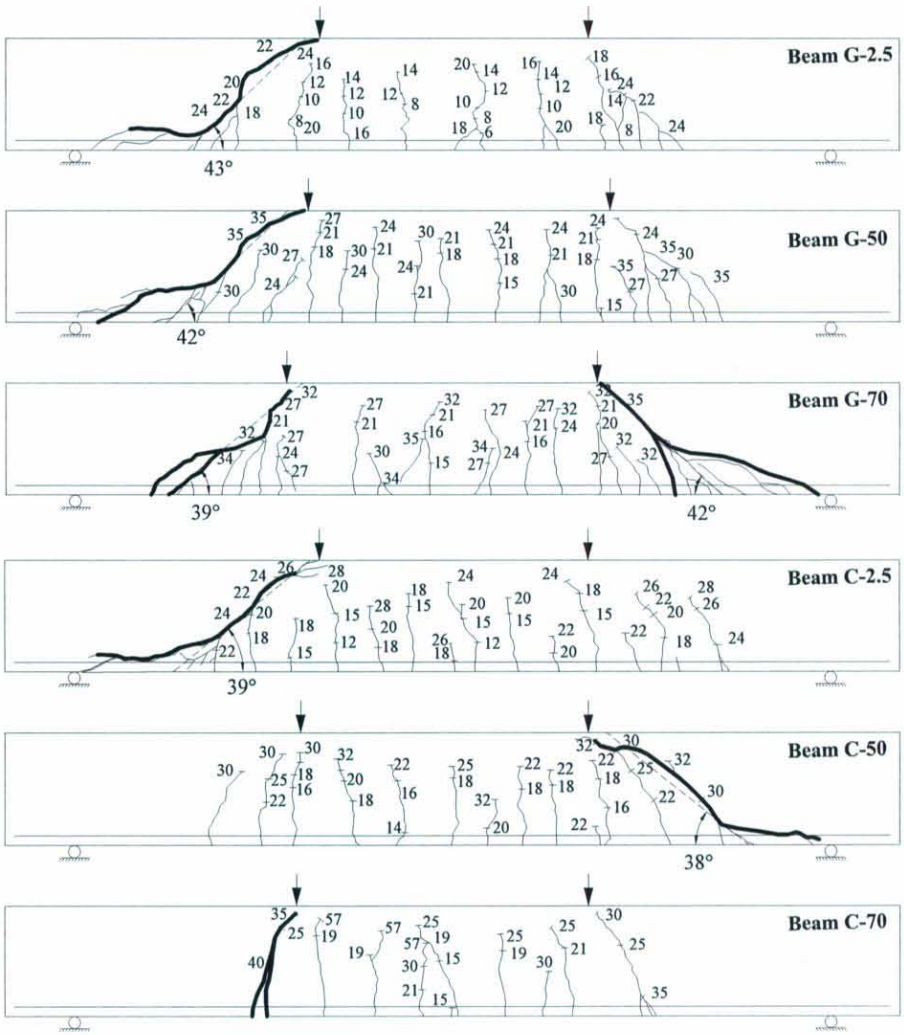

Figure 4.7: Crack patterns for beams with different concrete strengths

4.2.2 Cracking Loads

The load at first flexural cracking was recorded for all beams. The first flexural crack occurred when the moment at a section of the beam reached the cracking moment. The values of the experimental cracking moments (M_{cr-obs}) and the theoretical cracking moments ($M_{cr-calc}$) are shown in Table 4.1. The theoretical cracking moments were calculated using a transformed section analysis at a linear elastic stage. It should be noted that the moment is calculated as the shear load times the shear span of the beam. Therefore, the shear load, which created first cracking at midspan, V_{cr-obs}, will vary according to the loading position; i.e. the shear span of the beams. Hence, for beams with identical cross section, V_{cr-obs} may not be the same. The observed cracking loads (V_{cr-obs}), ultimate shear loads (V_{exp}), concrete strains at failure, and failure modes are tabulated in Table 4.1.

In general, and for all reinforcement types, the cracking load decreased as the shear span-to-depth ratio was increased, and the cracking loads increased with an increase in the reinforcement ratio, height of beam, and concrete strength. These results were expected according to the theoretical predictions of the cracking loads of these beams.

4.2.3 Load-Deflection Behaviour

The deflections of all beams were measured using linear variable differential transducer (LVDT) and were recorded using a high-speed data acquisition system as

Table 4.1: Experimental results

Beam ID	Beam properties						Experimental observations					
	b (mm)	h (mm)	d (mm)	f'_c (MPa)	ρ (%)	ρ/ρ_b	$M_{cr\text{-}calc}$ (kN.m)	$M_{cr\text{-}obs}$ (kN.m)	$V_{cr\text{-}obs}$ (kN)	V_{exp} (kN)	Concrete strain at failure	Failure mode
G-1.5	250	350	305	34.5	0.86	1.26	18.2	17.3	37.8	155.8	0.0020	CR
G-2.5	250	350	305	39.8	0.86	1.12	19.5	13.6	17.8	61.0	0.0014	ST
G-3.5	250	350	305	39.8	0.86	1.12	19.5	14.2	13.3	43.7	0.0023	DT
C-1.5	250	350	310	34.5	0.42	1.39	18.5	20.7	44.5	87.3	0.0005	BF
C-2.5	250	350	310	34.5	0.42	1.39	18.5	15.5	20.0	64.6	0.0018	SC
C-3.5	250	350	310	34.5	0.42	1.39	18.5	14.5	13.3	58.9	0.0017	SR
S-2.5	250	350	310	49.3	0.90	0.18	23.1	20.7	26.7	83.5	0.0004	DT
S-3.5	250	350	310	49.3	0.90	0.18	23.1	14.5	13.3	73.4	0.0011	Y-DT
G-500	250	500	440	44.7	0.90	1.07	42.1	29.3	26.7	77.2	0.0009	DT
G-650	300	650	584	37.4	0.91	1.25	78.3	58.4	40.0	103.7	*	ST
G-800	300	800	734	37.4	0.91	1.24	118.8	94.0	53.4	129.4	0.0022	SC
G-500-70	250	500	442	74.2	1.27	1.05	54.0	56.6	51.2	116.1	0.0007	DT
G-650-70	300	650	578	74.2	1.39	1.15	109.7	125.2	86.7	155.2	0.0009	SC
C-500	250	500	460	42.4	0.45	1.24	42.1	30.7	26.7	74.1	0.0014	DT
C-650	300	650	594	37.0	0.43	1.34	79.7	66.1	44.5	112.9	0.0009	SC
C-800	300	800	744	42.4	0.40	1.12	129.1	111.2	62.3	137.3	0.0026	SC
C-500-70	250	500	449	74.2	0.69	1.27	55.5	37.5	33.4	100.4	0.0010	DT
C-650-70	300	650	594	74.2	0.65	1.20	112.8	122.3	82.3	146.1	0.0004	DT
S-500	250	500	458	41.8	0.87	0.19	44.2	38.2	33.4	111.2	0.0007	DT
S-650	300	650	608	41.8	0.88	0.19	90.5	84.4	55.6	155.7	0.0013	DT
S-800	300	800	758	41.8	0.88	0.19	138.0	173.9	95.6	200.1	0.0007	SC
G-0.5-350	250	350	310	37.4	0.33	0.46	18.8	15.5	20.0	72.7	0.0018	FL
G-2.5-350(1)	250	350	296	39.8	1.43	1.86	19.5	N/A	N/A	65.5	0.0014	SC
G-2.5-350(2)	250	350	296	42.4	1.43	1.77	20.1	19.8	26.7	70.9	0.0008	SC

Table 4.1 (Contd.): Experimental results

Beam ID	Beam properties						Experimental observations					
	b (mm)	h (mm)	d (mm)	f_c' (MPa)	ρ (%)	ρ/ρ_b	$M_{cr\text{-}calc}$ (kN.m)	$M_{cr\text{-}obs}$ (kN.m)	$V_{cr\text{-}obs}$ (kN)	V_{exp} (kN)	Concrete strain at failure	Failure mode
G-0.5-500	250	500	455	37.4	0.35	0.48	38.4	30.4	26.7	68.0	0.0005	SC
G-2.5-500	250	500	434	37.4	1.47	2.02	38.8	33.8	31.1	92.2	0.0007	SC
C-0.5-350	250	350	310	42.4	0.18	0.51	20.2	13.8	17.8	58.7	0.0016	SC
C-2.5-350	250	350	310	34.5	0.67	2.17	18.8	20.7	26.7	72.5	*	DT
C-0.5-500	250	500	460	42.4	0.22	0.62	41.4	25.6	22.2	70.3	0.0012	DT
C-2.5-500	250	500	439	42.4	0.65	1.80	42.2	29.3	26.7	82.5	0.0025	DT
S-2.5-350	250	350	308	49.3	1.43	0.28	23.8	18.8	24.5	106.4	*	ST
S-2.5-500	250	500	458	41.8	1.40	0.31	46.2	50.9	44.5	111.4	0.0005	DT
G-50	250	350	291	65.3	0.89	0.80	24.8	16.2	22.2	75.6	0.0011	SC
G-70	250	350	291	88.3	0.89	0.66	28.8	24.3	33.4	80.2	0.0017	ST
C-50	250	350	310	65.3	0.42	0.85	25.2	22.4	28.9	71.6	0.0010	SC
C-70	250	350	310	88.3	0.42	0.71	29.2	25.9	33.4	77.8	0.0020	BF

* = Strain gauge malfunctioned
CR = Crushing of concrete
SC = Shear-compression failure
ST = Shear-tension failure
DT = Diagonal tension failure
Y-DT = Diagonal tension failure after yielding (steel reinforcement)
FL = Flexural failure
SR = Shear rupture failure
BF = Bond failure

mentioned in section 3.6. Typical load versus deflection curves obtained from the three LVDTs are shown in Figure 4.8. The reactions at the supports are equal to the applied load, which are one-half of the actuator load. The shear force in a beam is equal to the applied load. Hence, in the discussion of the results, the term shear load is used instead of the applied load. The load versus deflection diagram that is shown in the figures contains stage-1, stage-2, and part of stage-3 behaviour. Since the beams in this investigation failed shortly after the formation of diagonal cracks, the shear crack induced deformation was small and this was neglected.

The shape of the load-deflection diagram for middle of the shear spans was approximately the same as the load-deflection diagram for midspan. However, at a certain load level, the deflection at the middle of the shear spans was almost half of the deflection at midspan. In addition, the deflection measurements obtained from the two LVDTs that were placed at the center of each shear span were very close. This revealed that the beams were loaded symmetrically. In this section, the load-deflection behaviour obtained only from the midspan LVDT will be discussed for all beams in different groups. The load-deflection plots from the three LVDTs are shown in the plots of Appendix B for all beams tested in the current study.

Figure 4.9 shows the applied shear load versus midspan deflections for all of the beams in Group 1 with different shear span-to-depth ratio (a/d). In general, the load-deflection behaviour of the beams can be defined by three stages; before cracking, transition from un-cracked to cracked stage, and after cracking. Before flexural cracking

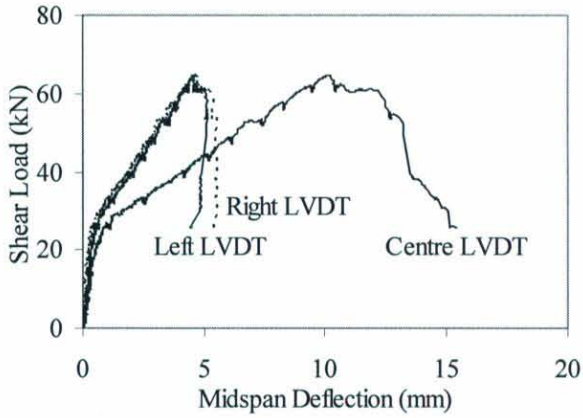

Figure 4.8: Typical load versus deflection curves

occurred, which can be defined as stage-1, the load-deflection behaviour was approximately linear. In this stage, the stiffness of the beams with the same shear span to depth ratio was approximately the same for different reinforcement types. This indicated that the deflections before cracking were not affected by the reinforcement type. However, a deviation from this behaviour was observed for beams G-2.5 and G-3.5. Beam G-2.5 was the first to be tested in this investigation followed by beam G-3.5. There might have been some initial settlement of the beams that affected the readings of the deflections. During stage-2, the beam progressively changed from an un-cracked to fully cracked state, where the existing cracks grew and new flexural cracks developed in the constant moment zone. Due to successive cracking, the stiffness of the beams gradually decreased as a portion of the beam section was no longer effective in carrying loads. At the end of this stage, the behaviour of the beams became linear. This linear behaviour continued until failure and can be defined as stage-3. At this stage, the stiffness of the

beams remained constant while the previously formed cracks grew and new cracks developed in the shear span zone.

For the same shear span-to-depth ratio, and at a certain load level, the deflections of the GFRP reinforced beams were higher than those reinforced with CFRP and steel. This could be attributed to the low axial stiffness of GFRP reinforcement. Nonetheless, it should be noted that GFRP reinforced members have greater tension stiffening than steel reinforced members (Bischoff and Paixao 2004).

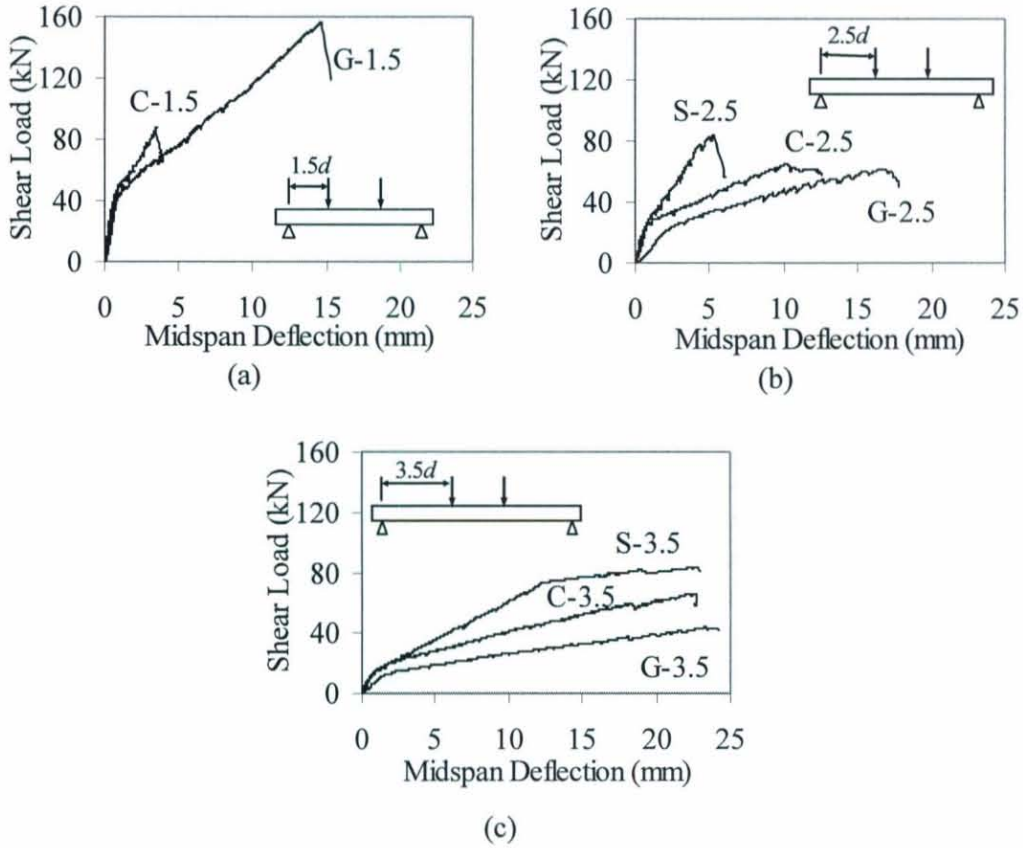

Figure 4.9: Load-deflection profile of beams in Group 1: (a) a/d =1.5, (b) a/d = 2.5, and (c) a/d = 3.5

As expected, the behaviour of beam S-3.5 with traditional steel reinforcement was different from the other beams in this group. A yield plateau occurred after stage-3 due to the yielding of steel reinforcement. Beam G-1.5, for which the shear span-to-depth ratio was 1.5, failed by arch action. Hence, this beam sustained the highest load compared to the other beams.

The stiffness of the beams in stage-3, increased with an increase in the axial stiffness of the reinforcing bars. Figure 4.10 shows the relation between the stiffness of the beams and the axial stiffness of the reinforcing bars at stage-3 for different shear span-to-depth ratios. It was observed that the stiffness of the beams at stage-3 increased with an increase in the axial stiffness of the reinforcing bars for all a/d ratio. It should be noted that for the beams in this group, the clear span increased as the a/d ratio increased. This could lead to a decrease in the stiffness of the beams as the a/d ratio is increased.

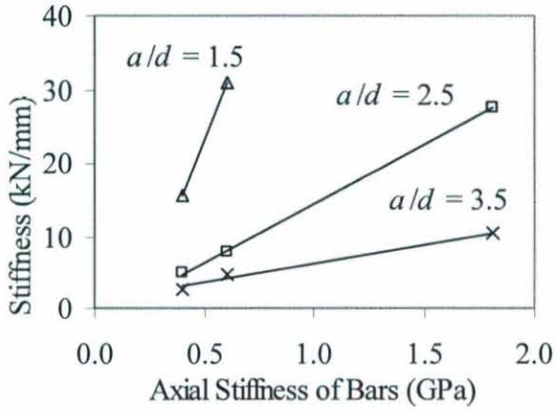

Figure 4.10: Beam stiffness versus axial stiffness of reinforcing bars

The load-deflection behaviour for the normal strength concrete (NSC) beams in Group 2 with different depths is shown in Figure 4.11. In general, the load-deflection curves were linear before the first flexural cracking occurred in the beams irrespective of their individual properties. The cracking loads were found to be close for identical GFRP and CFRP reinforced beams. After cracking, load-deflection curve became nonlinear as the depth of the beams increased. It should be noted that there were some limitations of the lengths of some beams in this investigation as mentioned in section 3.2. Consequently, for beams with height and length equal to 800 and 4040 mm, respectively, the load had to be applied at the centre of the beam to maintain the same shear span-to-depth ratio with other beams. As a result, the loading became similar to a three point loading instead of a four point loading. This could be attributed to the nonlinear behaviour of these beams.

In stage-3, the stiffness of CFRP and GFRP reinforced beams, for which the axial stiffness of CFRP reinforcement was 1.5 times the axial stiffness of GFRP reinforcement, were close. On the other hand, a noticeable increase in the stiffness of steel reinforced beams was observed, as these beams had the highest axial stiffness of the reinforcement, which was approximately 3.0 and 4.5 times the axial stiffness of CFRP and GFRP reinforcement, respectively. This shows that the post-cracking stiffness of the beam is a function of the axial stiffness of the reinforcing bars. This result is in good agreement with the other test results of FRP reinforced concrete beams without web reinforcements (Tureyen and Frosch 2002, El-Sayed et al. 2006a).

Similar to the previous observation, at a certain load level, the deflection in GFRP reinforced beams was higher than the CFRP and steel reinforced beams for each depth of the beams. The same reason as mentioned earlier could be used to account for this behaviour.

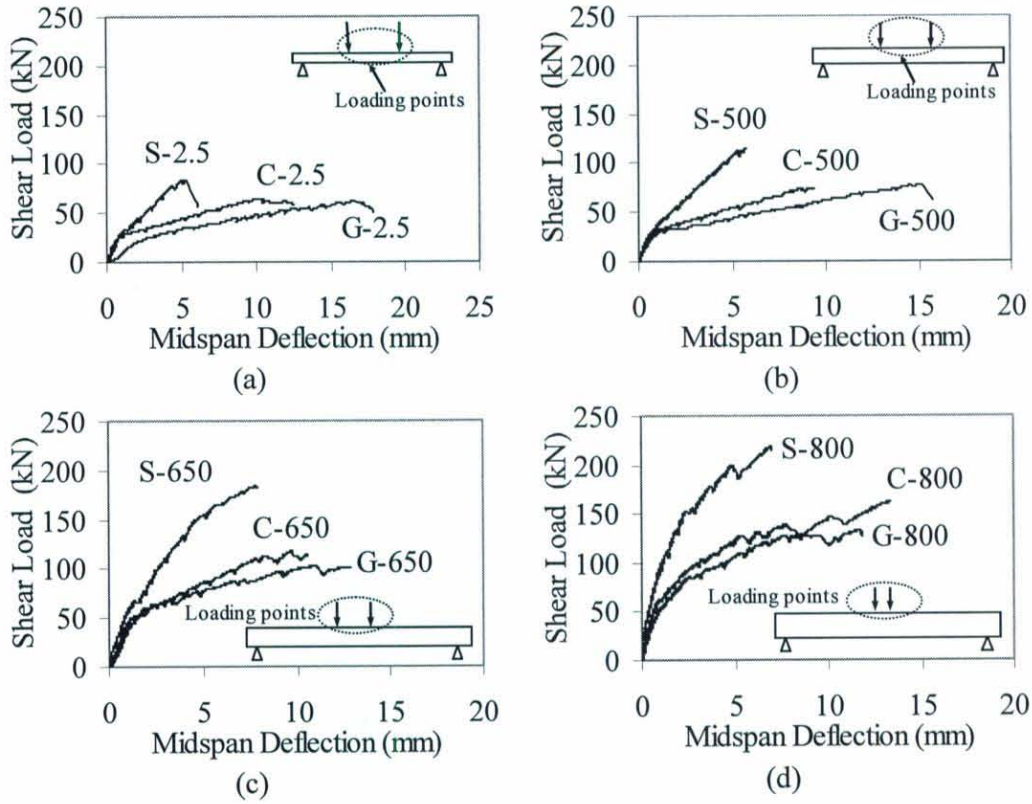

Figure 4.11: Load-deflection profile of NSC beams in Group 2: (a) 350, (b) 500, (c) 650, and (d) 800 mm thick beams

Figure 4.12 shows the load-deflection plots of the high strength concrete beams in Group 2. Similar to the previously mentioned behaviour, three stages of load-deflection behaviour were observed for all beams except beam G-50. This beam continued to carry

the peak load after the initial shear-compression failure, due to a wedging action. The behaviour of this beam will be discussed in Section 4.2.5. It should be noted here that the axial stiffness of CFRP reinforcement was 1.5 times the axial stiffness of GFRP reinforcement. Similar to the normal strength concrete, the first cracking load and the load-deflection behaviour were found to be close for identical GFRP and CFRP reinforced beams.

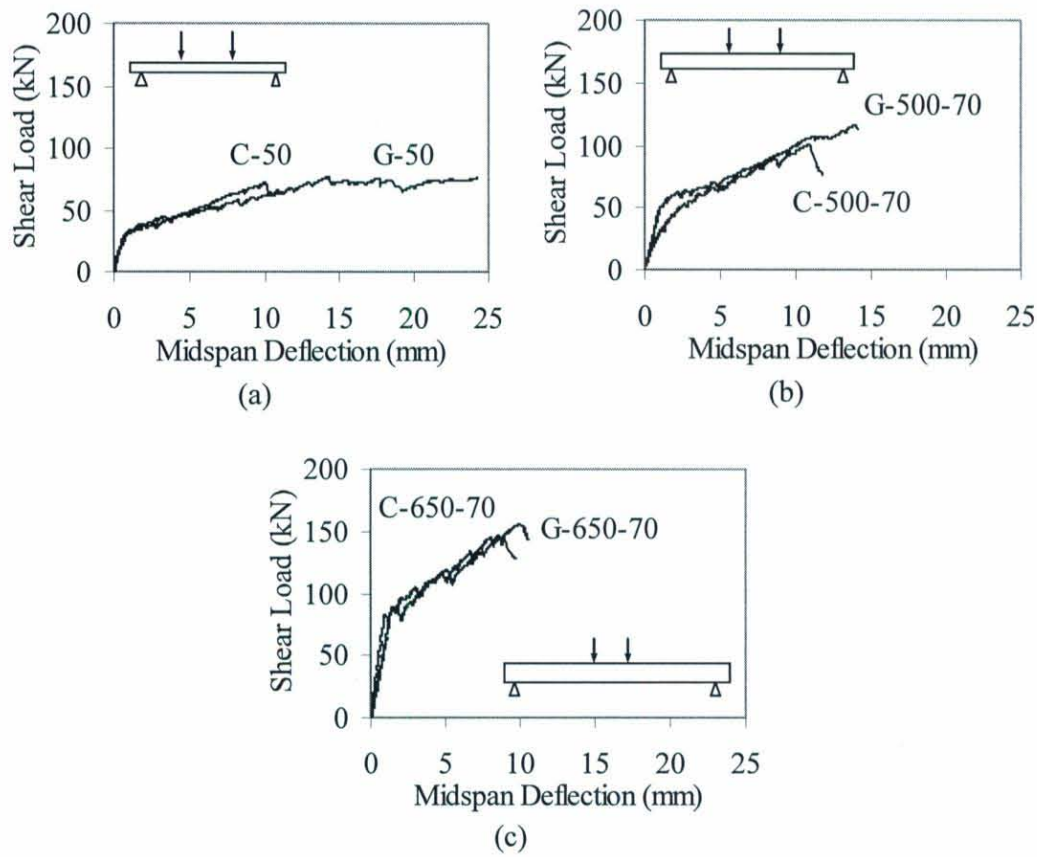

Figure 4.12: Load-deflection profile of HSC beams in Group 2: (a) 350, (b) 500, and (c) 650 mm thick beams

The load-deflection behaviour of 350 mm thick beams in Group 3, for different reinforcement ratios and different reinforcement types, is shown in Figure 4.13. The behaviour of these beams was similar to the behaviour of some beams in the previous groups. However, the load-deflection behaviour in stage-2, which is the transition zone from the uncracked to the cracked stage, was changed as the reinforcement ratio, i.e. the axial stiffness of the reinforcement, was changed. In fact, the transition zone for beam G-0.5-350 was negligible. This beam had a reinforcement ratio that was almost half of the balanced reinforcement ratio and the axial stiffness of the reinforcing bars was the lowest. This could indicate that the transition zone was a function of the axial stiffness of the reinforcing bars for FRP reinforced members.

The behaviour of the beams after stage-2 varied depending on the reinforcement type and ratio. For the same load level, and as expected, the deflection of the beam decreased as the axial stiffness of the reinforcing bars increased, irrespective of the reinforcement type. Table 4.2 shows the axial stiffness of the reinforcing bars. The post-cracking stiffness of the beams increased as the axial stiffness of the reinforcing bars increased. This result is in good agreement with the other test results of FRP reinforced concrete beams without web reinforcements (Tureyen and Frosch 2002, El-Sayed et al. 2006a).

Table 4.2: Axial stiffness of the reinforcing bars in different beams

Beam height = 350 mm		Beam height = 500 mm	
Beam ID	Axial stiffness, $\rho_f E_f$ (GPa)	Beam ID	Axial stiffness, $\rho_f E_f$ (GPa)
G-0.5-350	0.15	G-0.5-500	0.16
C-0.5-350	0.26	C-0.5-500	0.32
G-2.5	0.40	G-500	0.42
C-2.5	0.61	C-500	0.65
S-2.5	1.81	S-500	1.75
G-2.5-350	0.66	G-2.5-500	0.68
C-2.5-350	0.96	C-2.5-500	0.94
S-2.5-350	2.86	S-2.5-500	2.80

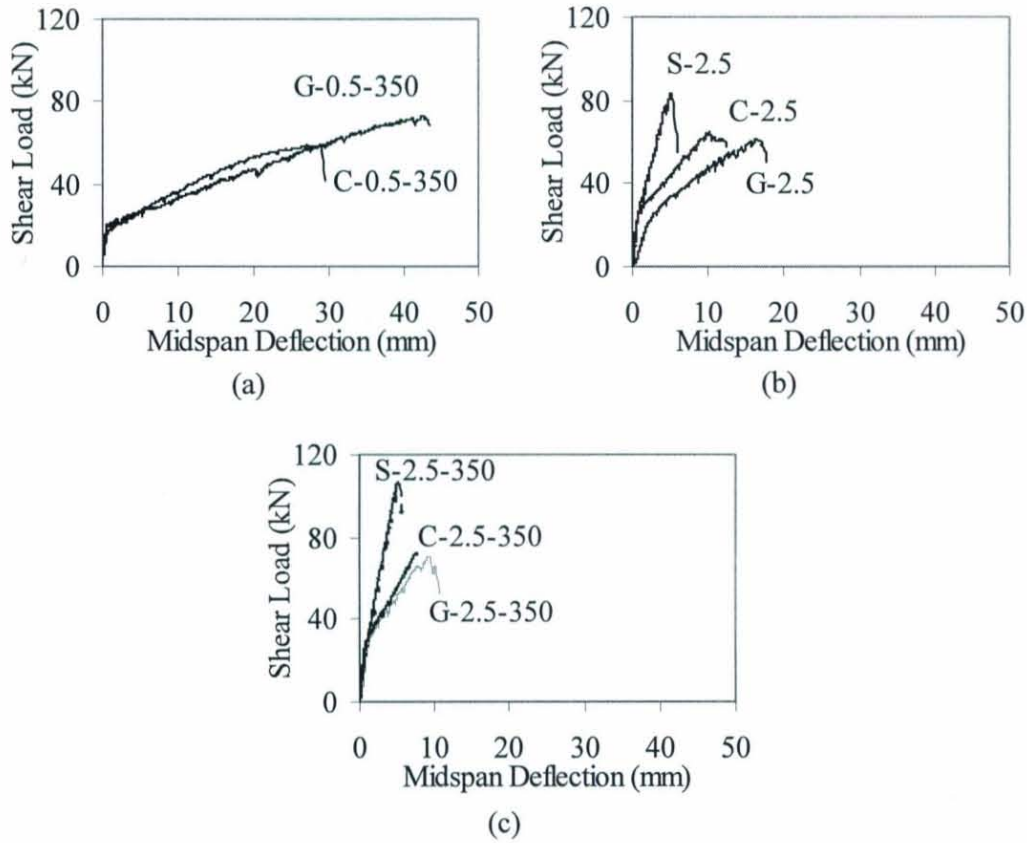

Figure 4.13: Load-deflection behaviour of 350 mm thick beams in Group 3: (a) ρ_f/ρ_b = 0.5, (b) ρ_f/ρ_b = 1.5, and (c) ρ_f/ρ_b = 2.5

The load-deflection behaviour of the 500 mm thick beams in Group 3 for different reinforcement ratios and different reinforcement types are shown in Figure 4.14. Almost similar load-deflection behaviour was observed for these beams as for 350 mm thick beams.

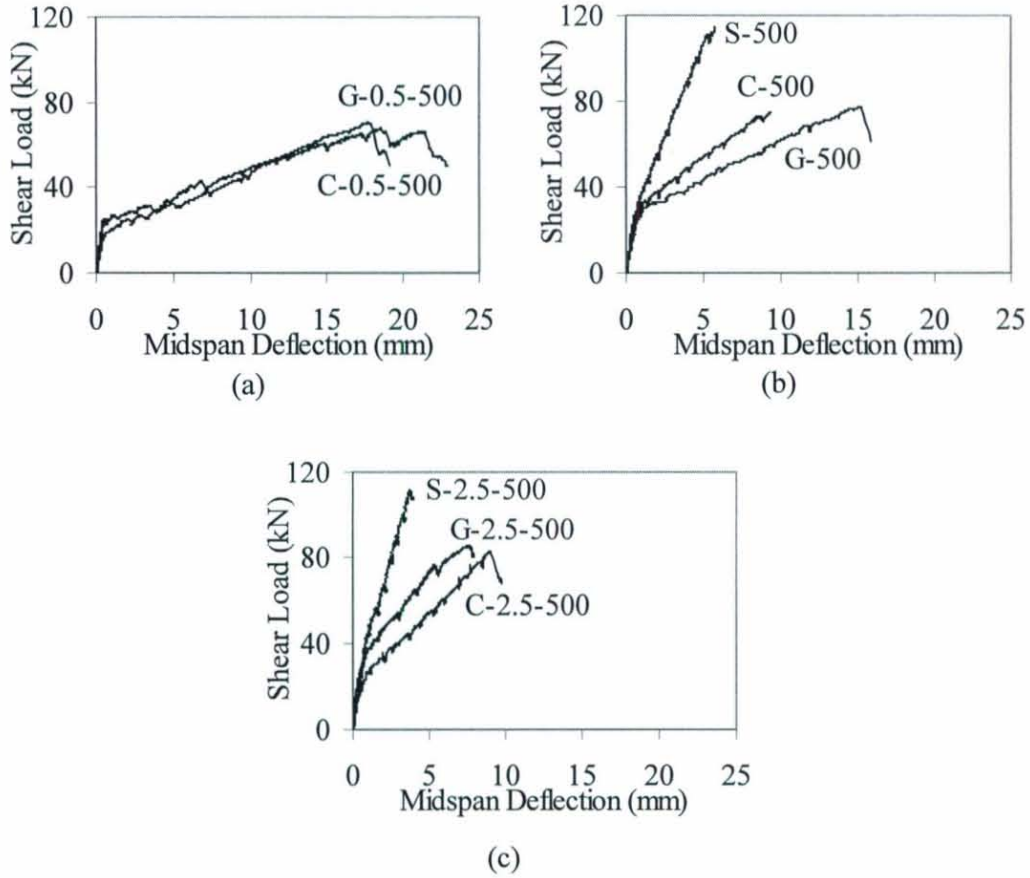

Figure 4.14: Load-deflection behaviour of 500 mm thick beams in Group 3: (a) ρ_f/ρ_b = 0.5, (b) ρ_f/ρ_b = 1.5, and (c) ρ_f/ρ_b = 2.5

The concrete strength did not have a significant effect on the shape of the load-deflection behaviour for 350 mm thick beams. However, beams C-70 and G-70 sustained

higher load compared to the other beams. This could be attributed to their flexural behaviour as will be discussed in section 4.2.5. Beam G-50 continued to carry the peak load after first diagonal cracking and this behaviour will be discussed in section 4.2.5. All other beams in Group 4 showed similar load-deflection characteristics as shown in Figure 4.15. A linear behaviour before cracking, a transition zone from the uncracked to the cracked stage, and post-cracking linear behaviour up to failure were observed for all beams.

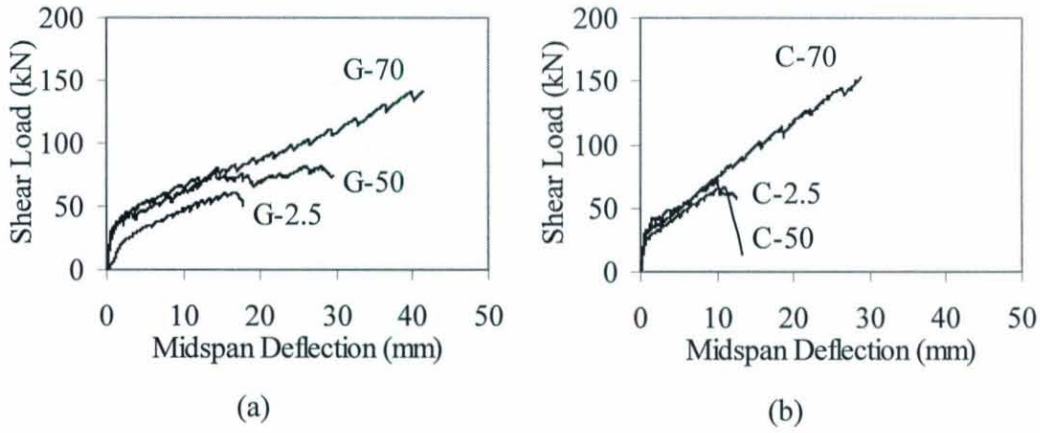

Figure 4.15: Load-deflection behaviour of 350 mm thick beams with different concrete strengths in Group 4: (a) GFRP and (b) CFRP reinforced beams

On the other hand, the effect of the concrete strength on load-deflection behaviour appeared to be more significant for beams with 650 mm height (Figure 4.16). It should be noted here that the axial stiffness of the reinforcing bars in the high strength concrete beams was approximately 1.5 times the axial stiffness of the reinforcing bars in the normal strength concrete beams. Although the behaviour of these beams was similar to the behaviour of 350 mm thick beams, the shear load at first flexural cracking of the

beams increased as the concrete strength was increased. This increase was more pronounced in these beams compared to the beams with 350 mm thick. This difference could be exaggerated by the differences in the axial stiffness of the reinforcing bars between the normal and the high strength concrete beams.

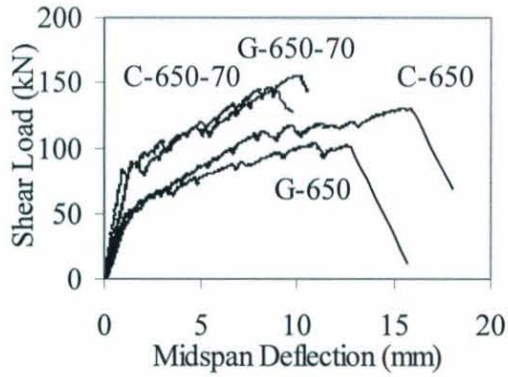

Figure 4.16: Load-deflection behaviour of 650 mm thick beams for different concrete strength

4.2.4 Load-Strain Behaviour

The measured applied loads were plotted as a function of the concrete and reinforcement strains for all beams and these are given in Appendix C. Typical load versus strain plot for concrete and reinforcement is shown in Figure 4.17. In the pre-cracking stage, all strain gauges exhibited a linear behaviour. The strains in the longitudinal bars were very small. After cracking, the strain in the bars at midspan increased as a portion of the concrete was not able to carry tension, which is evident from the Figure 4.17.

Before cracking, the reinforcement strains in the left and right shear span also showed a similar trend as the midspan. However, a sudden increase in the strains was observed at a load level that was approximately twice the first cracking load. While the strains in midspan of the beam increased gradually, the stains in the middle of the shear span increased rapidly after cracking. This could be due to the rapid opening up of the

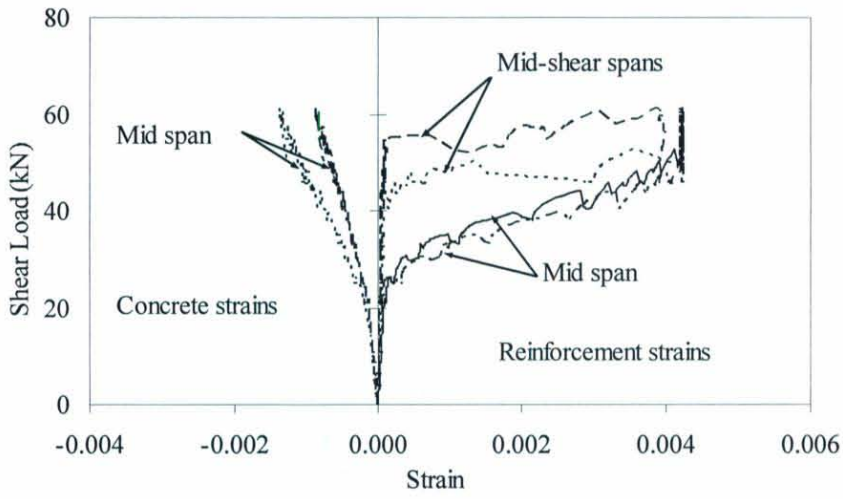

Figure 4.17: Typical stress-strain behaviour of beams

cracks near the strain gauge locations. The increase in load after cracking near the middle of the shear span was small. This behaviour suggests that the beam failed shortly after the formation of the cracks at the vicinity of that location. On the other hand, the concrete strains increased slowly compared to the reinforcement strains and showed approximately nonlinear behaviour up to failure. This behaviour can be attributed to the small compressive stress at the top fibre of the concrete, which is much smaller than the tensile stress in the reinforcement at the bottom of the beam. The concrete strains at failure were

shown in Table 4.1, which were in the range of 400 με to 2500 με. This could indicate that the beams failed in shear before reaching their flexural capacity.

4.2.5 Failure Modes

The observed failure modes for the beams tested in this investigation were reported in Table 4.1. Photographs of the failure mode of all beams are shown in Appendix A. Some of the failure modes are discussed in this section. In general, the failure modes of the beams were either by shear-tension, or shear-compression, or diagonal tension. For some beams, a secondary bond/anchorage failure was observed within the shear span as shown in Figure 4.18. When shear failure was imminent, new type of cracks developed from the existing flexural shear cracks and propagated along the longitudinal reinforcement towards the support leading to a bond or splitting failure. This can be attributed to the fact that when aggregate interlock was lost due to the opening of the inclined crack, the redistribution of the internal forces took place. As the aggregate interlock was lost, the dowel action in the longitudinal reinforcement would increase to maintain equilibrium. The sudden increase in the dowel action increased the vertical tensile stresses in the concrete surrounding the bars. This stress in combination with the existing splitting stress, due to the flexural bond, leads to the final splitting failure along the plane of the reinforcement. Two different failure scenarios were observed for bond/splitting failure. In the first scenario, splitting along the reinforcement passed the support, which occurred simultaneously with the diagonal tension crack propagating towards the concentrated load (Figure 4.18a). In the second scenario, splitting along the

reinforcement stopped before the support and did not cause any splitting past the support (Figure 4.18b).

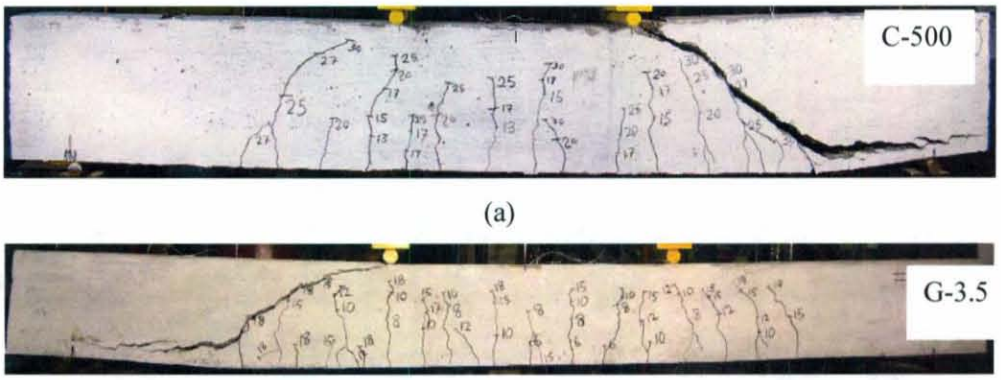

(a)

(b)

Figure 4.18: Bond/anchorage failure of beams

For beams in Group 1, it was observed that, due to the reduction in the shear span-to-depth ratio (a/d), the failure mode was more brittle. In beam G-1.5, with a/d equal to 1.5, few inclined cracks were observed in the shear span zone. These cracks propagated and merged into one crack, which penetrated into the top of the beam at the inner side of the loading point. As a result, an arch action formed in the compression strut between the loading point and the support above the inclined crack. This beam failed by crushing of the concrete near the loading point (Figure 4.19). On the other hand, in beam C-1.5 with a/d equal to 1.5, the flexural crack which developed in the shear span zone turned rapidly into an inclined crack and extended from the support to the loading point. This beam did not exhibit an arch action. One possible reason of this behaviour could be the

bond failure in the sand coating of CFRP bars that inhibited the arch action. Further investigation is needed for beams with a/d less than 2.5 to understand this behaviour. Beam S-3.5 failed by diagonal tension after yielding of the steel reinforcement. In beam C-3.5, the inclined crack, which formed in the shear span zone, penetrated into the top of the beam outside the loading point. Consequently, the beam failed simultaneously by diagonal tension and rupture of CFRP.

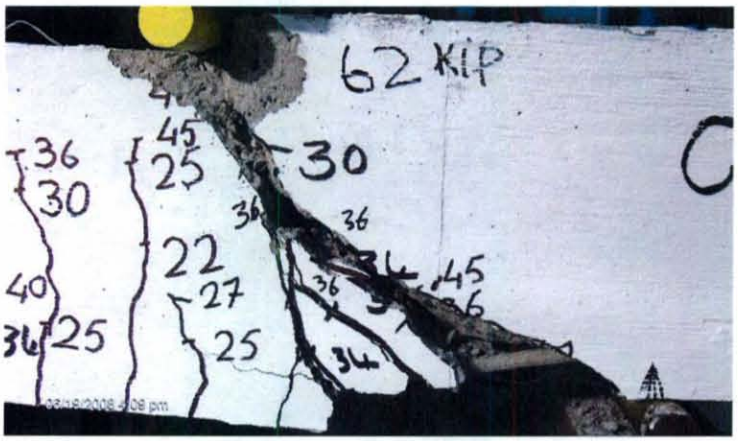

Figure 4.19: Failure pattern of beam G-1.5

In general, the failure modes were found to be more brittle, when the depth and the reinforcement ratio of the beams were increased for each type of reinforcing bars. This behaviour was observed for beams in Groups 2 and 3 (Figures 4.11, 4.13, and 4.14). Steel reinforced beams had the highest axial stiffness of the longitudinal bars and these beams showed more brittle behaviour than the GFRP and CFRP reinforced beams. This means, that the ductility of the beams that failed in shear decreased as the axial stiffness

of the beams increased, which is evident from the test results of the beams in these groups. Beam G-0.5-350 in Group 3, which had the lowest reinforcement ratio, failed by rupture of GFRP bars in a flexural failure mode. During loading, when the load reached the cracking load, a few flexural cracks were developed simultaneously at the bottom of this beam. As the load was increased, few additional cracks were developed at the bottom and these cracks did not propagate beyond the mid-depth of the beam. Instead, the previously formed cracks propagated vertically upward and the crack widths became wider. Consequently, the bars ruptured at the crack location below one of the loading point as shown in Figure 4.20.

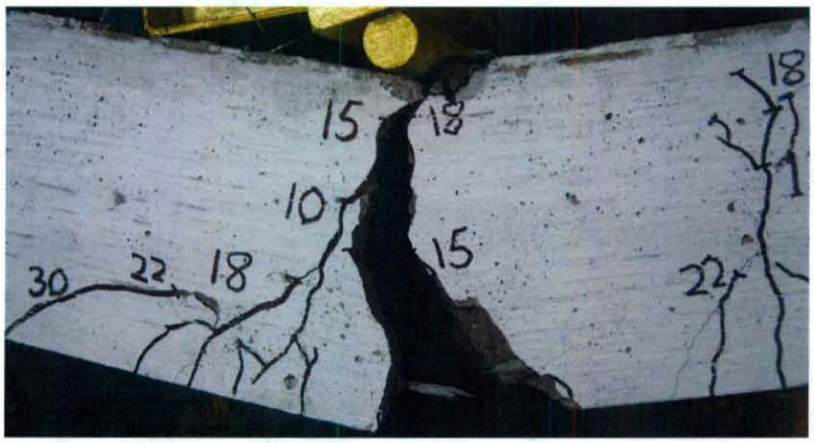

Figure 4.20: Failure pattern of beam G-0.5-3.5

Typical shear-compression failure mode was observed for high strength concrete beams in Group 4. However, beam C-70, for which the compressive strength was 88 MPa and reinforced with CFRP bars, failed by bond failure between the bars and the sand coating. One of the cracks near the loading point became excessively wide as the bars

pulled off. The failure of this beam was sudden and associated with the spalling of concrete around the bars as shown in Figure 4.21.

Figure 4.21: Failure pattern of beam C-70

Although beam G-50 failed by shear-compression near the loading point, this beam continued to carry load after the initial failure; which is explained below. The concrete compressive strength of this beam was 65 MPa. Flexural cracks initiated near the midspan and below one of the loading points of the beam at a load level of 33.4 kN. The number of flexural cracks increased with an increase in the loads, and a flexural crack developed in one of the shear span at 53.4 kN. With further increasing of the loads, several flexural-shear cracks developed in the shear span and one of these cracks extended through the beam to the loading point at 75.6 kN (Figure 4.22a). At this stage, the beam did not fail, rather, it continued to carry load after crushing of the concrete at 81.7 kN. The possible explanation of this is a secondary beam action. The secondary beam action can be explained as follows. The failure shear crack was almost vertical at the mid-height of the beam (Figure 4.22a). After crushing of the concrete, the crack width at the top and bottom of the beam became wider. Due to a wedging action, friction forces

developed in the vertical crack due to the sliding of one part of the beam on the other part as shown in Figure 4.22b. Also, a compressive force was developed at this point.

Hence, a new beam action developed with this compressive force and the tensile force in the GFRP bars, with depth that extended from the mid-height of the beam to the reinforcement level. A schematic diagram of this action is shown in Figure 4.23. It can be seen from the figure that the depth of this new beam was almost half of the original depth, and the shear-span-to-depth ratio (a/d) became twice, which is equal to 5.0. Consequently, the beam showed some signs of flexural behaviour.

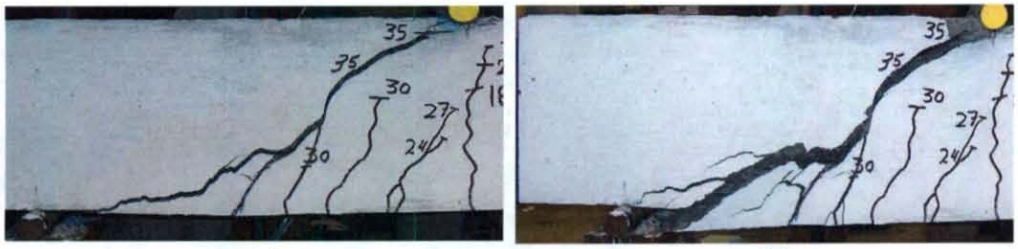

(a) (b)

Figure 4.22: Failure mechanism of beam G-50; (a) crack width before failure and (b) crack width after failure

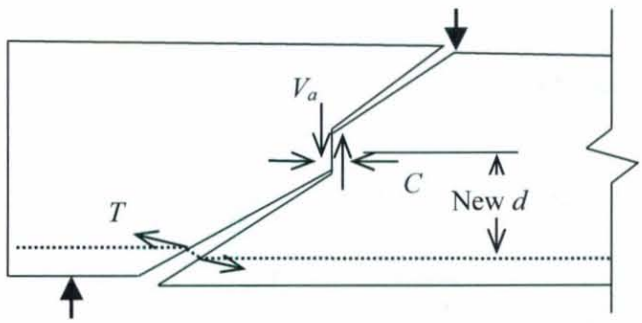

Figure 4.23: Schematic diagram of secondary beam action

4.3 Analysis of Test Data

4.3.1 Shear Strength

Tureyen and Frosch (2002) identified the shear strength of the flexural members by the formation of an inclined crack and the subsequent sudden drop in load carrying capacity. The differences between the formation of inclined cracking loads and the ultimate loads were within 15% of each other. According to Rebeiz (1999), the shear strength at ultimate failure is a more defined and reliable measure than the cracking shear strength. It should be noted that for some beams more than one peak might appear in the load-deflection curve. This would occur due to the formation of an inclined crack at one end of the beam that is arrested and eventually the beam fails due to the inclined crack at the other end of the beam. Bažant and Kazemi (1991) considered the first peak load as the shear strength of a beam as this load agreed reasonably well with the overall trend of the size effect that the authors proposed. The authors also mentioned that it is unreasonable to design a beam for the second main peak load, regardless of which main peak is higher.

In this investigation, the maximum load at which there was either a complete and abrupt failure, as shown in Figure 4.9 (Beam C-1.5), or at which there was a sudden drop in applied load, as shown in Figure 4.11d (Beam G-800), was considered as the failure shear strength. For a few beams, the inclined cracking load was considered as the failure shear strength. This failure shear strength, which is the concrete contribution, V_c, is identified as V_{exp} in this thesis and is reported in Table 4.1.

4.3.2 Effect of Main Variables

Effect of Shear Span-to-depth Ratio, a/d

The effect of shear span-to-depth ratio on concrete shear strength of the test beams is shown in Figure 4.24. In general, the shear strength decreased with an increase in the shear span-to-depth ratio. This effect was reduced when the shear span-to-depth ratio was increased from 2.5 to 3.5. This could be attributed to the fact that, as a/d ratio increases, the angle between the compression strut and the tension tie will decrease, and the load carrying capacity of the compression strut will decrease. Beam G-1.5 showed significantly higher load than the other beams, as this beam failed by arch action.

When the shear strengths were normalized by $\sqrt{f_c'}b_w d$ and plotted against a/d ratio, similar behaviour was observed (Figure 4.24b). Notice that the differences in the normalized shear strengths of steel reinforced beams with respect to GFRP and CFRP reinforced beams were not worth mentioning. One possible reason of this is the low reinforcement ratio, where the reinforcement ratio of steel reinforced beams was 18% of the balanced reinforcement ratio. For these beams, the redistribution of internal forces was limited or could not take place (Kani et al. 1979).

Figure 4.25 shows the variation of normalized shear strength with the square of the cubic root of the depth to shear span ratio $(d/a)^{2/3}$ of the beams. Except for beam G-1.5, the normalized shear strength varies almost linearly with $(d/a)^{2/3}$. Razaqpur and Isgor (2006) observed the similar behaviour for beams with a/d ratio greater than 2.5.

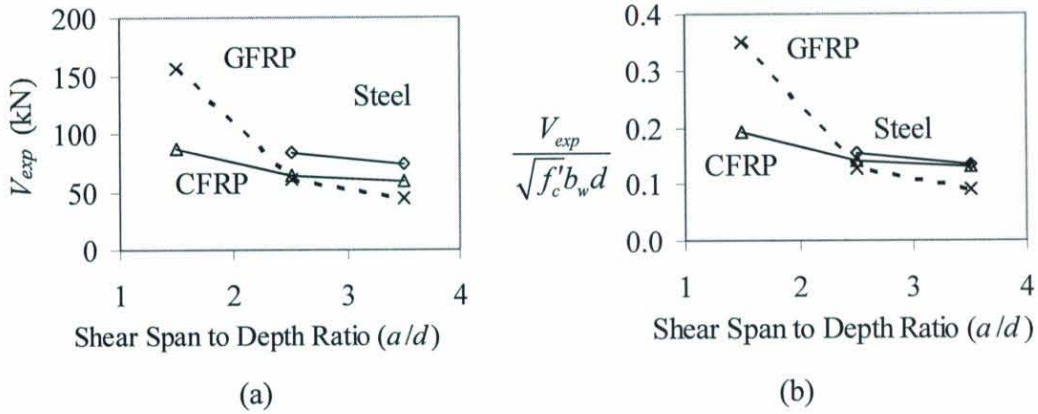

Figure 4.24: Effect of shear span-to-depth ratio; (a) experimental shear strength, (b) normalized shear strength

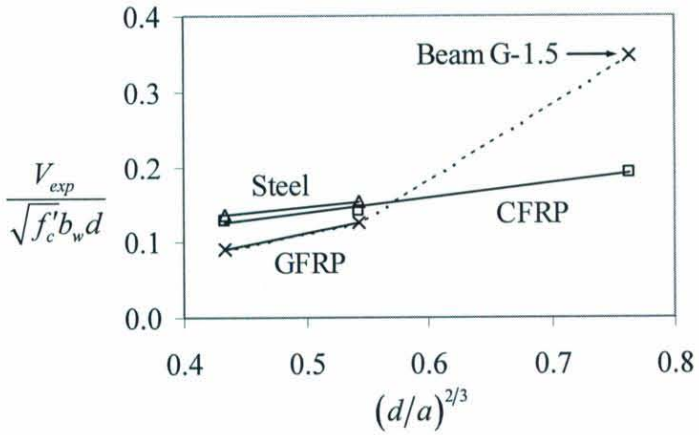

Figure 4.25: Variation of normalized shear strength with the square of the cubic root of depth to shear span ratio

Effect of Depth of Beam, *d* (Size Effect)

The shear strength obtained for beams with approximately 300, 450, 600, and 750 mm effective depths for each of three reinforcement types, showed that the shear strength increased with an increase in d. However, when the shear strengths were normalized

with respect to $\sqrt{f_c'}b_w d$, a reverse behaviour was observed. The observed behaviour for normal strength concrete is shown in Figure 4.26. In general, a decreasing trend was observed for normalized shear strengths ($V_{exp}/\sqrt{f_c'}b_w d$) with an increase in the depth for steel, GFRP, and CFRP reinforced concrete beams (Figure 4.26b). This could be due to the size effect in the shear strength of concrete beams.

It is noticeable that, although the axial stiffness of CFRP reinforcement was approximately 1.5 times the axial stiffness of GFRP reinforcement, approximately the same shear strengths were observed for identical CFRP and GFRP reinforced beams for different depths. However, the shear strength of steel reinforced beams was found to be more than the shear strength of GFRP and CFRP reinforced beams. This can be attributed to the higher axial stiffness of the steel reinforcement compared to the GFRP and CFRP reinforcement.

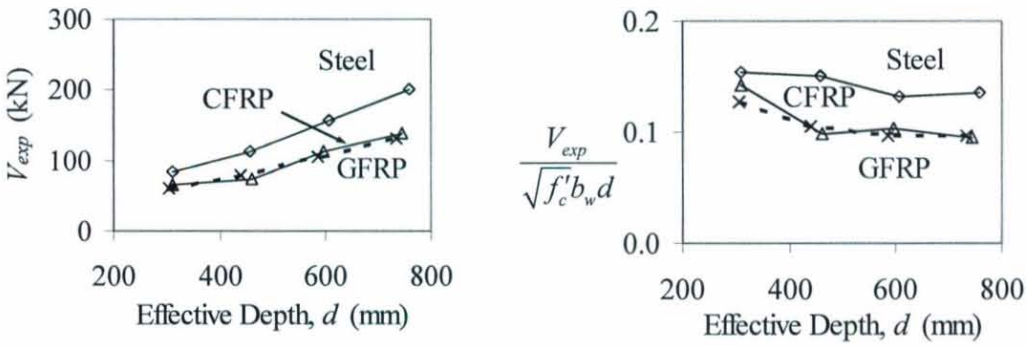

Figure 4.26: Effect of depth for normal strength concrete; (a) experimental shear strength, (b) normalized shear strength

Figure 4.27 shows the effect of depth on the shear strength of high strength concrete beams reinforced with GFRP and CFRP bars only. For this case, the effective depths of the beams were approximately 300, 450, 600 mm and the concrete strength was approximately 70 MPa. Similar to the normal strength concrete, size effect was observed for high strength concrete. The normalized shear strength decreased with an increase in the depth of the beams. The decease in the shear strengths were approximately the same for both reinforcement types.

To investigate the variation of normalized shear strengths with the effective depths, the normalized shear strengths $\left(V_{exp}/\sqrt{f_c'}b_w d\right)$ were plotted against the inverse of the cubic root of the effective depths, $1/d^{1/3}$ (Figure 4.28). It was observed that the normalized shear strength increased almost linearly with $1/d^{1/3}$, for both normal and high strength concrete beams. There were no considerable differences in the trend of normalized shear strength for normal and high strength concrete beams.

Effect of Reinforcement Ratio, ρ

The test results for different reinforcement ratios and different reinforcement types are illustrated in Figure 4.29 for beams with height equal to 350 mm. The reinforcement ratios were 0.90 and 1.43% for steel; 0.86 and 1.43% for GFRP; and 0.18, 0.42, and 0.67% for CFRP reinforced beams. Due to flexural failure, one of the GFRP

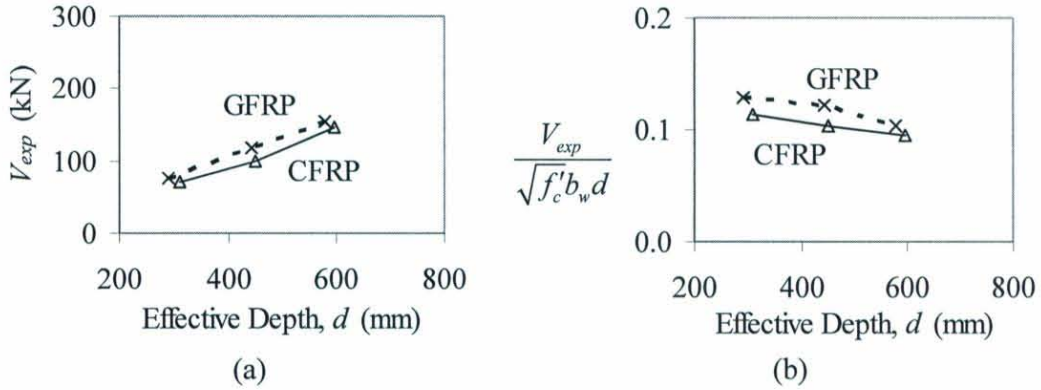

Figure 4.27: Effect of depth for high strength concrete; (a) experimental shear strength, (b) normalized shear strength

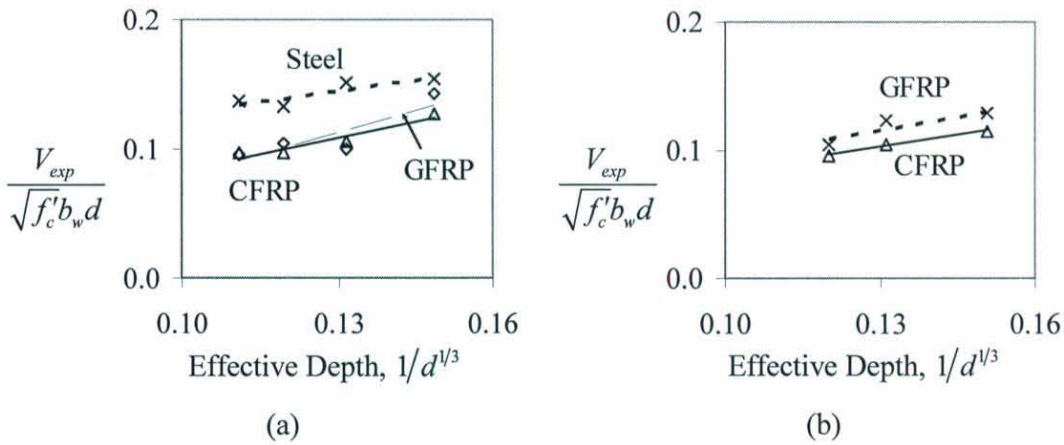

Figure 4.28: Variation of normalized shear strength with cubic root of depth: (a) NSC, and (b) HSC beams

reinforced beams with 0.33% reinforcement ratio was not included in this comparison. It can be seen (Figure 4.29a) that the shear strength increased with an increase in the longitudinal reinforcement ratio. This was more prominent in Figure 4.29b when the shear strengths were normalized by $\sqrt{f_c'}b_w d$. Gross et al. (2003) also observed a slight

increase in the shear strength of GFRP reinforced beams with an increase in the longitudinal reinforcement ratio. It can be shown here (Figure 4.30) that the increase in shear strength is related to approximately the cubic root of the axial stiffness of the reinforcing bars. The same relationship is used in CSA S806-02 guideline.

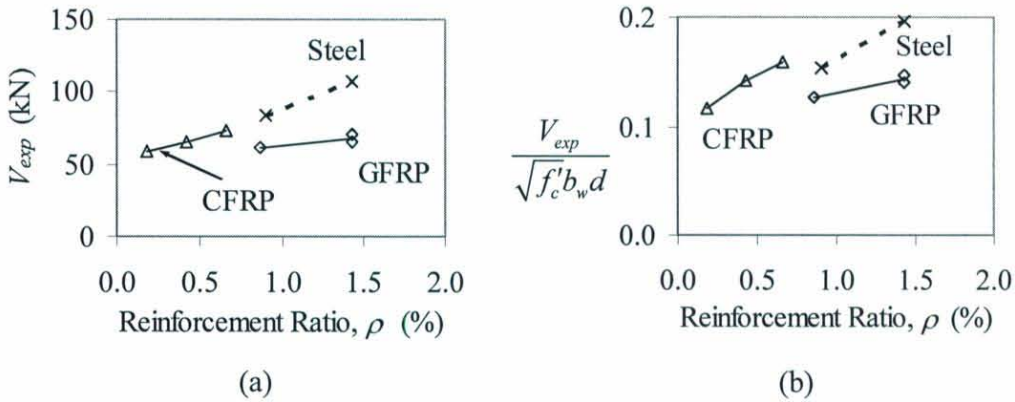

Figure 4.29: Effect of reinforcement ratio for 350 mm thick beams; (a) experimental shear strength, (b) normalized shear strength

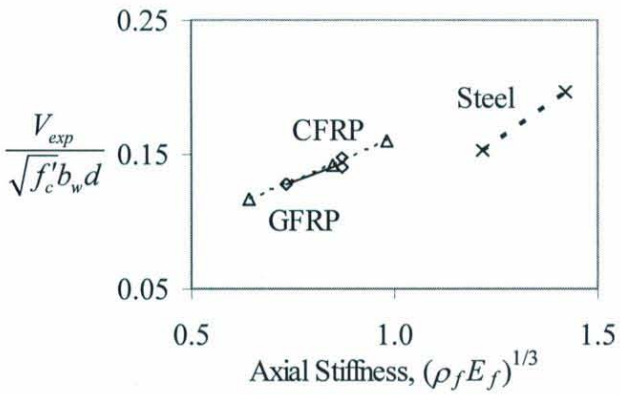

Figure 4.30: Variation of normalized shear strength with respect to the cubic root of the axial stiffness for 350 mm thick beams

Figure 4.31 shows the effect of reinforcement ratio for beams with height equal to 500 mm. While approximately the same behaviour was observed for 350 mm thick GFRP and CFRP reinforced beams, the behaviour of steel reinforced beams was different. In this study, the axial stiffness of steel reinforcement was approximately 3.0 and 4.5 times the axial stiffness of identical CFRP and GFRP reinforcement, respectively. No increase in the shear strength was observed for steel reinforced beams. It could be due to the fact that an increase in the reinforcement ratio can increase the shear strength of steel reinforced deep beams ($a/d \leq 2.5$) up to a certain limit, beyond which no more shear strength improvement could be achieved (Ashour 2000). When the normalized shear strengths were plotted against the cubic root of the axial stiffness of the reinforcing bars (Figure 4.32), almost similar behaviour was observed as of 350 mm thick beams. From this observation, it can be concluded that the shear strength is approximately directly proportional with the cubic root of the axial stiffness of the reinforcing bars.

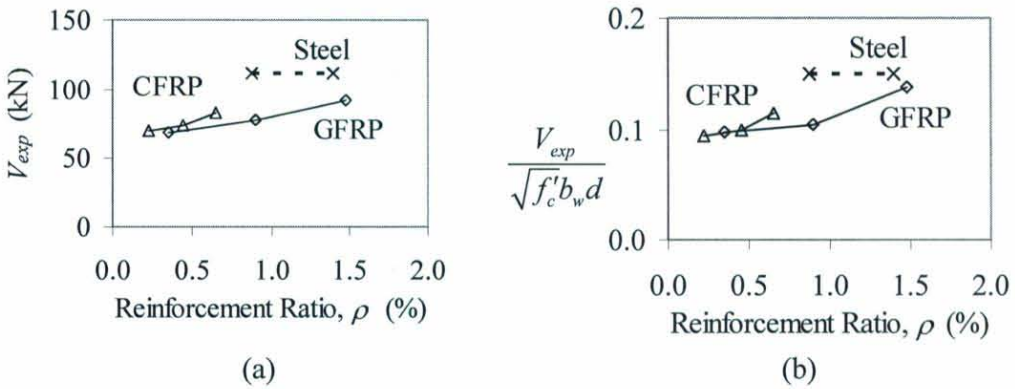

Figure 4.31: Effect of reinforcement ratio for 500 mm thick beams; (a) experimental shear strength, (b) normalized shear strength

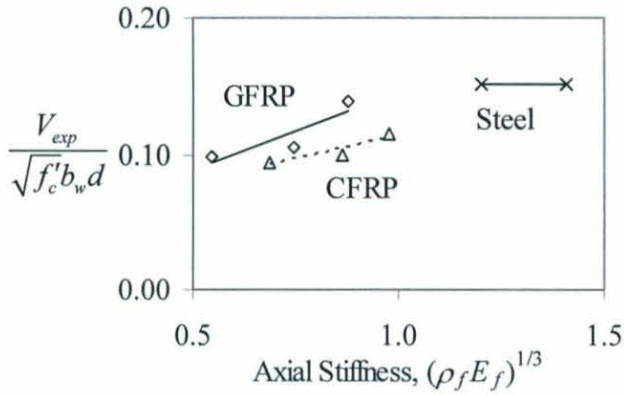

Figure 4.32: Variation of normalized shear strength with respect to the cubic root of the axial stiffness for 500 mm thick beams

Effect of Concrete Compressive Strength, f_c'

The effect of concrete strength was investigated for GFRP and CFRP reinforced beams only. The results of the beams with height equal to 350 mm and compressive strengths (f_c') of approximately 40, 65, and 88 MPa are shown in Figure 4.33. For these beams, a slight increase in shear strength was observed for an increase in the concrete strength (Figure 4.33a). Similar behaviour was observed for FRP reinforced slender beams by El-Sayed et al. (2006b). No noticeable differences were observed between the shear strength of GFRP and CFRP reinforced beams, since the axial stiffness of the GFRP and CFRP reinforcements was very close. However, the normalized shear strength ($V_{exp}/\sqrt{f_c'}b_w d$) shows a decreasing trend with an increase in the concrete strength (Figure 4.33b). A slightly lower relative shear strength for HSC beams than that of the NSC beams were observed by Gross et al. (2003). The decrease in normalized shear strength

with an increase in the concrete strength can be explained by the decrease in shear resistance by the aggregate interlock. For high strength concrete, the crack passes through the aggregate reducing the aggregate interlock forces (El-Sayed et al. 2006b). Another possible reason is the decrease in the neutral axis depth from extreme compression fibre for high strength concrete compared to the normal strength concrete (Gross et al. 2003). Consequently, the contribution of shear from uncracked concrete compression zone decreases.

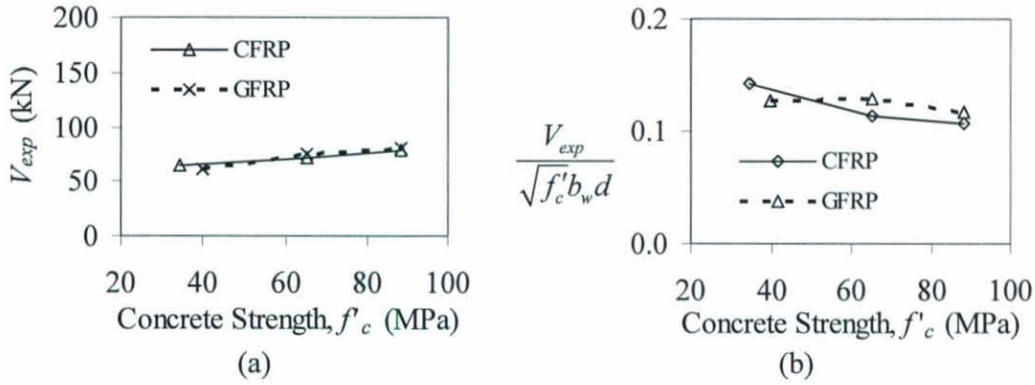

Figure 4.33: Effect of concrete compressive strength for 350 mm beam height; (a) experimental shear strength, (b) normalized shear strength

The effect of concrete strength on shear strength of beams with heights equal to 500 and 650 mm are shown in Figure 4.34a. The concrete strengths for these beams were approximately 40 and 70 MPa. It was observed that the shear strength increased with an increase in the concrete strength for both GFRP and CFRP reinforced beams. This behaviour seems more prominent for these beams compared to the 350 mm thick beams. This could be due to the fact that the axial stiffness of the reinforcing bars for HSC beams

was approximately 1.5 times the axial stiffness of NSC beams. The differences between the shear strength of GFRP and CFRP reinforced beams were negligible. This investigation reveals that the minor increase in the axial stiffness coupled with the high strength concrete would increase the concrete shear strength.

The normalized shear strengths for these beams are shown in Figure 4.34(b). When the shear strengths are normalized by the square root of the concrete strength and the axial stiffness $\left(\rho_f E_f\right)$, the normalized shear strengths $\left[V_{exp}/\sqrt{f'_c}b_w d\left(\rho_f E_f\right)\right]$ were found to be decreased with an increase in the concrete strength. The same reason indicated for 350 mm thick beams can be attributed to this behaviour.

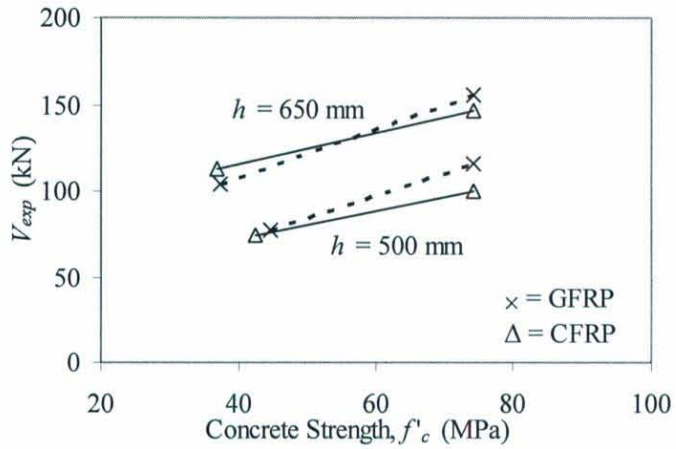

(a)

Figure 4.34: Effect of concrete compressive strengths for 500 and 650 mm thick beams; (a) experimental shear strength, (b) normalized shear strength

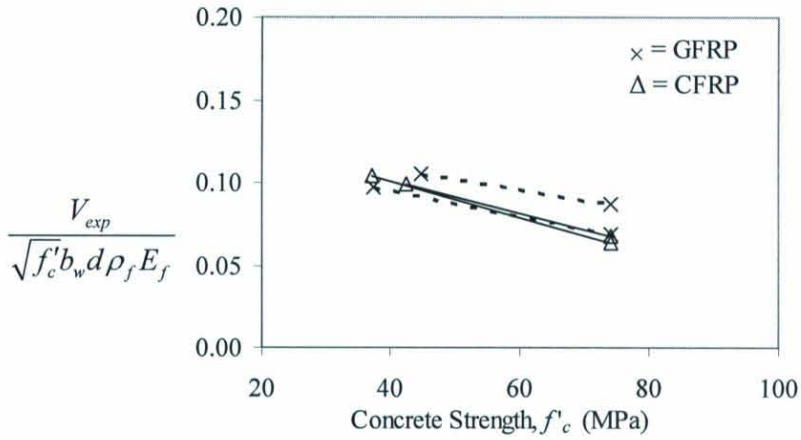

(b)

Figure 4.34 (Contd.): Effect of concrete compressive strengths for 500 and 650 mm beam depths; (a) experimental shear strength, (b) normalized shear strength

4.4 Comparison of Experimental Results with Major Design Equations

4.4.1 Introduction

The shear strengths of the beams were predicted using the theoretical prediction methods of the design codes and guidelines for FRP reinforced concrete members, which include the ACI440.1R-06 "Guide for the Design and Construction of Structural Concrete Reinforced with FRP Bars", the CSA S806-02 "Design and Construction of Building Components with Fibre-Reinforced Polymers", the JSCE (1997) "Recommendation for Design and Construction of Concrete Structures Using Continuous Fibre Reinforcing Materials", the ISIS (2007) "Reinforcing Concrete Structures with Fibre Reinforced Polymers", and the Canadian Highway Bridge Design Code (CSA S6-06). In addition to

these, the shear strengths were computed using the proposed shear design method of El-Sayed et al. (2005), Razaqpur and Isgor (2006), and Sherwood et al. (2008) for FRP reinforced members. All of these methods were discussed in Chapter 2. The predicted results were compared with the experimental results. The predicted shear strengths from different methods are presented and discussed in the following section.

4.4.2 Comparison of the Results

The experimental shear strength (V_{exp}) versus the predicted shear strength (V_{pred}) for different shear design methods are shown in Table 4.3. For clarity, the results of major design methods (CSA, ACI, JSCE, ISIS, and CHBDC) are plotted as a bar chart in Figures 4.35 to 4.39 and these will be discussed first. For consistency with different design methods, only the results of FRP reinforced beams are shown. It should be noted that the material resistance factor (ϕ_c) and the concrete density factor (λ) in CSA S806-02 method, and member safety factor (γ_b) in JSCE (1997) design methods were considered equal to 1.0. It can be seen from Table 4.3 that the average ratios of the shear strengths between the experimental and the predicted values are conservative for all design methods. Due to arch action in beam G-1.5, all predictions are highly conservative for this beam. Notice that the CSA S806-02 and the JSCE (1997) methods predicted shear strengths are better than the other methods for all beams. The average and the standard deviation of V_{exp}/V_{pred} for CSA S806-02 are less than the corresponding values of JSCE (1997) method. The CSA method shows more consistent results than all other

methods (Figure 4.35). This can be attributed to the fact that this method considers most of the shear strength parameters, which are believed to affect the shear strength. However, this method shows more conservative results for beams G-2.5-500, C-2.5-350, and C-2.5-500, where the effective depths of these beams are greater than 300 mm, and the reinforcement ratio is almost twice the balanced reinforcement ratio. This could be attributed to the fact that this method does not consider the amount of reinforcement for beams with effective depth greater than 300 mm. The consistency in the ratios of the experimental to the predicted values in the JSCE method (Figure 4.37) is less than the CSA method. On the other hand, the average and the standard deviation of V_{exp}/V_{pred} for ACI 440.1R-06 method are higher than the other methods. The consistency of the results in this method is less than the other methods (Figure 4.36). One of the possible reasons could be the fact that this method considers the shear strength for uncracked compression zone only, and neglects any interface shear transfer. Another possible reason is that this method does not consider the shear span-to-depth ratio and size effect in shear. Overall this method gives more conservative results for beams with low axial stiffness of FRP reinforcement. Although, the average ratio predicted using the ISIS M03-07 is very close to 1.0, the standard deviation of the results are the second highest followed by ACI 440.1R-06 and the number of unconservative results is the highest for this method. Figure 4.38 reveals that this method predicts the shear strength of GFRP reinforced beams in a better way than that of the CFRP reinforced beams. This can be attributed to the fact that this method assumes that the reduction in shear strength in the FRP reinforced concrete compared to the steel reinforced concrete is directly proportional with the square root of

the ratio of the modulus of elasticity of the reinforcing bars. This relationship is different from the behaviour that was observed in section 4.3.2. On the other hand, CHBDC predicted results are conservative for all beams and this conservatism is greater for GFRP reinforced beams than CFRP reinforced beams. The standard deviation of the ratio of V_{exp}/V_{pred} predicted using this method is the highest.

Among the design methods proposed by several authors, Razaqpur and Isgor (2006) method were found to be the best in terms of standard deviation. This method considers the shear span-to-depth ratio (a/d), the axial stiffness of the reinforcing bars ($\rho_f E_f$), and the effective depth of the beams (d). The average of the experimental to the predicted values $\left(V_{exp}/V_{pred}\right)$ of this method is 0.83 with 22% standard deviation. This value for El-Sayed et al. (2005) method is 1.29 with 32% standard deviation. The unconservative result in this method is 14% out of 29 beams. Although Razaqpur and Isgor and El-Sayed et al. proposed method used a modification factor for beams with a/d less than 2.5, these methods give unconservative results for beam C-1.5 with shear span-to-depth ratio equal to 1.5. On the other hand, MCFT predicted results (Sherwood et al. 2008) are very close to the experimental results with 34% standard deviation. Although this method shows 43% unconservative results, the results are the most consistent than all other methods. It was concluded that the CSA A23.3-04 code provides safe results for the shear strength of FRP reinforced members with the application of ACI reduction factor for shear, which is equal to 0.75 (Sherwood et al. 2008).

The comparison between the experimental results and the predicted values, using the several proposed and available design methods, revealed that most of the methods did not give close predictions of the experimental results for some of the beams. Some of the methods, which predicted the results in a relatively consistent way, contained some unconservative results. For example, the predicted results using Razaqpur and Isgor (2006) proposed method seem unconservative with the lowest standard deviation. On the other hand, the ACI design equation gave predictions that are very conservative with the highest standard deviation. Therefore, there is a need for a consistent shear design method, which reflects the effects of the various parameters on the shear strength in a realistic way.

Table 4.3: Comparison of the experimental results with different design methods

Beam ID	FRP type	V_{exp} (kN)	V_{exp}/V_{pred}							
			CSA S806-02	ACI 440.1R-06	JSCE (1997)	ISIS-M03-07	CHBDC (CSA S6-06)	El-Sayed et al. (2005)	Razaqpur and Isgor (2006)	Sherwood et al. (2008)
G-1.5	G	155.8	3.49	5.46	4.00	3.63	4.48	1.87	1.75	2.49
G-2.5	G	61.0	1.27	2.05	1.49	1.32	2.01	1.45	0.80	1.11
G-3.5	G	43.7	0.91	1.47	1.07	0.95	1.75	1.03	0.72	0.89
G-500	G	77.2	1.16	1.72	1.36	1.21	1.92	1.21	0.77	0.97
G-650	G	103.7	1.18	1.51	1.30	1.23	1.74	1.07	0.83	0.92
G-800	G	129.4	1.20	1.50	1.37	1.33	1.77	1.06	0.91	0.96
G-2.5-350(1)	G	65.5	1.16	1.81	1.38	1.46	1.97	1.35	0.76	1.02
G-2.5-350(2)	G	70.9	1.23	1.92	1.47	1.53	2.07	1.44	0.80	1.09
G-0.5-500	G	68.0	1.09	2.37	1.70	1.14	2.45	1.48	0.96	1.24
G-2.5-500	G	92.2	1.53	1.74	1.48	1.59	2.02	1.31	0.88	1.07
G-50	G	75.6	1.29	2.31	1.80	1.34	2.44	1.62	0.80	1.28
G-70	G	80.2	1.17	2.26	1.91	1.22	2.59	1.64	0.73	1.48
G-500-70	G	116.1	1.35	1.91	1.79	1.41	2.27	1.43	0.81	1.41
G-650-70	G	155.2	1.26	1.56	1.58	1.31	2.15	1.18	0.78	1.28
C-1.5	C	87.3	1.93	2.48	1.92	1.14	1.54	0.89	0.97	1.20
C-2.5	C	64.6	1.43	1.84	1.42	0.84	1.42	1.36	0.80	1.06
C-3.5	C	58.9	1.30	1.67	1.29	0.77	1.48	1.24	0.91	1.07
C-500	C	74.1	1.11	1.31	1.11	0.65	1.04	0.97	0.65	0.79
C-650	C	112.9	1.28	1.35	1.23	0.75	1.13	1.01	0.80	0.88
C-800	C	137.3	1.18	1.31	1.24	0.75	1.11	0.96	0.82	0.87
C-0.5-350	C	58.7	1.17	2.32	1.59	0.69	1.67	1.54	0.84	1.18
C-2.5-350	C	72.5	1.60	1.69	1.37	0.95	1.28	1.31	0.81	1.02
C-0.5-500	C	70.3	1.05	1.70	1.33	0.62	1.34	1.16	0.76	0.96
C-2.5-500	C	82.5	1.28	1.29	1.13	0.75	1.01	1.00	0.68	0.82

Table 4.3 (Contd.): Comparison of the experimental results with different design methods

Beam ID	FRP type	V_{exp} (kN)	V_{exp}/V_{pred}							
			CSA S806-02	ACI 440.1R-06	JSCE (1997)	ISIS-M03-07	CHBDC (CSA S6-06)	El-Sayed et al. (2005)	Razaqpur and Isgor (2006)	Sherwood et al. (2008)
C-50	C	71.6	1.15	1.71	1.42	0.68	1.25	1.26	0.64	1.00
C-70	C	77.9	1.08	1.71	1.55	0.63	1.27	1.31	0.60	1.19
C-500-70	C	100.4	1.16	1.28	1.28	0.68	1.03	1.02	0.62	1.02
C-650-70	C	146.1	1.17	1.21	1.29	0.69	1.03	0.95	0.66	1.06
Mean =			**1.34**	**1.94**	**1.56**	**1.13**	**1.92**	**1.29**	**0.83**	**1.14**
Standard deviation =			**0.46**	**0.85**	**0.55**	**0.58**	**1.13**	**0.32**	**0.22**	**0.34**
% of unconservative results =			**7**	**0**	**0**	**50**	**0**	**14**	**96**	**43**

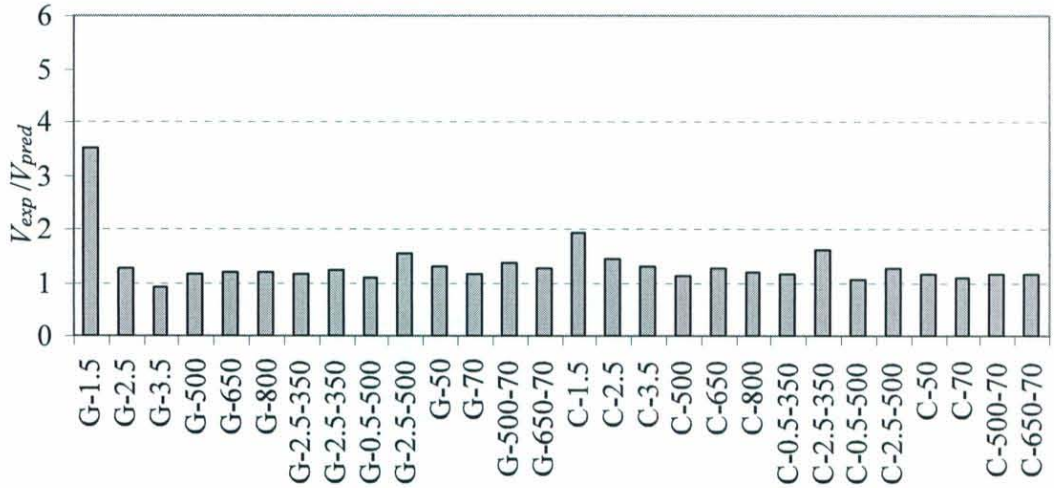

Figure 4.35: Comparison of the experimental results with CSA S806-02 predictions

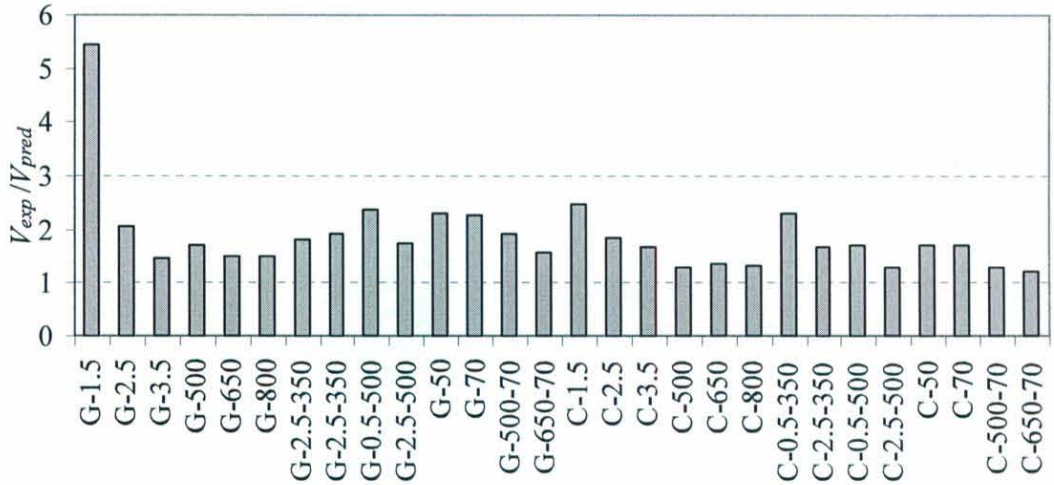

Figure 4.36: Comparison of the experimental results with ACI 440.1R-06 predictions

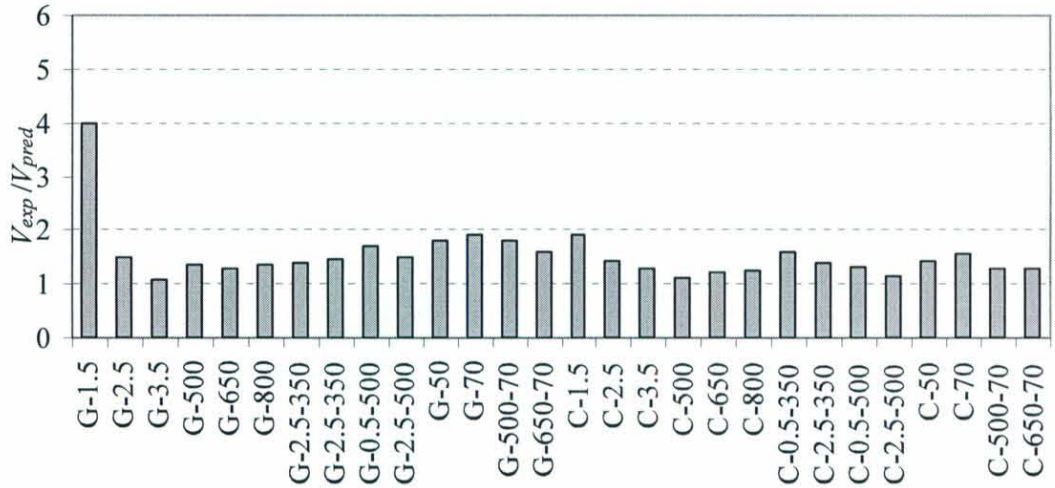

Figure 4.37: Comparison of the experimental results with JSCE (1997) predictions

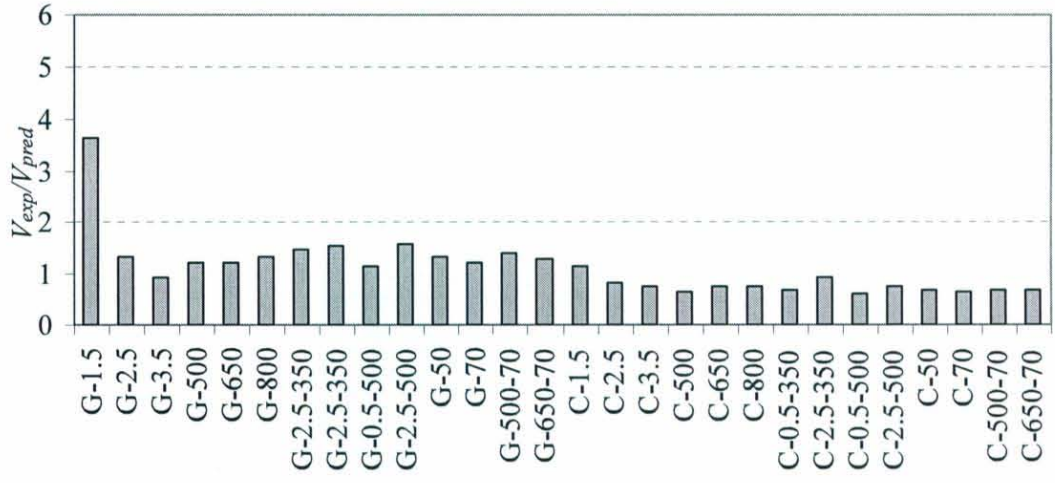

Figure 4.38: Comparison of the experimental results with ISIS M03-07 predictions

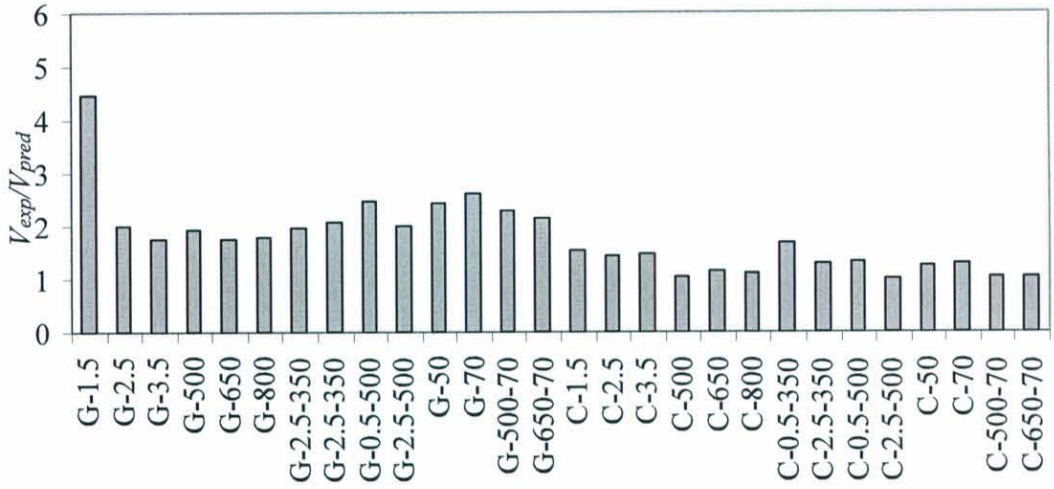

Figure 4.39: Comparison of the experimental results with CHBDC (CSA S6-06) predictions

Chapter 5 Design Method Development

5.1 Introduction

This chapter focuses on the development of a simple, yet robust shear design method to calculate the shear strength of FRP reinforced concrete beams without transverse reinforcement. A relationship between the shear load that causes a beam to crack at middle of the shear span and the shear strength of the beam is confirmed based on the experimental results. Based on this relationship, a shear design method is proposed. The shear strength predicted by the proposed method is compared with the experimental results available in the literature to examine the consistency of the predictions of the proposed method. The predicted results using this method are also compared with the predictions of the major design provisions to assess its reliability.

5.2 Cracking Load

The theoretical cracking moment, M_{cr}, of a beam is given by,

$$M_{cr} = f_r \frac{I_T}{y_t} \tag{5.1}$$

where,

f_r = modulus of rupture
I_T = moment of inertia of the transformed un-cracked section
y_t = distance from neutral axis to the extreme fibres in tension

The modulus of rupture, f_r, is given by CSA A23.03-04 as:

$f_r = 0.6\lambda\sqrt{f_c'}$, where

λ is the concrete density factor, and

f_c' is the concrete compressive strength.

For four-point loading, if the shear span is a, the cracking moment, M_{cr}, is equal to $V_{cr}a$, as shown in Figure 5.1, where V_{cr} is the shear load that causes the first crack in a beam. Substituting this value in Equation 5.1, results:

$$V_{cr} = P_{cr} = 0.6\lambda\sqrt{f_c'}\frac{I_T}{ay_t} \tag{5.2}$$

The corresponding moment at the centre of the shear span is $M_{cr}/2$. The beam will crack at the centre of the shear span when the moment at this location reaches M_{cr}. If it does occur, then the moment at the midspan of the beam is $2M_{cr}$ and the corresponding shear load is $2V_{cr}$. The shear load that causes a beam to crack at middle of the shear span is defined as $V_{cr-a/2}$. The corresponding shear force diagram is shown in Figure 5.1.

Hence, the shear load that causes a beam to crack at middle of the shear span can be calculated as:

$$V_{cr-a/2} = 2V_{cr} = 1.2\lambda\sqrt{f_c'}\frac{I_T}{ay_t} \tag{5.3}$$

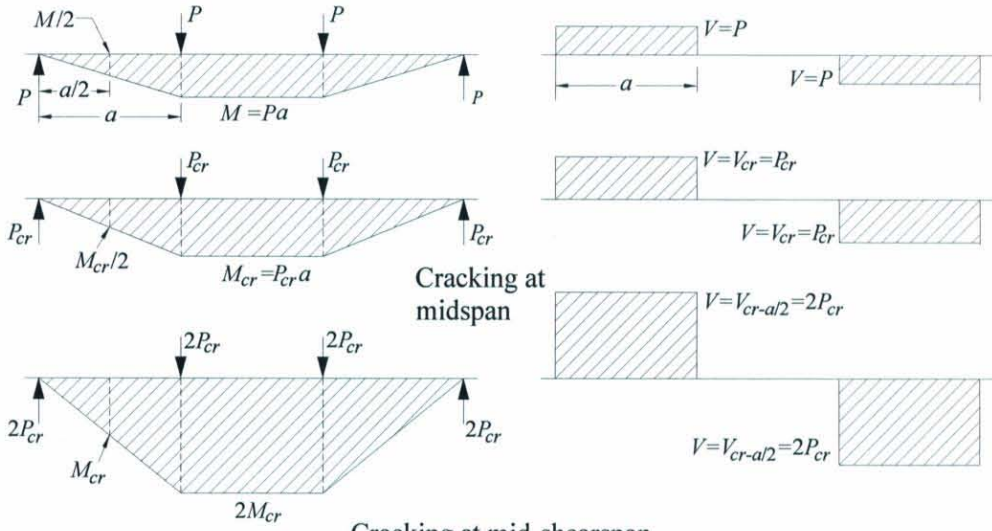

Figure 5.1: Bending moment and shear force diagrams with increasing loads

5.3 Load-Reinforcement Strain Behaviour

As mentioned in Chapter 3, the test beams were instrumented with four strain gauges to measure the reinforcement strain. Two of the strain gauges were placed at midspan of the beam and one at the centre of each shear span to compare the strains at those locations. The load-midspan reinforcement strains were presented and discussed in Chapter 4. Typical load versus reinforcement strains at midspan and middle of the shear span are shown in Figure 5.2 for some of the test beams. It was observed from the strain behaviour that the beam cracked at middle of the shear span at approximately twice the cracking load at midspan of the beam. For some cases, the beam failed just after the formation of a crack at middle of the shear span or just in a close location. This resulted

in the sudden increase in middle of the shear span strain (Figure 5.2a). Most of the beams continued to carry load after cracking at middle of the shear span. The failure loads were found to be approximately 5 to 20% more than the cracking load at middle of the shear span. Hence, it can be reasonably assumed that the cracking load at middle of the shear span, which is approximately twice the cracking load at midspan, is the failure load of the beams. During the experiments, the distance of the failure crack intersection (l_{cr}) with the bottom of the beams were measured from the loading point as shown in Figure 5.3(a). The comparison between this distance and the shear span (a) reveals that the failure cracks at the bottom of the beams approximately pass though the middle of the shear span. This is illustrated in Figure 5.3(b), where l_{cr} is plotted against the shear span (a) of the test specimens. The average and the standard deviation of the ratios of l_{cr}/a for the thirty six beams tested in this investigation were found to be 0.51 and 0.06, respectively. The ratio of l_{cr}/a is given in Table 5.1 for all test beams. The crack patterns at failure are shown in Appendix A for all beams that were tested in the current investigation.

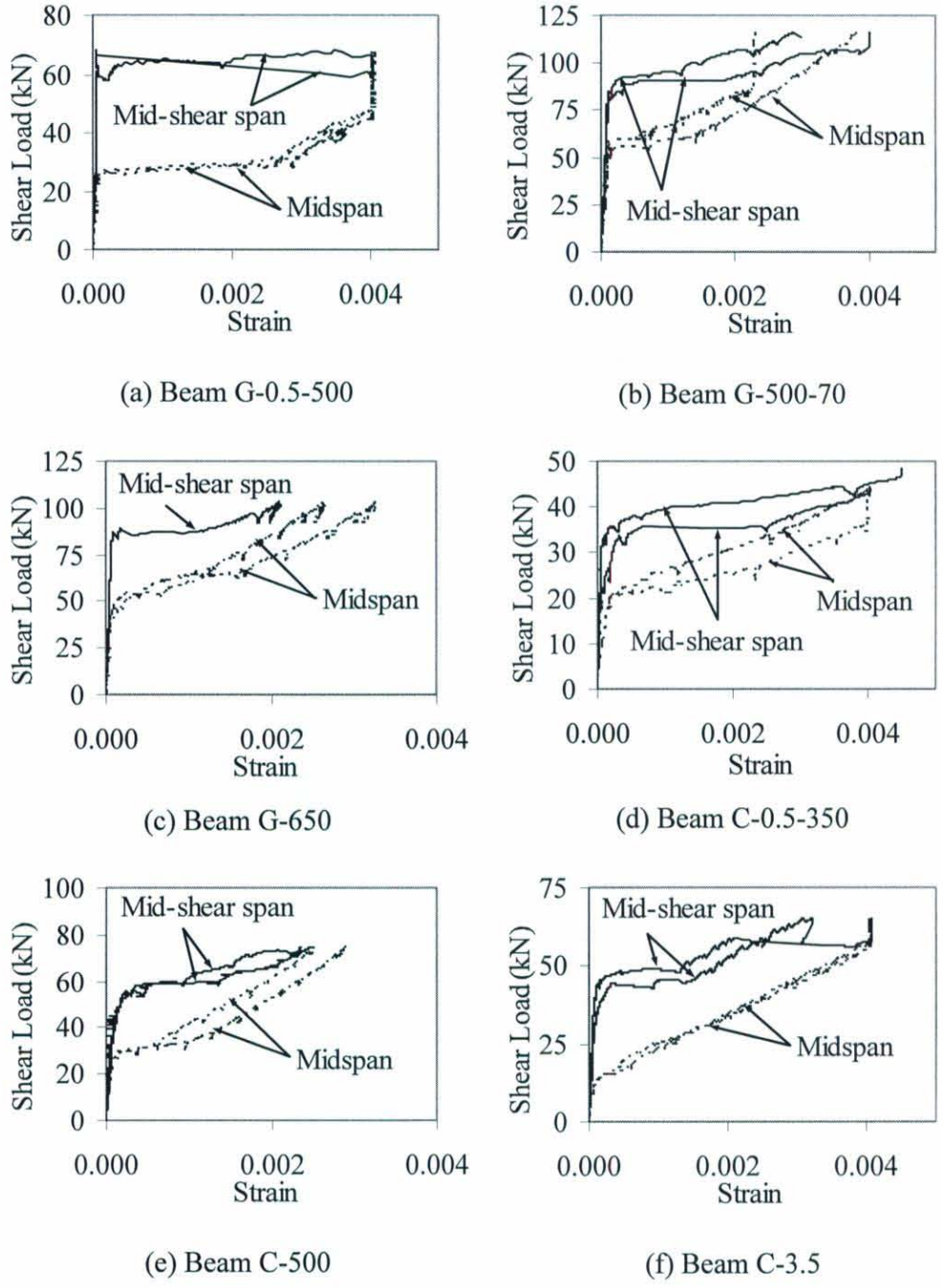

Figure 5.2: Typical load versus reinforcement strains for some beams at midspan and at middle of the shear span of the beam

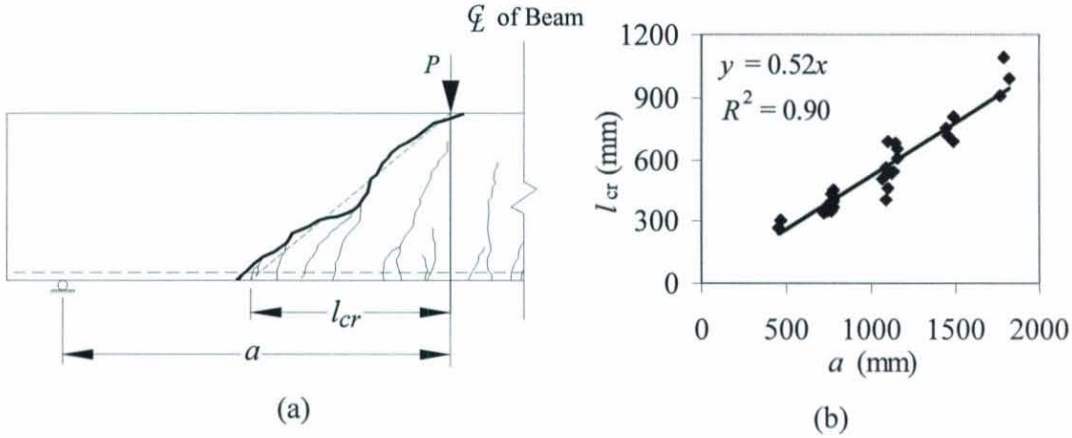

Figure 5.3: (a) Failure crack location at the bottom of the beam, and (b) failure crack location versus shear span ratio

Table 5.1: Comparison between the failure crack location and shear span

Beam ID	d (mm)	a (mm)	Crack location, l_{cr} (mm)	l_{cr}/a	Beam ID	d (mm)	a (mm)	Crack location, l_{cr} (mm)	l_{cr}/a
G-1.5	305	458	263	0.57	C-500	460	1150	608	0.53
G-2.5	305	763	350	0.46	C-650	594.17	1485	805	0.54
G-3.5	305	1068	500	0.47	C-800	744.29	1786	1094	0.61
G-500	440	1100	542	0.49	C-500-70	449	1123	529	0.47
G-650	584	1460	715	0.49	C-650-70	594	1485	688	0.46
G-800	734	1762	906	0.51	C-0.5-350	310	775	405	0.52
G-500-70	442	1105	455	0.41	C-2.5-350	310	775	448	0.58
G-650-70	578	1445	750	0.52	C-0.5-500	460	1150	653	0.57
G-0.5-350	310	775	N/A	-	C-2.5-500	439	1098	689	0.63
G-2.5-350(1)	296	740	350	0.47	C-50	310	775	403	0.52
G-2.5-350(2)	296	740	373	0.50	C-70	310	775	N/A	-
G-0.5-500	455	1138	541	0.48	S-2.5	310	775	370	0.48
G-2.5-500	434	1085	524	0.48	S-3.5	310	1085	560	0.52
G-50	291	728	361	0.50	S-500	457.5	1144	675	0.59
G-70	291	728	339	0.47	S-650	607.5	1519	N/A	-
C-1.5	310	465	299	0.64	S-800	757.5	1818	986	0.54
C-2.5	310	775	392	0.51	S-2.5-350	307.5	769	431	0.56
C-3.5	310	1085	404	0.37	S-2.5-500	457.5	1144	N/A	-
								Average =	0.51
								Standard Deviation =	0.06

5.4 Experimental Shear Strength versus Cracking Load

Table 5.2 shows the values of the analytical cracking load (V_{cr}), the observed cracking load (V_{cr-obs}) at first flexural cracking, and the shear strength (V_{exp}) of the beams tested in the current investigation. In calculating the analytical cracking loads, λ is assumed to be equal to 1.0, since all the beams were made with normal weight concrete. The analytical cracking loads were compared with the observed cracking load and a good agreement was observed as shown in Table 5.2. The average ratio of the computed cracking load to the observed cracking load is 1.19 with 22% standard deviation. The comparison between the analytical cracking loads at the middle of the shear span ($V_{cr-a/2}$) and the observed shear strength (V_{exp}) indicates that the shear strength corresponds well with the cracking loads. The average ratio of the shear strength to the corresponding analytical cracking load at middle of the shear span is 1.25 with 27% standard deviation. In this comparison, the analytical cracking load was used since it is more reliable than the observed cracking load. There were also some possibilities of human errors in capturing the cracking loads during the experiments. Although the average ratio of $V_{exp}/V_{cr-a/2}$ was close to one, however, a slight deviation in the results was observed for the different parameters. The ratio of $V_{exp}/V_{cr-a/2}$ increases with an increase in the shear span-to-depth ratio and the reinforcement ratio. On the other hand, it decreases with an increase in the depth of the beams and concrete strengths. This is illustrated in Figure 5.4.

Table 5.2: Comparison between the shear strength and the cracking loads

Specimen ID	d (mm)	f'_c (MPa)	ρ (%)	a/d	Analytical cracking load, V_{cr} (kN)	Observed cracking load, V_{cr-obs} (kN)	Shear strength V_{exp} (kN)	V_{cr} / V_{cr-obs}	V_{exp} / $V_{cr-a/2}$
G-1.5	305	34.5	0.86	1.5	39.6	37.8	155.8	1.05	1.97
G-2.5	305	39.8	0.86	2.5	25.5	17.8	61.0	1.43	1.20
G-3.5	305	39.8	0.86	3.5	18.2	13.3	43.7	1.36	1.20
C-1.5	310	34.5	0.42	1.5	39.5	44.5	87.3	0.89	1.10
C-2.5	310	34.5	0.42	2.5	23.7	20.0	64.6	1.18	1.36
C-3.5	310	34.5	0.42	3.5	16.9	13.3	58.9	1.27	1.74
S-2.5	310	49.3	0.90	2.5	29.2	26.7	83.5	1.10	1.43
S-3.5	310	49.3	0.90	3.5	20.9	13.3	73.4	1.56	1.76
G-500	440	44.7	0.90	2.5	38.1	26.7	77.2	1.43	1.01
G-650	584	37.4	0.91	2.5	53.3	40.0	103.7	1.33	0.97
G-800	734	37.4	0.91	2.4	67.0	53.4	129.4	1.26	0.97
G-500-70	442	74.2	1.27	2.5	48.8	51.2	116.1	0.95	1.19
G-650-70	578	74.2	1.39	2.5	75.8	86.7	155.2	0.87	1.02
C-500	460	42.4	0.45	2.5	35.9	26.7	74.1	1.34	1.03
C-650	594	37.0	0.43	2.5	52.7	44.5	112.9	1.18	1.07
C-800	744	42.4	0.40	2.4	71.1	62.3	137.3	1.14	0.97
C-500-70	449	74.2	0.69	2.5	48.6	33.4	100.4	1.46	1.03
C-650-70	594	74.2	0.65	2.5	74.5	82.3	146.1	0.91	0.98
S-500	458	41.8	0.87	2.5	36.7	33.4	111.2	1.10	1.51
S-650	608	41.8	0.88	2.5	56.3	55.6	155.7	1.01	1.38
S-800	758	41.8	0.88	2.4	72.1	95.6	200.1	0.75	1.39
G-0.5-350	310	37.4	0.33	2.5	24.2	20.0	72.7	1.21	1.50
G-2.5-350(1)	296	39.8	1.43	2.5	26.3	N/A	65.5	N/A	1.24
G-2.5-350(2)	296	42.4	1.43	2.5	27.2	26.7	70.9	1.02	1.30
G-0.5-500	455	37.4	0.35	2.5	33.7	26.7	68.0	1.26	1.01
G-2.5-500	434	37.4	1.47	2.5	35.5	31.1	92.2	1.14	1.30
C-0.5-350	310	42.4	0.18	2.5	25.9	17.8	58.7	1.46	1.13
C-2.5-350	310	34.5	0.67	2.5	24.0	26.7	72.5	0.90	1.51
C-0.5-500	460	42.4	0.22	2.5	35.6	22.2	70.3	1.60	0.99
C-2.5-500	439	42.4	0.65	2.5	37.7	26.7	82.5	1.41	1.09
S-2.5-350	308	49.3	1.43	2.5	30.2	24.5	106.4	1.24	1.76
S-2.5-500	458	41.8	1.40	2.5	37.5	44.5	111.4	0.84	1.48
G-50	291	65.3	0.89	2.5	34.1	22.2	75.6	1.53	1.11
G-70	291	88.3	0.89	2.5	39.5	33.4	80.2	1.19	1.01
C-50	310	65.3	0.42	2.5	32.4	28.9	71.6	1.12	1.11
C-70	310	88.3	0.42	2.5	37.6	33.4	77.8	1.13	1.04
							Average =	1.19	1.25
							Standard Deviation =	0.22	0.27
							Coefficient of Variation (%) =	4.9	7.1

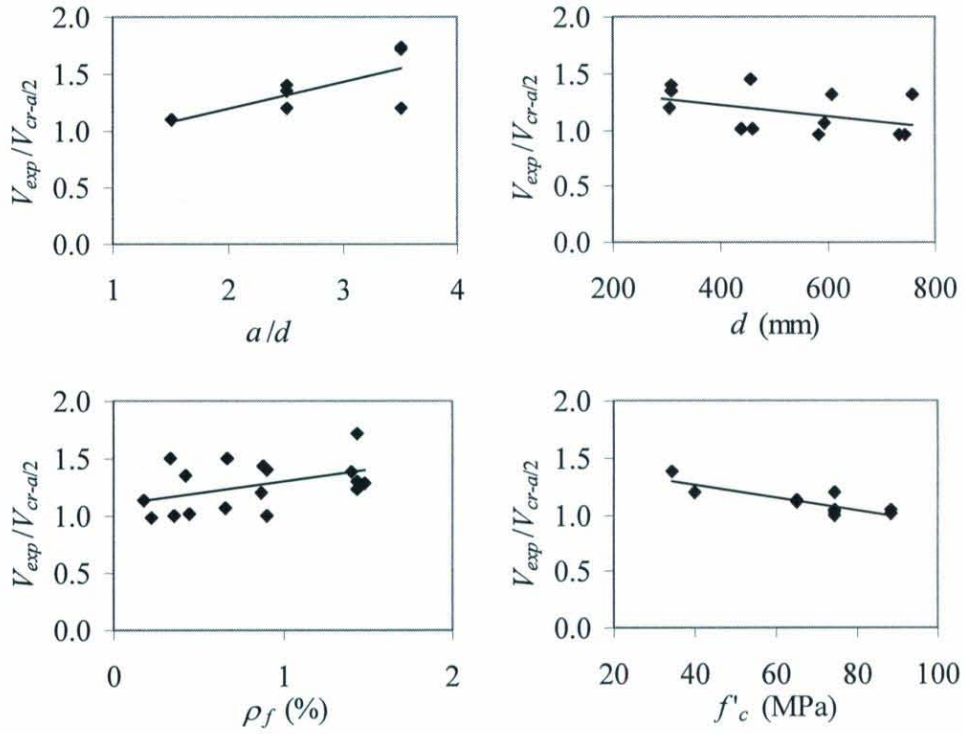

Figure 5.4: Effect of different parameters on the ratio between the shear strength and the cracking load

5.4.1 Consistency of the Relationship between the Shear Strength and the Cracking Load

In order to further examine the consistency of the relationship, the shear load predicted using Equation 5.3 were compared to 101 test results of FRP reinforced rectangular specimens without stirrups collected from the literature in addition to the 36 beams of the current study. Out of these 137 specimens, 81 were reinforced with GFRP, 47 were reinforced with CFRP, 2 were reinforced with AFRP, and 7 were reinforced with

steel. The test specimens were reinforced with longitudinal bars without transverse reinforcement. The concrete strength, reinforcement ratio, shear span-to-depth ratio, and depth of the beams were in the range of 24.1 to 88.3 MPa, 0.18 to 2.63%, 1.1 to 6.45, and 104 to 889 mm, respectively. The material and geometrical properties of the specimens are provided in Table 5.3.

The experimental shear strengths were divided by the predicted shear loads to evaluate the consistency of the relationship. The results are shown in Table 5.3. The average ratio of the experimental shear strength to the predicted shear load by equation 5.3 was found to be 1.67 with a coefficient of variation of 33% and a standard deviation of 55%. Out of 137 samples, only 5.8% of the sample was found to be unconservatively predicted by Equation 5.3 i.e. the predicted results were less than the experimental ones. Thus, it can be said that the predicted results using Equation 5.3 is a reasonable approximation of the shear strength of the specimens in the database.

Table 5.3: Database of 137 test specimens

	Experimental details									Predicted results	
Authors	Beam ID	b (mm)	d (mm)	a/d	f'_c (MPa)	ρ (%)	E_f (GPa)	FRP type	V_{exp} (kN)	$V_{cr\text{-}a/2}$ (kN)	$\frac{V_{exp}}{V_{cr\text{-}a/2}}$
Current study	G-1.5	250	305	1.50	34.5	0.86	46.3	G	155.8	79.7	1.96
	G-2.5	250	305	2.50	39.8	0.86	46.3	G	61.0	51.3	1.19
	G-3.5	250	305	3.50	39.8	0.86	46.3	G	43.7	36.6	1.19
	C-1.5	250	310	1.50	34.5	0.42	144.0	C	87.3	80.6	1.08
	C-2.5	250	310	2.50	34.5	0.42	144.0	C	64.6	48.4	1.34
	C-3.5	250	310	3.50	34.5	0.42	144.0	C	58.9	34.6	1.70
	G-500	250	440	2.50	44.7	0.90	46.3	G	77.2	76.8	1.01
	G-650	300	584	2.50	37.4	0.91	46.3	G	103.7	107.8	0.96
	G-800	300	734	2.40	37.4	0.91	46.3	G	129.4	135.5	0.95
	C-500	250	460	2.50	42.4	0.45	144.0	C	74.1	74.1	1.00
	C-650	300	594	2.50	37.0	0.43	144.0	C	112.9	108.8	1.04
	C-800	300	744	2.40	42.4	0.40	144.0	C	137.3	146.3	0.94
	C-500-70	250	449	2.50	74.2	0.69	144.0	C	100.4	100.2	1.00
	C-650-70	300	594	2.50	74.2	0.65	144.0	C	146.1	153.8	0.95
	G-500-70	250	442	2.50	74.2	1.27	46.3	G	116.1	98.0	1.19
	G-650-70	300	578	2.50	74.2	1.38	46.3	G	155.2	152.1	1.02
	G-0.5-350	250	310	2.50	37.4	0.33	46.3	G	72.7	48.6	1.50
	G-2.5-350(1)	250	296	2.50	39.8	1.43	46.3	G	65.5	53.1	1.23
	G-2.5-350(2)	250	296	2.50	42.4	1.43	46.3	G	70.9	54.7	1.30
	G-0.5-500	250	455	2.50	37.4	0.35	46.3	G	68.0	67.6	1.01
	G-2.5-500	250	434	2.50	37.4	1.47	46.3	G	92.2	71.9	1.28
	C-0.5-350	250	310	2.50	42.4	0.18	144.0	C	58.7	52.3	1.12
	C-2.5-350	250	310	2.50	34.5	0.67	144.0	C	72.5	49.5	1.47
	C-0.5-500	250	460	2.50	42.4	0.22	144.0	C	70.3	72.5	0.97
	C-2.5-500	250	439	2.50	42.4	0.65	144.0	C	82.5	78.2	1.06
	C-50	250	310	2.50	65.3	0.42	144.0	C	71.6	65.7	1.09
	C-70	250	310	2.50	88.3	0.42	144.0	C	77.9	76.0	1.03
	G-50	250	291	2.50	65.3	0.89	46.3	G	75.6	68.3	1.11
	G-70	250	291	2.50	88.3	0.89	46.3	G	80.2	79.2	1.01
	S-2.5	250	310	2.50	49.3	0.90	200.0	S	83.5	61.3	1.36
	S-3.5	250	310	3.50	49.3	0.90	200.0	S	73.4	43.8	1.68
	S-500	250	458	2.50	41.8	0.87	200.0	S	111.2	79.9	1.39
	S-650	300	608	2.50	41.8	0.88	200.0	S	155.7	123.6	1.26
	S-800	300	758	2.40	41.8	0.88	200.0	S	200.1	157.7	1.27
	S-2.5-350	250	308	2.50	49.3	1.43	200.0	S	106.4	64.7	1.65
	S-2.5-500	250	458	2.50	41.8	1.40	200.0	S	111.4	85.1	1.31
El-Sayed et al. (2005a)	S-C1	1000	165	6.05	40.0	0.39	114.0	C	140.0	51.5	2.72
	S-C2B	1000	165	6.05	40.0	0.78	114.0	C	167.0	52.3	3.19
	S-C3B	1000	161	6.23	40.0	1.18	114.0	C	190.0	52.8	3.60
	S-G1	1000	162	6.17	40.0	0.86	40.0	G	113.0	50.8	2.22

Table 5.3 (Contd.): Database of 137 test specimens

	Experimental details									Predicted results	
Authors	Beam ID	b (mm)	d (mm)	a/d	f'_c (MPa)	ρ (%)	E_f (GPa)	FRP type	V_{exp} (kN)	$V_{cr\text{-}a/2}$ (kN)	$\frac{V_{exp}}{V_{cr\text{-}a/2}}$
El-Sayed et al. (2005a) contd.	S-G2	1000	159	6.29	40.0	1.70	40.0	G	142.0	51.0	2.79
	S-G2B	1000	162	6.17	40.0	1.71	40.0	G	163.0	51.0	3.20
	S-G3	1000	159	6.29	40.0	2.44	40.0	G	163.0	51.1	3.19
	S-G3B	1000	158	6.33	40.0	2.63	40.0	G	168.0	51.2	3.28
El-Sayed et al. (2006a)	CN-1	250	326	3.07	50.0	0.87	128.0	C	77.5	58.7	1.32
	GN-1	250	326	3.07	50.0	0.87	39.0	G	70.5	56.7	1.24
	CN-2	250	326	3.07	44.6	1.25	134.0	C	104.0	56.7	1.83
	GN-2	250	326	3.07	44.6	1.21	42.0	G	60.0	53.8	1.12
	CN-3	250	326	3.07	43.6	1.71	134.0	C	124.5	57.3	2.17
	GN-3	250	326	3.07	43.6	1.70	42.0	G	77.5	53.4	1.45
El-Sayed et al. (2006b)	CH-1.7	250	326	3.07	63.0	1.70	135.0	C	130.0	67.8	1.92
	GH-1.7	250	326	3.07	63.0	1.70	42.0	G	87.0	63.8	1.36
	CH-2.2	250	326	3.07	63.0	2.19	135.0	C	174.0	68.9	2.52
	GH-2.2	250	326	3.07	63.0	2.19	42.0	G	115.5	63.9	1.81
Tureyen and Frosch (2002)	V-G1-1	457	360	3.40	39.7	0.96	40.5	G	108.1	78.6	1.37
	V-G2-1	457	360	3.40	39.9	0.96	37.6	G	94.7	78.6	1.21
	V-A-1	457	360	3.40	40.3	0.96	47.0	A	114.8	79.6	1.44
	V-G1-2	457	360	3.40	42.3	1.92	40.5	G	137.0	81.7	1.68
	V-G2-2	457	360	3.40	42.5	1.92	37.6	G	152.6	81.6	1.87
	V-A-2	457	360	3.40	42.6	1.92	47.0	A	177.0	82.8	2.14
Tariq and and Newhook (2003)	G07N1	160	346	2.75	37.3	0.72	42.0	G	54.5	30.0	1.82
	G07N2	160	346	2.75	37.3	0.72	42.0	G	63.7	30.0	2.13
	G10N1	160	346	3.32	43.2	1.10	42.0	G	42.7	26.7	1.60
	G10N2	160	346	3.32	43.2	1.10	42.0	G	45.5	26.7	1.70
	G15N1	160	325	3.54	34.1	1.54	42.0	G	48.7	23.9	2.04
	G15N2	160	325	3.54	34.1	1.54	42.0	G	44.9	23.9	1.88
	C07N1	130	310	3.06	37.3	0.72	120.0	C	49.2	25.0	1.97
	C07N2	130	310	3.06	37.3	0.72	120.0	C	45.8	25.0	1.83
	C10N1	130	310	3.71	43.2	1.10	120.0	C	47.6	22.5	2.12
	C10N2	130	310	3.71	43.2	1.10	120.0	C	52.7	22.5	2.35
	C15N1	130	310	3.71	34.1	1.54	120.0	C	55.9	20.6	2.71
	C15N2	130	310	3.71	34.1	1.54	120.0	C	58.3	20.6	2.83
Steiner et al. (2008)	A1	457	889	3.10	29.6	0.60	41.0	G	159.0	175.2	0.91
Ashour (2006)	S1B1	150	168	3.98	27.8	0.45	38.0	G	12.5	9.5	1.31
	S1B3	150	212	3.14	27.8	0.71	32.0	G	17.5	14.9	1.17
	S1B5	150	263	2.53	27.8	0.86	32.0	G	25.0	21.5	1.16
	S2B7	150	163	4.10	49.5	1.39	32.0	G	17.5	12.7	1.38
	S2B9	150	213	3.12	49.0	1.06	32.0	G	27.5	19.7	1.40
	S2B11	150	262	2.54	49.0	1.15	32.0	G	30.0	28.4	1.06

Table 5.3 (Contd.): Database of 137 test specimens

	Experimental details									Predicted results	
Authors	Beam ID	b (mm)	d (mm)	a/d	f'_c (MPa)	ρ (%)	E_f (GPa)	FRP type	V_{exp} (kN)	$V_{cr\text{-}a/2}$ (kN)	$\frac{V_{exp}}{V_{cr\text{-}a/2}}$
Yost et al. (2001)	1FRPa	229	225	4.06	36.3	1.11	40.3	G	39.1	24.7	1.58
	1FRPb	229	225	4.06	36.3	1.11	40.3	G	38.5	24.7	1.56
	1FRPc	229	225	4.06	36.3	1.11	40.3	G	36.8	24.7	1.49
	2FRPa	178	225	4.06	36.3	1.42	40.3	G	28.1	19.2	1.46
	2FRPb	178	225	4.06	36.3	1.42	40.3	G	35.0	19.2	1.82
	2FRPc	178	225	4.06	36.3	1.42	40.3	G	32.1	19.2	1.67
	3FRPa	229	225	4.06	36.3	1.66	40.3	G	40.0	24.7	1.62
	3FRPb	229	225	4.06	36.3	1.66	40.3	G	48.6	24.7	1.97
	3FRPc	229	225	4.06	36.3	1.66	40.3	G	44.7	24.7	1.81
	4FRPa	279	225	4.06	36.3	1.81	40.3	G	43.8	30.1	1.46
	4FRPb	279	225	4.06	36.3	1.81	40.3	G	45.9	30.1	1.53
	4FRPc	279	225	4.06	36.3	1.81	40.3	G	46.1	30.1	1.53
	5FRPa	254	224	4.08	36.3	2.05	40.3	G	37.7	27.4	1.38
	5FRPb	254	224	4.08	36.3	2.05	40.3	G	51.0	27.4	1.86
	5FRPc	254	224	4.08	36.3	2.05	40.3	G	46.6	27.4	1.70
	6FRPa	229	224	4.08	36.3	2.27	40.3	G	43.5	24.7	1.76
	6FRPb	229	224	4.08	36.3	2.27	40.3	G	41.8	24.7	1.69
	6FRPc	229	224	4.08	36.3	2.27	40.3	G	41.3	24.7	1.67
Gross et al. (2003)	1a-26-HS	203	225	4.06	79.6	1.24	40.3	G	41.6	32.4	1.29
	1b-26-HS	203	225	4.06	79.6	1.24	40.3	G	30.4	32.4	0.94
	1c-26-HS	203	225	4.06	79.6	1.24	40.3	G	42.1	32.4	1.30
	2a-26-HS	152	225	4.06	79.6	1.66	40.3	G	31.0	24.2	1.28
	2b-26-HS	152	225	4.06	79.6	1.66	40.3	G	33.0	24.2	1.37
	2c-26-HS	152	225	4.06	79.6	1.66	40.3	G	33.5	24.2	1.38
	3a-27-HS	165	224	4.08	79.6	2.09	40.3	G	38.4	26.3	1.46
	3b-27-HS	165	224	4.08	79.6	2.09	40.3	G	32.2	26.3	1.22
	3c-27-HS	165	224	4.08	79.6	2.09	40.3	G	36.7	26.3	1.40
	4a-37-HS	203	224	4.08	79.6	2.55	40.3	G	48.3	32.3	1.49
	4b-37-HS	203	224	4.08	79.6	2.55	40.3	G	45.7	32.3	1.42
	4c-37-HS	203	224	4.08	79.6	2.55	40.3	G	45.2	32.3	1.40
Gross et al. (2004)	8-2a	127	143	6.36	60.3	0.33	139.0	C	14.3	6.5	2.21
	8-2b	127	143	6.36	60.3	0.33	139.0	C	12.9	6.5	1.99
	8-2c	127	143	6.36	60.3	0.33	139.0	C	14.7	6.5	2.27
	8-3a	159	141	6.45	61.8	0.58	139.0	C	19.8	8.2	2.41
	8-3b	159	141	6.45	61.8	0.58	139.0	C	23.1	8.2	2.81
	8-3c	159	141	6.45	61.8	0.58	139.0	C	17.0	8.2	2.07
	11-2a	89	143	6.36	81.4	0.47	139.0	C	8.8	5.3	1.66
	11-2b	89	143	6.36	81.4	0.47	139.0	C	11.7	5.3	2.21

Table 5.3 (Contd.): Database of 137 test specimens

	Experimental details									Predicted results	
Authors	Beam ID	b (mm)	d (mm)	a/d	f'_c (MPa)	ρ (%)	E_f (GPa)	FRP type	V_{exp} (kN)	$V_{cr\text{-}a/2}$ (kN)	$\frac{V_{exp}}{V_{cr\text{-}a/2}}$
Gross et al. (2004)	11-2c	89	143	6.36	81.4	0.47	139.0	C	8.9	5.3	1.69
	11-3a	121	141	6.45	81.4	0.76	139.0	C	14.3	7.2	1.98
	11-3b	121	141	6.45	81.4	0.76	139.0	C	15.3	7.2	2.12
	11-3c	121	141	6.45	81.4	0.76	139.0	C	16.6	7.2	2.29
Razaqpur et al. (2004)	BR1	200	225	2.67	40.5	0.25	145.0	C	36.1	27.1	1.33
	BR2/BA2	200	225	2.67	49.0	0.50	145.0	C	47.0	30.4	1.54
	BR3	200	225	2.67	40.5	0.63	145.0	C	47.2	28.1	1.68
	BR4	200	225	2.67	40.5	0.88	145.0	C	42.7	28.7	1.49
	BA1	200	225	1.82	40.5	0.50	145.0	C	96.2	40.8	2.36
	BA3	200	225	3.56	40.5	0.50	145.0	C	47.0	20.8	2.26
	BA4	200	225	4.50	40.5	0.50	145.0	C	38.5	16.5	2.33
Alkhrdaji et al. (2001)	BM7	178	279	2.69	24.1	2.30	40.0	G	53.4	26.2	2.04
	BM8	178	287	2.61	24.1	0.77	40.0	G	36.1	25.7	1.40
	BM9	178	287	2.61	24.1	1.34	40.0	G	40.1	25.9	1.54
Deitz et al. (1999)	GFRP1	305	158	4.50	28.6	0.73	40.0	G	26.8	13.0	2.06
	GFRP2	305	158	4.50	30.1	0.73	40.0	G	28.3	13.3	2.12
	GFRP3	305	158	4.50	27.0	0.73	40.0	G	29.2	12.6	2.31
Guadagnini et al. (2006)	GB43	150	223	3.30	42.8	1.28	45.0	G	27.2	16.6	1.63
	GB44	150	223	2.20	42.8	1.28	45.0	G	44.7	24.9	1.79
	GB45	150	223	1.10	42.8	1.28	46.0	G	81.0	49.9	1.62
										Mean =	**1.67**
										Standard deviation =	**0.55**
										Coefficient of variation (%) =	**33**
										Perecnt of unconservative results =	**5.8**

The ratio of the experimental shear strength (V_{exp}) and the predicted shear load ($V_{cr-a/2}$) are plotted against the shear span-to-depth ratio (a/d), the depth of the beams (d), concrete strength (f_c'), and axial stiffness ($\rho_f E_f$) as shown in Figure 5.5. As the modulus of elasticity of the reinforcing bars was different, the axial stiffness was considered instead of the reinforcement ratio. The trendline shows that the shear load predicted using Equation 5.3 overestimates the shear strength for higher values of the

shear span-to-depth ratio (Figure 5.5). This can be attributed to the fact that the shear load predicted using Equation 5.3 uses a linear approximation of the shear strength with the shear span of the beam and does not incorporate the effect of a/d in a realistic way. It was observed in Chapter 4 that the normalized shear strength was inversely proportional to the square of the cubic root of the shear span-to-depth ratio, $(d/a)^{2/3}$. This effect was not reflected in Equation 5.3. Similarly, the effect of reinforcement ratio was considered through the transformed section as a linear relationship with the moment of inertia, which was also different than the actual relationship between the shear strength and the reinforcement ratio. The shear strength was found to be proportional with the cubic root of the axial stiffness $(\rho_f E_f)^{1/3}$ of the reinforcement. This relationship was not incorporated into this model.

On the other hand, the trendline shows that the Equation 5.3 underestimates the shear strength of the beams with higher depths (Figure 5.5). The possible reason of this could be the size effect of the members. It was observed in the current study and by several authors that the shear strength decreases with an increase in the depth of the beams. The normalized shear strength increased with the inverse of the cubic root of the depth of the beam $(1/d^{1/3})$ as discussed in Chapter 4. It is interesting to note that the scatter in the results seems to be decreased as the depth of the beams was increased. Additional data is needed to see the actual behaviour. No direct trend was observed for the effect of concrete strength of the beams (Figure 5.5). In order to obtain better consistency in the prediction of shear strength, these parameters must be included in the

prediction equation as will be further illustrated in the next sections. Hence, the shear load that causes a beam to crack at middle of the shear span can be used as a parameter to predict the shear strength of the beams by incorporating the parameters, which are believed to affect the shear strength, in Equation 5.3.

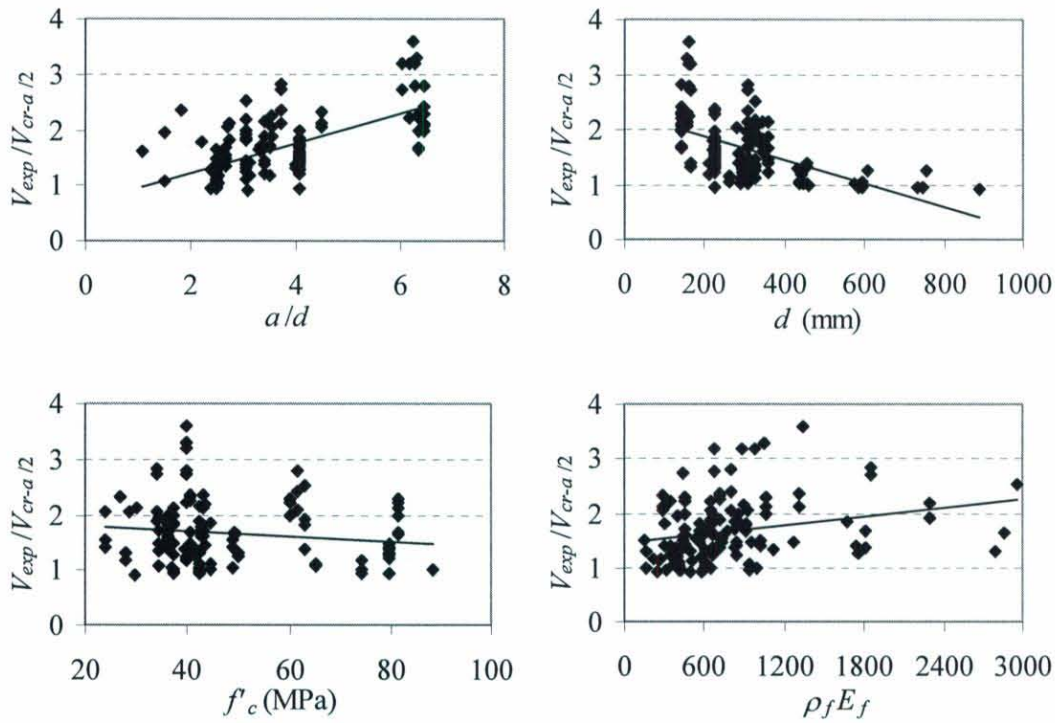

Figure 5.5: Effect of different parameters on the prediction of the shear load

5.5 Proposed Shear Design Method

In the previous sections, it was observed that the shear strength of the beams is related to the shear load that causes a beam to crack at middle of the shear span. Hence, the shear load predicted using Equation 5.3 can be reasonably assumed as the concrete contribution to the shear strength (V_c) of a beam. Thus, Equation 5.3 can be re-written as:

$$V_c = 1.2\lambda\sqrt{f_c'}\,\frac{I_T}{ay_t} \tag{5.4}$$

In the above equation, the reinforcement ratio, cross sectional properties of the section, and concrete strength (f_c') are incorporated through the transformed moment of inertia (I_T) of the section. Equation 5.4 implies that the shear strength is a function of transformed moment of inertia, concrete compressive strength, shear span, and depth of members and the shear strength varies inversely with the shear span.

Although Equation 5.4 predicted the shear strength of the members in a reasonable way as presented in Section 5.4, the scatter in the results was noticeable. This can be attributed to the fact that some of the parameters, which are believed to affect the shear strength, were not incorporated in the prediction equation. Thus, introducing these factors in a realistic way improves the accuracy of predicting the shear strength by any model. An attempt is made to improve the accuracy and to propose a simplified model for design purposes.

The transformed area of reinforcement is a function of modulus of elasticity of reinforcement and concrete. The modulus of elasticity of FRP bars, especially the GFRP bars, is less than that of the steel bars and is vary close to the modulus of elasticity of concrete. Therefore, the use of gross section moment of inertia (I_g) instead of the transformed section moment of inertia (I_T) is a reasonable approximation. Similarly, the depth of neutral axis, y_t, can be taken as half of the beam height, $h/2$. Thus, Equation 5.4 can be written as:

$$V_c = \frac{2.4I_g}{ah}\lambda\sqrt{f_c'} \tag{5.5}$$

The value of I_g for rectangular section is $I_g = b_w h^3/12$. Substituting the value of I_g in Equation 5.5, the following formula is obtained:

$$V_c = \frac{0.2b_w h^2}{a}\lambda\sqrt{f_c'} \tag{5.6}$$

The effective depth (d) of 137 specimens was found to be within 75~95% of the height of the specimens (h). The average ratio of the effective depth to height of 137 specimens was found to be equal to 0.84. Figure 5.6 shows the variation of the ratio of effective depth to the height of the specimens (d/h) with respect to the height of the specimens (h). A slight increase in the ratio was observed with an increase in the depth of the specimens. However, this difference is small and can be neglected. Hence, the effective depth, d, of the specimens can be assumed to be equal to $0.84h$.

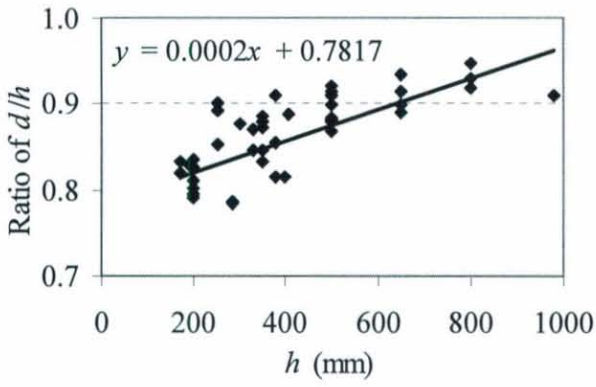

Figure 5.6: Variation of the ratio of d/h with depth of the specimens

Substituting the value of $h = d/0.84$ in Equation 5.6, and after simplification, results the following equation to determine the concrete contribution to the shear strength (V_c):

$$V_c = \frac{0.28}{a/d}\lambda\sqrt{f_c'}\,b_w d \tag{5.7}$$

5.5.1 Incorporation of the Parameters in the Proposed Design Method

It was observed in Figure 5.5 that the ratio of the experimental to the predicted shear strength increases with an increase in the shear span-to-depth ratio (a/d), axial stiffness of the reinforcement ($\rho_f E_f$) and decreases with an increase in the depth of beam (d). This is because the equation does not incorporate the parameters a/d, $\rho_f E_f$, and d in an appropriate way. From Chapter 4, it was observed that the shear strength is proportional to $(a/d)^{2/3}$, $(\rho_f E_f)^{1/3}$ and $(1/d)^{1/3}$. The relationships between the ratio of

the experimental shear strength (V_{exp}) to the predicted shear strength (V_{pred}) using Equation 5.4 and these parameters are shown in Figure 5.7. These relationships are almost the same as the relationships observed in the test results.

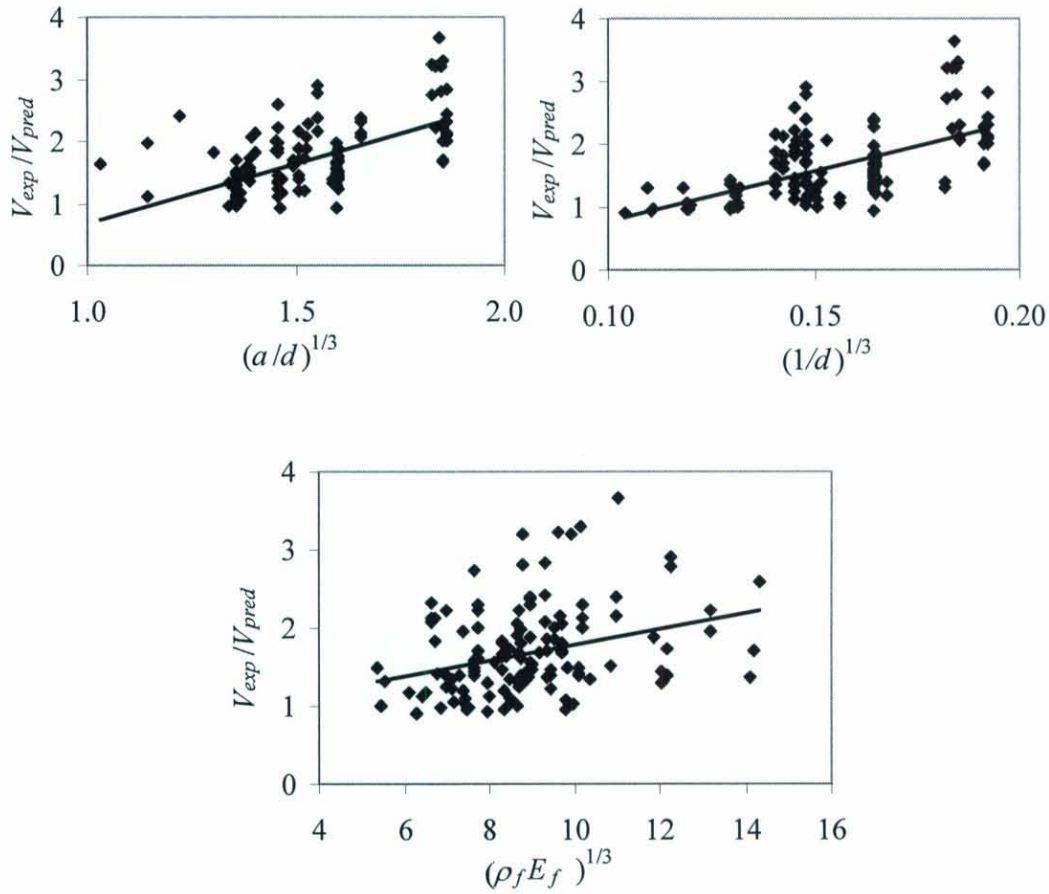

Figure 5.7: Effect of shear span-to-depth ratio, reinforcement ratio, and depth of beam on the predicted results

Incorporating these three parameters in Equation 5.7 leads to:

$$V_c = \frac{0.28}{a/d}\lambda\sqrt{f_c'}\,b_w d \times A(a/d)^{1/3} \times B(1/d)^{1/3} \times C(\rho_f E_f)^{1/3} \qquad (5.8)$$

where A, B, and C are regression coefficients. Simplifying the above equation results in:

$$V_c = \frac{0.28K}{(a/d)^{2/3} d^{1/3}} (\rho_f E_f)^{1/3} \lambda \sqrt{f_c'} b_w d \tag{5.9}$$

where K is a constant and is equal to $A \times B \times C$.

The value of K is determined from regression analysis of the database with respect to $(a/d)^{1/3}$, $(\rho_f E_f)^{1/3}$, and $(1/d)^{1/3}$. The proposed final form of Equation 5.9 is given as follows:

$$V_c = \frac{0.2\lambda}{(a/d)^{2/3}} \left(\frac{\rho_f E_f}{d} \right)^{1/3} \sqrt{f_c'} b_w d \tag{5.10}$$

It should be noted that in deriving this equation, the shear strength was assumed to be directly proportional to the square root of the concrete compressive strength. This assumption is true up to a certain limit. CSA A23.3-04 limits the value of $\sqrt{f_c'}$ up to a maximum of 8 MPa, similar to the ACI restriction for high strength concrete. Similarly, the "equivalent crack spacing factor" in CSA A23.3-04 accounts for the aggregate fracture for HSC by reducing the aggregate size (a_g) in the crack spacing equation linearly to zero as f_c' increases from 60 to 70 MPa. For f_c' greater than 70 MPa, the value of a_g is equal to zero. This is because the crack passes through the aggregate for high strength concrete elements, which results a relatively smoother surface (El-Sayed et al. 2006b). A smooth surface has relatively lower shear transfer capacity.

On the other hand, plain concrete can resist the applied load up to it's maximum tensile strength capacity. Thus, the specimen will fail just after the formation of a flexural crack at the midspan of the beam as the redistribution of internal forces cannot take place. For a plain concrete rectangular section, the moment of inertia (I) is equal to $b_w h^3/12$ and the depth of neutral axis (y_t) is equal to $h/2$. Replacing h by d, the shear load at first flexural cracking for plain concrete specimen is:

$$V_{cr} = \frac{0.1}{a/d}\lambda\sqrt{f_c'}\,b_w d \tag{5.11}$$

This is, in fact, the minimum shear strength of the members. Hence, the minimum shear strength of a section can be given as:

$$V_{c(\min)} = \frac{0.1}{a/d}\lambda\sqrt{f_c'}\,b_w d \tag{5.12}$$

On the other hand, according to CSA S806-02, the maximum shear strength should not exceed $0.2\lambda\phi_c\sqrt{f_c'}b_w d$, where ϕ_c is the concrete resistance factor.

Introducing the limit of $\sqrt{f_c'}$ equal to 8 MPa for HSC specimens and the concrete resistance factor in Equation 5.10, the proposed shear design method for determining the concrete contribution to the shear strength can be given as:

$$V_c = \frac{0.2\lambda\phi_c}{(a/d)^{2/3}}\left(\frac{\rho_f E_f}{d}\right)^{1/3}\sqrt{f_c'}\,b_w d \text{, and}$$

$$\frac{0.1}{a/d}\lambda\phi_c\sqrt{f_c'}\,b_w d \le V_c \le 0.2\lambda\phi_c\sqrt{f_c'}\,b_w d \tag{5.13}$$

where,

a = shear span
d = depth of specimen
ρ_f = reinforcement ratio = $A_f / b_w d$
b_w = web width of specimen
E_f = modulus of elasticity of reinforcement
f_c' = concrete compressive strength, and
λ = concrete density factor determined as per CSA A23.3-04
ϕ_c = concrete resistance factor determined as per CSA A23.3-04

In this equation, the value of a/d can be replaced by $M_f / V_f d$, which represents the moment-shear interaction as mentioned in Section 5.2, where the M_f and V_f are the factored moment and shear force occurring simultaneously at a section of interest.

The proposed equation considers almost all of the shear strength parameters. It does not give zero shear strength for plain concrete. The calculation by this method is straight forward, does not require any constants, and has no limitations on a/d or the depth of the beam.

5.5.2 Verification of the Proposed Design Equation

The proposed shear design method is verified by comparing the predictions of the equation with the experimental results of all specimens in the database discussed in Section 5.4.1. The experimental shear strengths are divided by the predicted shear strengths. The test results are also plotted against the predicted values in Figure 5.8 to examine the consistency of the predictions. A trend line is fitted to the data using

regression analysis and is shown in Figure 5.8. The trend line is forced to pass through the origin (0, 0). It was observed that the predicted shear strengths are in good agreement with the experimental ones especially in the lower range. The slope of the trend line is equal to 1.09, which indicates that the predicted shear strengths are generally conservative. The R^2 value of the regression line is 0.82, which indicates a good correlation between the experimental and the predicted results.

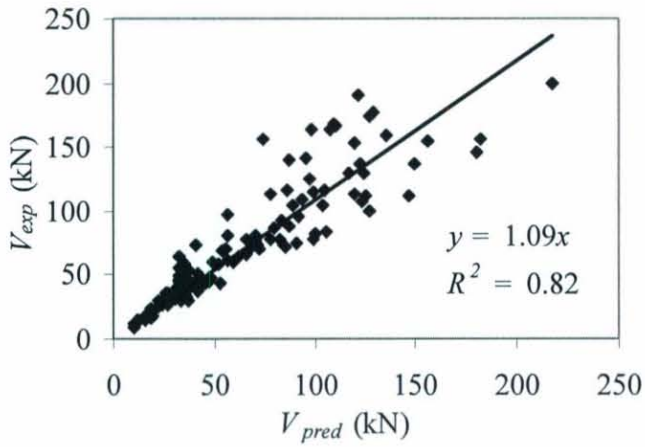

Figure 5.8: Experimental versus predicted shear strength using the proposed method

For further assessment of the consistency of predictions of the proposed method, the ratio of the experimental to the predicted shear strengths (V_{exp}/V_{pred}) are plotted against the shear span-to-depth ratio (a/d), depth of beam (d), concrete strength (f_c'), and axial stiffness of the reinforcement ($\rho_f E_f$) as shown in Figure 5.9. It can be observed that the proposed design equation predicted the shear strength in a consistent way over the entire range of the parameters included in the data set. There is no

noticeable increase or decrease in the shear strength as the value of the variables increase. This suggests that the influence of these variables has been captured realistically. However, the scatter in the lower range of the parameters is noticeable. This could be due to the larger number of data points in this region. The variability in the number, size, clear cover, and arrangement of the reinforcing bars, size of aggregate, and atmospheric condition may lead to the scatter in the result as the data point increases.

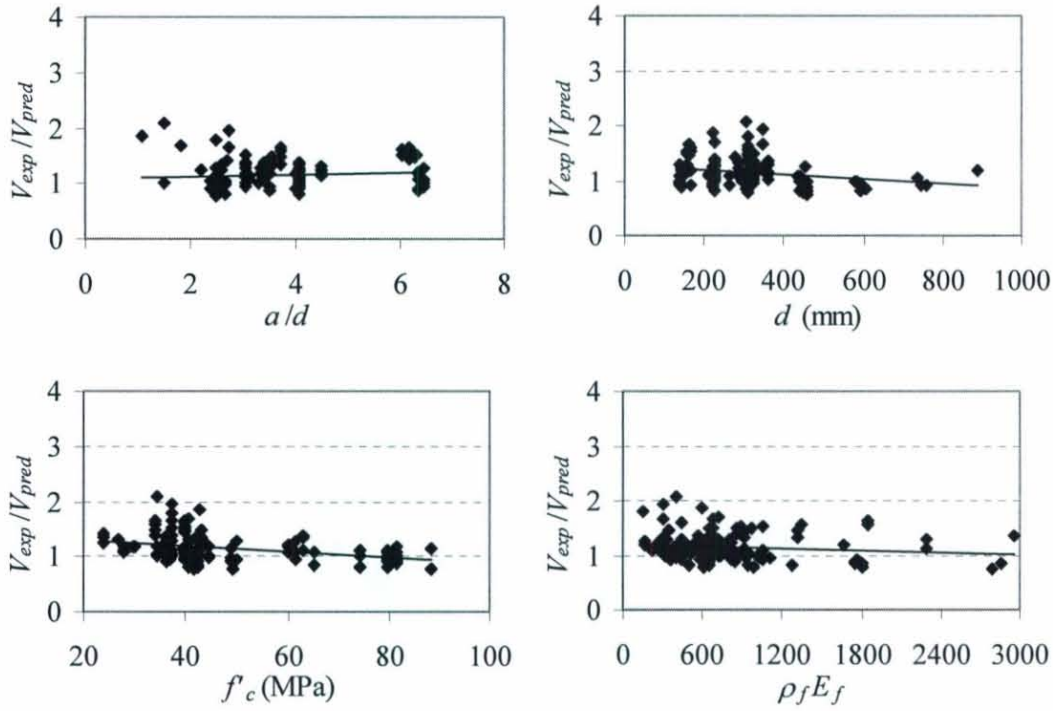

Figure 5.9: Effect of different parameters on the proposed shear design method

The ratios of the predicted to experimental results are presented graphically using a histogram as shown in Figure 5.10. The horizontal axis of the figure shows the ratio of

V_{exp}/V_{pred}, while the vertical axis represents the frequency of the test specimens for a certain V_{exp}/V_{pred} ratio. It appears that the results follow a normal distribution. It was observed that approximately 61% of the data points fall between a narrow range of 1.0 and 1.4, and 24% of the data points fall below 1.0. Also, the proposed method is able to predict the results with reasonable accuracy for all types of reinforcement included in the database.

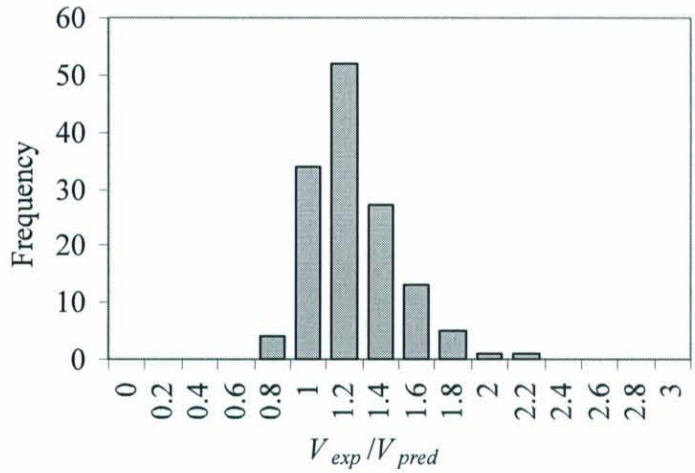

Figure 5.10: Statistical behaviour of the results

5.5.3 Comparison with Major Design Equations

To further verify the level of accuracy of the proposed shear design method, the ratios of the experimental to the predicted results of this method are compared with the ratios obtained using the shear design provisions of ACI 440.1R-06, CSA S806-02, JSCE design guideline (1997), ISIS-M03-07, and CHBDC (CSA S6-06). Also, the results are compared with the predictions of the shear design method proposed by El-Sayed et al.

(2005), Razaqpur and Isgor (2006), and Sherwood et al. (2008). The comparison is made using the same database used earlier in this section. Only FRP reinforced specimens are considered. In calculating the shear strength using CSA S806-02 and ISIS-M03-07, the material resistance factors are taken to be equal to 1.0. For JSCE (1997) design method, the member safety factor (γ_b) is taken equal to 1.0, and no axial force or decompression moment is used. The comparison between the experimental and the predicted shear strengths for 129 specimens in the database are shown in Table 5.4.

From the results shown in Table 5.4, it can be seen that the proposed method has the lowest mean and standard deviation than the CSA, ACI, JSCE, ISIS, and CHBDC design methods. The mean and standard deviation of V_{exp}/V_{pred} using the proposed method are 1.17 and 0.24, respectively. The corresponding values for CSA, ACI, and JSCE methods are 1.34 and 0.42; 1.93 and 0.60; and 1.42 and 0.43, respectively. Clearly, the proposed method gives better prediction than the other three methods. The proposed method has the lowest coefficient of variation than the other three methods. Similarly, the proposed method has lower mean, standard deviation, and coefficient of variation than the ISIS and CHBDC method.

The predictions of the proposed method are also compared with those obtained using the expressions by El-Sayed et al. (2005), Razaqpur and Isgor (2006), and Sherwood et al. (2008). From Table 5.4, it can be seen that the mean and standard deviation of El-Sayed et al. method are 1.32 and 0.26, respectively. Clearly, these values are higher than the proposed method. The mean value and the standard deviation of the predictions of the Sherwood et al. equation are higher than that of the proposed method.

On the other hand, the standard deviation of the proposed model predictions is equal to that obtained using the Razaqpur and Isgor equation. However, the Razaqpur and Isgor method is unconservative with a mean value of 0.98 and the coefficient of variation of this method is higher than the proposed method. Some of the possible reasons behind these differences are explained in Section 5.5.4.

The histograms of the results obtained using the different equations are shown in Figure 5.11. For clarity, the values of V_{exp}/V_{pred} beyond 4.0, obtained from ACI and CHBDC methods, are excluded. It can be seen from Figure 5.11 that all of the predictions using different methods follow an approximately normal distribution. However, the scatter in V_{exp}/V_{pred} varies widely for the different methods except for the equations by the Sherwood et al., Razaqpur and Isgor, and the proposed method. Approximately 62% of the data points for Razaqpur and Isgor method fall in the range of 0.6 and 1.0. Within the same range, the amount of data points for Sherwood et al. method is around 21% and for the proposed method is 24%. The proposed method seems to give more consistent prediction than the other methods.

Table 5.4: Comparison between the experimental and the predicted shear strengths

	Experimental details			Ratio of experimental to predicted shear strength, V_{exp}/V_{pred}								
Authors	Beam ID	FRP type	V_{exp} (kN)	CSA S806-02	ACI440.1R-06	JSCE (1997)	ISIS-M03-07	CHBDC (CSA S6-06)	El-Sayed et al. (2005)	Razaqpur and Isgor (2006)	Sherwood et al. (2008)	Proposed method
Current study	G-1.5	G	155.8	3.49	5.46	4.00	3.63	4.48	1.87	1.75	2.49	2.08
	G-2.5	G	61.0	1.27	2.05	1.49	1.32	2.12	1.45	0.80	1.11	1.07
	G-3.5	G	43.7	0.91	1.47	1.07	0.95	1.67	1.04	0.72	0.89	0.96
	C-1.5	C	87.3	1.93	2.48	1.92	1.14	1.50	0.89	0.97	1.20	1.00
	C-2.5	C	64.6	1.43	1.84	1.42	0.84	1.35	1.37	0.80	1.06	1.04
	C-3.5	C	58.9	1.30	1.67	1.29	0.77	1.42	1.25	0.91	1.07	1.19
	G-500	G	77.2	1.16	1.72	1.36	1.21	1.92	1.22	0.77	0.97	0.99
	G-650	G	103.7	1.18	1.51	1.30	1.23	1.74	1.07	0.83	0.92	0.99
	G-800	G	129.4	1.20	1.50	1.37	1.33	1.77	1.07	0.88	0.96	1.04
	C-500	C	74.1	1.11	1.31	1.11	0.65	1.04	0.98	0.65	0.79	0.81
	C-650	C	112.9	1.28	1.35	1.23	0.75	1.13	1.01	0.80	0.88	0.94
	C-800	C	137.3	1.18	1.31	1.24	0.75	1.11	0.97	0.79	0.87	0.92
	C-500-70	C	100.4	1.16	1.28	1.28	0.68	1.29	1.02	0.62	1.02	0.79
	C-650-70	C	146.1	1.17	1.21	1.29	0.69	1.32	0.96	0.66	1.06	0.81
	G-500-70	G	116.1	1.35	1.91	1.79	1.41	2.56	1.43	0.81	1.43	1.10
	G-650-70	G	155.2	1.26	1.56	1.58	1.31	2.42	1.19	0.78	1.29	1.00
	G-0.5-350	G	72.7	1.54	3.82	2.46	1.61	3.61	2.38	1.29	1.87	1.78
	G-2.5-350(1)	G	65.5	1.15	1.81	1.38	1.46	1.85	1.36	0.76	1.02	0.99
	G-2.5-350(2)	G	70.9	1.22	1.92	1.47	1.53	2.01	1.44	0.80	1.09	1.04
	G-0.5-500	G	68.0	1.09	2.37	1.70	1.14	2.45	1.49	0.96	1.24	1.27
	G-2.5-500	G	92.2	1.53	1.74	1.48	1.59	1.95	1.32	0.88	1.07	1.10
	C-0.5-350	C	58.7	1.17	2.32	1.59	0.69	1.67	1.55	0.84	1.18	1.13
	C-2.5-350	C	72.5	1.60	1.69	1.37	0.95	1.28	1.32	0.81	1.02	1.01
	C-0.5-500	C	70.3	1.05	1.70	1.33	0.62	1.34	1.17	0.76	0.96	0.97
	C-2.5-500	C	82.5	1.28	1.29	1.13	0.75	1.01	1.01	0.68	0.82	0.82
	C-50	C	71.6	1.15	1.71	1.42	0.68	1.31	1.27	0.64	1.00	0.84
	C-70	C	77.9	1.08	1.71	1.55	0.63	1.54	1.31	0.60	1.21	0.79
	G-50	G	75.6	1.29	2.31	1.80	1.34	2.44	1.63	0.80	1.28	1.07
	G-70	G	80.2	1.17	2.26	1.91	1.22	2.91	1.65	0.73	1.48	1.13
El-Sayed et al. (2005a)	S-C1	C	140.0	1.34	2.12	1.36	0.89	2.26	1.48	1.47	1.47	1.60
	S-C2B	C	167.0	1.60	1.85	1.29	1.06	2.00	1.40	1.43	1.36	1.51
	S-C3B	C	190.0	1.65	1.81	1.32	1.24	1.97	1.43	1.50	1.39	1.56
	S-G1	G	113.0	1.10	1.96	1.22	1.23	2.78	1.33	1.32	1.33	1.44
	S-G2	G	142.0	1.41	1.84	1.25	1.58	2.72	1.36	1.40	1.32	1.48
	S-G2B	G	163.0	1.59	2.07	1.40	1.78	3.09	1.53	1.56	1.49	1.65
	S-G3	G	163.0	1.59	1.80	1.27	1.81	2.60	1.38	1.45	1.35	1.51
	S-G3B	G	168.0	1.61	1.81	1.28	1.88	2.68	1.40	1.47	1.35	1.53

Table 5.4 (Contd.): Comparison between the experimental and the predicted shear strengths

	Experimental details			Ratio of experimental to predicted shear strength, V_{exp}/V_{pred}								
Authors	Beam ID	FRP type	V_{exp} (kN)	CSA S806-02	ACI440.1R-06	JSCE (1997)	ISIS-M03-07	CHBDC (CSA S6-06)	El-Sayed et al. (2005)	Razaqpur and Isgor (2006)	Sherwood et al. (2008)	Proposed method
El-Sayed et al. (2006a)	CN-1	C	77.5	1.37	1.45	1.21	0.86	1.23	1.14	0.74	0.93	0.94
	GN-1	G	70.5	1.25	2.25	1.64	1.41	2.60	1.55	0.96	1.28	1.27
	CN-2	C	104.0	1.95	1.69	1.45	1.19	1.47	1.39	0.99	1.14	1.17
	GN-2	G	60.0	1.12	1.64	1.24	1.23	1.86	1.19	0.77	0.98	1.00
	CN-3	C	124.5	2.36	1.79	1.57	1.44	1.60	1.51	1.20	1.27	1.27
	GN-3	G	77.5	1.47	1.83	1.44	1.60	2.17	1.39	0.90	1.14	1.17
El-Sayed et al. (2006b)	CH-1.7	C	130.0	2.05	1.67	1.60	1.25	1.56	1.42	1.04	1.20	1.11
	GH-1.7	G	87.0	1.37	1.86	1.58	1.50	2.25	1.40	0.84	1.16	1.09
	CH-2.2	C	174.0	2.74	2.02	1.97	1.67	2.16	1.75	1.39	1.51	1.36
	GH-2.2	G	115.5	1.82	2.20	1.93	1.99	2.56	1.71	1.04	1.43	1.33
Tureyen and Frosch (2002)	V-G1-1	G	108.1	1.09	1.71	1.29	1.21	2.03	1.21	0.88	1.05	1.15
	V-G2-1	G	94.7	0.95	1.55	1.16	1.10	1.93	1.08	0.78	0.94	1.03
	V-A-1	A	114.8	1.15	1.69	1.30	1.19	2.08	1.21	0.88	1.05	1.15
	V-G1-2	G	137.0	1.34	1.56	1.27	1.49	1.89	1.19	0.88	1.03	1.12
	V-G2-2	G	152.6	1.49	1.79	1.45	1.72	2.32	1.36	0.99	1.18	1.27
	V-A-2	A	177.0	1.72	1.88	1.56	1.78	2.19	1.46	1.08	1.26	1.37
Tariq and and Newhook (2003)	G07N1	G	54.5	1.67	2.93	2.12	1.82	3.20	2.00	1.24	1.62	1.65
	G07N2	G	63.7	1.95	3.42	2.48	2.13	3.74	2.34	1.45	1.89	1.93
	G10N1	G	42.7	1.22	1.81	1.38	1.33	2.22	1.30	0.91	1.11	1.19
	G10N2	G	45.5	1.29	1.93	1.47	1.41	2.37	1.39	0.97	1.19	1.26
	G15N1	G	48.7	1.63	2.02	1.59	1.78	2.56	1.51	1.14	1.31	1.48
	G15N2	G	44.9	1.51	1.86	1.47	1.64	2.36	1.40	1.05	1.21	1.37
	C07N1	C	49.2	2.01	2.26	1.81	1.30	1.97	1.75	1.16	1.45	1.50
	C07N2	C	45.8	1.88	2.10	1.68	1.21	1.84	1.63	1.08	1.35	1.39
	C10N1	C	47.6	1.81	1.75	1.44	1.17	1.68	1.41	1.04	1.23	1.33
	C10N2	C	52.7	2.00	1.93	1.60	1.29	1.86	1.56	1.15	1.36	1.47
	C15N1	C	55.9	2.39	1.91	1.64	1.55	1.84	1.58	1.24	1.40	1.57
	C15N2	C	58.3	2.50	1.99	1.71	1.61	1.92	1.65	1.30	1.46	1.64
Steiner et al. (2008)	A1	G	159.0	0.90	1.36	1.24	0.79	1.89	0.91	1.07	0.95	1.17
Ashour (2006)	S1B1	G	12.5	0.94	2.08	1.24	1.08	2.53	1.32	1.03	1.17	1.18
	S1B3	G	17.5	1.04	2.02	1.27	1.30	2.35	1.32	0.90	1.09	1.09
	S1B5	G	25.0	1.20	2.13	1.45	1.50	2.34	1.43	0.85	1.11	1.10
	S2B7	G	17.5	1.02	1.65	1.10	1.27	2.12	1.18	0.86	0.99	0.93
	S2B9	G	27.5	1.23	2.25	1.46	1.53	2.66	1.55	0.94	1.22	1.12
	S2B11	G	30.0	1.09	1.92	1.33	1.36	2.12	1.34	0.71	1.00	0.91

Table 5.4 (Contd.): Comparison between the experimental and the predicted shear strengths

	Experimental details			Ratio of experimental to predicted shear strength, V_{exp}/V_{pred}								
Authors	Beam ID	FRP type	V_{exp} (kN)	CSA S806-02	ACI440.1R-06	JSCE (1997)	ISIS-M03-07	CHBDC (CSA S6-06)	El-Sayed et al. (2005)	Razaqpur and Isgor (2006)	Sherwood et al. (2008)	Proposed method
Yost et al. (2001)	1FRPa	G	39.1	1.26	2.27	1.30	1.40	2.31	1.36	1.06	1.18	1.27
	1FRPb	G	38.5	1.24	2.23	1.28	1.38	2.27	1.34	1.04	1.16	1.25
	1FRPc	G	36.8	1.19	2.14	1.23	1.32	2.17	1.28	1.00	1.11	1.20
	2FRPa	G	28.1	1.16	1.87	1.11	1.30	1.94	1.16	0.91	1.00	1.09
	2FRPb	G	35.0	1.45	2.33	1.38	1.62	2.42	1.45	1.13	1.25	1.35
	2FRPc	G	32.1	1.33	2.14	1.26	1.48	2.21	1.32	1.04	1.14	1.24
	3FRPa	G	40.0	1.22	1.93	1.16	1.44	2.15	1.22	0.96	1.05	1.14
	3FRPb	G	48.6	1.48	2.34	1.41	1.74	2.61	1.48	1.17	1.28	1.39
	3FRPc	G	44.7	1.37	2.16	1.30	1.60	2.40	1.36	1.07	1.17	1.27
	4FRPa	G	43.8	1.07	1.67	1.02	1.29	1.83	1.07	0.84	0.91	1.00
	4FRPb	G	45.9	1.12	1.75	1.07	1.35	1.92	1.12	0.88	0.96	1.04
	4FRPc	G	46.1	1.12	1.75	1.07	1.36	1.92	1.12	0.89	0.96	1.05
	5FRPa	G	37.7	0.97	1.50	0.93	1.23	1.64	0.97	0.77	0.82	0.91
	5FRPb	G	51.0	1.32	2.03	1.25	1.66	2.22	1.31	1.05	1.11	1.23
	5FRPc	G	46.6	1.20	1.85	1.14	1.51	2.02	1.20	0.96	1.02	1.12
	6FRPa	G	43.5	1.20	1.83	1.14	1.57	1.98	1.20	0.96	1.03	1.12
	6FRPb	G	41.8	1.16	1.76	1.10	1.50	1.90	1.15	0.92	0.99	1.08
	6FRPc	G	41.3	1.14	1.74	1.09	1.49	1.88	1.14	0.91	0.98	1.07
Gross et al. (2003)	1a-26-HS	G	41.6	1.02	1.86	1.38	1.14	2.56	1.29	0.83	1.29	1.11
	1b-26-HS	G	30.4	0.74	1.36	1.01	0.83	1.87	0.94	0.60	0.94	0.81
	1c-26-HS	G	42.1	1.03	1.88	1.39	1.15	2.59	1.31	0.84	1.31	1.12
	2a-26-HS	G	31.0	1.02	1.62	1.25	1.13	2.31	1.17	0.76	1.16	1.00
	2b-26-HS	G	33.0	1.08	1.73	1.33	1.21	2.47	1.25	0.81	1.25	1.07
	2c-26-HS	G	33.5	1.10	1.75	1.35	1.22	2.50	1.26	0.82	1.26	1.08
	3a-27-HS	G	38.4	1.16	1.67	1.32	1.30	2.37	1.24	0.81	1.23	1.06
	3b-27-HS	G	32.2	0.98	1.40	1.11	1.09	1.99	1.04	0.68	1.03	0.89
	3c-27-HS	G	36.7	1.11	1.60	1.26	1.24	2.27	1.18	0.78	1.17	1.02
	4a-37-HS	G	48.3	1.11	1.56	1.26	1.33	2.29	1.19	0.78	1.19	1.02
	4b-37-HS	G	45.7	1.06	1.48	1.20	1.26	2.17	1.12	0.74	1.13	0.96
	4c-37-HS	G	45.2	1.04	1.46	1.18	1.24	2.14	1.11	0.73	1.11	0.95
Gross et al. (2004)	8-2a	C	14.3	1.02	2.04	1.19	0.61	1.75	1.21	1.14	1.19	1.18
	8-2b	C	12.9	0.91	1.83	1.07	0.55	1.57	1.09	1.03	1.07	1.06
	8-2c	C	14.7	1.04	2.09	1.23	0.63	1.80	1.24	1.18	1.22	1.21
	8-3a	C	19.8	1.13	1.77	1.11	0.68	1.57	1.12	1.08	1.08	1.09
	8-3b	C	23.1	1.31	2.06	1.29	0.79	1.83	1.31	1.26	1.26	1.27
	8-3c	C	17.0	0.97	1.52	0.95	0.58	1.35	0.96	0.93	0.93	0.94
	11-2a	C	8.8	0.76	1.33	0.92	0.46	1.41	0.89	0.77	0.97	0.89

Table 5.4 (Contd.): Comparison between the experimental and the predicted shear strengths

	Experimental details			Ratio of experimental to predicted shear strength, V_{exp}/V_{pred}								
Authors	Beam ID	FRP type	V_{exp} (kN)	CSA S806-02	ACI440.1R-06	JSCE (1997)	ISIS-M03-07	CHBDC (CSA S6-06)	El-Sayed et al. (2005)	Razaqpur and Isgor (2006)	Sherwood et al. (2008)	Proposed method
Gross et al. (2004) contd.	11-2b	C	11.7	1.02	1.78	1.23	0.61	1.88	1.19	1.03	1.30	1.19
	11-2c	C	8.9	0.78	1.35	0.94	0.47	1.43	0.91	0.79	0.99	0.91
	11-3a	C	14.3	0.93	1.30	0.96	0.56	1.39	0.93	0.82	1.00	0.93
	11-3b	C	15.3	0.99	1.39	1.03	0.60	1.49	0.99	0.88	1.06	0.99
	11-3c	C	16.6	1.08	1.51	1.11	0.64	1.61	1.07	0.95	1.15	1.07
Razaqpur et al. (2004)	BR1	C	36.1	1.26	2.15	1.42	0.74	1.52	1.50	0.85	1.13	1.04
	BR2/BA2	C	47.0	1.26	1.93	1.40	0.88	1.46	1.46	0.82	1.09	0.97
	BR3	C	47.2	1.25	1.85	1.37	0.97	1.39	1.44	0.85	1.08	0.99
	BR4	C	42.7	1.01	1.45	1.11	0.88	1.13	1.17	0.75	0.88	0.80
	BA1	C	96.2	2.42	4.17	3.01	1.97	2.53	1.98	1.68	2.09	1.69
	BA3	C	47.0	1.48	2.04	1.47	0.96	1.68	1.55	1.09	1.28	1.30
	BA4	C	38.5	1.31	1.67	1.20	0.79	1.50	1.27	1.05	1.13	1.24
Alkhrdaji et al. (2001)	BM7	G	53.4	1.52	2.19	1.75	2.45	2.68	1.67	1.13	1.35	1.42
	BM8	G	36.1	1.42	2.34	1.67	1.61	2.55	1.57	1.01	1.27	1.33
	BM9	G	40.1	1.32	2.02	1.54	1.79	2.26	1.45	0.95	1.17	1.23
Deitz et al. (1999)	GFRP1	G	26.8	1.04	1.81	1.16	1.17	2.53	1.23	1.06	1.22	1.16
	GFRP2	G	28.3	1.07	1.88	1.20	1.20	2.61	1.28	1.09	1.27	1.19
	GFRP3	G	29.2	1.17	2.00	1.28	1.31	2.84	1.35	1.19	1.36	1.30
Guadagnini et al. (2006)	GB43	G	27.2	1.19	1.73	1.21	1.31	1.98	1.28	0.84	1.04	1.00
	GB44	G	44.7	1.72	2.85	1.99	2.15	2.76	1.73	1.02	1.48	1.26
	GB45	G	81.0	2.45	5.10	3.58	3.86	4.06	1.25	1.85	2.10	1.85
			Mean =	**1.34**	**1.93**	**1.42**	**1.27**	**2.07**	**1.32**	**0.98**	**1.19**	**1.17**
			Standard deviation =	**0.42**	**0.60**	**0.43**	**0.50**	**0.58**	**0.26**	**0.24**	**0.25**	**0.24**
			Coefficient of variation (%) =	**31**	**31**	**30**	**39**	**28**	**20**	**25**	**21**	**21**

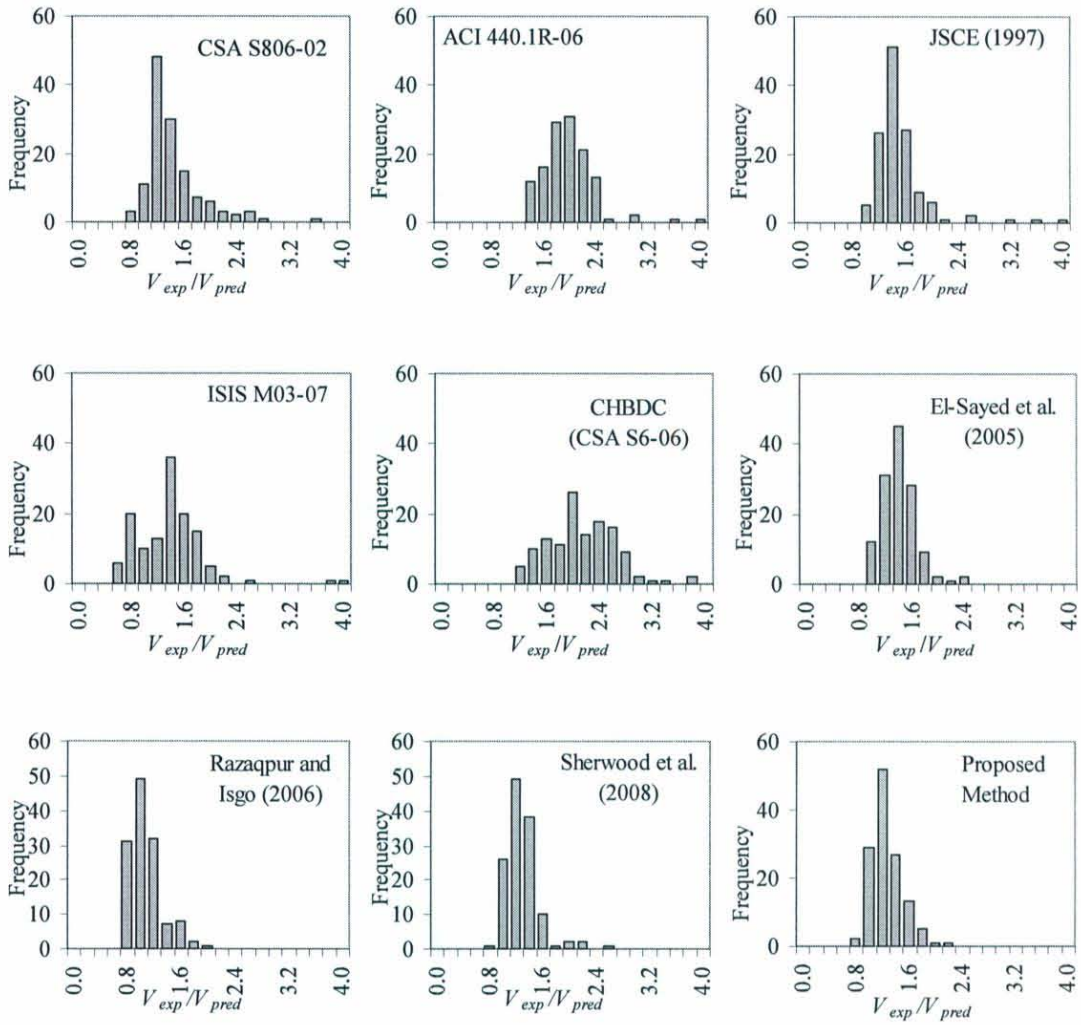

Figure 5.11: Comparison between the experimental and the predicted shear strengths using different shear strength equations

5.5.4 Influence of Different Parameters on the Predictions of Design Methods

The effect of the different parameters on the ratio of the experimental to the predicted shear strength (V_{exp}/V_{pred}) using different methods are shown in Figures 5.12 to

5.15. Figure 5.12 shows that the ratio of V_{exp}/V_{pred} decreases for higher values of a/d ratio for almost all of the methods. The only exception in Razaqpur and Isgor and the proposed methods. These two methods predict the shear strength approximately with the same level of accuracy for a/d ratio that range from 1.1 to 6.45. This could be expected as these two equations accounted for a/d ratio in a similar way as observed in the test results. Although, these two methods give more conservative results for a/d ratio less than 2.5, these conservatisms are less than the El-Sayed et al. and Sherwood et al. methods. An arch effect factor is included in the Razaqpur and Isgor method. However, the equation is found to give an unconservative prediction of the result of beam C-1.5, which had an a/d ratio of 1.5. The method by Sherwood et al. accounts for the parameters through the size effect and strain rate effect. The highest decrease in the ratio of V_{exp}/V_{pred} with an increase in the values of a/d is observed for ACI method. The ACI equation gives very conservative results for a/d values that are less than 2.5. This could be due to the fact that this method does not reflect the influence of this parameter. The effect of depth on the ratio of V_{exp}/V_{pred} for the different design methods are shown in Figure 5.13. The beams have depth that varies in the range of 104 to 889 mm. The scatter in the results could be noticed in the CSA, ACI, JSCE, ISIS, and CHBDC methods. The low scatter in the proposed method indicates that the size effect is accounted for in a reasonable manner. Figure 5.14 shows the effect of concrete strength on the predictions using different methods. Similar to the effect of depth on the ratio of V_{exp}/V_{pred}, scatter in the results could be noticed in the CSA, ACI, JSCE, ISIS, and CHBDC methods.

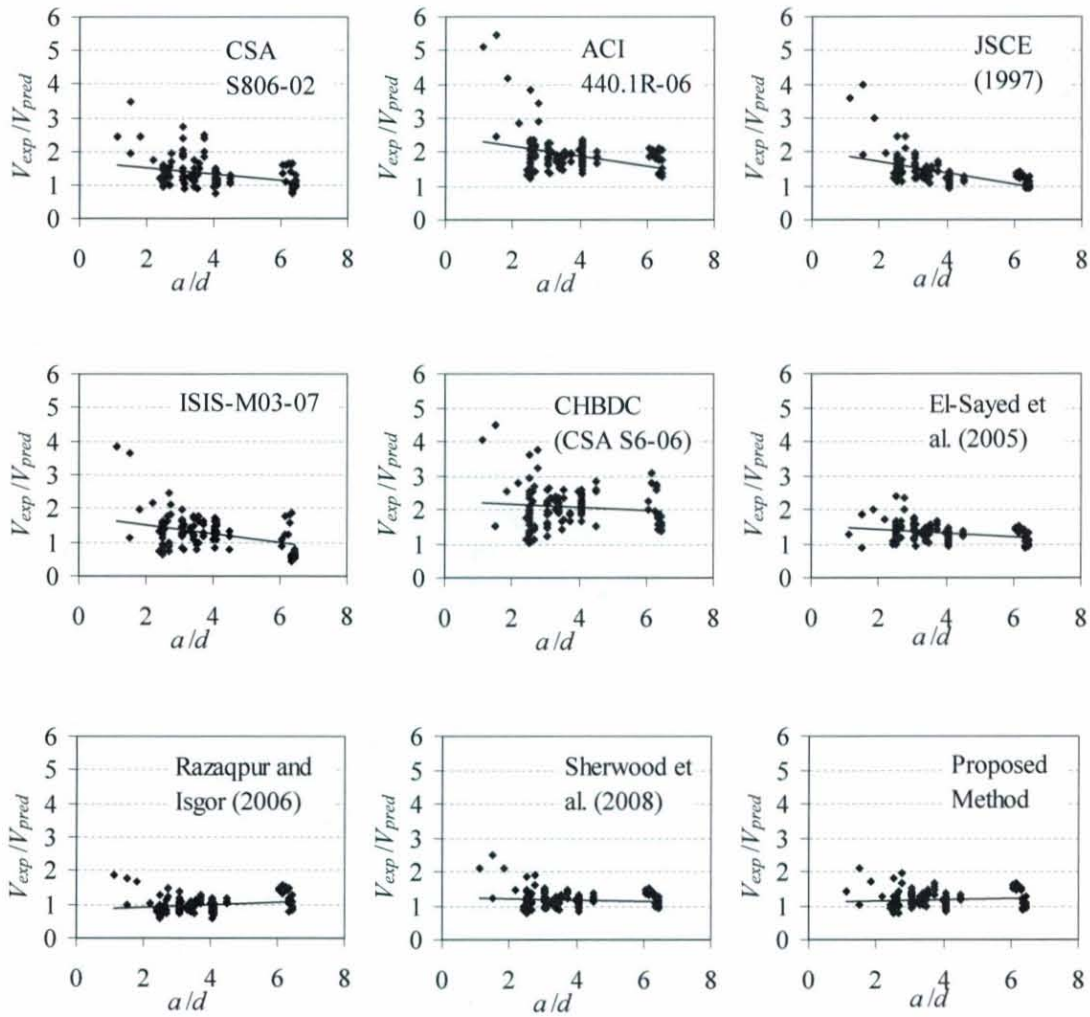

Figure 5.12: Effect of shear span-to-depth ratio on the different equations

The effect of axial stiffness on the ratio of V_{exp}/V_{pred} for the different design methods are shown in Figure 5.15. In this case also, scatter in the results could be noticed in the CSA, ACI, JSCE, ISIS, and CHBDC methods. However, an increasing trend in the ratio of V_{exp}/V_{pred} for CSA S806-02 method and a decreasing trend for ACI440.1R-06

and CHBDC methods are noticed for an increase in the axial stiffness of the reinforcement.

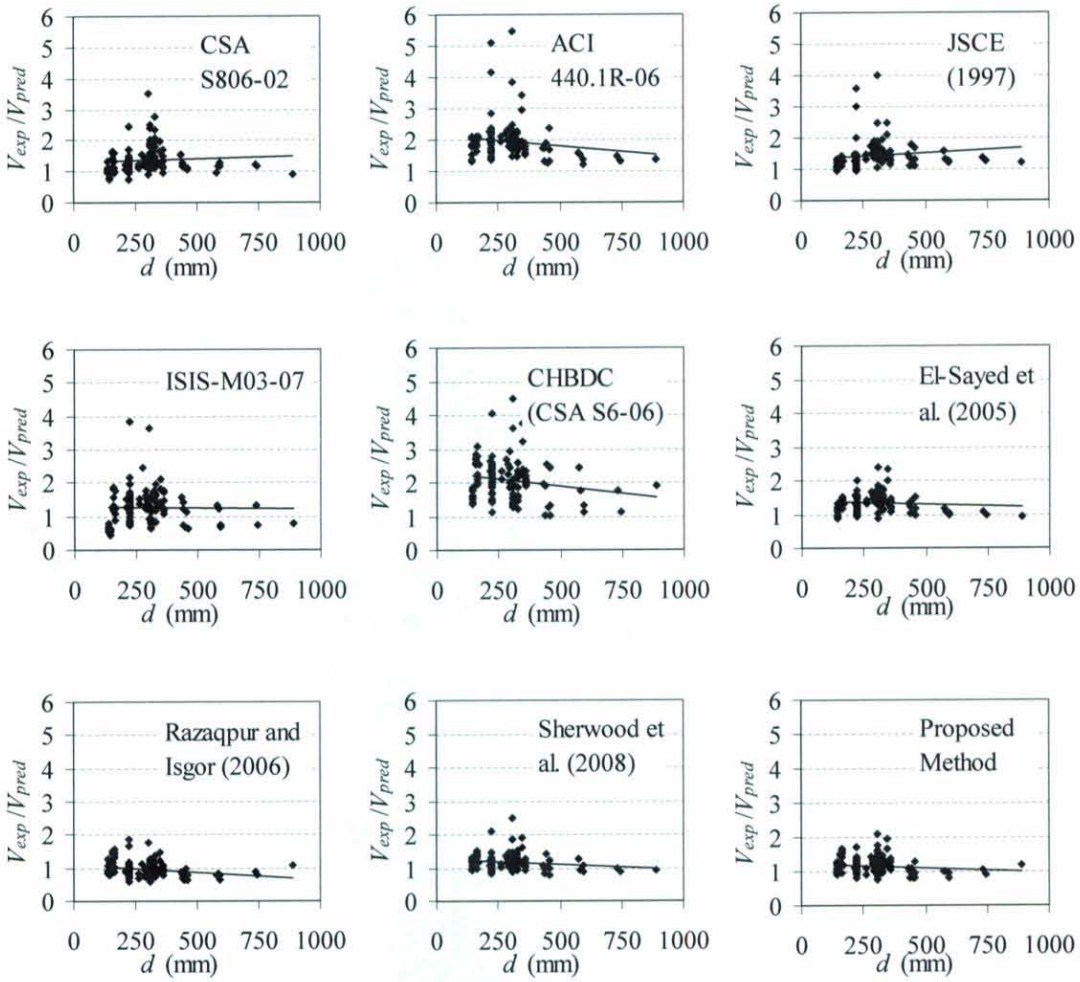

Figure 5.13: Effect of depth of specimens on the different equations

As mentioned in section 5.5.3, the scatter in the results of El-Sayed et al. and Sherwood et al. methods is greater than the proposed method. However, the Razaqpur and Isgor method is close to the proposed method, this method seems to be slightly

unconservative. Hence, the comparisons mentioned in this section reveal that the proposed method gives a consistent and reliable prediction than the other methods presented, for predicting the concrete contribution to the shear strength of rectangular beams that are reinforced longitudinally with FRP bars and without transverse shear reinforcement.

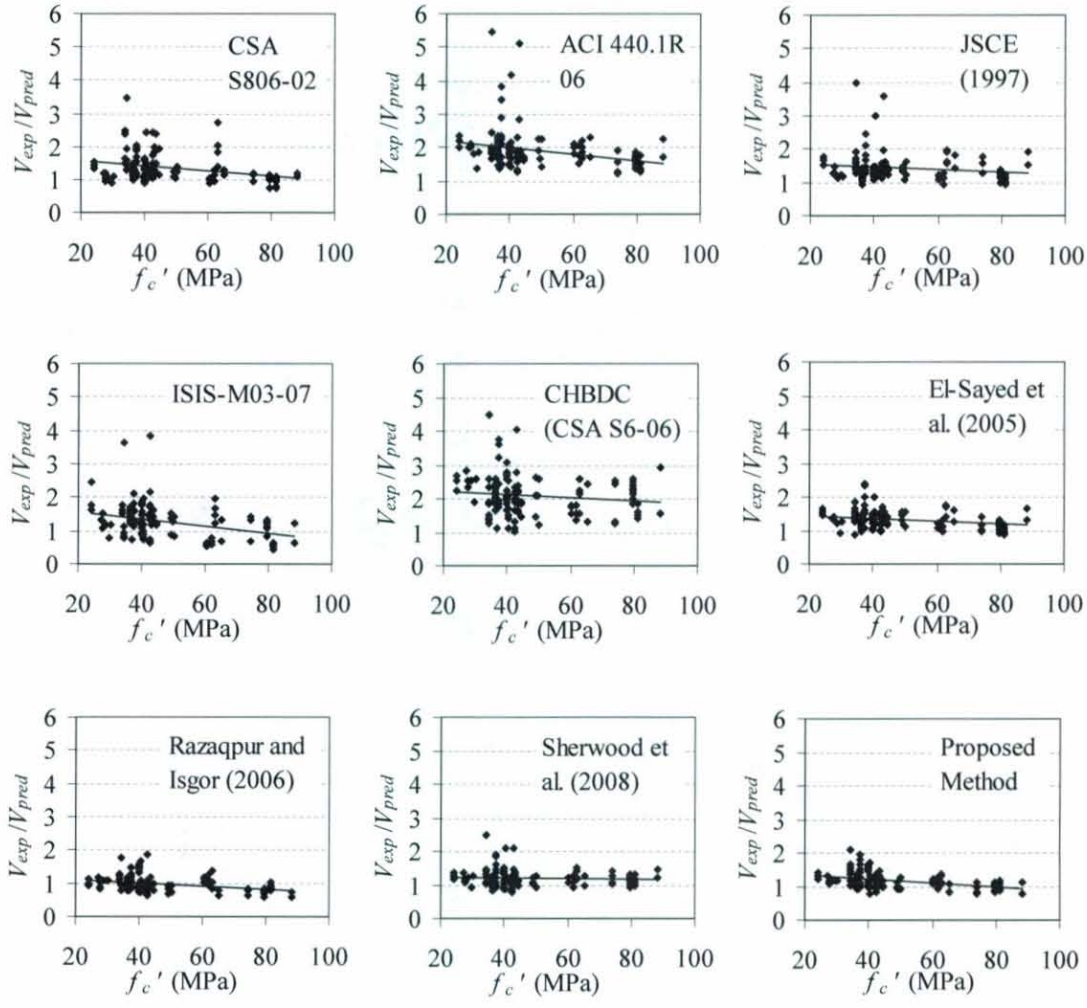

Figure 5.14: Effect of concrete compressive strengths on the different equations

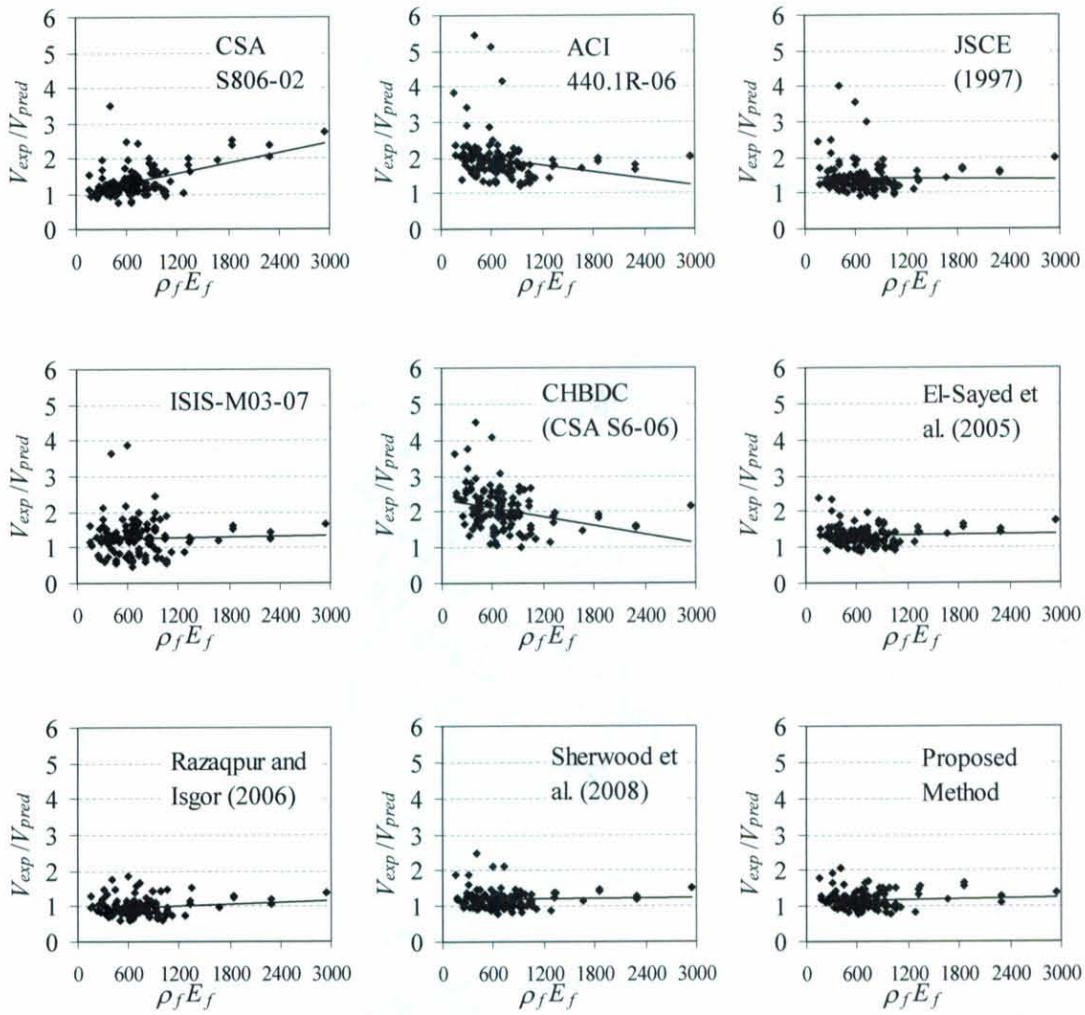

Figure 5.15: Effect of axial stiffness of reinforcement on the different equations

Chapter 6 Finite Element Analysis of the Test Beams

6.1 Introduction

Most of the present shear design methods for FRP reinforced members are based on an empirical approach. Despite enormous progress, there remains a pressing need to establish analysis methods that provide a rational assessment of the strength, stiffness, ductility, and capacity of shear critical element. Finite element analysis combined with the experimental data constitutes a promising approach for this purpose.

Finite element analysis can model the complex behaviour of reinforced concrete such as cracking, tension stiffening, nonlinear material properties, and reinforcement-concrete interface. The information gained through such studies may provide a firmer basis for the codes and specifications on which ordinary design is based (ASCE 1982).

This chapter deals with the nonlinear finite element analysis of shear critical FRP reinforced concrete beams. The analysis covers a wide range of design parameters such as shear span-to-depth ratio, depth of beams, reinforcement ratio, concrete strength, and reinforcement type. Two concrete material models namely concrete damage plasticity model (Model-1) and hypoelastic concrete model (Model-2) are used. The modelling approaches focus on the material models for concrete in tension and compression that form the basis of the concrete constitutive models. The interaction between the concrete and FRP bars are modelled with different tension stiffening models. The tension stiffening models are proposed based on the reinforcement type and vary as a function of the member strain. The models are implemented in the general purpose finite element programs: ABAQUS and ADINA, respectively, to simulate the experimental results of some of the

beams tested in this investigation. The results obtained from FEA are compared with the experimental results in term of the estimated ultimate load, deflection, and the structural behaviour of the beams.

6.2 Behaviour of Concrete

6.2.1 Uniaxial Compressive Behaviour

The behaviour of concrete in compression is nonlinear and appears to be somewhat ductile. This is explained by the gradual development of micro-cracking within the concrete (Hsu et al. 1963). The stress-strain diagram of plain concrete of typical uniaxial compression is shown in the left hand side of Figure 6.1. There are four major stages in the development of micro-cracking and failure in concrete subjected to uniaxial compression. Before the concrete is loaded (point a), bond cracks develops due to the incomplete hydration along the interface zone and from drying shrinkage. Even though there are some bond cracks before loading, the curve shows linear elastic behaviour up to about 30% of its maximum compressive strength, f_c' (point b). When concrete is subjected to stress greater than 30 to 40% of its compressive strength, a gradual curving of the stress-strain curve occurs. At this stage, bond cracks develop and propagate as the load is increased. At 50 to 60% of the ultimate load, localized mortar cracks develop between bond cracks. At about 75 to 80% of the ultimate load, the number of mortar cracks begin to increase and a continuous pattern of micro-cracks begins to form (point c). At this stage, the stress-strain curve bends sharply and approaches the peak point of the compressive strength. Beyond

this peak, the curve descends until crushing failure occurs at ultimate strain (Mang et al. 2003). This descending behaviour is defined as softening.

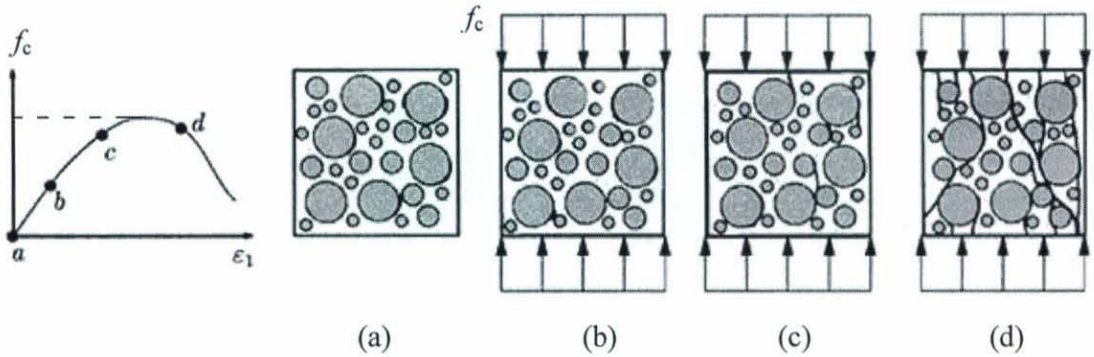

Figure 6.1: Failure mechanism of concrete under uniaxial compression: load-displacement diagram and the evolution of micro-cracks at four stages of deformation (Mang et al. 2003)

It is not always possible to get the descending part of the compressive stress-strain curve experimentally. There are several models available to define the compressive stress-strain curve mathematically. The model proposed by Collins and Mitchell (1997) is used in the current study. This model is given by:

$$\frac{f_c}{f_c'} = \frac{n\left(\frac{\varepsilon_c}{\varepsilon_0}\right)}{n-1+\left(\frac{\varepsilon_c}{\varepsilon_0}\right)^{nk}} \tag{6.1}$$

where,

ε_o = concrete strain at f_c'

n = curve fitting factor = $0.8+f_c'/17$

k = stress decay factor, taken as 1.0 for $\varepsilon_c/\varepsilon_0 < 1.0$ and as a number greater than 1.0 for $\varepsilon_c/\varepsilon_0 > 1.0$.

Figure 6.2 shows the stress-strain relationship obtained from this model for concrete with different compressive strengths.

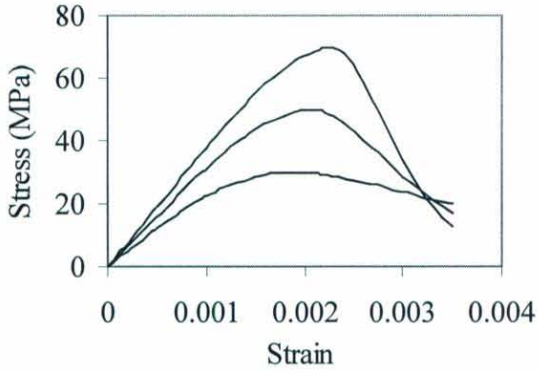

Figure 6.2: Predicted compressive stress-strain curves of concrete

6.2.2 Uniaxial Tensile Behaviour

A typical stress-strain diagram of plain concrete under uniaxial tension obtained from a displacement control test is shown on the left hand side of Figure 6.3 (Mang et al. 2003). The stress-strain response of concrete in uniaxial tension is nearly linear up to cracking. The shape of the curve shows many similarities with the uniaxial compression curve (Figure 6.1). The creation of micro-cracks is negligible for the stress less than 60% of the uniaxial tensile strength, f_t' (point b). If the load is increased, additional micro-cracks between the aggregates and the mortar can be observed (point c). The direction of crack propagation for uniaxial tension is transverse to the stress direction. The initiation and growth of new cracks reduce the stiffness. Consequently, the stress-strain relationship becomes nonlinear. Prior to the peak stress, the micro-cracks form a band which is restricted to a small localized zone. These continuous cracks result in a rapid decrease of

the residual strength in the post-peak regime. In contrast to the crack pattern observed in compression tests, the failure in tension is caused by a few bridging cracks rather than by numerous cracks.

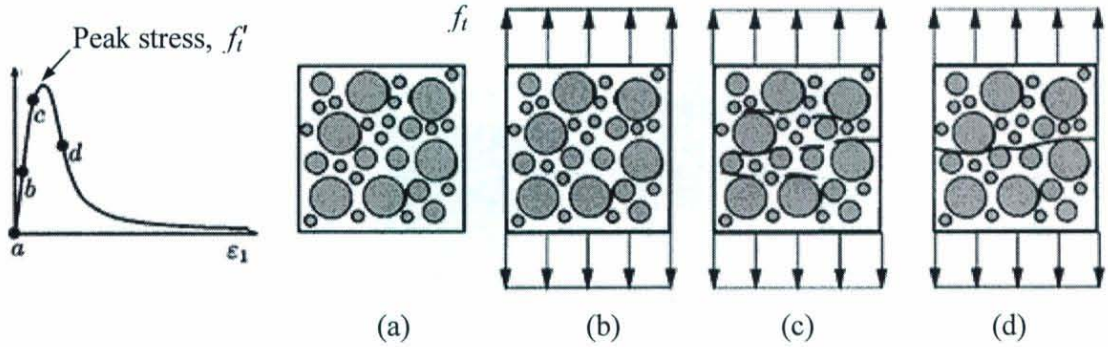

Figure 6.3: Failure mechanism of concrete under uniaxial tension: load-displacement diagram and the evolution of micro-cracks at four stages of deformation (Mang et al. 2003)

As a consequence of the rapid crack propagation, it is difficult to follow the descending part of the stress-strain curve in an experimental test even with a very stiff machine. Therefore, the limited experimental data on post-cracking softening behaviour of concrete subjected to uniaxial tension shows the scattered and conflicting behaviour. As stated by Gopalaratnam and Shah (1985), no unique stress-strain relationship may exist due to the localized nature of post-peak deformation. Therefore, different stress-strain relationships describing tension softening behaviour for finite element analysis were proposed as shown in Figure 6.4 (Gopalaratnam and Shah 1985, Darwin 1986). In this figure, ε_{cr} is the strain corresponding to the tensile strength, f_t', in uniaxial tension.

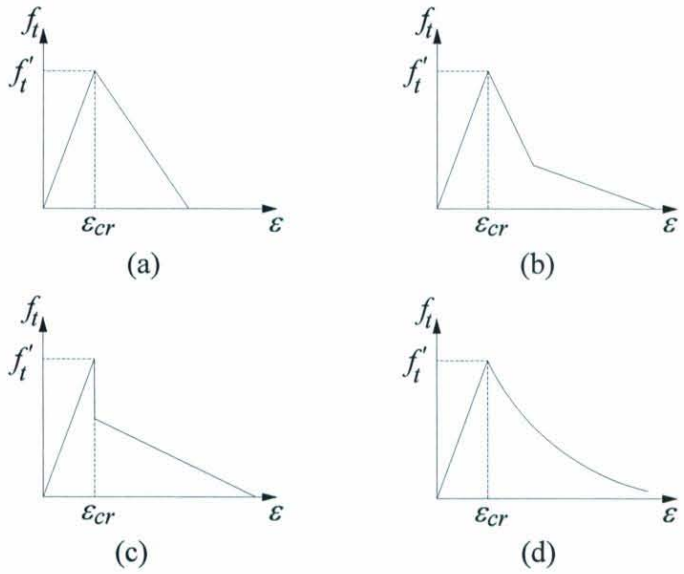

Figure 6.4: Different models for post-cracking behaviour of concrete: (a) simple linear unloading model; (b) bilinear unloading model; (c) discontinuous unloading model; and (d) smooth unloading model

6.2.3 Biaxial Behaviour

The strength and stress-strain behaviour of concrete in biaxial compression differs from that under uniaxial compression for different combinations of biaxial loading. Figure 6.5 shows a typical biaxial strength envelope for concrete subjected to proportional biaxial loading. Under conditions of biaxial compression, concrete exhibits values of increased compressive strength up to about $1.25 f_c'$ (Kupfer et al. 1969). Under biaxial tension, concrete exhibits constant or perhaps slightly increased tensile strength compared with values obtained under uniaxial loading (Tasuji et al. 1978). Under combinations of tension and compression, concrete exhibits a noticeably reduced strength.

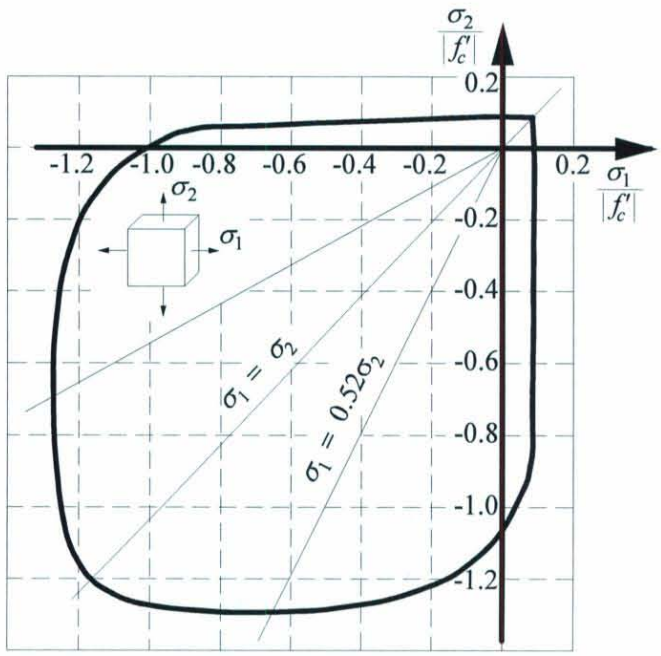

Figure 6.5: Biaxial behaviour of concrete (Kupfer et al. 1969)

6.3 Constitutive Models for Concrete

6.3.1 Concrete Damage Plasticity Model (Model-1)

Concrete damage plasticity model is based on the classical theory of plasticity. This model has the ability to define compression and tension degradation. Damage is associated with the failure mechanisms of the concrete and, therefore, results in a reduction in the elastic stiffness. In the current study, a plastic damage model without stiffness degradation as proposed by Lubliner et al. (1989) is used. The model consists of: yield and failure criteria, strain rate decomposition into elastic and inelastic strain rates, hardening, and flow rule.

6.3.1.1 Yield and Failure Criteria

The yield surface defines the material behaviour beyond the elastic region and the failure surface is based on the ultimate strength. Based on the shape of failure surface of concrete, various failure criteria have been proposed. Chen (1982) discussed many of these criteria according to the number of material constants used. One to five parameters have been used in the different proposed expressions. Figure 6.6 shows some of the common failure surfaces. The experimental data from Kupfer and Gerstle (1969) are shown in Figure 6.6. Among the failure surface, von Mises one parameter failure surface, for ductile metals, has been used in early finite element analysis of concrete under compressive stress. Two-parameter Drucker-Prager and Mohr-Coulomb yield criterions are most often used for concrete materials. These criterions, however, cannot capture the characteristics of concrete failure surface very well unless suitably modified (Lubliner et al. 1989). One modification is to use a combination of the Mohr-Coulomb and the Drucker-Prager yield functions. The Drucker-Prager is used for biaxial compression and the Mohr-Coulomb is used otherwise. To model the surface of concrete in a more realistic way, Menetrey and William (1995) proposed a three parameter generalized failure criteria, which includes both Drucker-Prager and Mohr-Coulomb criterions.

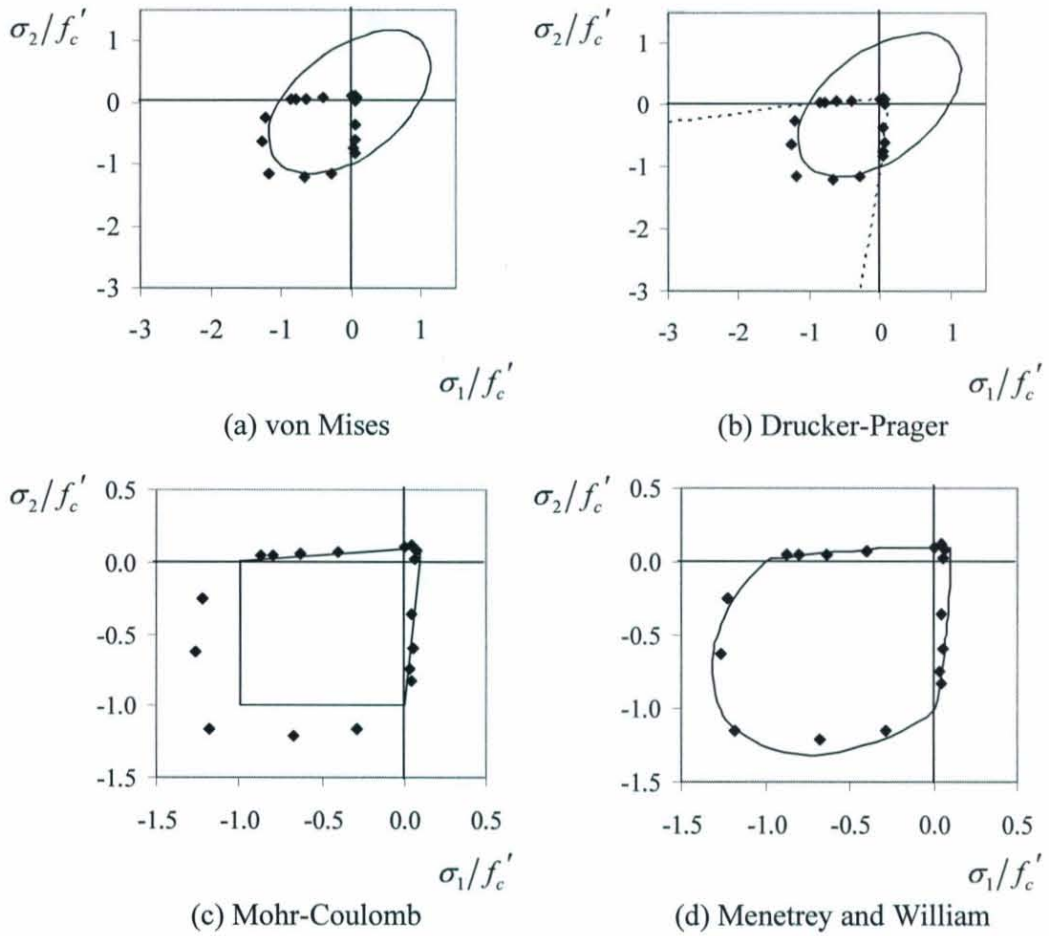

Figure 6.6: Different failure criteria for biaxial stress state

The concrete model used in the current study utilizes the yield condition proposed by Lubliner et al. (1989) which is similar to the Menetrey and William (1995) model. The model incorporates the modifications proposed by Lee and Fenves (1998) to account for different evolution of strength under tension and compression. The yield function used in the current study is illustrated in Figure 6.7 for a biaxial state of stress.

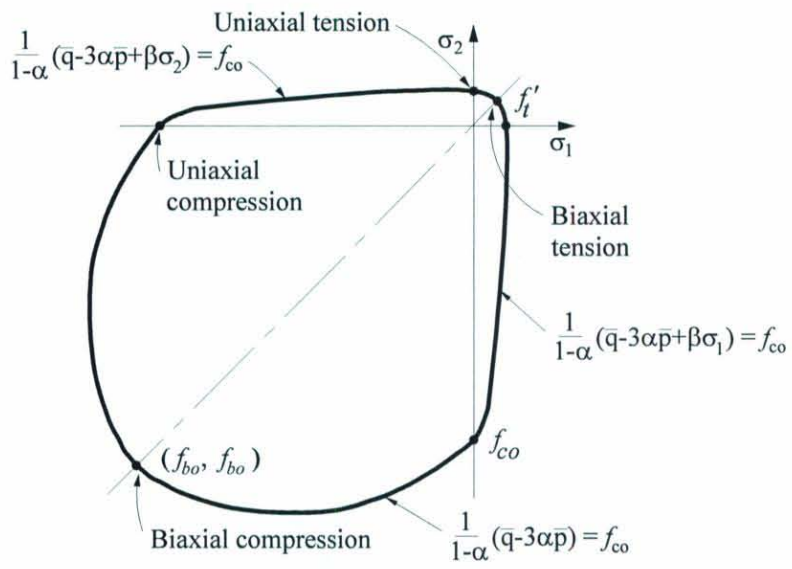

Figure 6.7: Biaxial yield surface used in damage plasticity model

The parameters used in Figure 6.7 are:

α is a dimensionless coefficient, and $\alpha = \frac{f_{b0} - f_{c0}}{2f_{b0} - f_{c0}}$, where $0 \le \alpha \le 0.5$

f_{b0} is the initial equibiaxial compressive yield stress

f_{c0} is the initial uniaxial compressive yield stress

f_t' is the uniaxial tensile stress at failure

$\bar{p}$ is the effective hydrostatic pressure stress, which is a function of first stress invariant I_1, and $\bar{p} = -I_1/3 = -(\sigma_{11} + \sigma_{22} + \sigma_{33})/3$

$\bar{q}$ is the Mises equivalent effective stress,

$\bar{q} = \sqrt{\frac{3}{2}\bar{S} : \bar{S}}$ where $\bar{S}$ is the efeective deviatoric stress tensor $= \bar{p}I + \bar{f}$

β is dimensionless coefficient

$$\beta = \frac{\bar{f}_c\left(\tilde{\varepsilon}_c^{pl}\right)}{\bar{f}_t\left(\tilde{\varepsilon}_t^{pl}\right)}(1-\alpha) - (1+\alpha),$$

where $\bar{f}_t, \bar{f}_c$ is the effective tensile and compresive cohesion stress, respectively.

6.3.1.2 Strain Rate Decomposition

Concrete in compression is considered elastic until a yield point is reached after which irrecoverable plastic strain occurs. Hence, the strain rate is decomposed into elastic and plastic strain rates followed by flow and hardening according to the following formula:

$$\dot{\varepsilon} = \dot{\varepsilon}^{el} + \dot{\varepsilon}^{pl} \tag{6.2}$$

where,

$\dot{\varepsilon}$ is the total strain rate, $\dot{\varepsilon}^{el}$ is the elastic part of the strain rate, and $\dot{\varepsilon}^{pl}$ is the plastic part of the strain rate.

The stress-strain relation under uniaxial tension and compression loading in the damage plasticity model are given by,

$$f_t = (1-d_t)E_0(\varepsilon_t - \tilde{\varepsilon}_t^{pl}), \tag{6.3}$$

$$f_c = (1-d_c)E_0(\varepsilon_c - \tilde{\varepsilon}_c^{pl}), \tag{6.4}$$

where,

E_o is the initial undamaged elastic modulus
ε_t is the total strain in tension
$\tilde{\varepsilon}_t^{pl}$ is the equivalent plastic strain in tension
ε_c is the total strain in compresion
$\tilde{\varepsilon}_c^{pl}$ is the equivalent plastic strain in compression
d_t and d_c is the degradion variable for tension and compression, respectively

The current model assumes no damage in uniaxial tensile and compressive response of concrete. Thus the equivalent plastic strain in tension and compression will be replaced by cracking strain and inelastic strain, respectively and the stress-strain relationship can be written as:

$$f_t = E_0(\varepsilon_t - \tilde{\varepsilon}_t^{ck}), \tag{6.5}$$

$$f_c = E_0(\varepsilon_c - \tilde{\varepsilon}_c^{in}), \tag{6.6}$$

where,

$\tilde{\varepsilon}_t^{ck}$ is the cracking strain

$\tilde{\varepsilon}_c^{in}$ is the inelastic strain

The uniaxial tensile and compressive response of concrete for undamaged material is shown in Figure 6.8. Under uniaxial tension, the stress-strain response follows a linear elastic relationship until the value of the tensile strength, f_t', is reached (Figure 6.8a). When the element is subjected to tension exceeding its tensile strength, the material will crack. A descending portion occurs as the material is stressed beyond that point. Under uniaxial compression, the response is linear until the value of initial yield. In the plastic regime, the response is typically characterized by stress hardening followed by strain softening beyond the ultimate stress, f_c' (Figure 6.8b).

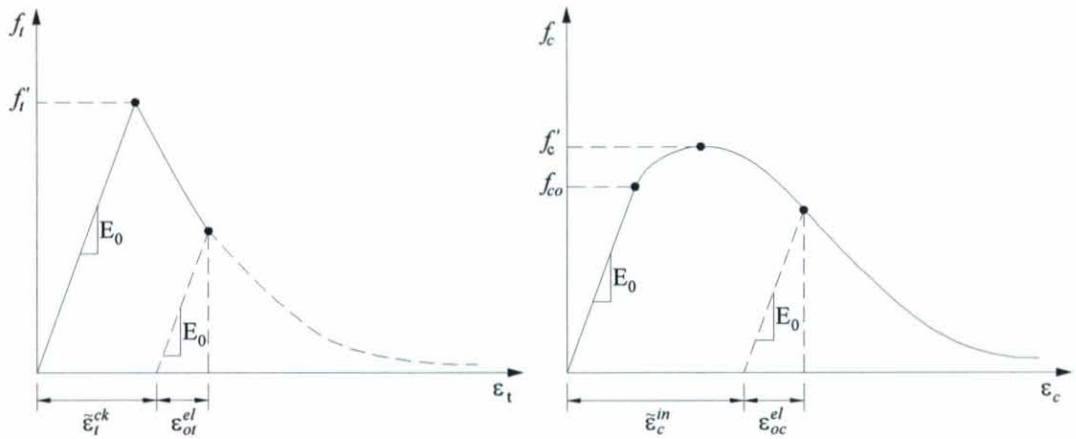

(a) (b)

Figure 6.8: Uniaxial response of concrete; (a) in tension, and (b) in compression

6.3.1.3 Hardening

The hardening rule defines the motion of subsequent yield surfaces during plastic loading. An increase in yield surface is termed as *hardening*, a decrease is termed as *softening*, and no change in yield surface is termed as *perfect-plasticity*. In plastic damage model, damage states in tension and compression are characterized independently by two hardening variables, $\tilde{\varepsilon}_t^{pl}$ and $\tilde{\varepsilon}_c^{pl}$, which are referred to as equivalent plastic strains in tension and compression, respectively. Since no damage is assumed in the current model, the equivalent plastic strains in tension and compression are replaced by the cracking strain ($\tilde{\varepsilon}_t^{ck}$) and the inelastic strain ($\tilde{\varepsilon}_c^{in}$), respectively. Micro-cracking and crushing of the concrete are represented by an increase in the values of the hardening variables. These variables control the evolution of the yield surface and degradation of elastic response.

6.3.1.4 Flow Rule

It was known that the shape of the yield surface at any given loading condition can be determined by the hardening rule. The connection between the yield surface and the stress-strain relationship is determined with a flow rule. The flow rule is defined as:

$$d\varepsilon^p = d\kappa \frac{dG}{d\sigma} \tag{6.8}$$

where $d\kappa \geq 0$ is a scalar hardening parameter which can vary throughout the straining process. The gradient of potential surface $\frac{dG}{d\sigma}$ defines the direction of plastic strain rate increment vector and the hardening parameter $d\kappa$ determines its length (Chen 1982).

6.3.2 Tension Stiffening Model

The post cracking behaviour of concrete in tension is based on the brittle fracture concept of Hillerborg et al. (1976). This fracture energy approach is represented by the area under the stress versus deformation softening curve for tension-softening behaviour. This model can be characterized as stress-strain softening model as proposed by Bažant and Oh (1983). This strain-softening model is used to represent the behaviour of plain concrete in tension.

Prakhya and Morley (1990) recommended that the softening branch of the complete stress-strain diagram of plain concrete in tension can be used with some modifications to reflect the tension-stiffening behaviour of a reinforced concrete member. Bischoff and Paixao (2004) and Sooriyaarachchi et al. (2007) proposed tension-stiffening models for GFRP reinforced concrete member to characterize this behaviour. Based on those models, a simplified bilinear tension stiffening model (Figure 6.9) as proposed by Cope et al. (1979) for steel reinforced concrete beams is used for the FRP reinforced concrete beams with some modifications.

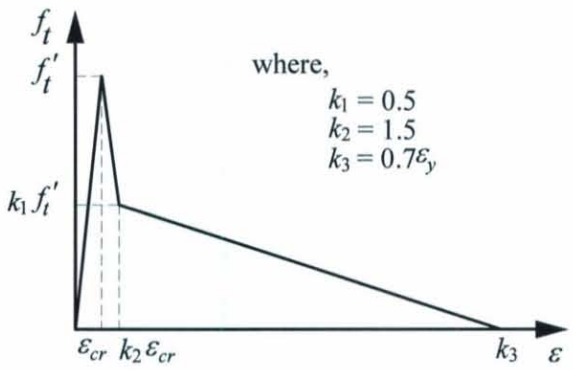

Figure 6.9: Tension stiffening model for steel reinforced members (Cope et al. 1979)

For FRP reinforced beams, k_2 is multiplied by the ratio of the elastic modulus of steel and FRP, E_s/E_f (Bischoff and Paixao 2004), which is approximately equal to 4.0 for GFRP bars. The value of k_3 can be taken as the ultimate strain of FRP bars, ε_u (Nour et al. 2007). Hence, the following tension stiffening model is recommended for Model-1 and is shown in Figure 6.10. The inside of this figure shows the comparison between the Bischoff and Paixao model and the proposed model.

$$f_t = \begin{cases} f_t' \dfrac{\varepsilon}{\varepsilon_{cr}} & \text{for } \varepsilon < \varepsilon_{cr} \\ \dfrac{f_t'}{10}\left(11 - \varepsilon/\varepsilon_{cr}\right) & \text{for } \varepsilon_{cr} < \varepsilon < \varepsilon_1 \\ \dfrac{f_t'}{2}\left(\dfrac{\varepsilon - \varepsilon_1}{\varepsilon_1 - \varepsilon_2} + 1\right) & \text{for } \varepsilon_1 < \varepsilon < \varepsilon_2 \end{cases} \tag{6.11}$$

where,

$\varepsilon_1 = 6\varepsilon_{cr}$

ε_2 = Ultimate strain of FRP bars, ε_u

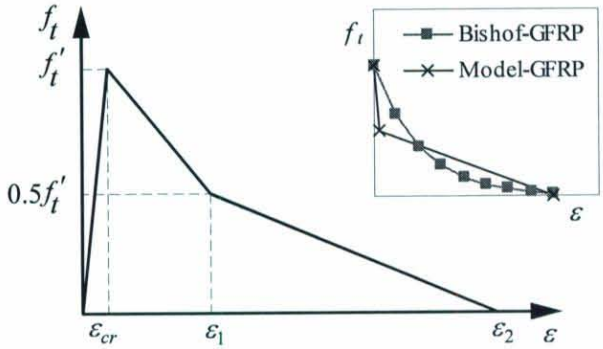

Figure 6.10: Tension stiffening model for FRP reinforced members (Model-1)

6.3.3 Hypoelastic Concrete Model (Model-2)

A hypoelastic concrete model is based on a uniaxial stress-strain relationship that is generalized to cover the biaxial and triaxial stress conditions (ADINA 2006). The basic features of this model are: a) a nonlinear stress-strain relation to allow for the weakening of the material under increasing compressive stresses, b) failure envelopes that define failure in tension and crushing in compression, c) a strategy to model the post-cracking and crushing behaviour of the material. A typical uniaxial stress-strain relationship is shown in Figure 6.11, where a nonlinear response is considered for both tension and compression. The compressive behaviour is defined using four parameters that are the maximum and ultimate uniaxial compressive stresses and the corresponding uniaxial strains. The ultimate uniaxial compressive stress, f_u, is taken as 0.85 f_c', and the ultimate uniaxial compressive strain, ε_u, is taken as 0.0035.

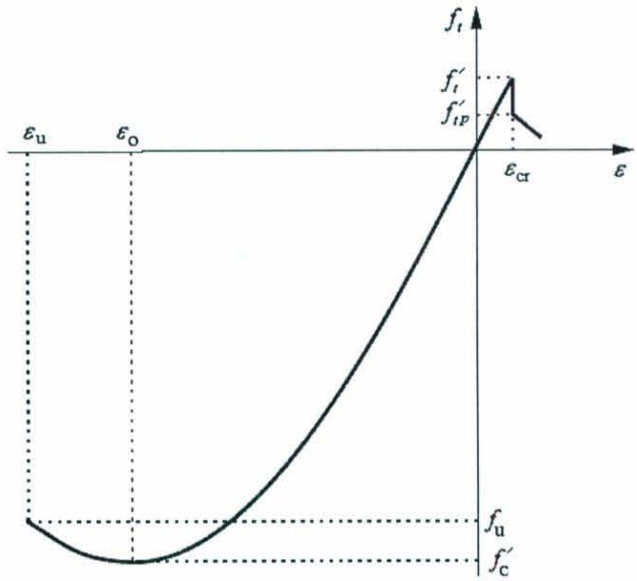

Figure 6.11: Uniaxial stress-strain relation for concrete used in Model-2

The post-cracking behaviour of concrete in tension is modelled using a bilinear model as shown in Figure 6.12. In this model, the ultimate strain (ε_u) at which the tensile stress will become zero is equal to $\xi\varepsilon_{cr}$, where ξ is a dimensionless coefficient given by the following equation:

$$\xi = \frac{2E_0 G_f}{f_t'^2 l} \tag{6.9}$$

where,

E_0 is the uniaxial initial tangent modulus,
f_t' is the uniaxial tensile strength,
G_f is fracture energy, and
l is the element length.

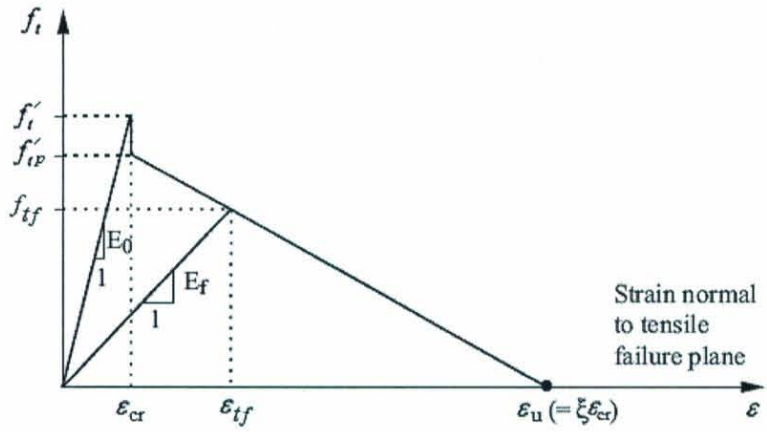

Figure 6.12: Post cracking model for concrete used in Model-2

The post cracking uniaxial cut-off tensile stress (f_{tp}') is assumed as 70% of the ultimate tensile strength (f_t') based on the recommendation of Kaklauskas and Ghaboussi (2001). The ultimate strain at which the concrete tensile stress becomes zero is determined

from Equation 6.9. Since the modulus of elasticity of GFRP is almost one-fourth of that of steel, the calculated value of ξ is multiplied by 4.0.

Tensile cracking and compression crushing conditions are identified using failure surfaces. The general multiaxial stress-strain relations are derived from the nonlinear uniaxial stress-strain relation shown in Figure 6.11. The biaxial concrete failure envelope is depicted in Figure 6.13. Failure envelopes are used to establish the uniaxial stress-strain law accounting for multiaxial stress conditions and to identify whether tensile or crushing failures of the concrete have occurred.

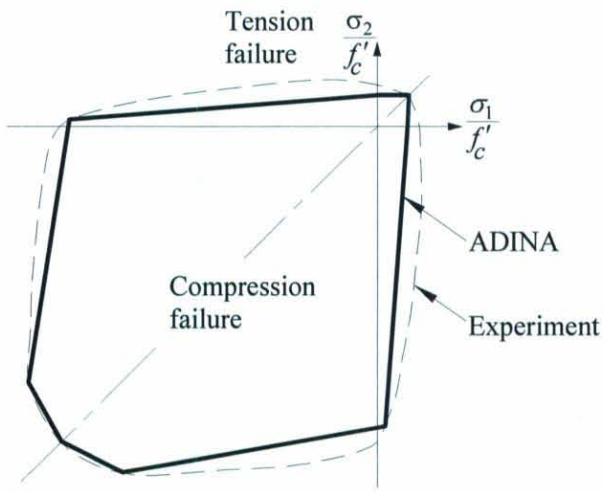

Figure 6.13: Biaxial failure envelope of concrete (ADINA 2006)

6.4 Modelling of the Reinforcement

Sand coated GFRP, CFRP bars, and steel reinforcements are used in this analysis. Steel reinforcement is used for control beams. This reinforcement is modelled as bilinear elastic-plastic materials, with the tangent modulus in the strain hardening regime taken to

be one-tenth of the elastic modulus. The FRP bars are modelled as linear elastic material until failure. The properties of the FRP bars are used as specified by the manufacturer and are given in Table 3.2. A full bond is assumed between the concrete and the reinforcement.

6.5 Implementation of Model-1

6.5.1 General

Model-1 (concrete damage plasticity model) is implemented in the general purpose finite element program ABAQUS (2007). ABAQUS has the capability of modeling reinforced concrete in a realistic way because it can simulate the user own elements and constitutive laws. Tension stiffening behaviour can be incorporated in ABAQUS. The proposed tension stiffening model (Section 6.3.2) was used. The analysis was carried out to simulate the experimental results conducted in the current investigation. The model was verified by comparing the experimental results with the predicted ones for different shear span-to-depth ratio, depth of beam, reinforcement ratio, and concrete strength.

6.5.2 Calibration of the Model

A simple model as shown in Figure 6.14 was generated to calibrate and verify the constitutive relationships. The model consisted of one solid element only with 50×50×50 mm dimensions. The tensile behaviour was the same as the tension stiffening model described in Section 6.3.2 with ultimate strain equal to 0.015. The compressive behaviour was given by Equation 6.1. The element was subjected to a uniaxial tensile and uniaxial

compressive stresses to verify the stress-strain relation for the concrete model. The responses obtained from ABAQUS are shown in Figure 6.15. The obtained stress-strain results were fairly the same as the input behaviour, which verify the applicability of the model.

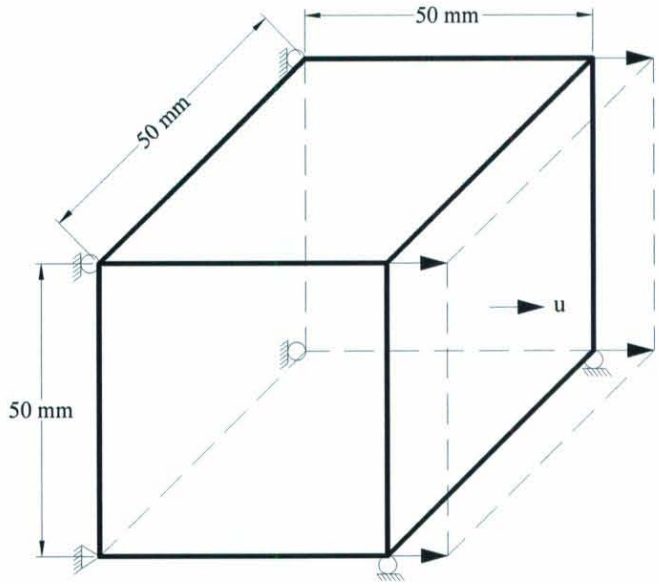

Figure 6.14: Calibration model

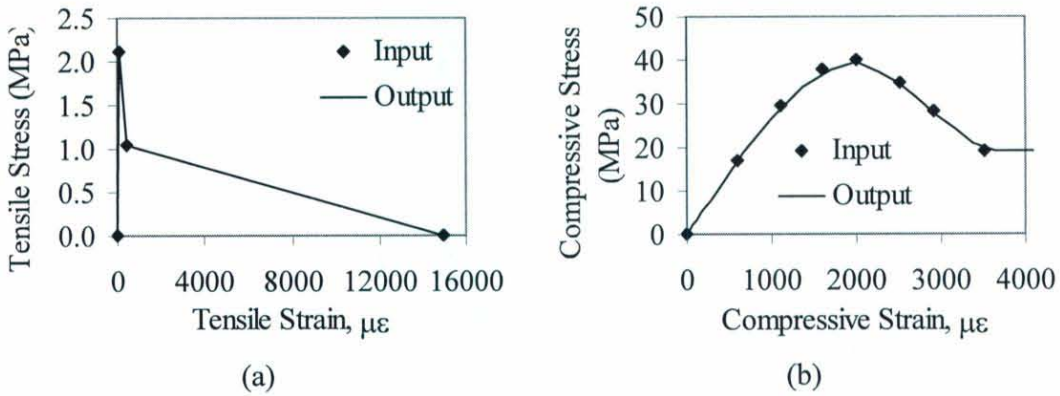

Figure 6.15: Verification model response from ABAQUS: (a) tension and (b) compression

6.5.3 Geometrical Modelling of the Beams

The analysis was performed on the simply supported beams with 4-point loading that were tested in this investigation. The geometry and material properties given in Chapter 3 were used in this analysis. Due to symmetry, half of the beam was modeled. The symmetrical boundary condition was applied at the center of the beam. A roller support condition was used at 220 mm from the end of the beam.

The beam was modelled using 8-node 3-D solid elements with reduced integration point for concrete and the reinforcement was modelled using 2-node 3-D truss elements embedded in the concrete. To avoid the shear locking effect, reduced integration point was used. Figure 6.16 shows a typical finite element mesh. Embedded formulation for reinforcement was used because it can model the rebars without interrupting the desired mesh size of concrete. This formulation also allowed the determination of the total internal resisting forces that were directly added to those of concrete (Nour et al. 2007). The displacement-controlled loading was applied in the analysis. A Poisson's ratio equal to 0.2 (Chen 1982) was used in the analysis of the beams.

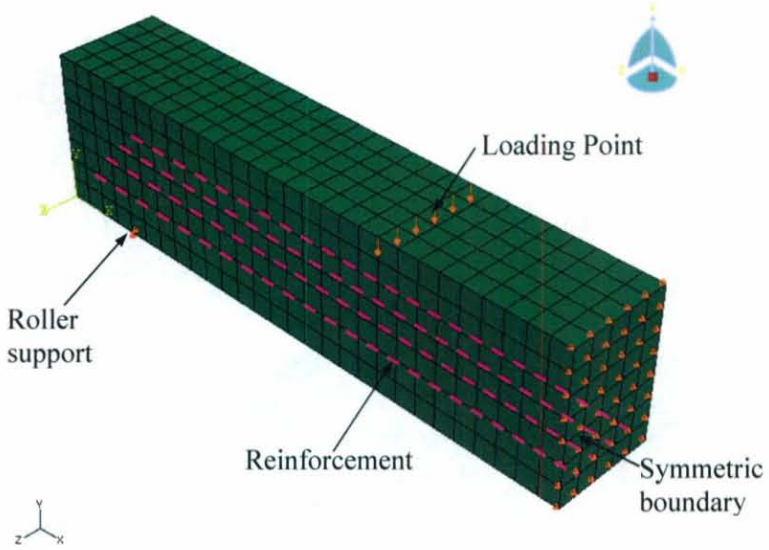

Figure 6.16: Finite element model

6.5.4 Results and Discussion

6.5.4.1 Effect of Element Size

The sensitivity of the element size was examined using the results of beam G-2.5. According to Bažant and Oh (1983), element size should be greater than three times the maximum aggregate size. The maximum aggregate size in this investigation was 20 mm and the element sizes were chosen as 50×50×50 mm, 70×83×70 mm, and 100×125×87 mm. The generated mesh for these three element sizes were termed as fine, medium, and coarse mesh, respectively. The load-displacement behaviour and stress distribution for these element sizes are shown in Figures 6.17 and 6.18, respectively. The results showed some differences in the load-deflection behaviour between the coarse mesh and the other two meshes. The results using the medium mesh were slightly better than the fine mesh in terms of load-deflection behaviour. However, the fine mesh gave better results in terms of

the stress distribution. To keep the element size around three times of the maximum aggregate size and for better representation of the stress contour, fine mesh with 50 mm cubic element was used in the analysis. In addition, due to the hourglassing effect in reduced integration element, a reasonably fine mesh should be used to obtain better results.

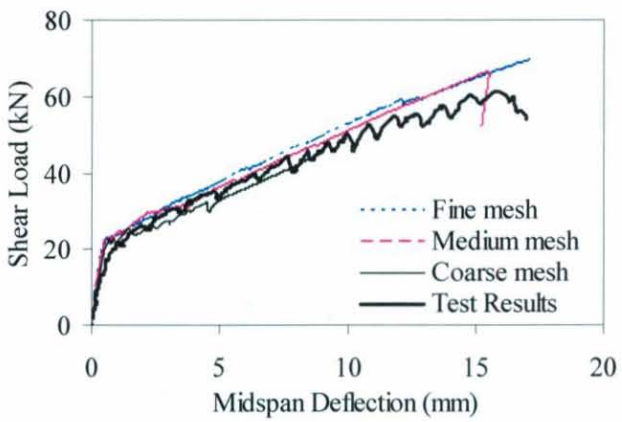

Figure 6.17: Load-deflection behaviour for the different mesh sizes

6.5.4.2 Effect of Dilation Angle

Dilation angle (ψ) is the ratio of volume change to shear strain. In Drucker-Prager formulation, the value of the dilation angle is to be determined for an element under biaxial compression with high confining pressure. The value of the dilation angle used in the current investigation was 30°. To check the suitability of this value, the effect of the dilation angle was examined for a beam with 50×50×50 mm element size. Three values of dilation angle were checked, namely; 20, 30 and 40 degrees. The results are presented in Figure 6.19. The differences in the load-deflection responses for the three dilation angles

were rather small, where the variation in the peak load is less than 10%. Hence, a dilation angle of 30 degrees was used in the analysis.

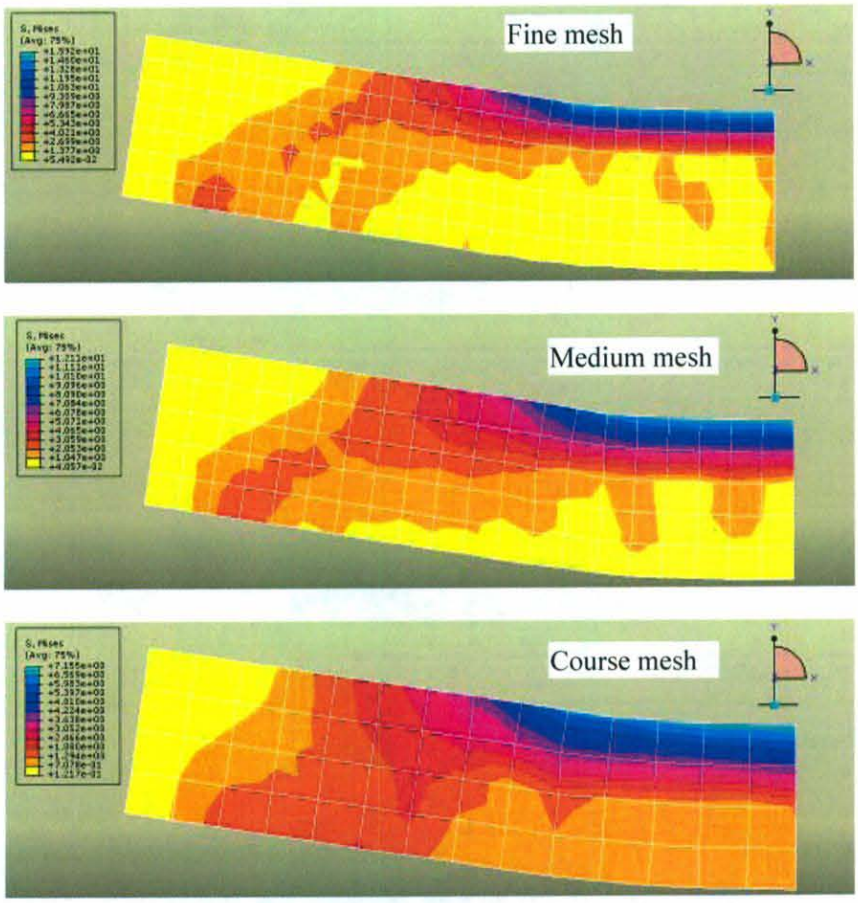

Figure 6.18: Stress contour for different meshes with different sizes

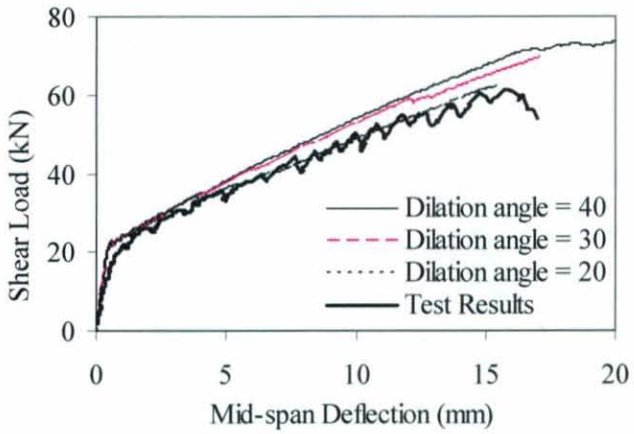

Figure 6.19: Effect of dilation angle used in the concrete damage plasticity model

6.5.4.3 Behaviour of the Beams

One of the steel reinforced beams (beam S-2.5) was modelled using Model-1 to predict the behaviour and to compare it to the behaviour of FRP reinforced beams. The reinforcement ratio of this beam was 0.90%, which was only 18% of the balanced reinforcement ratio. Although the failure load and deflection are underestimated slightly by the FE model, the overall load-deflection behaviour is quite reasonable (Figure 6.20).

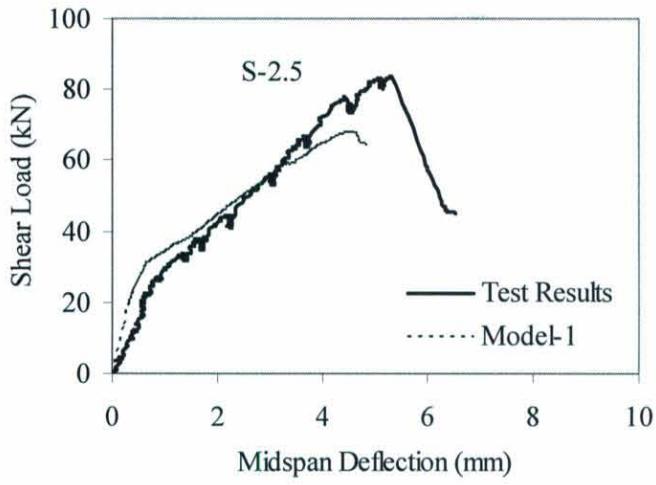

Figure 6.20: Comparison of load-deflection behaviour between test results and Model-1 for beam S-2.5

For the FRP reinforced beams, the comparison between the load-deflection behaviour obtained from Model-1 together with the experimental results are presented for different groups of beams. Figure 6.21 shows the predicted and experimental load-deflection behaviour of GFRP and CFRP reinforced beams for different shear span-to-depth ratio. For all of the beams, the predicted results using Model-1 followed the same characteristics as the load-deflection behaviour of the test results; however, the behaviour differed at the ultimate load level for few beams. The Model-1 predicted results gave a good estimation of both failure load and deflection for GFRP reinforced beams. On the other hand, for beams C-1.5 and C-2.5, Model-1 overestimated the load and deflection. Two possible reasons were considered for these differences. First, the axial stiffness of the CFRP reinforcement was 1.5 times the axial stiffness of the GFRP reinforcement. Second, the tension stiffening model used for both GFRP and CFRP reinforced beams was the same.

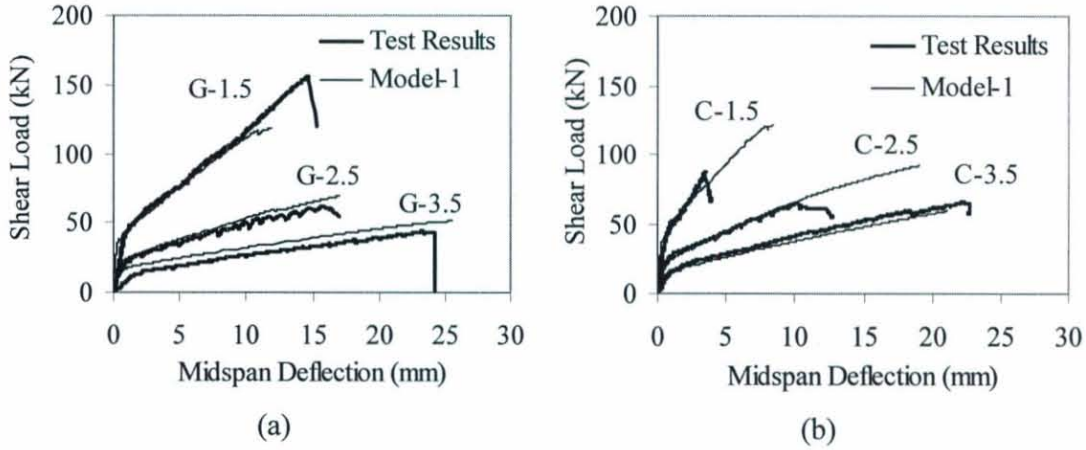

Figure 6.21: Comparison between the load-deflection behaviour and the prediction of Model-1 for different *a/d* ratio; (a) GFRP, (b) CFRP beams

The comparison between the crack patterns and principal stresses of some GFRP reinforced beams with different a/d ratios are shown in Figure 6.22. The stresses shown in the figure are the maximum and the minimum principal stress, their locations and directions. It was observed that the maximum stress direction was oriented perpendicularly to the crack directions. At midspan, the maximum stress direction was parallel to the axis of the beams representing the vertical crack propagations. In the shear span zone, the stress direction at the bottom of the beams was parallel to the axis of the beams, which represented the vertical flexural cracks development as in the case of experimental observations. Away from the bottom of the beams, due to the presence of shear stress, the maximum principal stress direction rotated and aligned perpendicularly to the direction of the inclined cracks. The minimum principal stress direction was oriented parallel to the crack direction. A fair match was observed for these beams between the experimental crack patterns and the Model-1 stress directions.

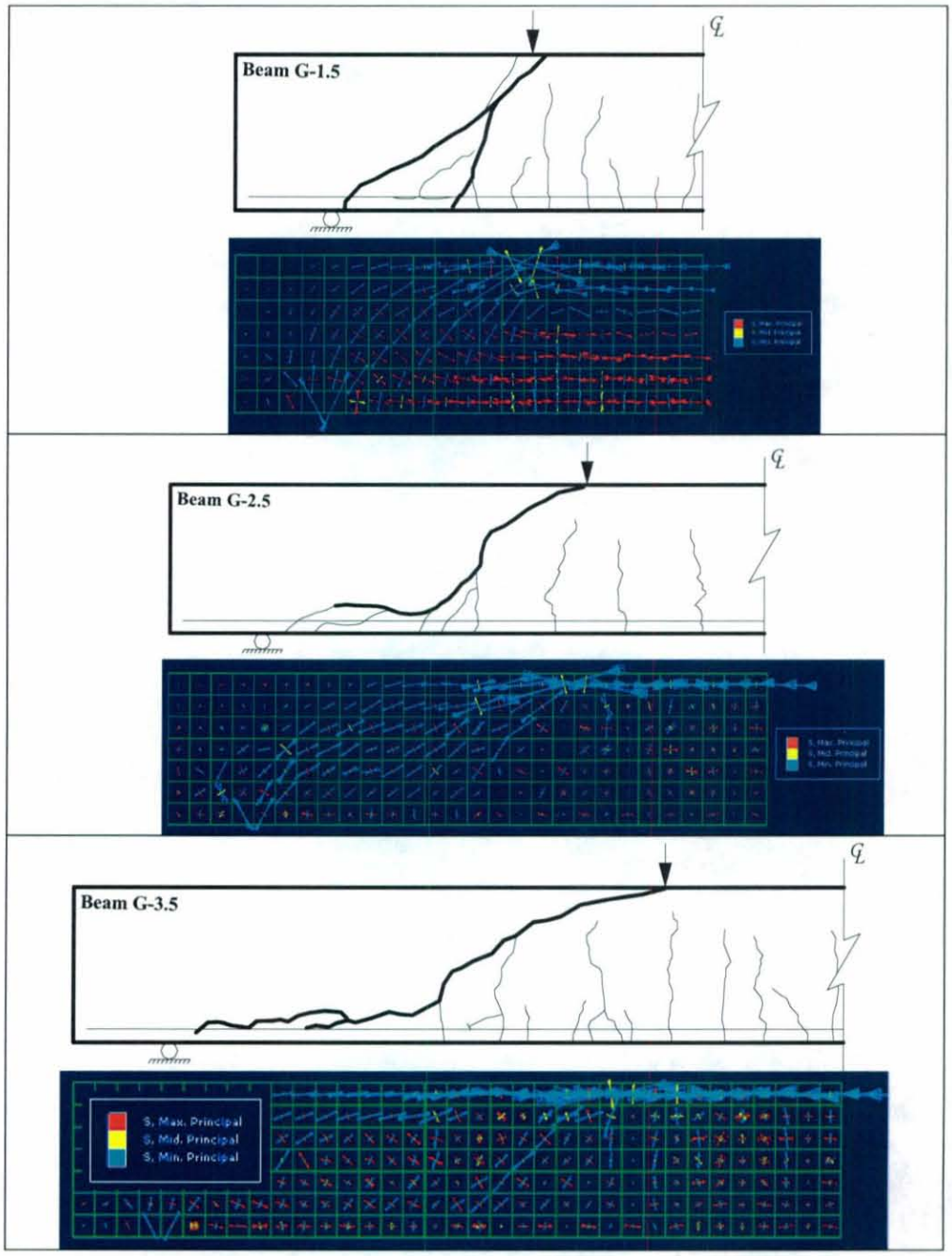

Figure 6.22: Comparison of crack patterns and stress tensor obtained from Model-1 for GFRP reinforced concrete beams

The load-deflection behaviour for different depths of GFRP and CFRP reinforced concrete beams are shown in Figure 6.23. The ultimate deflections obtained from Model-1 for all of the beams were close to the experimental ones. However, the failure load differed slightly for beam G-800. The predicted stiffness of the beam was lower after cracking, which resulted in greater deflection than the test results for the same load level. The experimental versus Model-1 predicted failure loads for this beam were 129.5 kN and 112.8 kN, respectively. That is, Model-1 underestimated the failure load by approximately 13%. For all other beams, Model-1 overestimated the failure loads by approximately 12%.

Model-1 overestimated all the failure loads for CFRP reinforced concrete beams with different depths. For beams C-2.5 and C-650, both loads and deflections were overestimated by approximately 40 and 80%, respectively. These are considerably higher than the corresponding GFRP reinforced beams. This can be attributed to the higher axial stiffness of the CFRP reinforcement compared to the GFRP reinforcement. Again, the same tension stiffening models was used for both the GFRP and CFRP reinforcement.

Figure 6.24 shows the load-deflection behaviour for different reinforcement ratios of GFRP reinforced concrete beams with heights equal to 350 and 500 mm. For both beam heights, the predicted results of Model-1 underestimated the failure load and deflection for beams with reinforcement ratios of less than the balanced reinforcement ratio (Beams G-0.5-350 and G-0.5-500). The failure load and deflection were overestimated for beams with reinforcement ratio greater than the balanced reinforcement ratio (Beams G-2.5-350 and G-2.5-500). However, for beams with reinforcement ratio approximately equal to the balanced reinforcement ratio, Model-1 gave good estimation of the failure load and

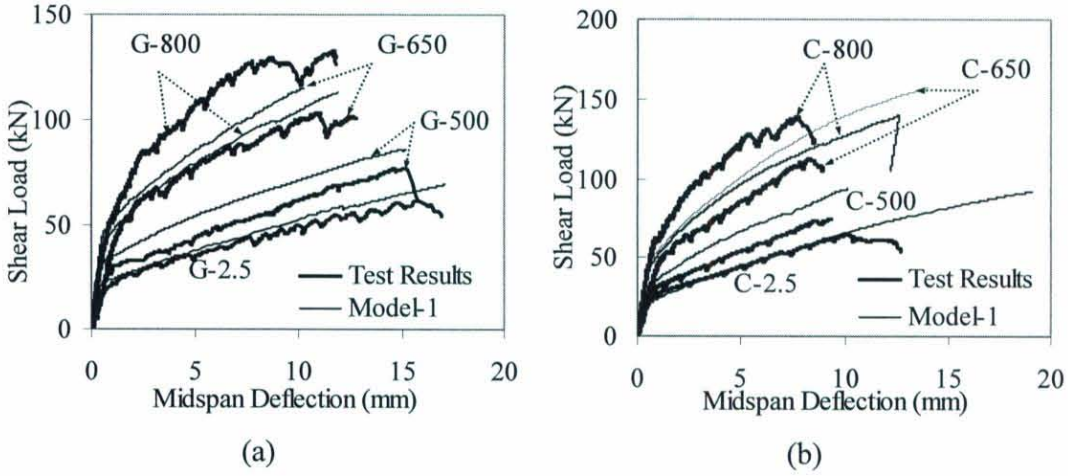

Figure 6.23: Comparison between the load-deflection behaviour and the prediction of Model-1 for different depths; (a) GFRP, (b) CFRP beams

deflection (Beams G-2.5 and G-500). This could be due to the approximation in the tension-stiffening model that depends on the type of reinforcement. It was observed in the uniaxial tension specimens that the tension-stiffening effect in the low reinforced members is greater than that in the highly reinforced members (Sooriyaarachchi et al. 2005).

Figure 6.25 shows the load-deflection behaviour of GFRP reinforced normal (NSC) and high strength concrete (HSC) beams. The predicted result using Model-1 underestimated the failure load and deflection slightly for high strength concrete beams. This could be attributed to the use of the same tension-stiffening model for both normal and high strength concrete beams. According to Sooriyaarachchi et al. (2005), high strength concrete has higher tension-stiffening than that of normal strength concrete. Therefore, minor changes in the tension stiffening values could further improve the results.

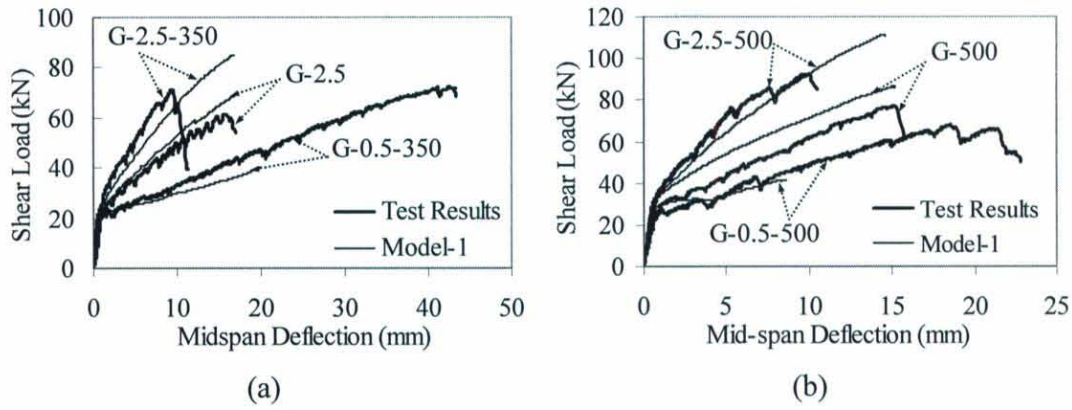

Figure 6.24: Comparison between the load-deflection behaviour and the prediction of Model-1 for different reinforcement ratios; (a) 350 mm, (b) 500 mm thick beams

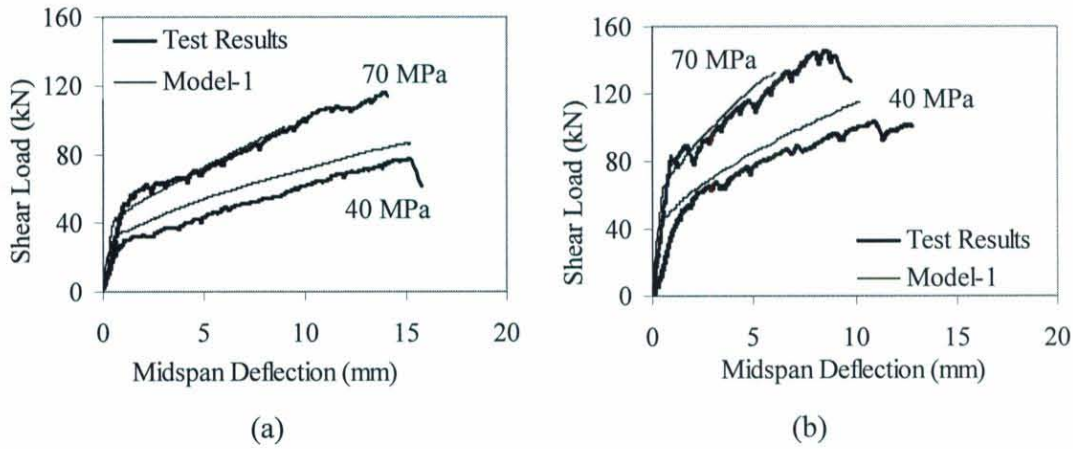

Figure 6.25: Comparison between the load-deflection behaviour and the prediction of Model-1 for different concrete strengths; (a) 500 mm, (b) 650 mm thick beams

6.5.4.4 Effect of Tension Stiffening

According to Maekawa et al. (2003), for beams without web reinforcement, there exists both a reinforced concrete (RC) and a plain concrete (PC) zones as shown in Figure 6.26. The RC zone extends to a depth, h_{rc}, which depends on the reinforcement ratio and

the bar diameter. The remaining portion of the beam depth is the PC zone. The tensile stress in the RC zone is transferred to the cracked concrete through bond effect, while the tensile stress in the PC zone is transferred only through the bridging action at the crack surface. Thus, the elements in the PC zone exhibit a tension-softening behaviour with a discrete localization, while the elements in RC zone exhibit a tension-stiffening behaviour with distributed fractures. Therefore, the overall behaviour should be expressed by a mixed discrete-smeared fracture varying from place to place over the whole domain (Maekawa et al. 2003). This zoning concept is also applied to the shear stress transfer along the propagating cracks. Use of this technique could further improve the results. However, there are some drawbacks of this approach. These are: 1) the transition between the RC and the PC zone is abrupt and sudden. The effect of reinforcement is neglected beyond the RC zone. However, the crack in the PC zone is usually the continuation of the crack in the RC zone. Thus, the crack width in the PC zone is governed by the crack width in the RC zone, which depends on the reinforcement types and arrangements; 2) the elements in the PC zone may contain at most a single crack due to strong localization, while the elements in the RC zone have smeared cracking. This will result in discontinuity in the elements behaviour adjacent to the interface between the RC and PC zones. It was observed in Chapter 4 that, for most of the beams, the cracks in the RC zone extended to the PC zone; 3) due to continuation of the cracks from the RC to the PC zone, there is a possibility that the concrete in between cracks in the PC zone may contribute in resisting tensile stress; 4) according to Mörsch (1909), shear stress varies uniformly from reinforcement level to the neutral axis; and 5) in this approach, the elements in each beam should be divided for the RC and PC zones, according to the depth and the reinforcement arrangements of the beam.

Therefore, use of a single post-cracking behaviour of reinforced concrete will maintain the continuity in the elements and simplify the work. This approximation has been utilized in the current investigation. This could lead to some of the deviations in the predicted results for different depth of the beams. However, the use of a single post-cracking behaviour could be considered as an easier and simpler approximation that yields reasonable results within a practical range.

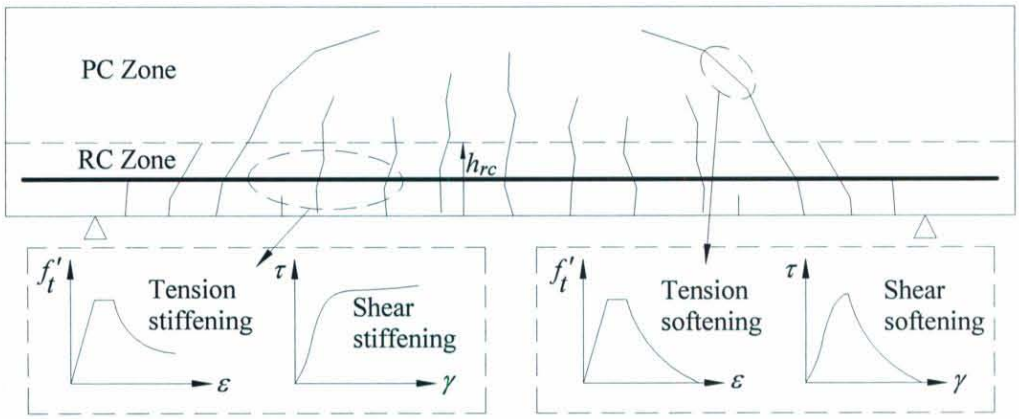

Figure 6.26: Location and behaviour of RC and PC zones (Maekawa et al. 2003)

To investigate the effect of tension stiffening and to examine whether a better prediction could be achieved in predicting the load-deflection behaviour of these beams, a parametric study was carried out using different tension stiffening values for different depths of beams. In this case, the strain, at which the concrete tensile stress will become zero, varied from 60 to 110 % of the ultimate tensile strain of FRP bars (ε_u). Figure 6.27 shows some of the results of this modelling. It can be noticed that a better agreement between the experimental and the predicted results was achieved for beams of G-650, C-2.5, C-500, and C-650. Therefore, it can be concluded that the proposed tension stiffening

idealization can be used, with a minor modification, to simulate the behaviour of shear critical FRP reinforced concrete beams. Overall, the predicted results using Model-1 are in reasonable agreement with the test results.

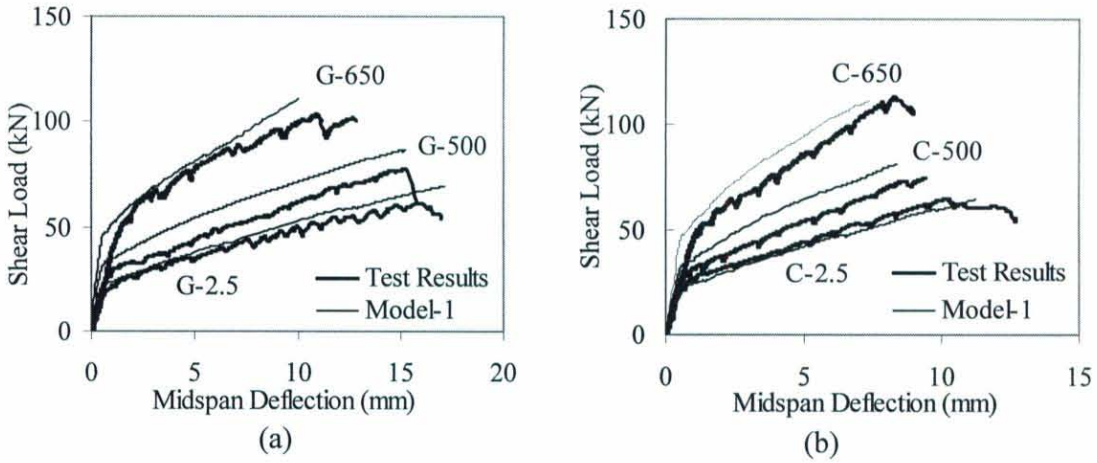

Figure 6.27: Comparison between the load-deflection behaviour and the prediction of Model-1 using different tension stiffening values; (a) GFRP and (b) CFRP reinforced beams

6.6 Implementation of Model-2

6.6.1 General

Model-2 is implemented in the general purpose finite element program ADINA (2006). Only GFRP reinforced beams were analyzed by this model. In order to achieve the convergence, automatic time stepping (ATS) with energy convergence tolerance (ETOL) equal to 0.001 and line search convergence tolerance (STOL) equal to 0.5 were used in the analysis. The remaining parameters were used as default.

6.6.2 Calibration of the Model

The same model as shown in Figure 6.14 was calibrated and verified in ADINA. For G_f = 110 N/m, the corresponding value of ξ is equal to 29. The model responses are shown in Figure 6.28. A small discrepancy was observed in the ultimate tensile strain at which the tensile stress is zero. According to the input, the ultimate value of the tensile strain should be 29 times the cracking strain. The model predicted value was 21 times the cracking strain. This might be due to the discontinuous modelling of the post cracking tensile behaviour of concrete. On the other hand, exactly the same behaviour was obtained when linear descending behaviour was used (Figure 6.29). It appears that the value of ξ should vary according to the modelling of post-cracking behaviour.

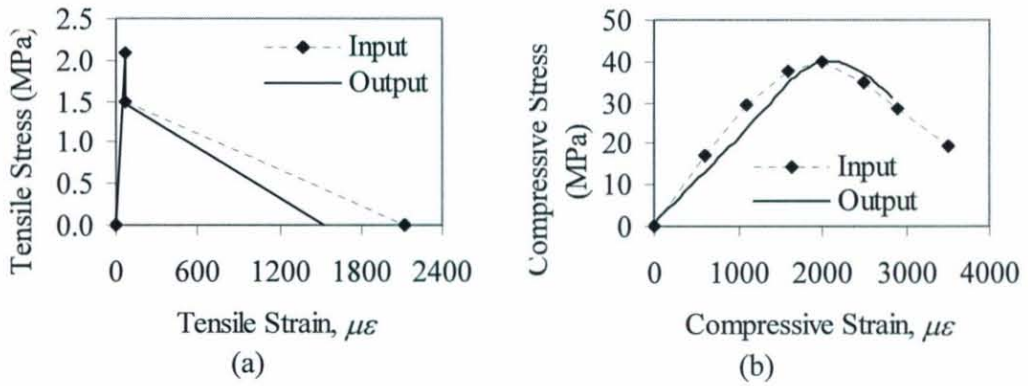

Figure 6.28: Calibration of the concrete model response from ADINA: (a) discontinuous tension behaviour and (b) compression

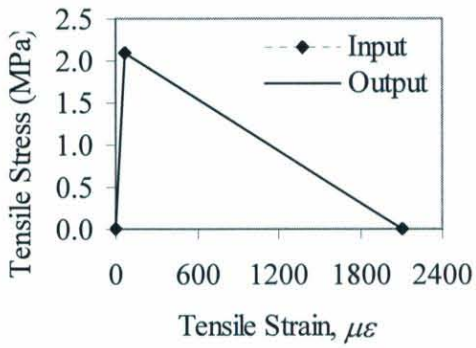

Figure 6.29: Calibration of the concrete model response from ADINA for bilinear tension model

6.6.3 Geometrical Modelling of the Beams

The geometry and material properties of the beams analyzed using this model are described in Chapter 3. In this analysis one quarter of the beam was modelled using 3-D solid element with 2×2 integration points. Since the ultimate strain, at which the concrete tensile stress will become zero, depends on the element size, 100×125×116 mm element was chosen for this analysis. Based on this element size and assuming a value of the fracture energy of 110 N/m for all of the beams, the corresponding value of ξ would be 14.5. Assuming that this value of ξ was valid for a bilinear tension stiffening model as discussed in Section 6.6.2, the value of ξ for a discontinuous tension stiffening model was determined according to Massicotte et al. (1990), keeping the same strain energy density between the bilinear and discontinuous tension stiffening models.

6.6.4 Results and Discussion

The same beam used in Model-1 (beam S-2.5) was modelled using Model-2 to examine the predicted behaviour and to compare it with the behaviour of GFRP reinforced beam. A good agreement was observed in the load-deflection behaviour between the test result and the Model-2 result (Figure 6.30). The estimated values of failure load and deflection were close to the test results, which suggest that the model worked well for steel reinforced beams.

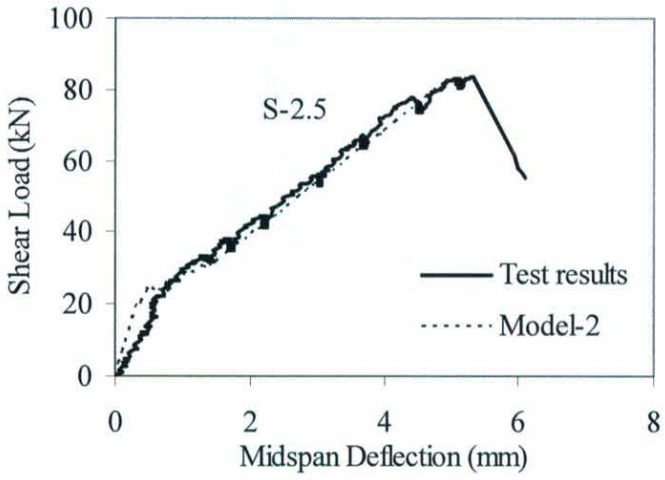

Figure 6.30: Comparison between the load-deflection behaviour and the prediction of Model-2 for beam S-2.5

The load-deflection behaviour of GFRP reinforced concrete beams obtained from Model-2 for different shear span-to-depth ratios is shown in Figure 6.31. The Model-2 results followed the same trend as the test results at the beginning of the loading. However, it predicted failure loads and deflections were considerably lower than the test results. All of the beams suffered convergence problems after cracking. This might be due to the lack

of proper modelling of concrete and tension-stiffening behaviour that could be used for FRP reinforced beams. Convergence tolerance and loading rate might also cause these discrepancies in the results. On the other hand, although the reinforcement ratios of these beams were equal to those of the steel reinforced beams, the axial stiffness of the GFRP bars is almost one-fifth of that of steel bars. This is another possible reason for poor behaviour of these beams.

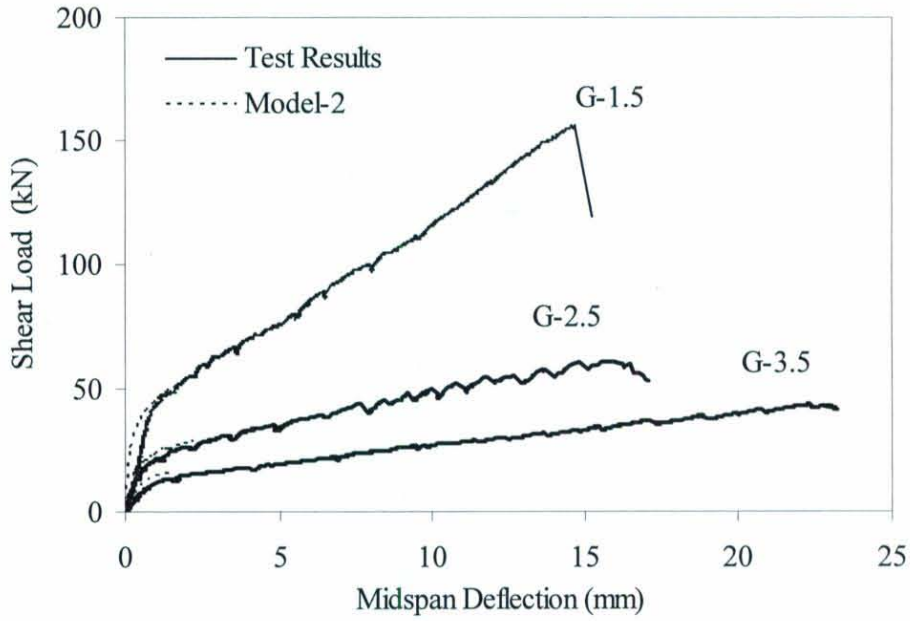

Figure 6.31: Comparison between the load-deflection behaviour and the prediction of Model-2 for different *a/d* ratio

The predicted load-deflection response together with the test results for beams with different depths are shown in Figure 6.32. It was observed that the predicted results improved slightly with an increase in the depth of the beam, however, most of them underestimated the failure load and deflection. Beam G-650 with effective depth 584 mm

shows better agreement with the measured failure load and deflection. The increase in stiffness of the beam with an increase in the depth could contribute to better performance of the model. The same reasoning as mentioned for Model-1 could be used to explain the performance of this model.

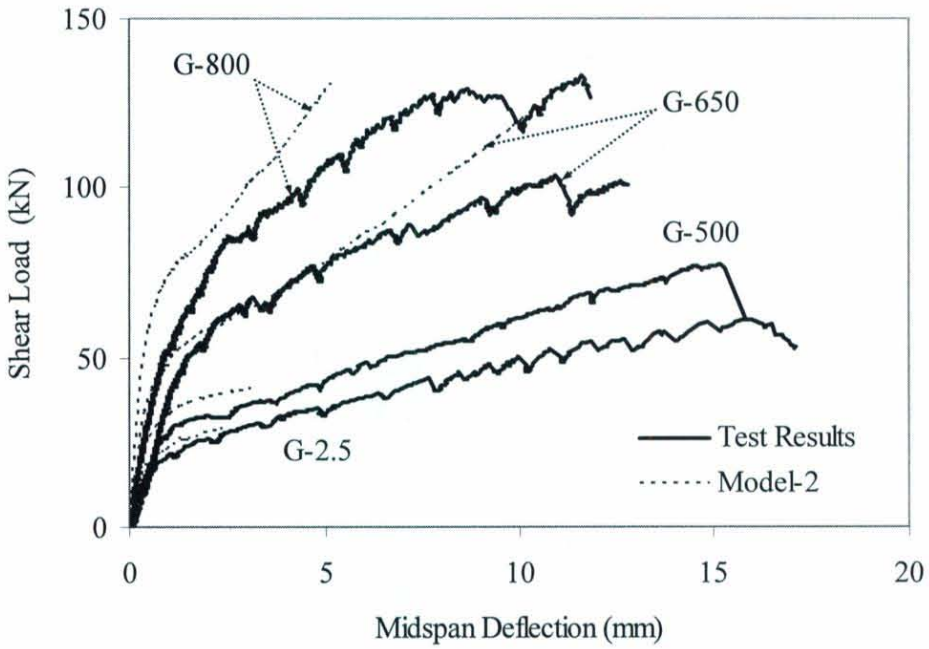

Figure 6.32: Comparison between the load-deflection behaviour and the prediction of Model-2 for different heights of beams

Similar to the results of Model-1, Model-2 results showed better agreement with the test results for beams with higher reinforcement ratios. Figure 6.33 shows these results for different reinforcement ratios for beams with height equal to 350 and 500 mm. Both beams G-2.5-350 and G-2.5-500, with reinforcement ratio equal to twice the balanced reinforcement ratio showed relatively good correlation with the test results. For low reinforced beams, the predicted behaviour was poor.

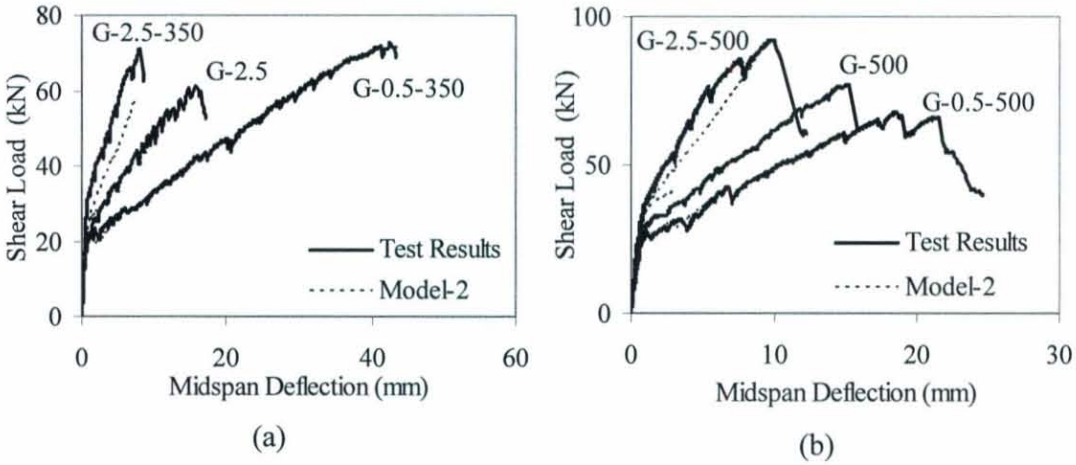

Figure 6.33: Comparison between the load-deflection behaviour and the prediction of Model-2 for different reinforcement ratios; (a) 350 mm, (b) 500 mm thick beams

For further verification, the crack patterns and stress contours predicted from Model-2 for beams G-2.5-350 and G-2.5-500 were compared with the experimental crack patterns. A good agreement in both crack patterns and stress contours were observed between the Model-2 and the test results (Figure 6.34).

The FEA predicted results for beams with different shear span-to-depth ratios, depth of beams, reinforcement ratios, and concrete compressive strengths are discussed. It was noticed that the consistency of the predicted results varied depending on the parameters used in the model. This could be attributed mainly to the approximation in the tension-stiffening idealization. It was observed that a better prediction can be achieved using the proposed tension-stiffening idealization with a minor change in the strain at which the concrete tensile stress will become zero.

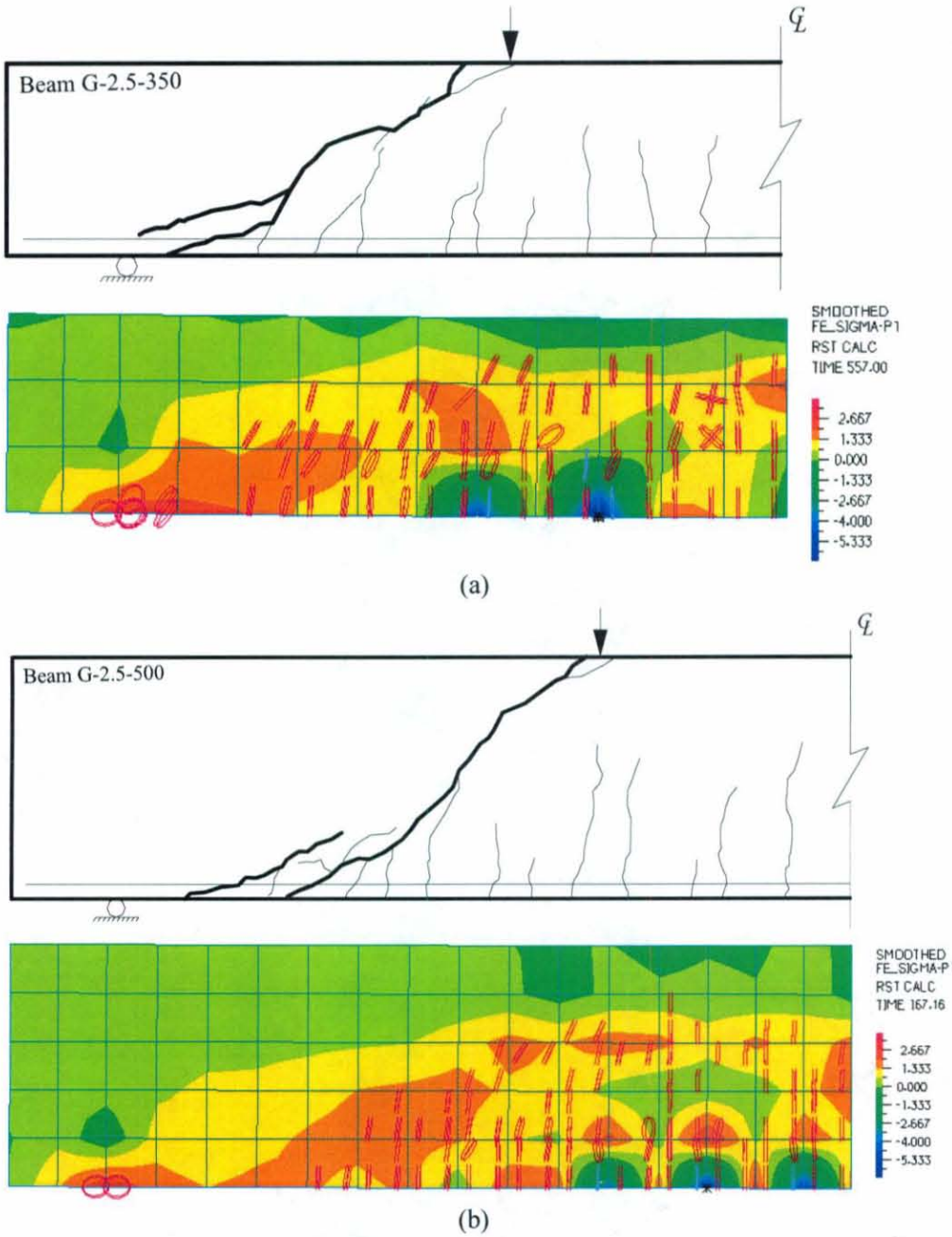

Figure 6.34: Comparison between the crack patters of the test results and Model-2 stress contours; (a) beam G-2.5-350, and (b) beam G-2.5-500

Chapter 7 Summary and Conclusions

7.1 Introduction

In this thesis, the shear behaviour of FRP reinforced concrete beams without transverse reinforcement was investigated. A new test set-up was designed and constructed for testing the beams of the current investigation. Based on the experimental investigation, a simple, yet robust shear design method was proposed to calculate the concrete contribution to the shear strength of FRP reinforced members. Finally, finite element modelling of shear critical FRP reinforced concrete beams was carried out to predict the experimental results of some of the beams tested in this investigation.

7.2 Experimental Investigation

A systematic experimental investigation was carried out to investigate the shear strength of FRP reinforced concrete beams without transverse reinforcement. Glass, carbon FRP bars as well as conventional steel bars were used as longitudinal reinforcement. The steel reinforced beams were used as control beams. A total of thirty-six beams were tested in the investigation. Out of thirty-six beams, fifteen of them were GFRP reinforced, fourteen were CFRP reinforced, and seven were steel reinforced beams. The test variables were the shear span-to-depth ratio (a/d), the depth of the beam (d), the longitudinal reinforcement ratio (ρ_f), concrete compressive strength (f_c'), and reinforcement type. The beams were divided into four groups according to the four parameters investigated.

In the first group, the effect of the shear span-to-depth ratio was investigated. A total of eight beams, three beams for each of GFRP and CFRP bars, with a/d equal to 1.5, 2.5, and 3.5, and two for steel reinforced beams with a/d equal to 2.5 and 3.5, were tested. The reinforcement ratio for GFRP, CFRP, and steel reinforced beams were 0.86, 0.42, and 0.90%, respectively.

The effect of depth or size effect was investigated for both normal and high strength concrete beams in Group 2. For NSC, four beams for each type of reinforcement were investigated. The effective depths of the beams were approximately 300, 450, 600, and 750 mm. The reinforcement ratios for GFRP, CFRP, and steel beams were approximately 0.86, 0.45, and 0.90%, respectively. For HSC, three beams for each of the GFRP and CFRP reinforcement, with effective depths approximately equal to 300, 450, and 600 mm, were tested.

The effect of the reinforcement ratio was investigated for two sets of beams with effective depths approximately equal to 300 and 450 mm, respectively. For each set of beams, three beams for each of GFRP and CFRP reinforcement, and two beams with steel reinforcement were tested. The reinforcement ratios were approximately 0.33, 0.84, and 1.41% for GFRP; 0.20, 0.42, and 0.65% for CFRP; and 0.90 and 1.43% for steel reinforced beams for both sets of beams.

The effect of concrete compressive strength was investigated for GFRP and CFRP reinforced beams in Group 4. The concrete strengths were approximately 40, 65, and 88 MPa for both reinforcement types. The reinforcement ratios were 0.86 and 0.42% for GFRP and CFRP reinforced beams, respectively.

The following conclusions can be drawn from the experimental investigation:

1. The influences of different parameters that affect the shear strength were investigated systematically for FRP reinforced concrete beams.
2. An inclined crack was formed for almost all of the beams before failure. The angle of the inclined crack, at failure, decreased with an increase in the shear span-to-depth ratio. For beams with the same shear span-to-depth ratio, the angle of inclined cracks at failure was almost the same for different reinforcement types and concrete strengths.
3. For beams with low axial stiffness of the bars, the number of flexural cracks which penetrated deeper into the beam was less, and several cracks were developed at the level of reinforcement due to the relatively higher strain in the bars.
4. For almost all beams, the inclined failure cracks intersected the reinforcement level at the middle of the shear span. The distance of this location from the loading point is greater than the effective depth, d, for beams with a/d greater than 2.5. Therefore, use of d as a critical shear distance from the loading point or the face of the support for beams with a/d greater than 2.5 is a conservative measure.
5. The depth of the compression zone, before failure, increased with an increase in the axial stiffness of the reinforcing bars for both NSC and HSC beams, and decreased with an increase in the compressive strength.
6. The load-deflection behaviour of the beams before cracking was governed by the gross section properties of the beams, and the behaviour after cracking was approximately directly proportional with the axial stiffness of the reinforcing bars. For beams with higher depth, the behaviour after cracking became progressively nonlinear as the constant moment zone of the beam decreased.

7. The strain in the reinforcement at middle of the shear span increased suddenly at a load level that was approximately twice the first cracking load and the beams failed shortly after the formation of crack near the middle of the shear span.
8. Most of the beams in this investigation failed in shear. The observed failure modes were shear-tension, shear-compression, or diagonal-tension. For few beams, a secondary bond/anchorage failure was observed.
9. The failure of GFRP and CFRP reinforced beams with a/d equal to 1.5 was different from each other. The GFRP reinforced beam failed by arch action and the CFRP reinforced beam would fail due to the loss of bond between the bar and the sand coating. Further investigation is needed to understand the behaviour of these beams.
10. The shear strength of the beams decreased with an increase in the shear span to depth ratio. The normalized shear strength ($V_{exp}/\sqrt{f'_c}b_w d$) increased almost linearly with the square of the cubic root of the depth to shear span ratio $(d/a)^{2/3}$ and inversely with the cubic root of the depths ($1/d^{1/3}$) of the beam.
11. Similar to the steel reinforced beams, size effect was observed was observed in FRP reinforced beams for both normal and high strength concrete beams.
12. The shear strength of the beams, for both 300 and 450 mm effective depths, increased with an increase in the axial stiffness of the reinforcing bars. The normalized shear strengths increased linearly with approximately the cubic root of the axial stiffness of the reinforcing bars. Therefore, it is expected that the use of axial stiffness in CSA S806-02 shear design method for beams with effective depth greater than 300 mm will further improve the prediction.

13. The increase in shear strength was observed for an increase in the concrete compressive strength for all beam thicknesses. This increase was more pronounced in the HSC beams that had a higher axial stiffness of the reinforcing bars than the NSC beams.
14. The shear strength of a beam is related to the shear load at first flexural cracking.

7.3 Proposed Shear Design Method

The comparison between the test results and the predicted results using different design methods revealed that the results varied widely. The methods are not robust for predicting consistent results in terms of the mean, standard deviation, and percent of unconservative results. This was attributed to the fact that some of the methods did not account for the various shear strength parameters in a realistic way.

The experimental investigation revealed that the shear strength of a concrete beam is approximately equal to the shear load that causes a beam to crack at middle of the shear span. This relationship was confirmed using test results of 137 beams that were gathered from the literature, including the test results in this investigation. The test results consisted of 81 GFRP, 47 CFRP, 2 AFRP, and 7 steel reinforced beams. The concrete strength, reinforcement ratio, shear span-to-depth ratio, and depth of beams were in the range of 24.1 to 88.3 MPa, 0.18 to 2.63%, 1.1 to 6.45, and 104 to 889 mm, respectively. The average of the ratios of the experimental shear strengths to the predicted shear loads that cause a beam to crack at middle of the shear span was 1.67, with a coefficient of variation of 33%, and a standard deviation of 55 %.

Based on this relationship, a simple, yet robust shear design method was proposed, using the test results of current investigation and the data collected from the literature, to determine the concrete contribution to the shear strength of FRP reinforced rectangular concrete beams, without transverse reinforcement. The proposed shear design method was verified by comparing the predicted results using the proposed equation with the experimental results of the database. The predicted results were also compared with the results obtained using the shear design provisions of ACI 440.1R-06, CSA S806-02, JSCE (1997), ISIS-M03-07, CHBDC (CSA S6-06) method, and the methods proposed by El-Sayed et al. (2005), Razaqpur and Isgor (2006), and Sherwood et al. (2008). Only the FRP reinforced specimens were considered. Based on the comparison, following conclusions can be drawn:

1. The proposed method considers almost all of the shear strength parameters in a realistic way, which corresponds well with the experimental results. The calculation by this method is straight forward, does not require any constant, no limitations for a/d and depth of beams. It does not give zero shear strength for plain concrete. The method is not a modification of any other methods and is based on theoretical foundation.
2. The proposed method predicts the shear strength with approximately the same level of accuracy over the entire range of the parameters included in the database.
3. The comparison with the other methods indicates that the proposed method is more consistent in predicting the shear strength of FRP reinforced concrete members without transverse reinforcement.

7.4 Finite Element Analysis (FEA)

A finite element analysis was carried out to simulate the behaviour of shear critical FRP reinforced concrete beams with a wide range of design parameters such as shear span-to-depth ratio, depth of beams, reinforcement ratio, concrete strength, and reinforcement type. For this purpose, two concrete material models were used. The models were a concrete damage plasticity model (Model-1) and a hypoelastic concrete model (Model-2). The interaction between the concrete and FRP bar was modelled with different tension-stiffening models. A tension-stiffening model was proposed based on the reinforcement type and varies as a function of the member strain. The models were implemented in the general purpose finite element programs ABAQUS and ADINA, respectively. The models were used to simulate the experimental results of some of the beams tested in this investigation and to examine how well these models could predict the behaviour of shear critical FRP reinforced concrete beams.

Based on the analysis, the following conclusions can be made:

1. The post cracking modelling of concrete in tension has significance on the FE modelling.
2. A simple, easy to use tension stiffening idealization was proposed. The proposed tension stiffening idealization predicted the test results of shear critical GFRP reinforced beams successfully. The model needs some refinement to improve the prediction of CFRP reinforced beams.
3. The finite element modelling of beams without web reinforcement is complicated. This complication arises from the fact that the beams without web reinforcement

have both a reinforced concrete (RC) and a plain concrete (PC) zone. The PC zone exhibits a tension-softening behaviour and the RC zone exhibits a tension-stiffening behaviour. For beams with different depths and different reinforcement ratio, the PC zone is different. Therefore, this effect should be considered for modeling the shear critical FRP reinforced beams.

4. Model-1 was based on damage plasticity model of the concrete in compression and the proposed tension stiffening idealization. The elements used were 8 node 3-D reduced integration elements. The model predictions were in good agreement with the test results for different shear span-to-depth ratio, depth of beams, concrete strength, reinforcement ratios, and reinforcement type.
5. Model-2 was based on a hypoeastic concrete model. The elements used were 3-D plane stress solid element with 4 integration points. The tension stiffening model used was a discontinuous unloading model. The model gave good prediction for steel reinforced beams. This model did not provide a good result for GFRP reinforced beams. This could be due to the low axial stiffness of the GFRP bar for which higher tension stiffening value is required.

7.5 Recommendation for Future Research

The problems in determining the shear strength of reinforced concrete beams remains an area of discussion after more than 100 years of study. Based on the investigation in this dissertation, the following recommendations can be made:

1. More systematic test series need to be conducted to observe the size effect for different shear span-to-depth ratio, axial stiffness of the reinforcing bars, and arch effect on the shear strength of FRP reinforced concrete members.
2. The proposed shear design method was verified for rectangular concrete section with concentrated load only. Tests should be conducted for uniformly distributed loads and beams with T-section.
3. Tests should also be conducted with different aggregate sizes for FRP reinforced concrete beams.
4. One of the high strength concrete beams failed by bond failure between the bars and sand coating. This should be further investigated for HSC in future study.
5. Test should be conducted for beams with axial load.
6. More research is needed for suitable tension-stiffening model which will include reinforcement properties and concrete strength.

References

Abdel Baky, H.; Ebead, U. A.; and Neale, K. W. (2008), "Numerical Aspects Concerning the Accuracy of Finite Element Simulations of Concrete Beams Strengthened in Flexure Using FRP Sheets," International Conference on "*Advanced Composite Materials in Bridges and Structures*", ACMBS-V, Winnipeg, Manitoba, Canada, September 22-24.

ACI-ASCE Committee 326 (1962), "Shear and Diagonal Tension," *ACI Journal, Proceedings*, V. 59, No. 1, 2, 3.

ACI Committee 224 (1986), "Cracking of Concrete Members in Direct Tension (ACI 224.2R-86)," American Concrete Institute, Detroit, Michigan.

ACI Committee 318 (1995), "Building Code Requirements for Reinforced Concrete (ACI 318M-95) and Commentary (ACI 318RM-95)," Detroit, Michigan.

ACI Committee 440 (2003), "Guide for the Design and Construction of Concrete Reinforced with FRP Bars (ACI 440.1R-03)," Farmington Hills, Mich.

ACI Committee 440 (2006), "Guide for the Design and Construction of Structural Concrete Reinforced with FRP Bars (ACI 440.1R-06)," Farmington Hills, Mich.

Alkhrdaji, T.; Wideman, M; Belarbi, A.; and Nanni, A. (2001), "Shear Strength of GFRP RC Beams and Slabs," *Composites in Construction*, Figueiras et al (eds), Swets and Zeitlinger, Lisse.

ASCE-ACI Committee 426 (1973), "The Shear Strength of Reinforced Concrete Members," *Journal of Structural Division*, ASCE, Vol. 99, No. ST6.

ASCE Committee 447 (1982), "State-of-the-Art Report on Finite Element Analysis

of Reinforced Concrete," American Society of Civil Engineers.

ASCE-ACI Committee 445 on Shear and Torsion (1998), "Recent Approaches to Shear Design of Structural Concrete, *Journal of Structural Division*, ASCE, Vol. 124, No. 12.

Ashour, A. F. (2000), "Shear Capacity of Reinforced Concrete Deep Beams," *Journal of Structural Engineering*, ASCE, Vol. 126, No. 9.

Bažant, Z. P. (1976), "Instability, Ductility and Size Effect in Strain-Softening Concrete," *Journal of Engineering Mechanics Division*, ASCE, Vol. 102, No. EM2.

Bažant, Z. P. and Cedolin, L. (1979), "Blunt Crack Band Propagation in Finite Element Analysis," *Journal of Engineering Mechanics*, ASCE, Vol. 106, No. 6.

Bažant, Z. P. and Kazemi, M. T. (1991), "Size effect on Diagonal Shear Failure of Beams without Stirrups," *ACI Structural Journal*, Vol. 88, No. 3.

Bažant, Z. P. and Oh, B. H. (1983), "Crack Band Theory for Fracture of Concrete," *Materials and Structures*, RILEM, 16.

Bažant, Z. P. and Oh, B. H. (1984), "Deformation of Progressively Cracking Reinforced Concrete Beams," *ACI Journal* Vol. 81, No. 3.

Bentz, E. C. and Collins, M. P. (2006), "Development of the 2004 Canadian Standards Association (CSA) A23.3 Shear Provisions for Reinforced Concrete," *Canadian Journal of Civil Engineering*, Vol. 33.

Biggs, M. R.; Barton, F. W.; Gomez, J. P.; Massarelli, P. J.; and Mckeel, W. T. (2000), "Final Report on Finite Element Modeling and Analysis of Reinforced-Concrete Bridge Decks," Virginia Transportation Research Council, VTRC 01-R4, Virginia.

Bischoff, P. H. and Paixao, R. (2004), "Tension Stiffening and Cracking of Concrete

Reinforced with Glass Fibre Reinforced Polymer (GFRP) Bars," *Canadian Journal of Civil Engineering*, Vol. 31.

Brown, M. D.; Bayrak, O.; and Jirsa, J. O. (2006), "Design for Shear Based on Loading Conditions," *ACI Structural Journal*, Vol. 103, No. 4.

Canadian Standard Association (2002), "Design and Construction of Building Components with Fibre Reinforced Polymers," CSA S806-02, Rexdale, Ontario, Canada.

Canadian Standard Association (2006), "Canadian Highway Bridge Design Code (CHBDC)," CSA-S6-06, Rexdale, Ontario, Canada.

CEB-FIP (1978), "CEB-FIP Model Code for Concrete Structures," *Comite Euro-International du Beton and Federation Internale de la Precontrainte*, CEB.

Chen, W. F. (1982), "Plasticity in Reinforced Concrete," McGraw-Hill Book Company Inc., New York.

Collins, M. P. and Mitchell, D. (1997), "Prestressed Concrete Structures," Response Publications, Toronto, Canada.

Cope, R. J.; Rao, P. V.; and Clark, L. A. (1979), "Nonlinear Design of Concrete Bridge Slabs using Finite Element Procedures," In: "Nonlinear Design of Concrete Structures," Edited by M.Z. Cohn, University of Waterloo, Canada.

Coronelli, D. and Mulas, M. G. (2006), "Modelling of Shear Behaviour in Reinforced Concrete Beams," *ACI Structural Journal*, Vol. 103, No. 3.

Damjanic, F. and Owen, D. R. J. (1984), "Practical Considerations for Modelling of Post-Cracking Concrete Behaviour for Finite Element Analysis of Reinforced Concrete Structures," In: " Computer Aided Analysis and Design of Concrete Structures", Edited by N. Bicanic and V. Simovic, Pineridge Press, Swansea, UK.

Darwin, D. (1986), "Concrete Crack Propagation-Study of Model Parameters," Finite Element Analysis of Reinforced Concrete Structures, edited by Meyer, C. and Okamura, H., ASCE.

Darwin, D. (1993), "Finite Element Analysis of Reinforced Concrete Structures II," *Proceeding of the International Workshop*, edited by Isenberg, J., ASCE, New York, USA

Deitz, D. H.; Harik, I. E.; and Gesund, H. (1999), "One-Way Slabs Reinforced with Glass Fibre Reinforced Polymer Reinforcing Bars," *ACI Proceeding*, 4th International Symposium, Detroit.

El-Sayed, A. K.; El-Salakawy, E. F.; and Benmokrane, B. (2005), "Shear Strength of Concrete Beams Reinforced with FRP Bars: Design Method," *Proceedings of the 7th International Symposium on Fiber Reinforced Polymer (FRP) Reinforcement for Concrete Structures (FRPRCS-7)*, ACI Special Publication, SP 230-54.

El-Sayed, A. K.; El-Salakawy, E. F.; and Benmokrane, B. (2005a), "Shear Strength of One-Way Concrete Slabs Reinforced with Fibre-Reinforced Polymer Composite Bars," *Journal of Composites for Construction*, ASCE, Vol. 9, No. 2.

El-Sayed, A. K. (2006), "Concrete Contribution to the Shear Resistance of FRP-Reinforced Concrete Beams," *Ph.D. Dissertation*, University of Sherbrooke, Quebec, Canada.

El-Sayed, A. K.; El-Salakawy, E. F, and Benmokrane, B. (2006a), "Shear Strength of FRP-Reinforced Concrete Beams without Transverse Reinforcement," *ACI Structural Journal*, V. 103, No. 2.

El-Sayed, A. K.; El-Salakawy, E. F.; and Benmokrane, B. (2006b), "Shear Capacity of High-Strength Concrete Beams Reinforced with FRP Bars," *ACI Structural Journal*, Vol. 103, No. 3.

Faza, S. S. and Gangarao, H. V. S. (1993), "Theoretical and Experimental Correlation of Behaviour of Concrete Beams Reinforced with Fibre Reinforced Plastic Rebars," *Fibre-Reinforced-Plastic Reinforcement for Concrete Structures- International Symposium*, SP-138, A. Nanni and C. W. Dolan, eds., American Concrete Institute, Farmington Hills, Mich.

Feeser, W. K. and Brown, V. L. (2005), "Guide Examples for Design of Concrete Reinforced with FRP Bars," *Proceedings of the 7th International Symposium on Fibre Reinforced Polymer (FRP) Reinforcement for Concrete Structures (FRPRCS-7)*, ACI Special Publication, SP 230-53

Fenwick, R. C., and Paulay, T. (1968), "Mechanisms of Shear Resistance of Concrete Beams," *Journal of Structural Division*, ASCE, Vol. 94, No. 10.

Gerstle, K. H.; Linse, D. H.; et al. (1978), "Strength of Concrete Under Multi Axial Stress State," *ACI Publication*, SP-55,

Gopalaratnam, V. S. and Shah, S. P. (1985), "Softening Response of Plain Concrete in Direct Tension," *ACI Journal*, Vol. 82, No. 3.

Grieef, S. (1996), "ISOROD GFRP Dowel Bars in Concrete Pavements," MS Thesis, Department of Civil and Geological Engineering, University of Manitoba, Winnipeg, Manitoba, Canada.

Gross, S. P.; Yost, J. R.; Dinehart, D. W.; Svensen, E.; and Liu, N. (2003), "Shear Strength of Normal and High Strength Concrete Beams Reinforced with GFRP Bars," *Proc. of the Int. Conference on High Performance Materials in Bridges*, ASCE.

Gross, S. P.; Dinehart, D. W.; and Yost, J. R. (2004), "Experimental Test of High-Strength Concrete Beams Reinforced CFRP Bars", International Conference on "*Advanced Composite Materials in Bridges and Structures*," ACMBS-IV, Calgary, Alberta, Canada, July 20-23.

Guadagnini, M.; Pilakoutas, K.; and Waldron, P. (2006), "Shear Resistance of FRP RC Beams: Experimental Study," *Journal of Composites for Constructions*, ASCE, Vol. 10, No. 6.

Guo, Z. H. and Zhang, X. Q. (1987), "Investigation of Complete Stress Deformation Curves for Concrete in Tension," *ACI Material Journal*, Vol. 84, No. 4.

Hillerborg, A.; Modéer, M.; and Peterson, P. (1976), "Analysis of Crack Formation and Crack Growth in Concrete by Means of Fracture Mechanics and Finite Element," *Cement and Concrete Research*, Vol. 6.

Hoult, N. A.; Sherwood, E. G.; Bentz, E. C.; and Collins M. P. (2008), "Does the use of FRP Reinforcement Changes the One-Way Shear behaviour of Reinforced Concrete Slabs?" *Journal of Composites for Constructions*, ASCE, Vol. 12, No. 2.

Hsu, T. T. C.; Slate, F. O.; Sturman, G. M.; and Winter, G. (1963), "Micro-cracking of Plain Concrete and the Shape of the Stress-Strain Curve," *ACI Journal, Proceedings*, Vol. 60, No. 2.

ISIS-M03-07 (2007), "Reinforcing Concrete Structures with Fibre Reinforced Polymers," The Canadian Network of Centers of Excellence on Intelligent Sensing for Innovative Structures, ISIS Canada, University of Winnipeg, Manitoba.

Japan Society of Civil Engineers (JSCE) (1997), "Recommendations for Design and Construction of Concrete Structures Using Continuous Fibre Reinforced Materials,"

Research Committee on Continuous Fibre Reinforced Materials, A. Machida, ed. Tokyo, Japan.

Ju, J. (1989), "On Energy-Based Coupled Elastiplastic Damage Theories: Constitutive Modelling and Computational Aspects," *International Journal of Solids and Structures*, Vol. 25, No. 7.

Kaklauskas, G. and Ghaboussi, J. (2001), "Stress-Strain Relations for Cracked Tensile Concrete from RC Beam Tests," *Journal of Structural Engineering*, ASCE, Vol. 127, No 1.

Kani, G. N. J. (1966), "Basic Facts Concerning Shear Failure," *ACI Journal*, Vol. 63, No. 6.

Kani, G. N. J. (1967), "How Safe are our Large Reinforced Concrete Beams?" *ACI Journal*, Vol. 64, No. 3.

Kani, M. W.; Huggins, M. W.; and Wiltkopp, P. F. (1979), "Kani on shear in Reinforced concrete," Department of Civil Engineering, University of Toronto, Canada.

Karihaloo, B. (2003), "Failure of Concrete," *Comprehensive Structural Integrity*, Vol. 2.10.

Khuntia, M. and Stojadinovic, B. (2001), "Shear Strength of Reinforced Concrete Beams without Transverse Reinforcement," *ACI Structural Journal*, Vol. 98, No. 5.

Kotsovos, M. D. and Pavlovic, M. N. (1999), "Ultimate limit state design of concrete structures – a new approach," London: Thomas Telford, Ltd.

Kupfer, H.; Hilsdof, H. K.; and Rusch, H. (1969), "Behaviour of Concrete Under Biaxial Stresses," *ACI Journal, Proc.*, Vol. 66, No. 8.

Lee, J.; and Fenves, G. (1998), "Plastic-Damage Model for Cyclic Loading of Concrete Structures," *Journal of Engineering Mechanics*, ASCE, Vol. 124, No. 8.

Lin, C. S. and Scordelis, A. C. (1975), "Nonlinear Analysis of Reinforced Concrete Shells of general form," *Journal of the Structural Division*, ASCE, Vol. 101, No. ST3.

Lubell, A.; Sherwood, T.; Bentz, E.; and Collins, M. P. (2004), "Safe Shear Design of Large, Wide Beams," *Concrete International*, 66.

Lubliner, J.; Oliver, J.; Oller, S.; and Onate, E. (1989), "A Plastic Damage Model for Concrete," *International Journal of Solids and Structures,* Vol. 25, No. 3.

MacGregor, J. G. and Bartlett, F. M. (2000), "Reinforced Concrete: Mechanics and Design," First Canadian Edition.

Maekawa, A.; Pimanmas, A.; and Okamura, H. (2003), "Nonlinear Mechanics of Reinforced Concrete," Spon Press, London and New York, First Edition.

Mang, H.; Lackner, R.; Meschke, G.; and Mosler, J. (2003), "Computation Modelling of Concrete Structures," *Comprehensive Structural Integrity*, Vol. 3.10.

Massicotte, B.; Elwi, A. E.; and MacGregor, J. G. (1990), "Tension Stiffening Model for Planner Reinforced Concrete Members," *Journal of Structural Engineering*, ASCE.

Menetrey, P. H. and William, K. J. (1995), "Triaxial Failure Criterion for Concrete and Its Generalization," *ACI Structural Journal*, Vol. 92, No. 3.

Michaluk, C. R.; Rizkalla, S. H.; Tadros, G.; and Benmokrane, B. (1998), "Flexural Behaviour of One-way Slabs Reinforced by Fibre Reinforced Plastic Reinforcement," *ACI Structural Journal*, Vol. 95, No. 3.

Mörsch, E. (1909), "*Concrete-steel construction*," McGraw-Hill, New York, (English translated by E.P. Goodrich, First Edition 1992).

Nanni, A (1993), "Flexural Behaviour and Design of Reinforced Concrete Using FRP Rods," *Journal of Structural Engineering*, ASCE, Vol. 119, No 11.

National Cooperative Highway Research Program (NCHRP) (2005), "Simplified Shear Design of Structural Concrete Members," Report #549, USA.

Nielsen, M. P. (1984), "Limit analysis and concrete plasticity," Prentice-Hall, Englewood Cliffs, N. J., USA.

Nour, A.; Massicotte, B.; Yildiz, E.; and Koval, V. (2007), "Finite Element Modelling of Concrete Structures Reinforced with Internal and External Fibre-Reinforced Polymers," *Can. J. of Civil Engineering,* Vol. 34.

Pillai, S. U.; Kirk, D.W.; and Erki, M. A. (1999), "Reinforced Concrete Design," Third edition, MacGraw-Hill Ryerson Limited.

Prakhya, G. K. V. and Morley, C. T. (1990), "Tension Stiffening and Moment Curvature Relations of Reinforced Concrete Elements," *ACI Journal*, Vol. 87, No. 5.

Razaqpur, A. G.; Isgor, B. O.; Greenway, S.; and Selley, A. (2004), "Concrete Contribution to the Shear Resistance of Fibre Reinforced Polymer Reinforced Concrete Members," *Journal of Composites for Constructions*, ASCE, Vol. 8, No. 5.

Razaqpur, A. G.; Isgor, B. O. (2006), "Proposed Shear Design Method for FRP-Reinforced Concrete Members without Stirrups," *ACI Structural Journal*, Vol. 103, No. 1.

Rebeiz, K. S. (1999), "Shear Strength Prediction for Concrete Members," *Journal of Structural Engineering*, ASCE, Vol. 125, No. 3.

Reineck, K. H. (1991), "Ultimate Shear Force of Structural Concrete Members without Transverse Reinforcement Derived from a Mechanical Model," *ACI Structural Journal*, Vol. 85, No. 5.

Shioya, T.; Iguro, M.; Nojiri, Y.; Akiyama, H.; and Okada, T. (1989), "Shear Strength of Large Reinforced Concrete Beams, Fracture Mechanics: Application to Concrete," SP-118, ACI, Detroit.

Sherwood, E. G.; Bentz, E. C.; and Collins, M. P. (2008), "Prediction of the Shear Strength of FRP-Reinforced Slabs using the 2004 CSA A23.3 Design Code," *CSCE Annual Conference*, Quebec, Canada, June 10-13.

Sonobe, Y. et. al, (1997), "Design Guidelines of FRP Reinforced Concrete Building Structures," *Journal of Composite for Construction*, ASCE, Vol. 1, No. 3.

Sooriyaarachchi, H., Pilakoutas, K. and Byars, E. (2005), "Tension Stiffening Behaviour of GFRP-Reinforced Concrete," *7th International Symposium on Fibre Reinforced Polymer Reinforcement for Reinforced Concrete Structures (FRPRCS-7),* New Orleans, Louisiana, USA, ACI special publication SP-230-55.

Sooriyaarachchi, H., Pilakoutas, K. and Byars, E. (2007), "Model for Tension Stiffening for Deflections of GFRP-RC," *8th International Symposium on Fibre Reinforced Polymer Reinforcement for Reinforced Concrete Structures (FRPRCS-8),* University of Patras, Patras, Greece, July 16-18.

Steiner, S.; El-Sayed, A. K. and Benmokrane, B. (2008), "Shear Behaviour of Large-Size Concrete Beams Reinforced with Glass FRP Bars," *CSCE Annual Conference*, Quebec, Canada, June 10-13.

Tariq, M., and Newhook, J. P. (2003), "Shear Testing of FRP Reinforced Concrete without Transverse Reinforcement," *CSCE Annual Conference*, Moncton, Canada.

Tasuji, M. E.; Slate, F. O.; and Nilson, A. H. (1978), "Stress-Strain Response and Fracture of Concrete in Biaxial Loading," *ACI Journal*, Vol. 75, No. 7.

Taylor, H. P. J. (1970), "Investigations of the Forces Carried Across Cracks in Reinforced Concrete Beams in Shear by Interlock of Aggregate," Technical Report 42.447, Cement and Concrete Association, London, England.

Taylor, H. P. J. (1972), "Shear Strength of Large Beams," *Journal of Structural Division*, ASCE, Vol. 98, No. ST11.

Tottori, S. and Wakui, H. (1993), "Shear capacity of RC and PC beams using FRP reinforcement," In: Nanni A, Dolan C, editors. ACI SP-138. Detroit, Mich: American Concrete Institute.

Tureyen, A. K. and Frosch, J. (2002), "Shear Test of FRP-Reinforced Concrete Beams without Stirrups," *ACI structural Journal*, Vol. 99, No. 4.

Tureyen, A. K. and Frosch, R. J. (2003), "Concrete Shear Strength: Another Perspective," *ACI Structural Journal*, Vol. 100, No. 5.

Vecchio, F. J. and Collins, M. P. (1986), "The Modified Compression Field Theory for Reinforced Concrete Elements Subjected to Shear," *ACI Journal, Proceedings*, Vol. 83 No. 2.

Vecchio, F. J. (2001), "Non-Linear Finite Element Analysis of Reinforced Concrete: At the Crossroads?" *Structural Concrete*, fib, Vol. 2, No. 4.

Yost, J. R.; Gross, S. P., and Dinehart, D. W. (2001), "Shear Strength of Normal Strength Concrete Beams Reinforced with Deformed GFRP Bars," *Journal of Composites for Construction*, Vol. 5, No. 4.

Yost, J. R. and Gross, S. P. (2002), "Flexural Design Methodology for Concrete Beams Reinforced with Fiber-Reinforced Polymers," *ACI Structural Journal*, V. 99, No. 3.

Appendix A

Photographs of the Failure Mode and Crack Patterns

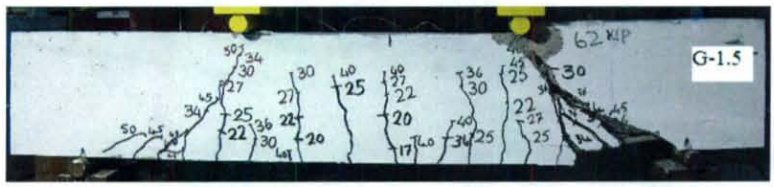

Figure A.1: Crack patterns of beam G-1.5

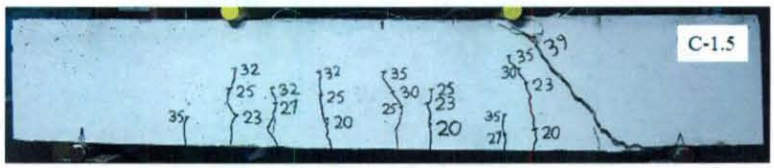

Figure A.2: Crack patterns of beam C-1.5

Figure A.3: Crack patterns of beam G-2.5

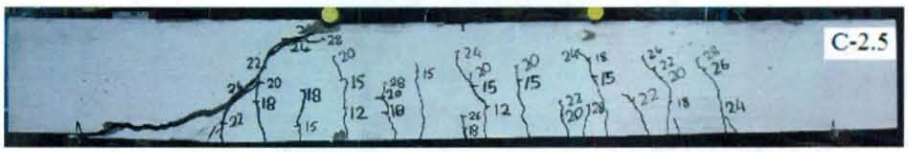

Figure A.4: Crack patterns of beam C-2.5

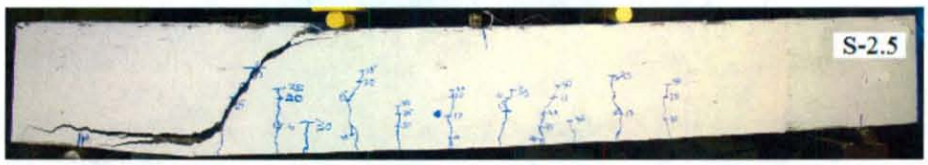

Figure A.5: Crack patterns of beam S-2.5

Figure A.6: Crack patterns of beam G-3.5

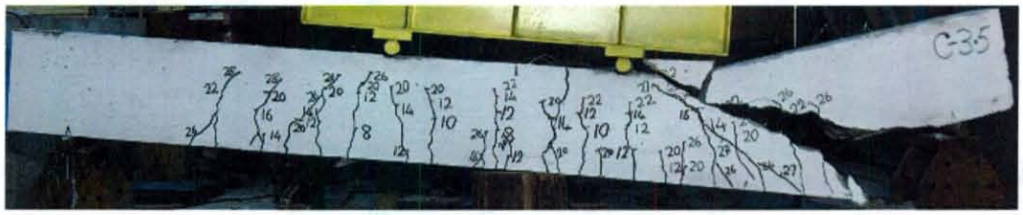

Figure A.7: Crack patterns of beam C-3.5

Figure A.8: Crack patterns of beam S-3.5

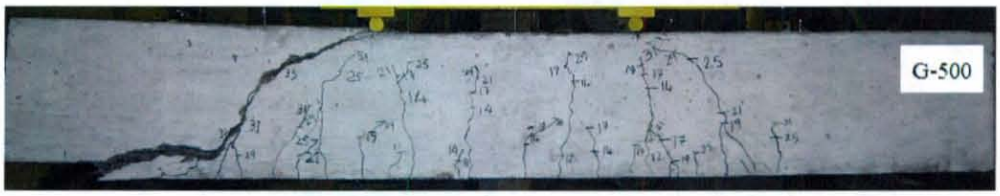

Figure A.9: Crack patterns of beam G-500

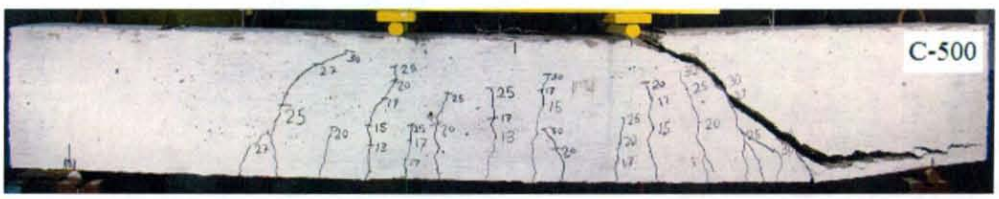

Figure A.10: Crack patterns of beam C-500

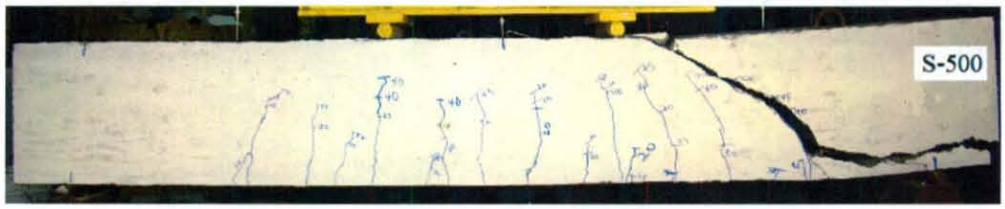

Figure A.11: Crack patterns of beam S-500

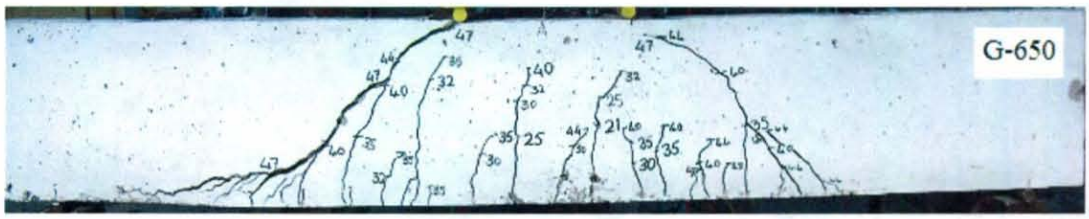

Figure A.12: Crack patterns of beam G-650

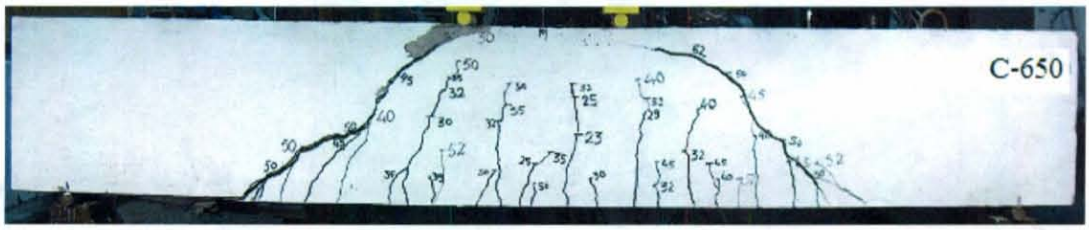

Figure A.13: Crack patterns of beam C-650

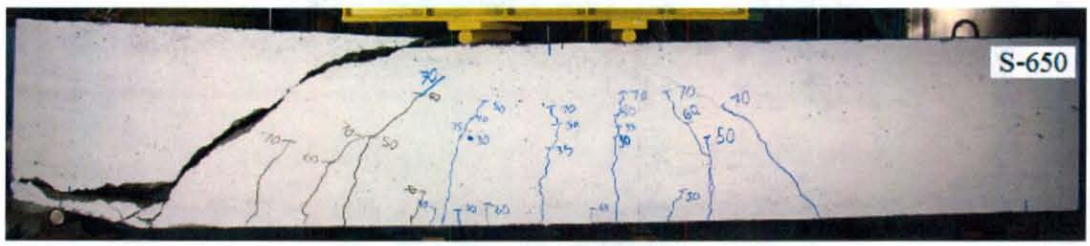

Figure A.14: Crack patterns of beam S-650

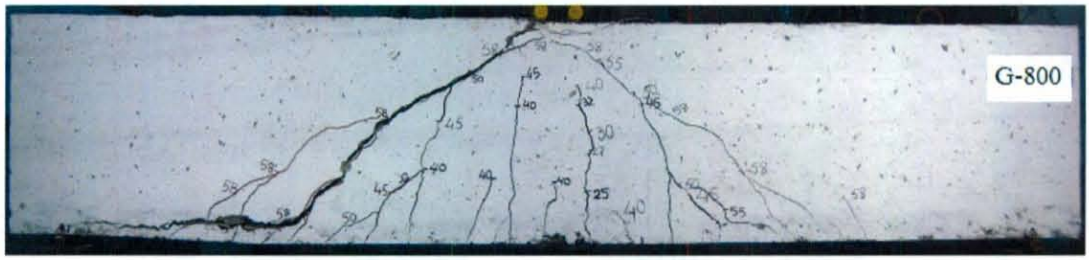

Figure A.15: Crack patterns of beam G-800

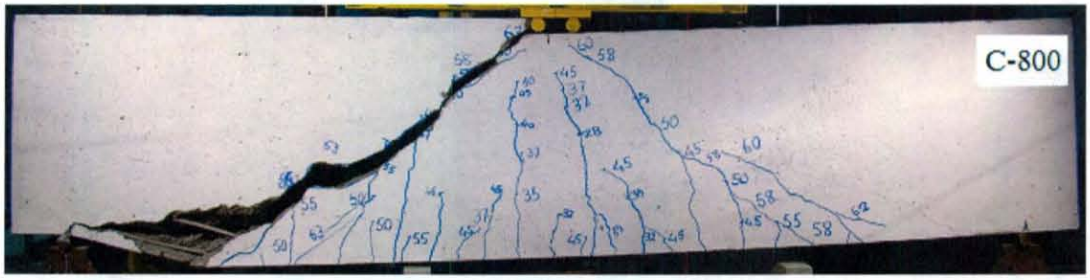

Figure A.16: Crack patterns of beam C-800

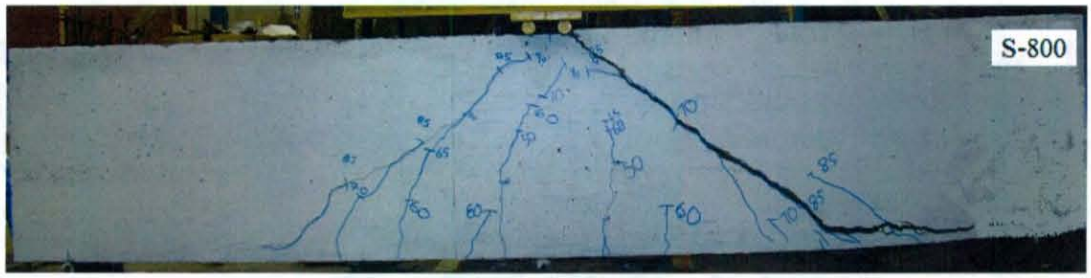

Figure A.17: Crack patterns of beam S-800

Figure A.18: Crack patterns of beam G-0.5-350

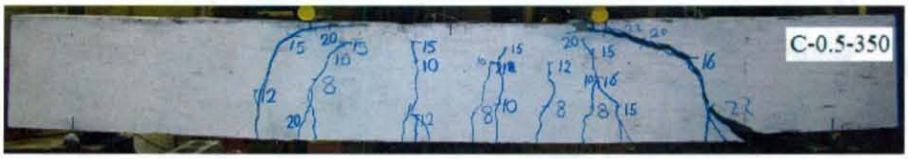

Figure A.19: Crack patterns of beam C-0.5-350

Figure A.20: Crack patterns of beam G-2.5-350

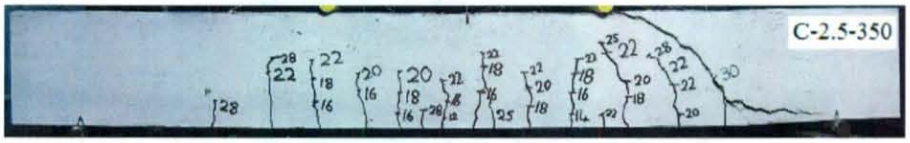

Figure A.21: Crack patterns of beam C-2.5-350

Figure A.22: Crack patterns of beam S-2.5-350

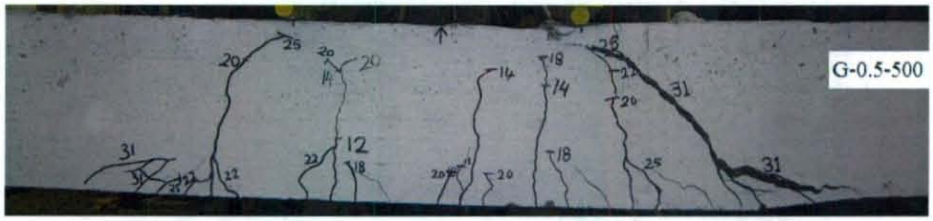

Figure A.23: Crack patterns of beam G-0.5-500

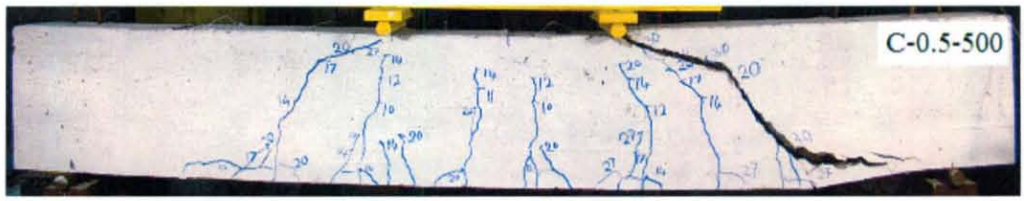

Figure A.24: Crack patterns of beam C-0.5-500

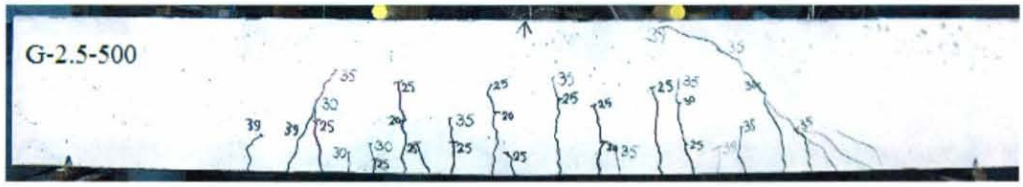

Figure A.25: Crack patterns of beam G-2.5-500

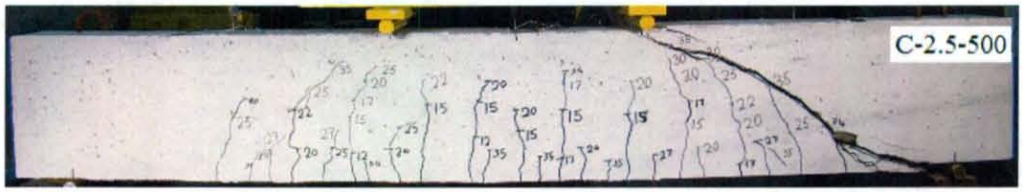

Figure A.26: Crack patterns of beam C-2.5-500

Figure A.27: Crack patterns of beam S-2.5-500

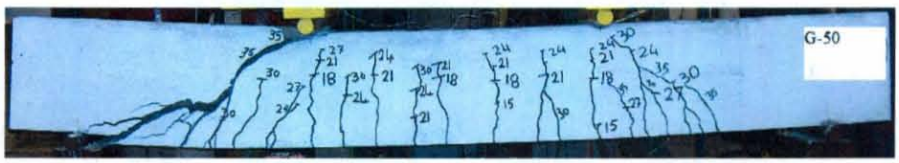

Figure A.28: Crack patterns of beam G-50

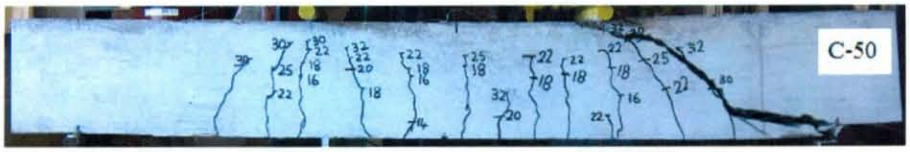

Figure A.29: Crack patterns of beam C-50

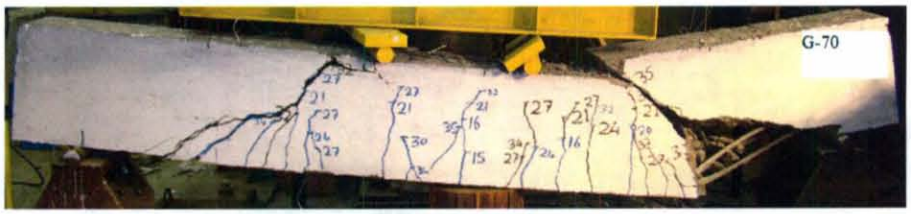

Figure A.30: Crack patterns of beam G-70

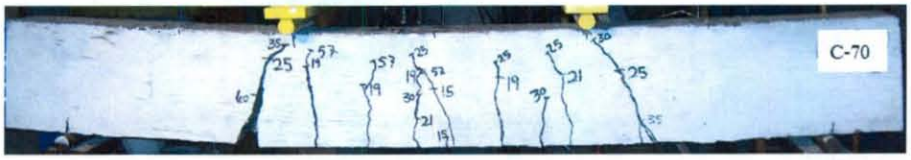

Figure A.31: Crack patterns of beam C-70

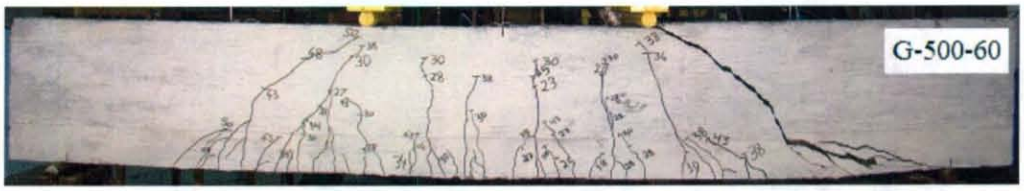

Figure A.32: Crack patterns of beam G-500-70

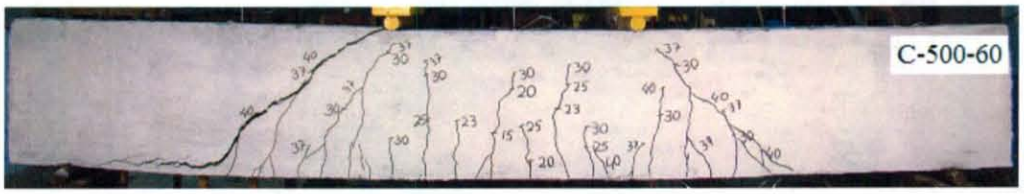

Figure A.33: Crack patterns of beam C-500-70

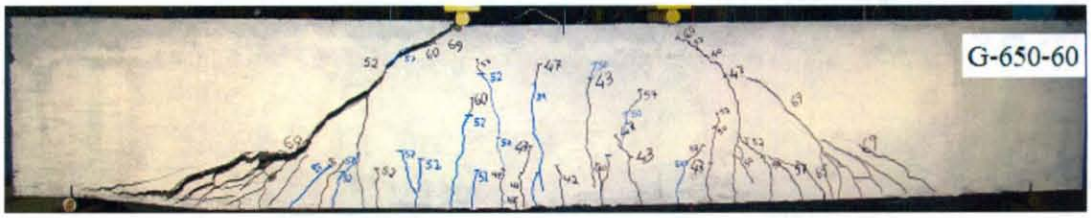

Figure A.34: Crack patterns of beam G-650-70

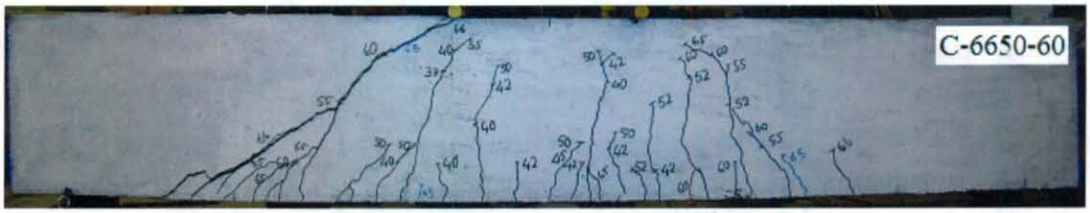

Figure A.35: Crack patterns of beam G-650-70

Appendix B

Plots of the Load versus Deflection Obtained from the Different LVDTs

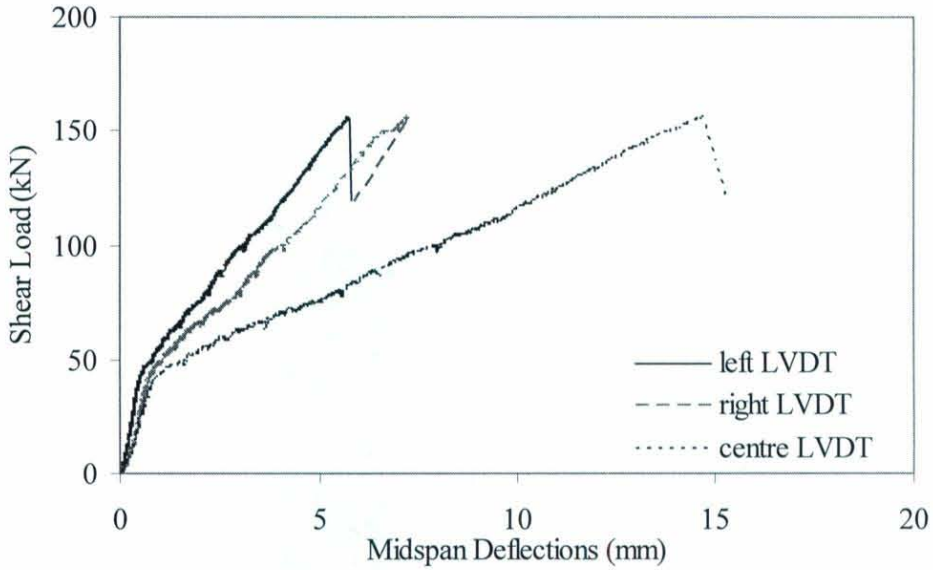

Figure B.1: Load versus deflection of beam G-1.5

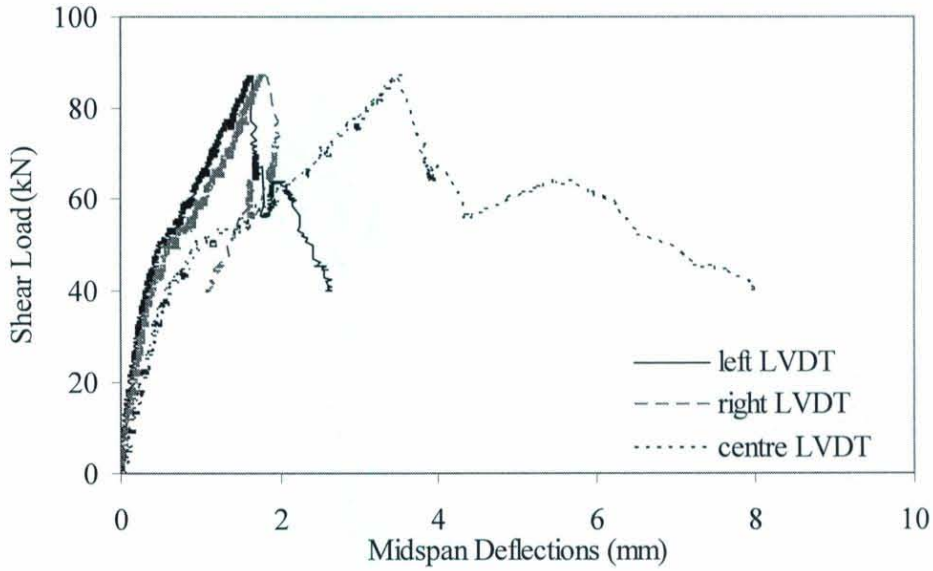

Figure B.2: Load versus deflection of beam C-1.5

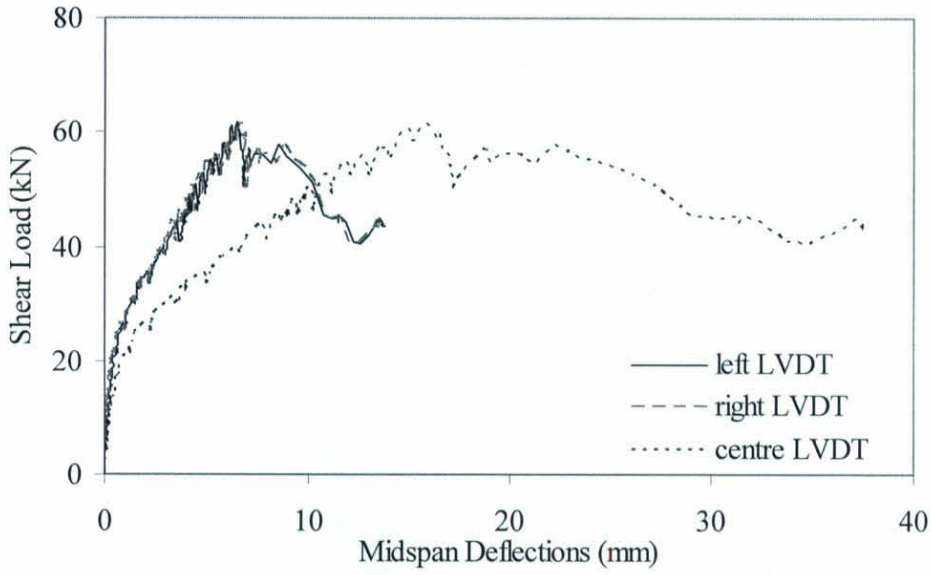

Figure B.3: Load versus deflection of beam G-2.5

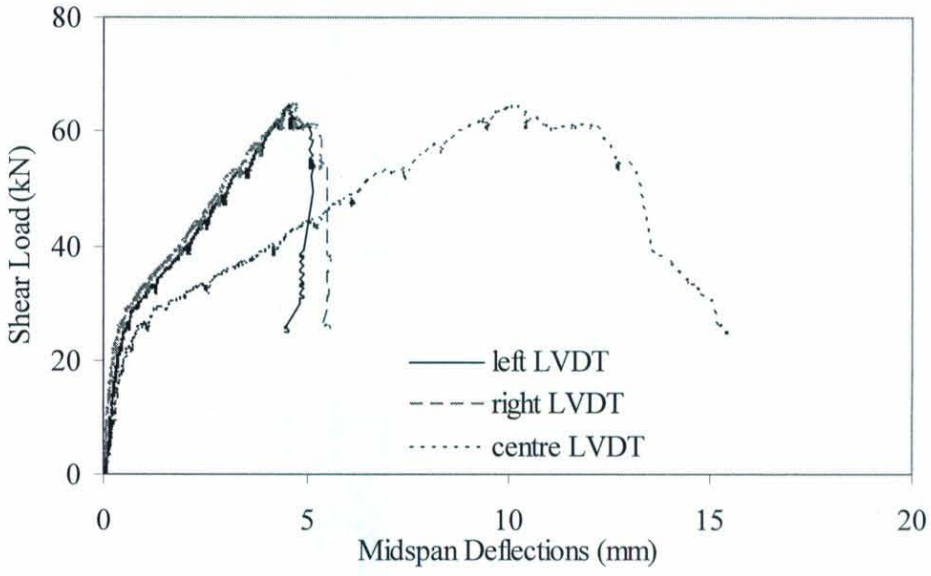

Figure B.4: Load versus deflection of beam C-2.5

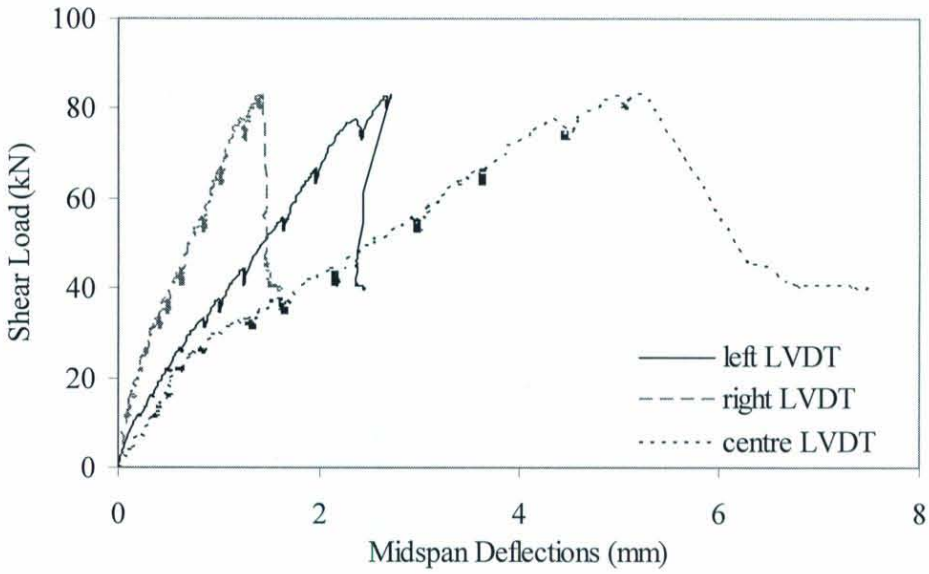

Figure B.5: Load versus deflection of beam S-2.5

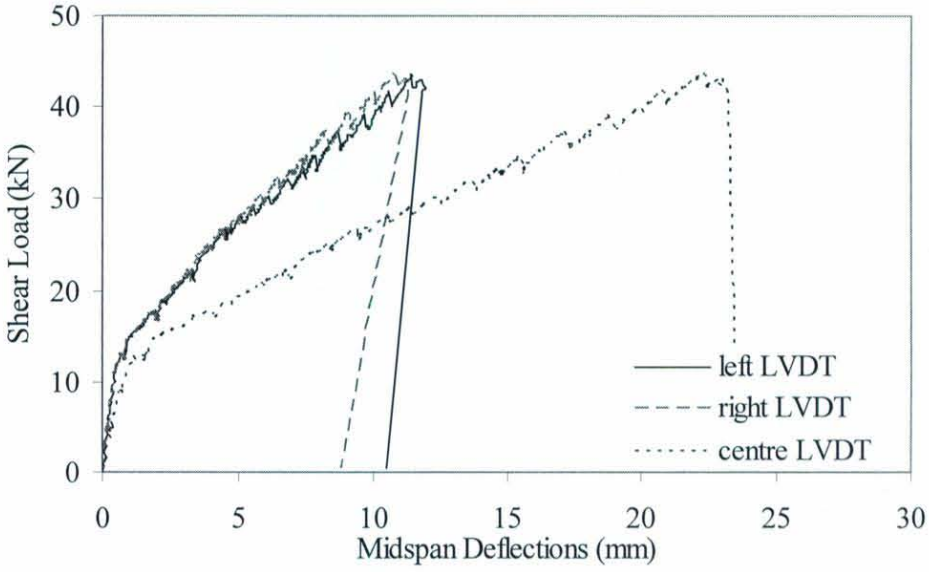

Figure B.6: Load versus deflection of beam G-3.5

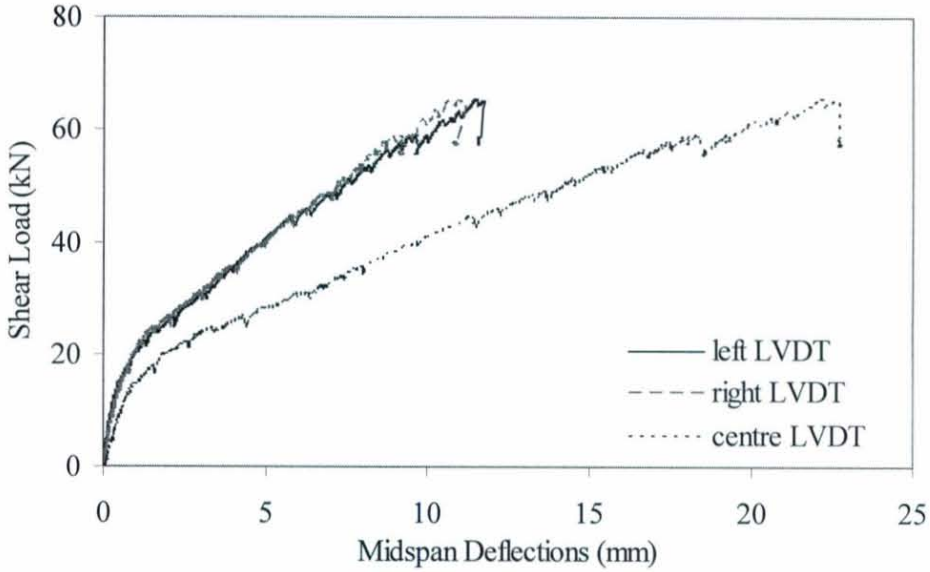

Figure B.7: Load versus deflection of beam C-3.5

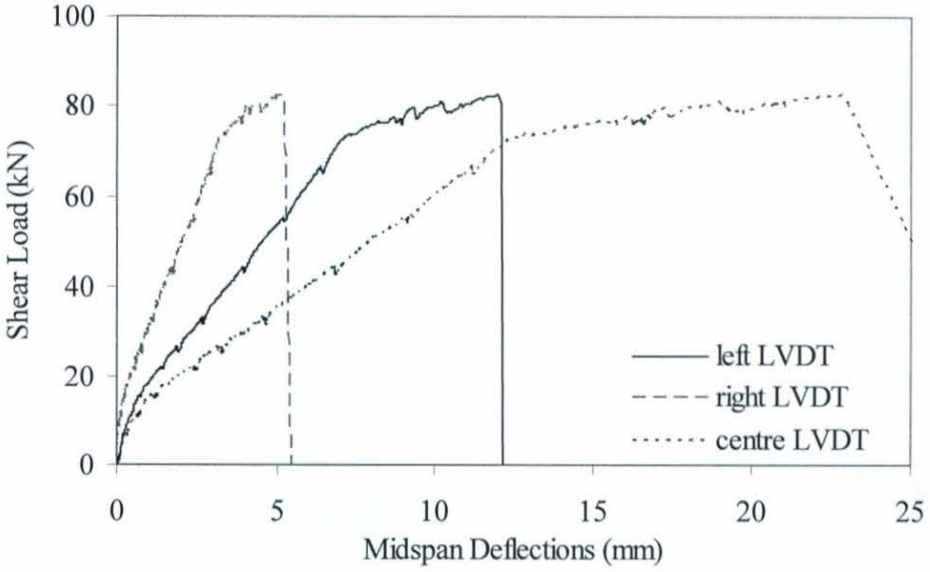

Figure B.8: Load versus deflection of beam S-3.5

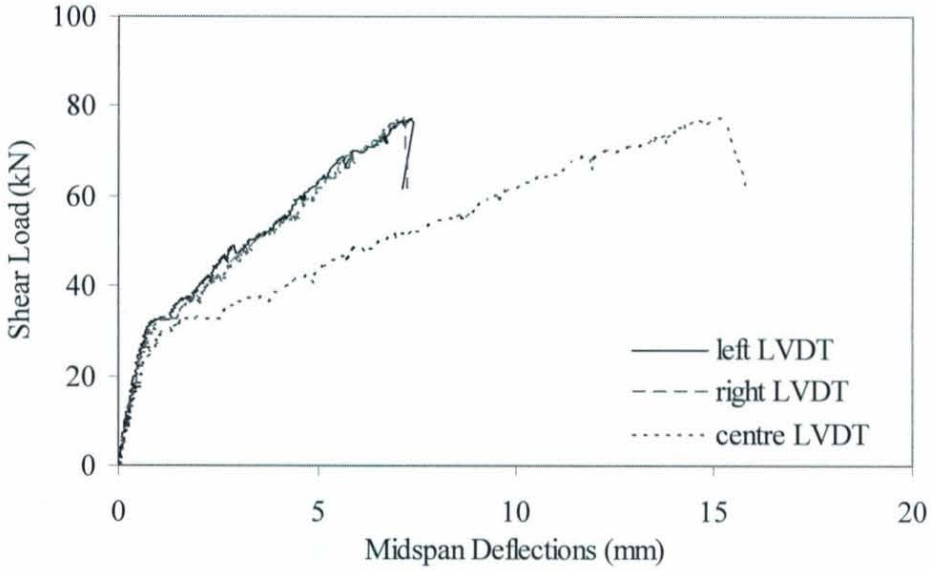

Figure B.9: Load versus deflection of beam G-500

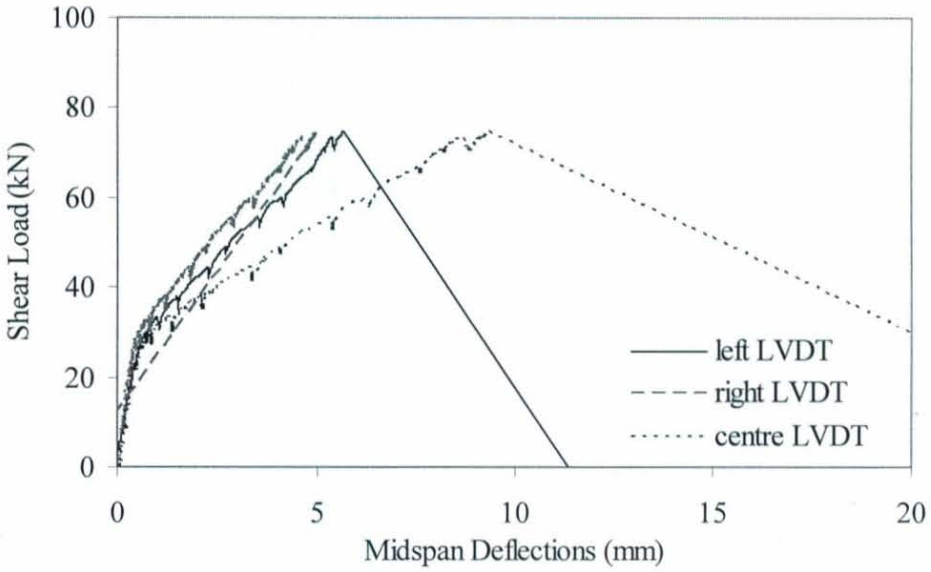

Figure B.10: Load versus deflection of beam C-500

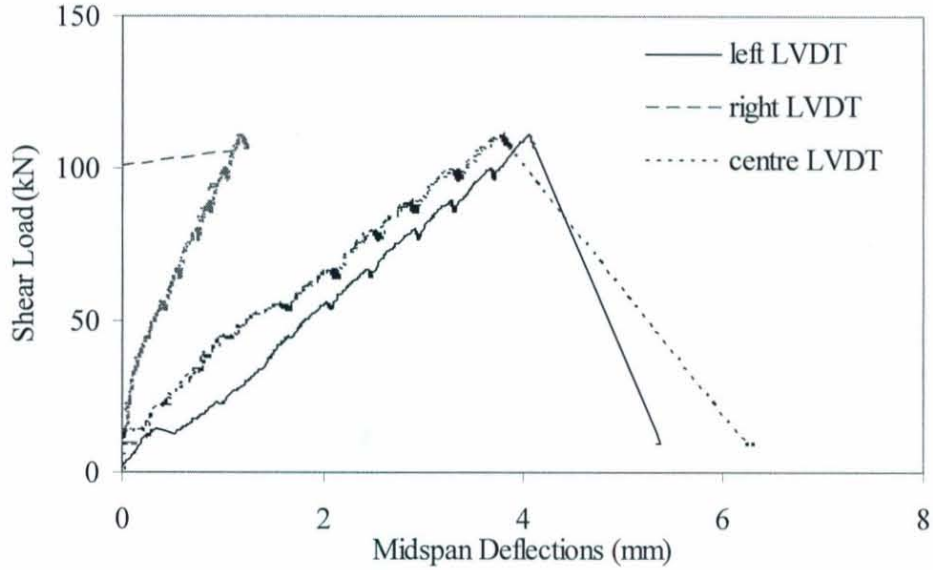

Figure B.11: Load versus deflection of beam S-500

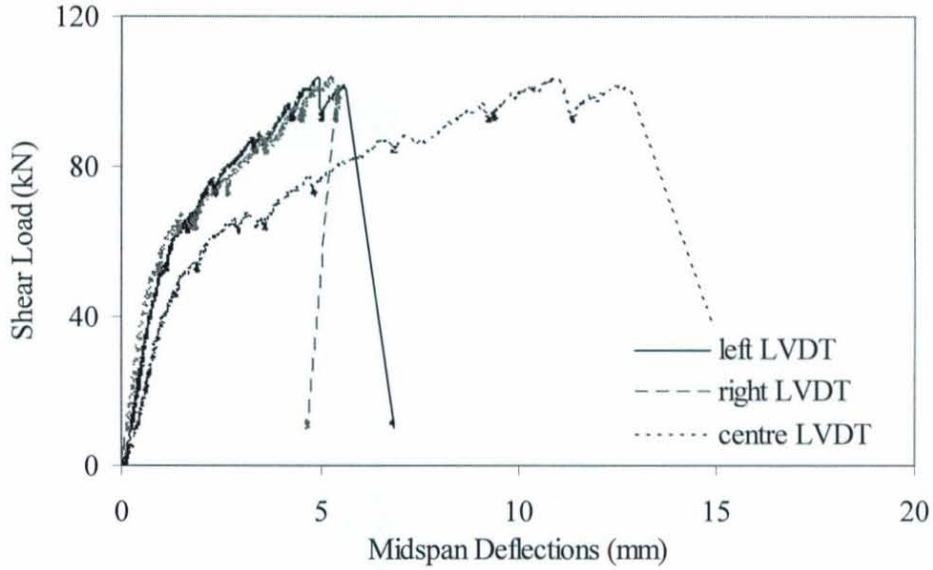

Figure B.12: Load versus deflection of beam G-650

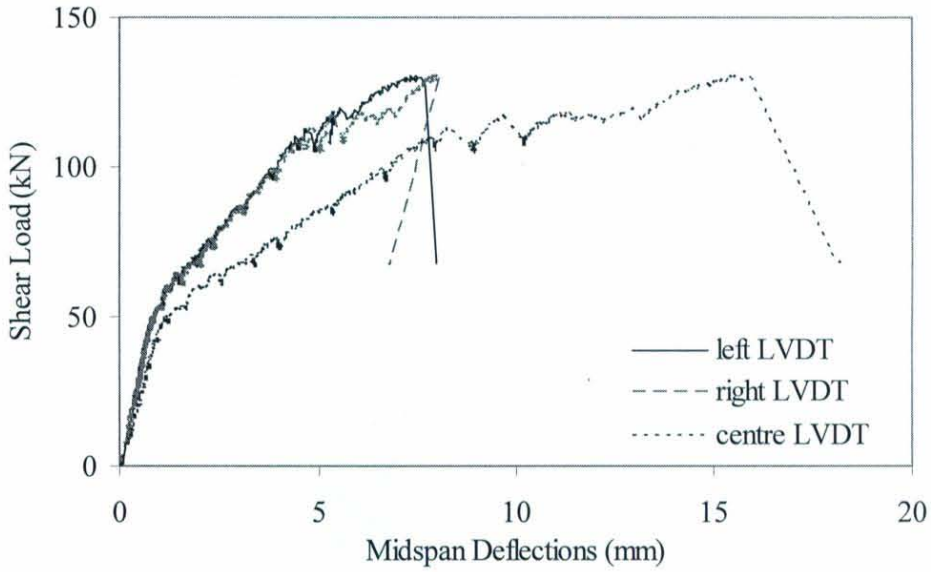

Figure B.13: Load versus deflection of beam C-650

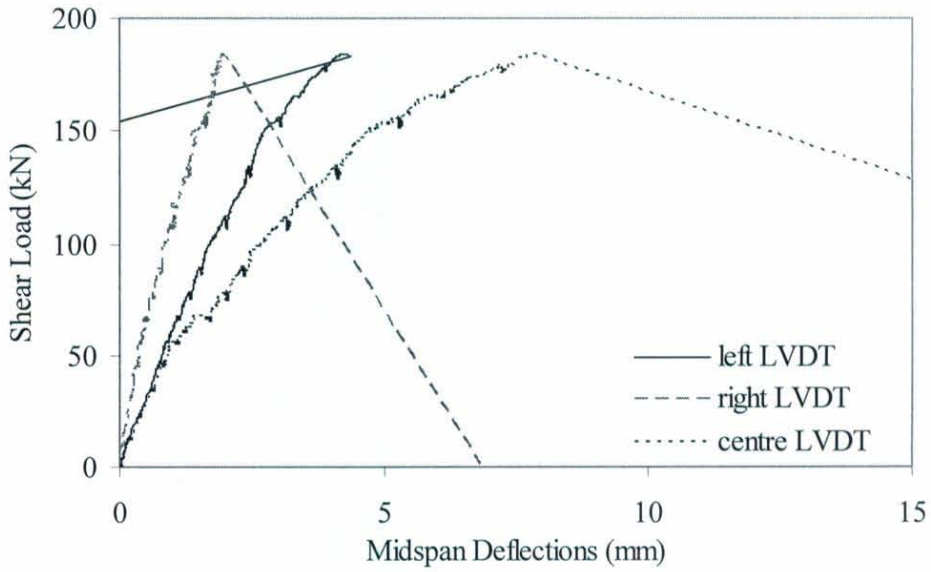

Figure B.14: Load versus deflection of beam S-650

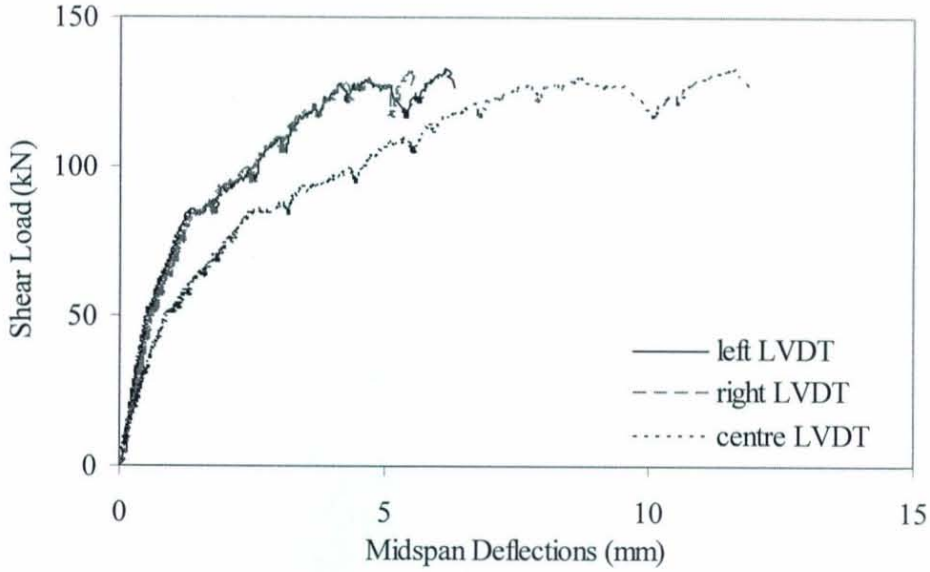

Figure B.15: Load versus deflection of beam G-800

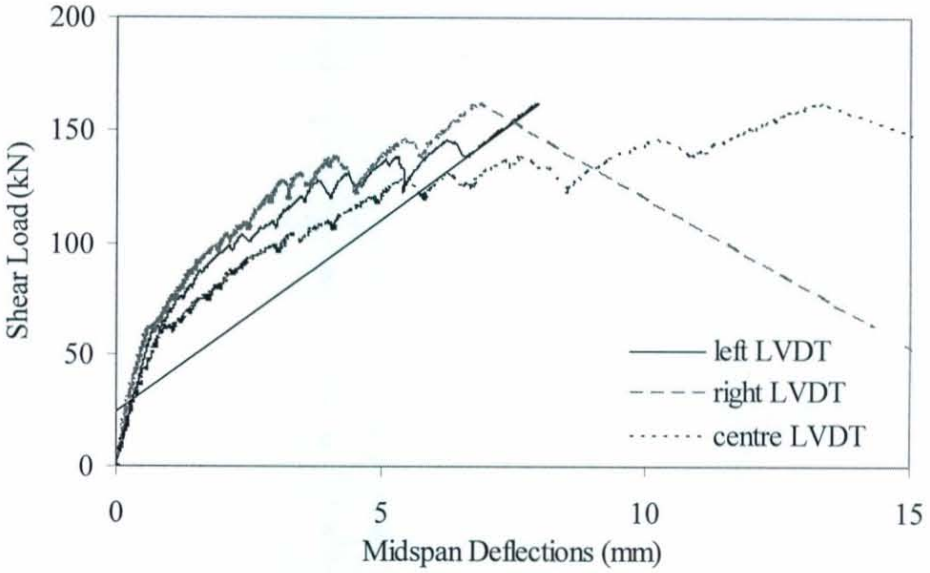

Figure B.16: Load versus deflection of beam C-800

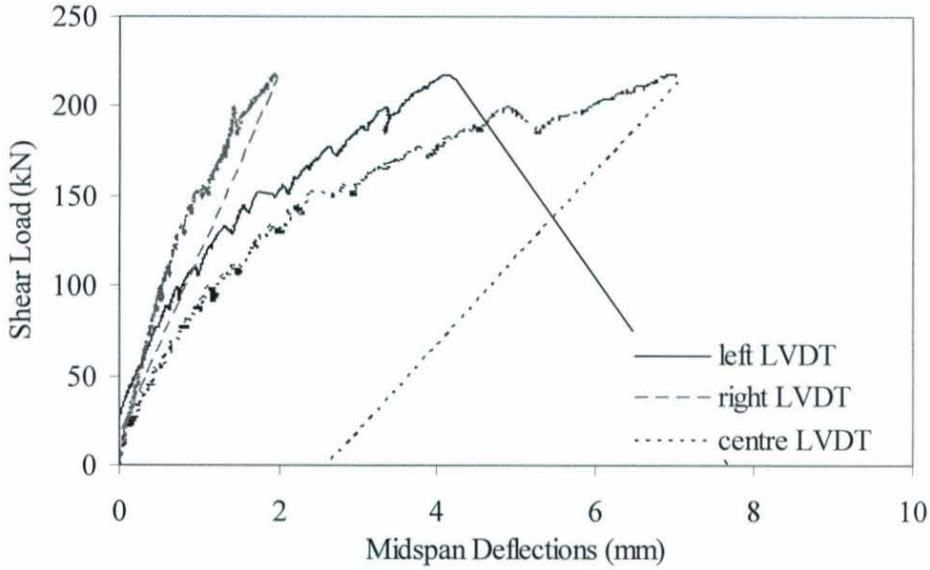

Figure B.17: Load versus deflection of beam S-800

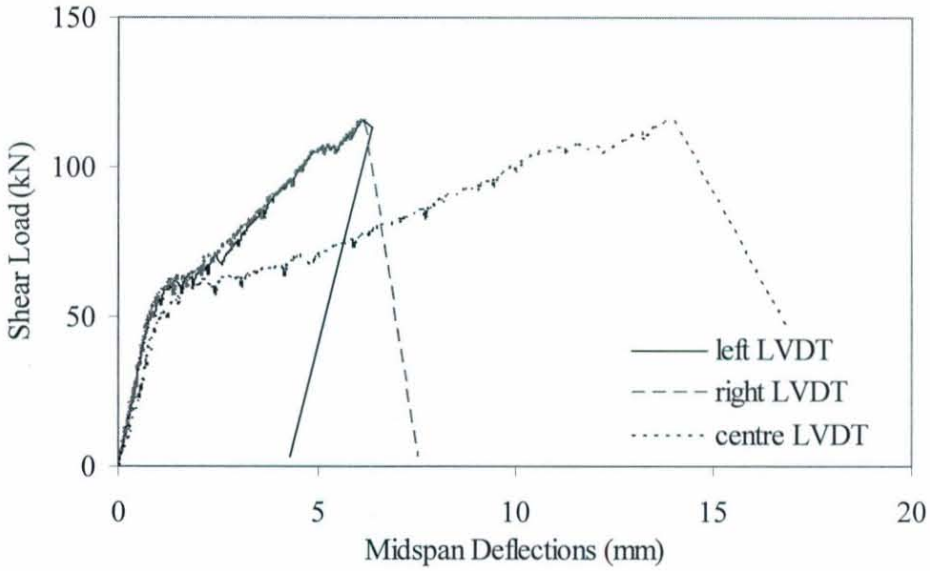

Figure B.18: Load versus deflection of beam G-500-70

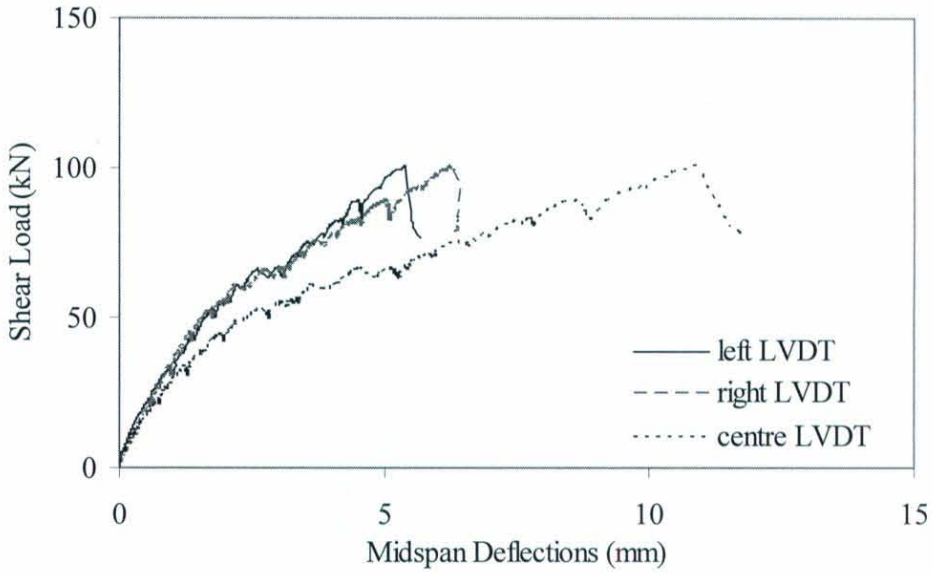

Figure B.19: Load versus deflection of beam C-500-70

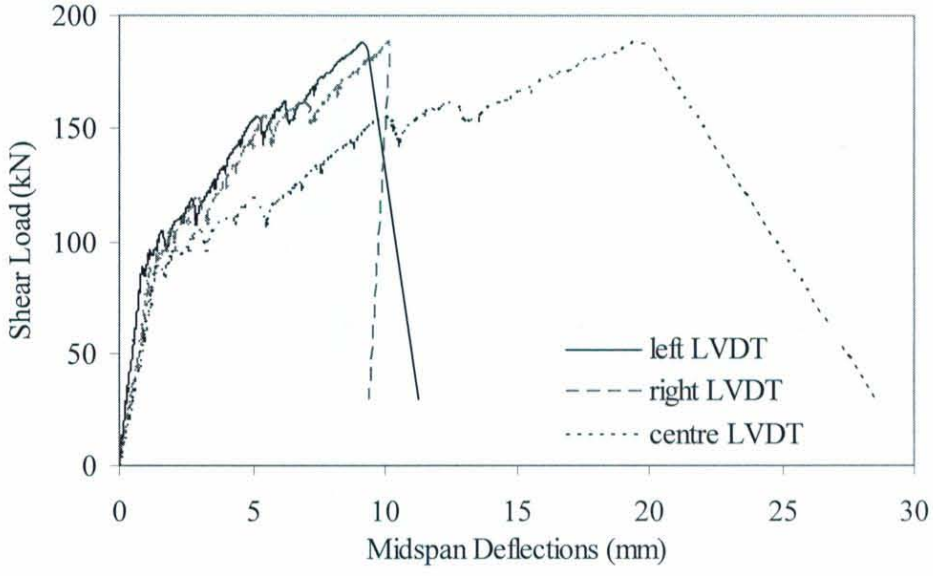

Figure B.20: Load versus deflection of beam G-650-70

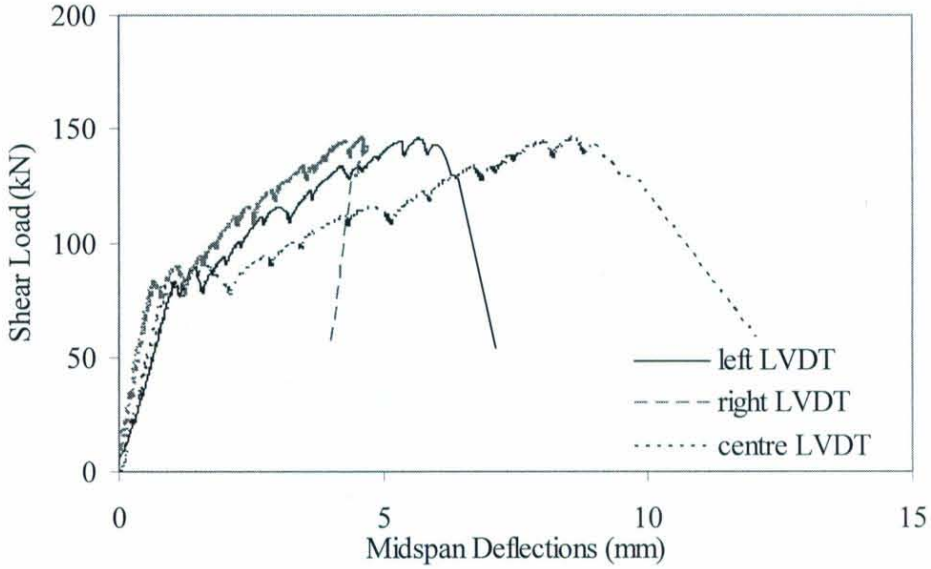

Figure B.21: Load versus deflection of beam C-650-70

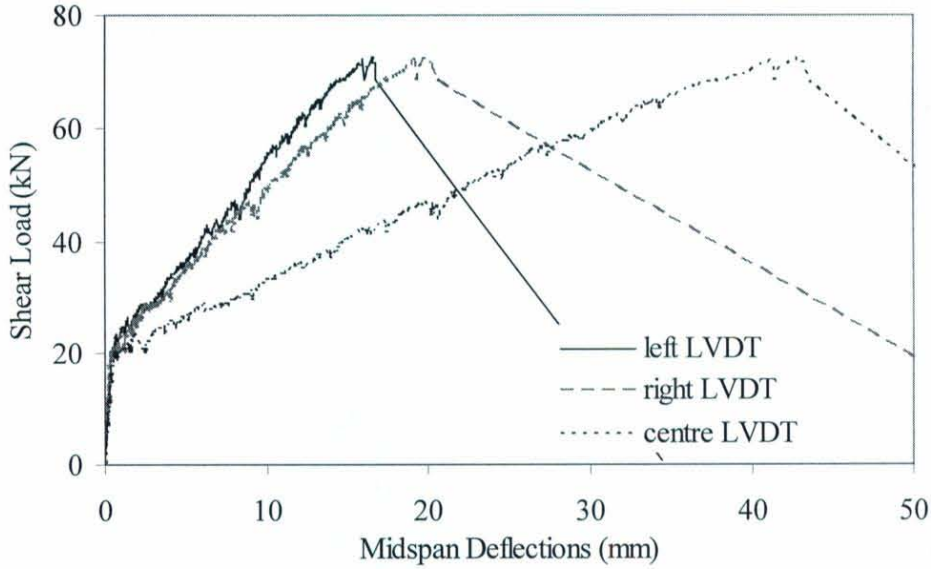

Figure B.22: Load versus deflection of beam G-0.5-350

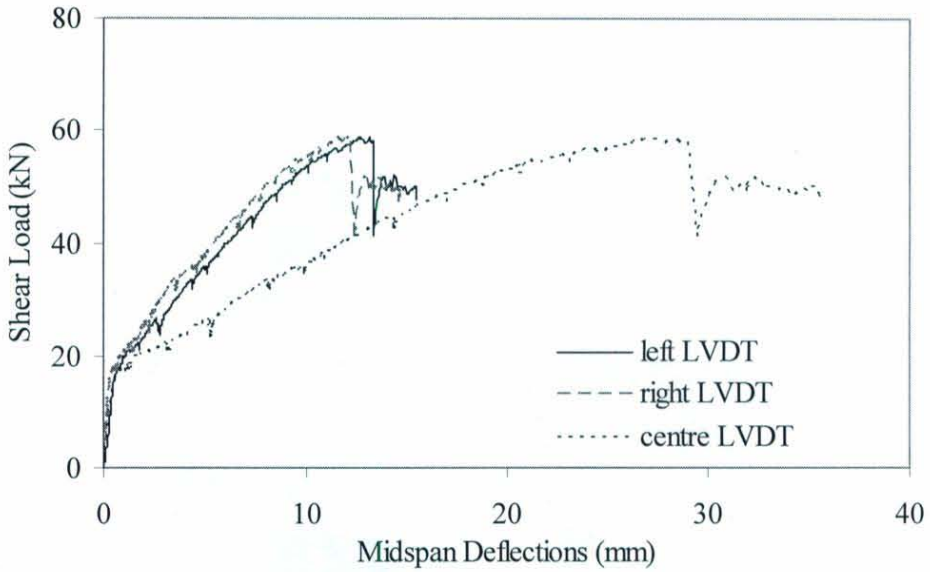

Figure B.23: Load versus deflection of beam C-0.5-350

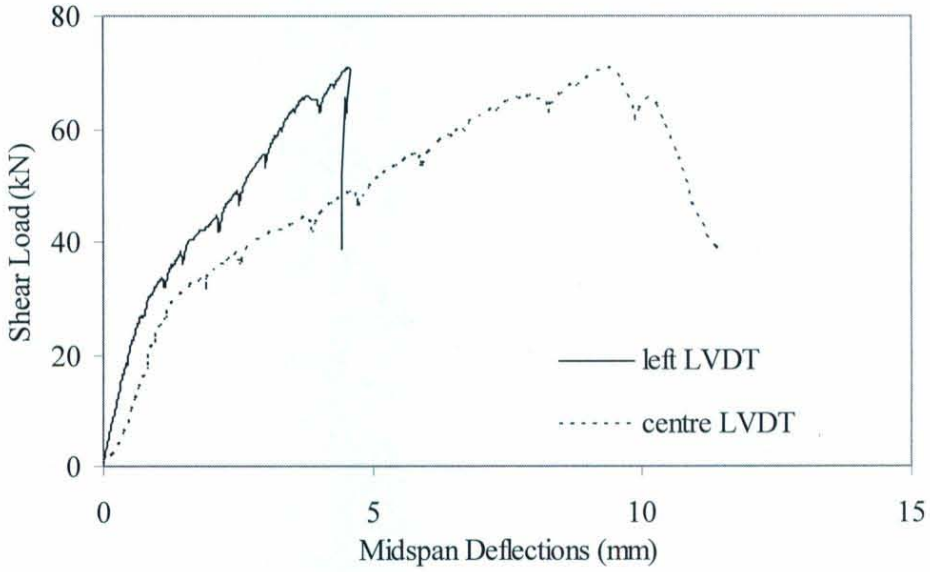

Figure B.24: Load versus deflection of beam G-2.5-350

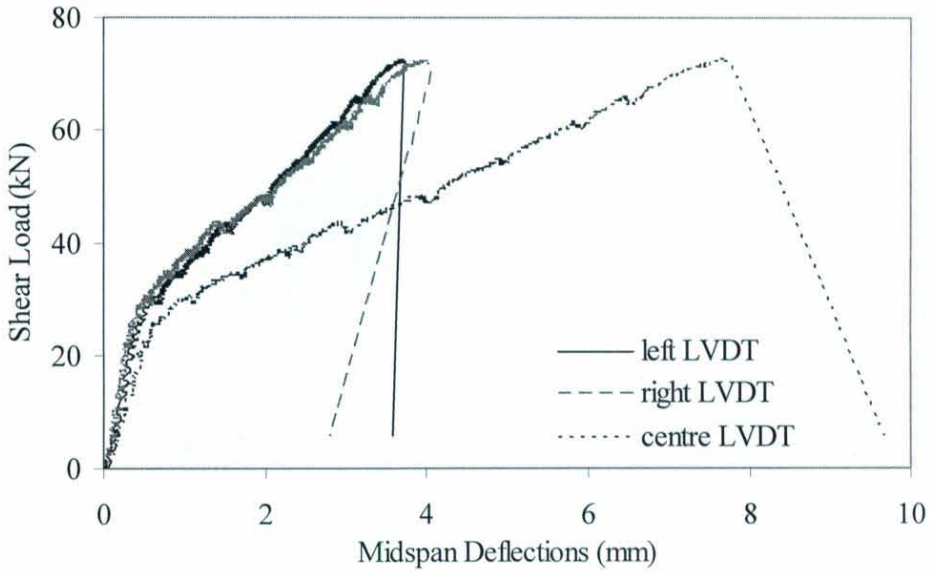

Figure B.25: Load versus deflection of beam C-2.5-350

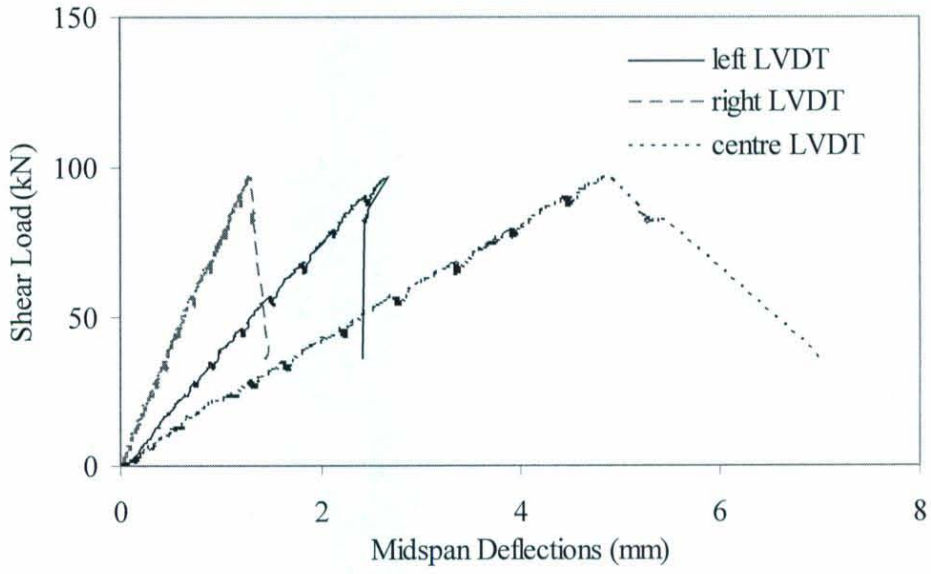

Figure B.26: Load versus deflection of beam S-2.5-350

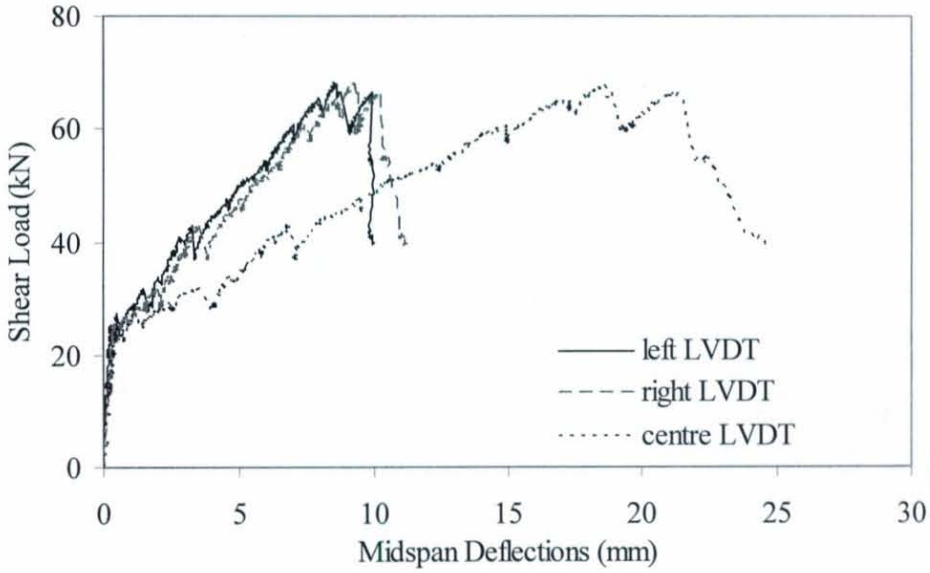

Figure B.27: Load versus deflection of beam G-0.5-500

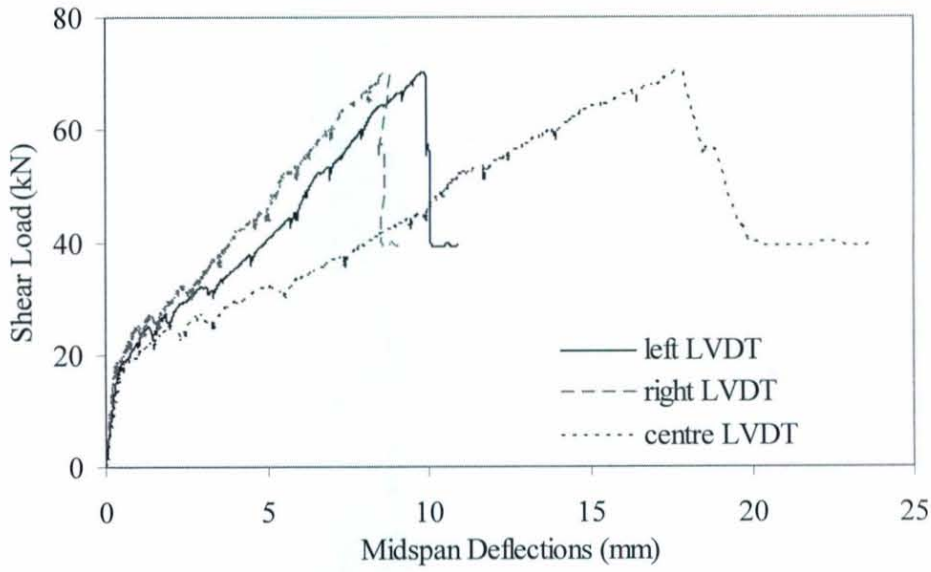

Figure B.28: Load versus deflection of beam C-0.5-500

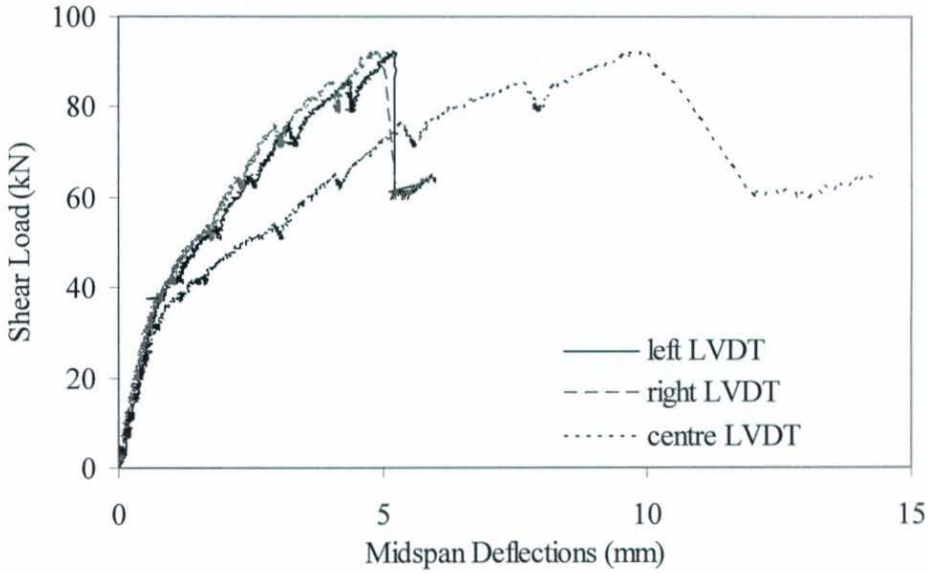

Figure B.29: Load versus deflection of beam G-2.5-500

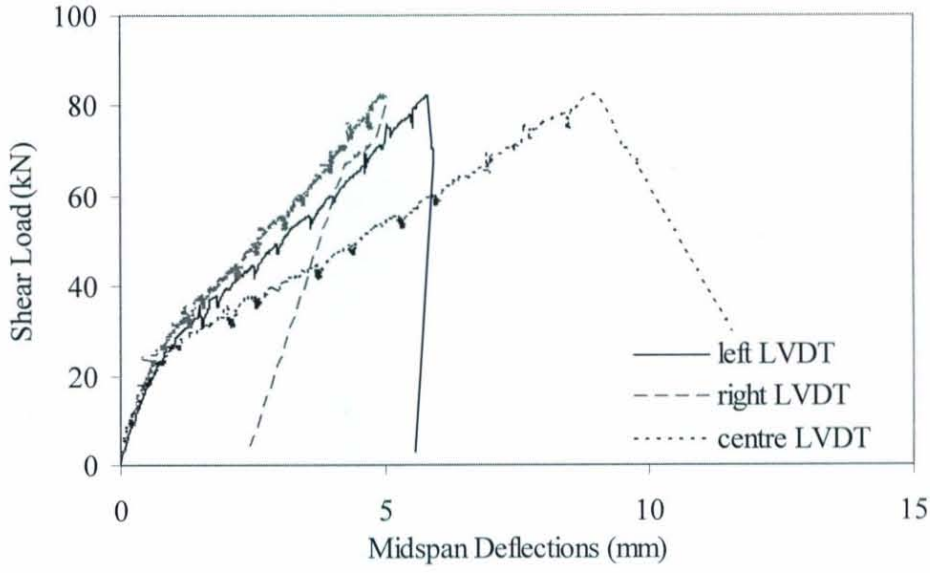

Figure B.30: Load versus deflection of beam C-2.5-500

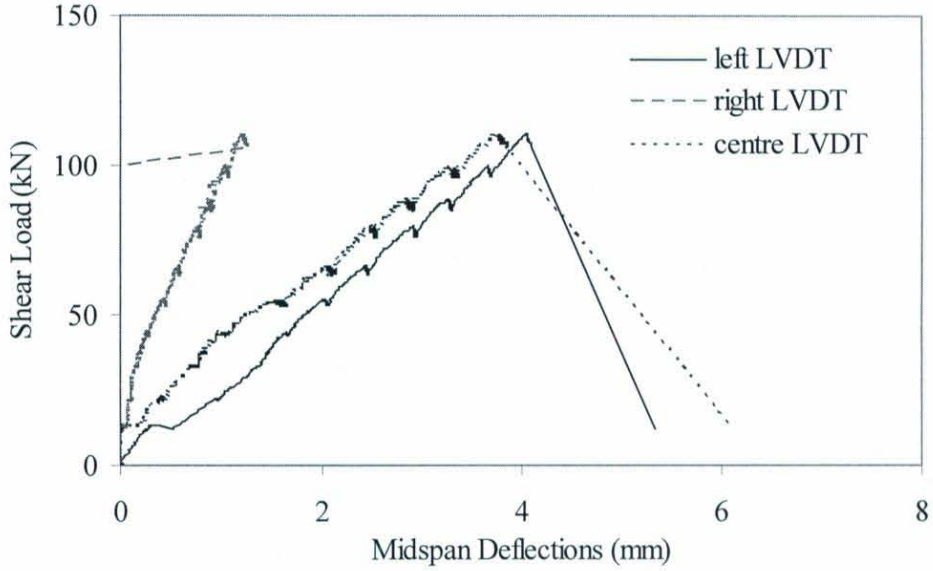

Figure B.31: Load versus deflection of beam S-2.5-500

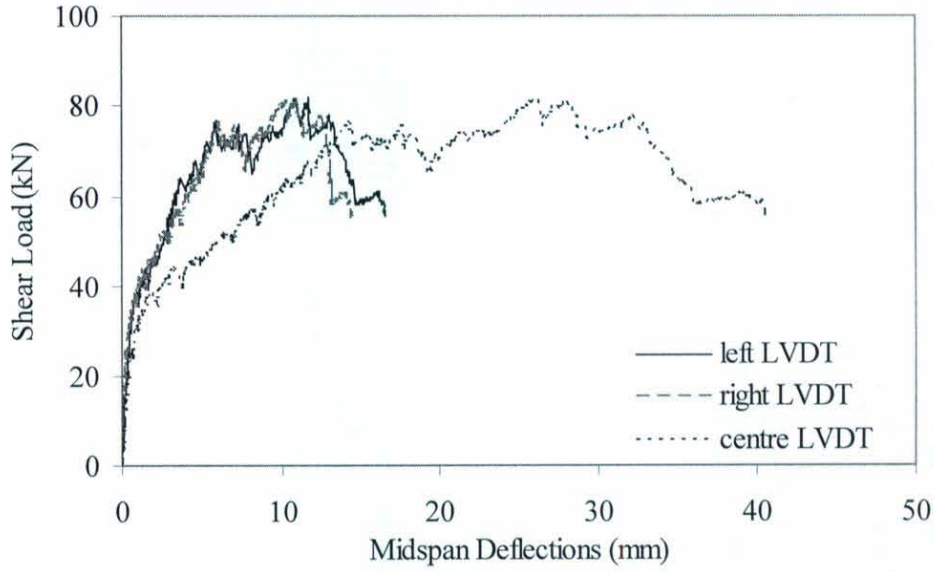

Figure B.32: Load versus deflection of beam G-50

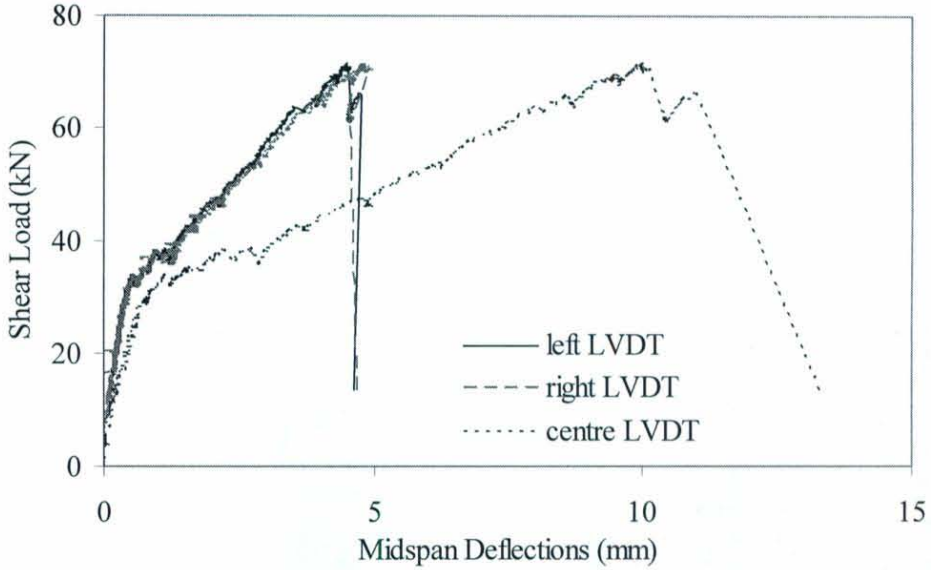

Figure B.33: Load versus deflection of beam C-50

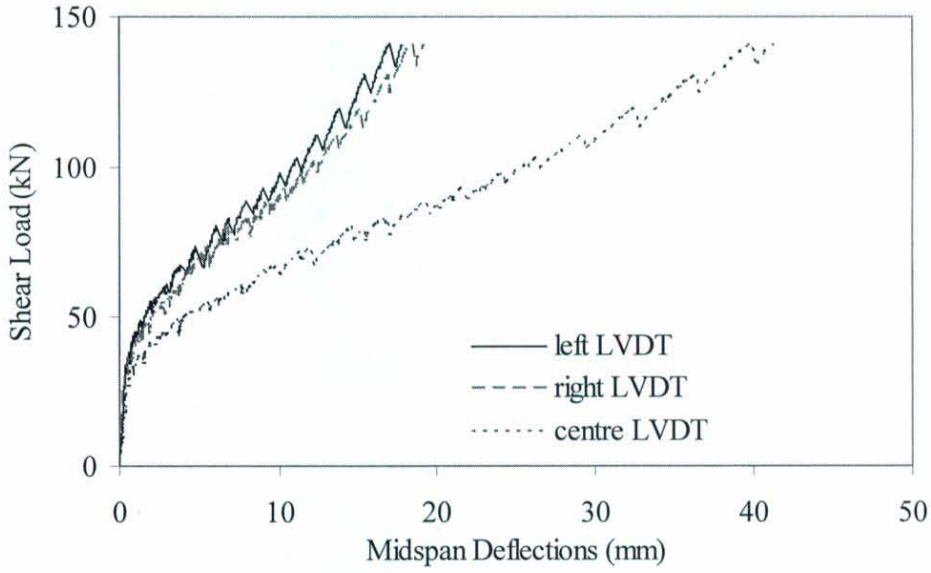

Figure B.34: Load versus deflection of beam G-70

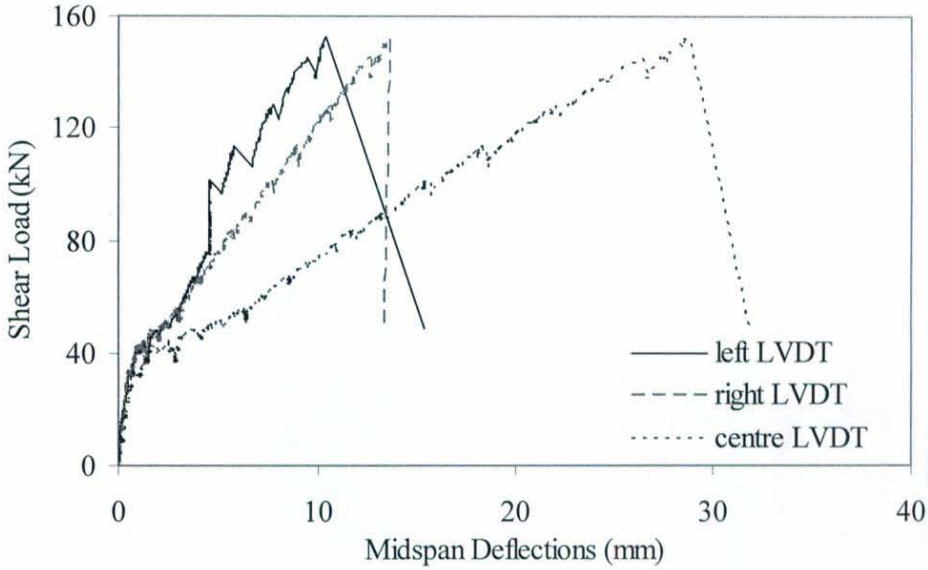

Figure B.35: Load versus deflection of beam C-70

Appendix C

Plots of Load versus Strain Obtained from the Different Strain Gauges

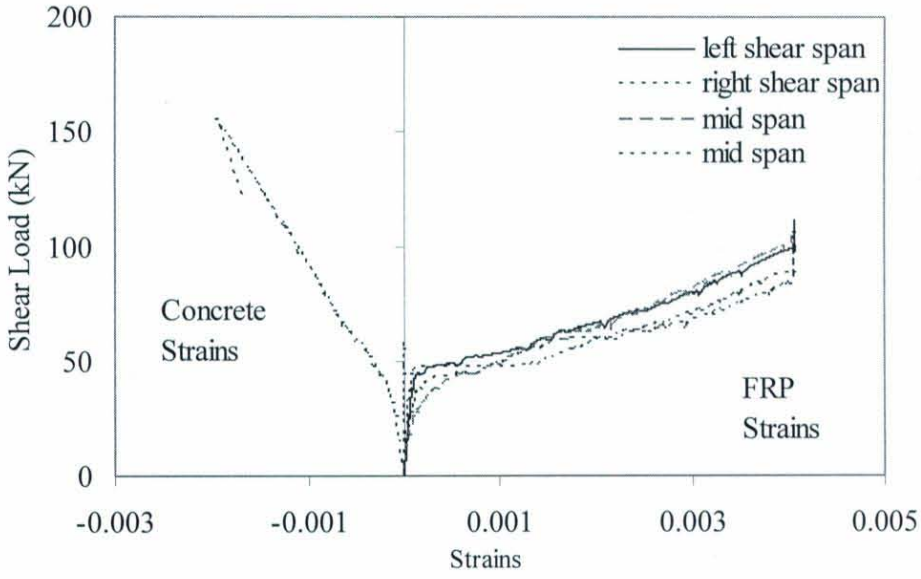

Figure C.1: Load versus strain in beam G-1.5

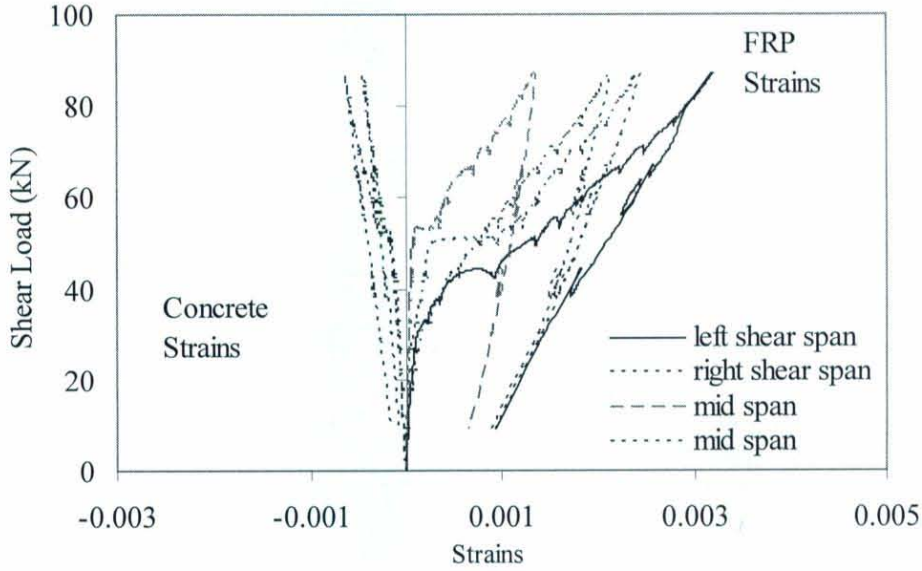

Figure C.2: Load versus strain in beam C-1.5

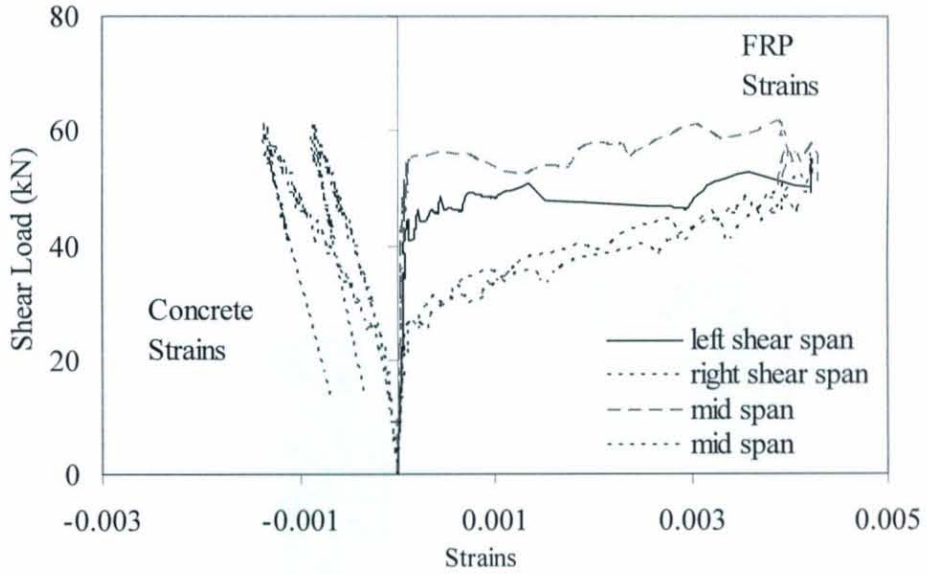

Figure C.3: Load versus strain in beam G-2.5

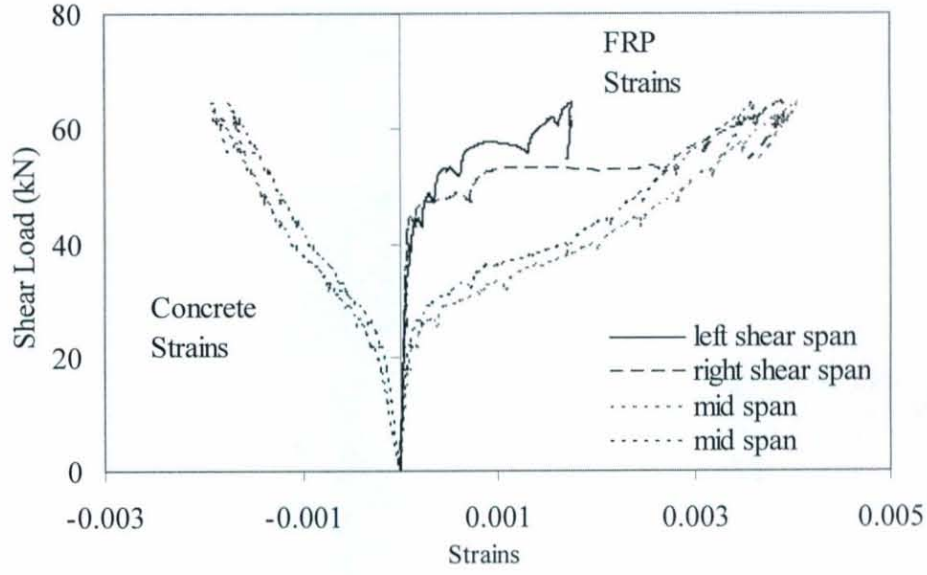

Figure C.4: Load versus strain in beam C-2.5

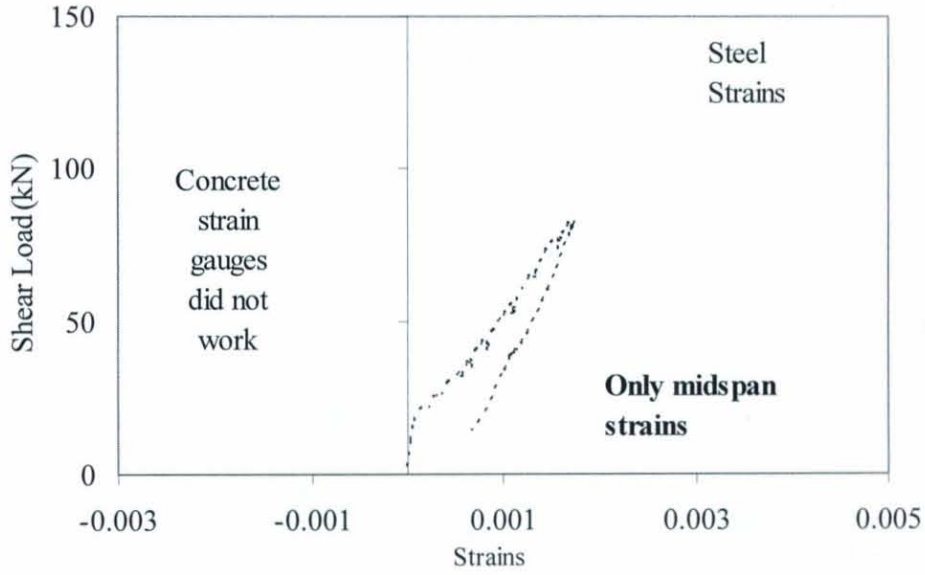

Figure C.5: Load versus strain in beam S-2.5

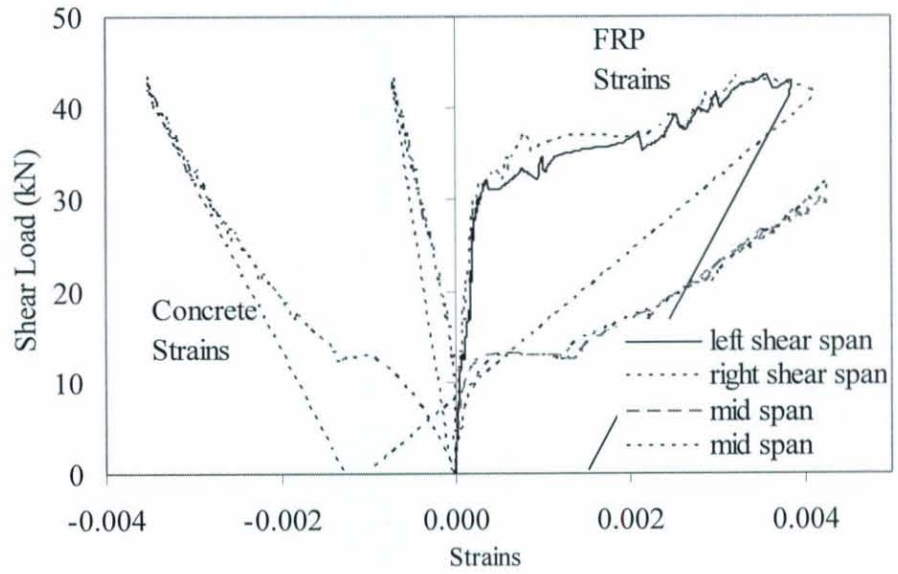

Figure C.6: Load versus strain in beam G-3.5

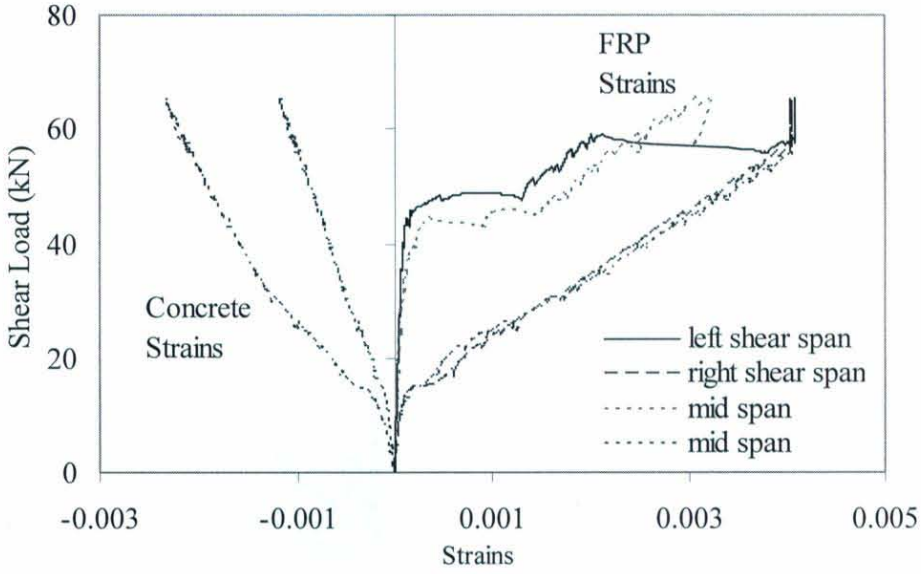

Figure C.7: Load versus strain in beam C-3.5

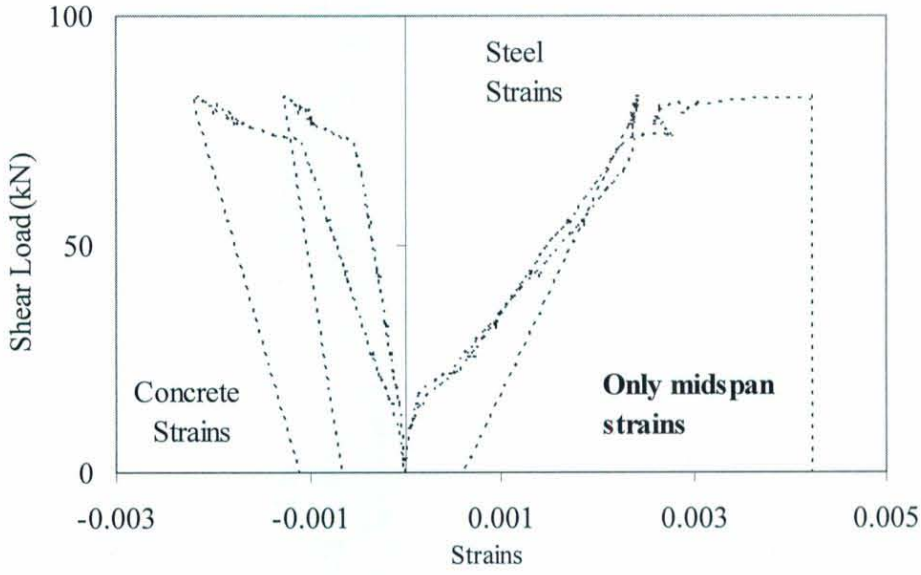

Figure C.8: Load versus strain in beam S-3.5

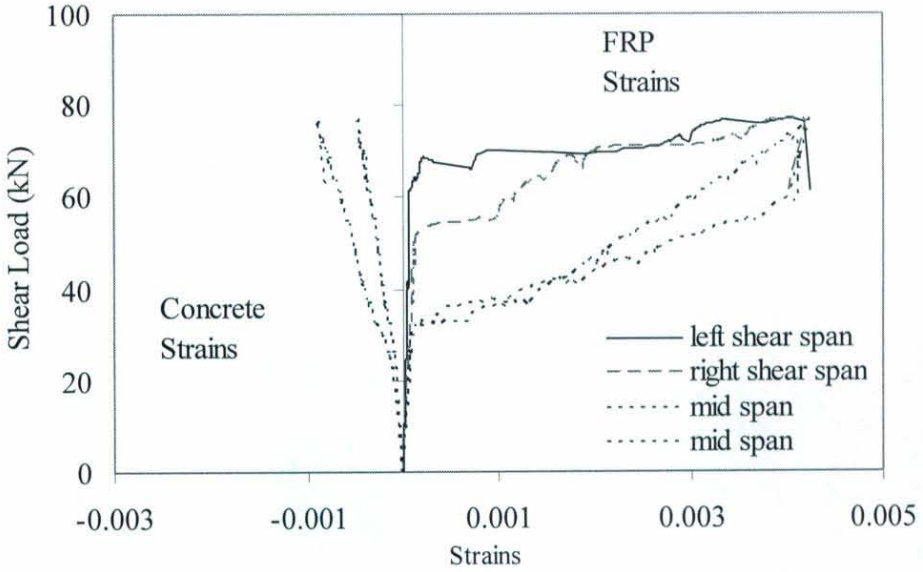

Figure C.9: Load versus strain in beam G-500

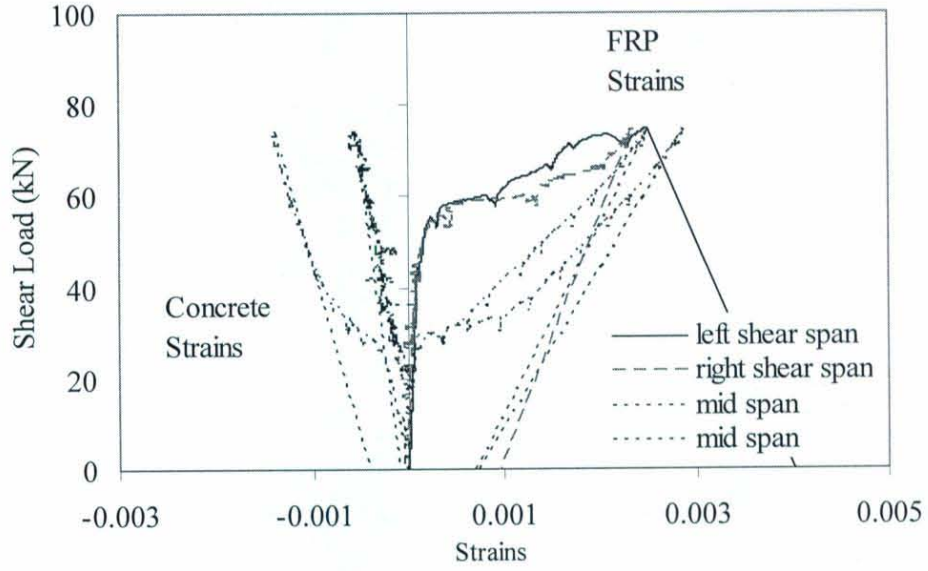

Figure C.10: Load versus strain in beam C-500

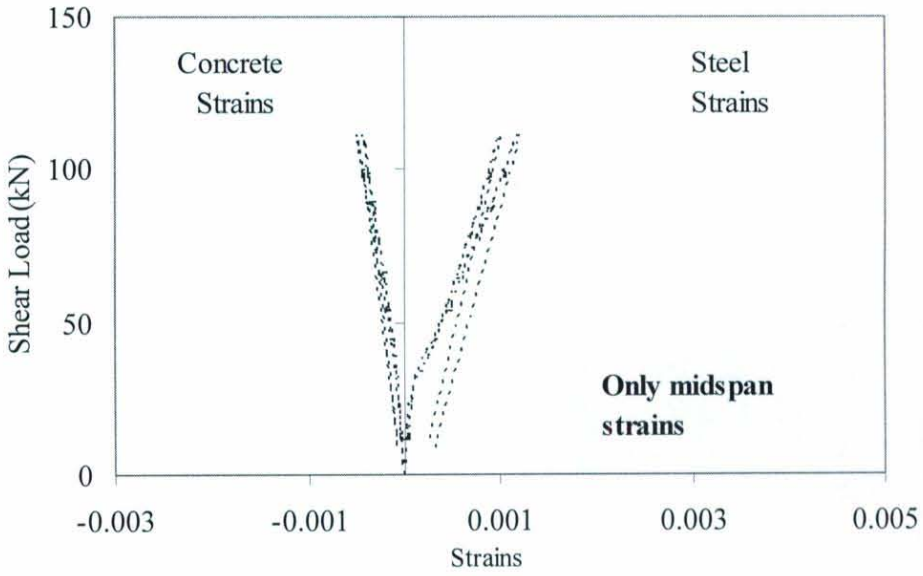

Figure C.11: Load versus strain in beam S-500

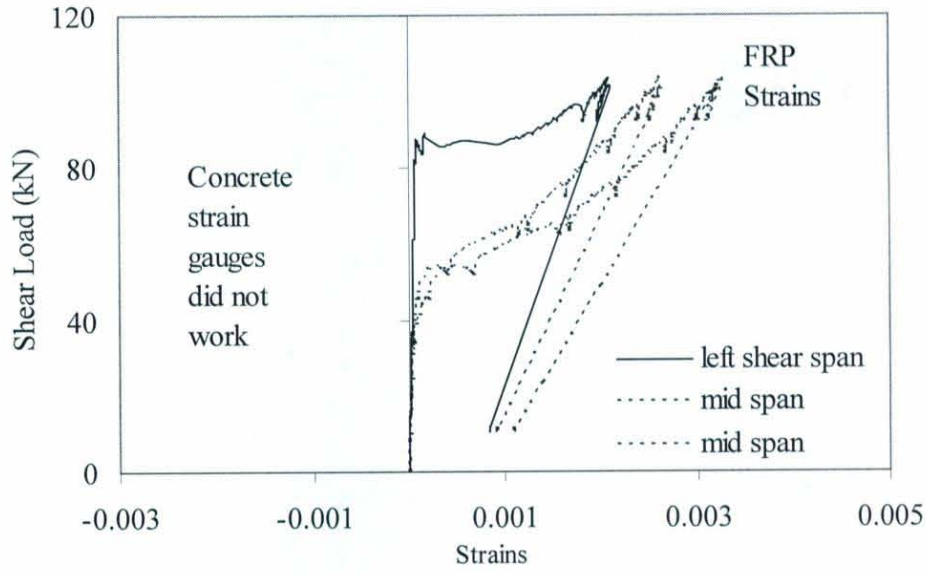

Figure C.12: Load versus strain in beam G-650

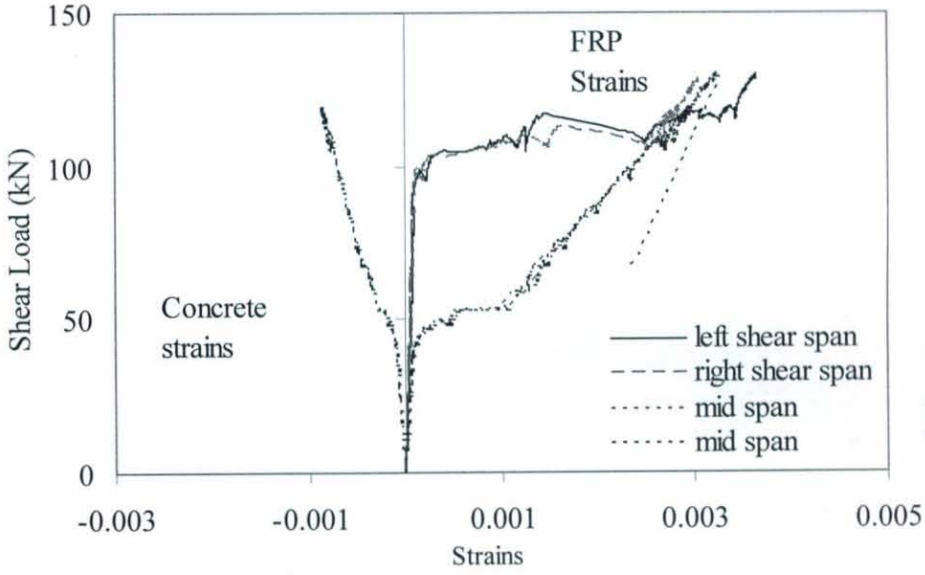

Figure C.13: Load versus strain in beam C-650

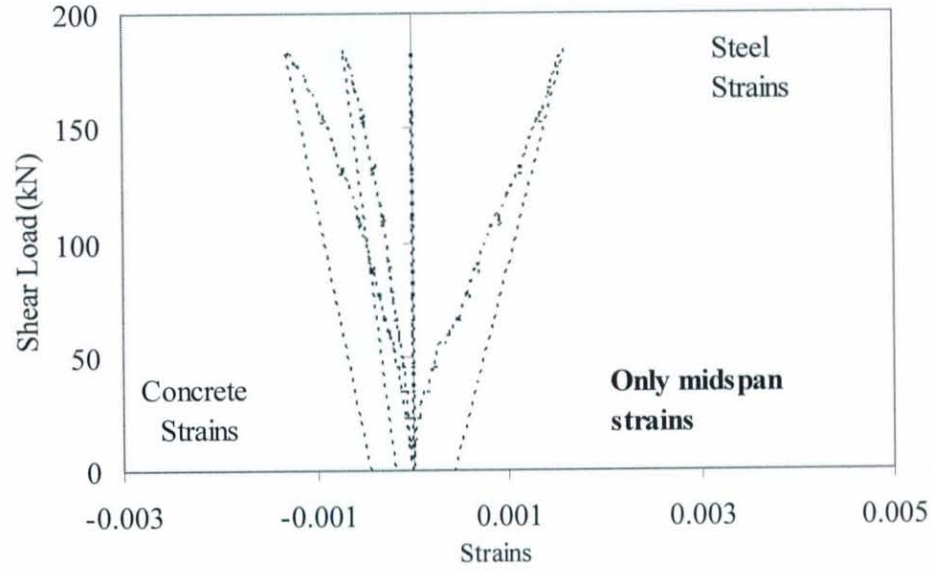

Figure C.14: Load versus strain in beam S-650

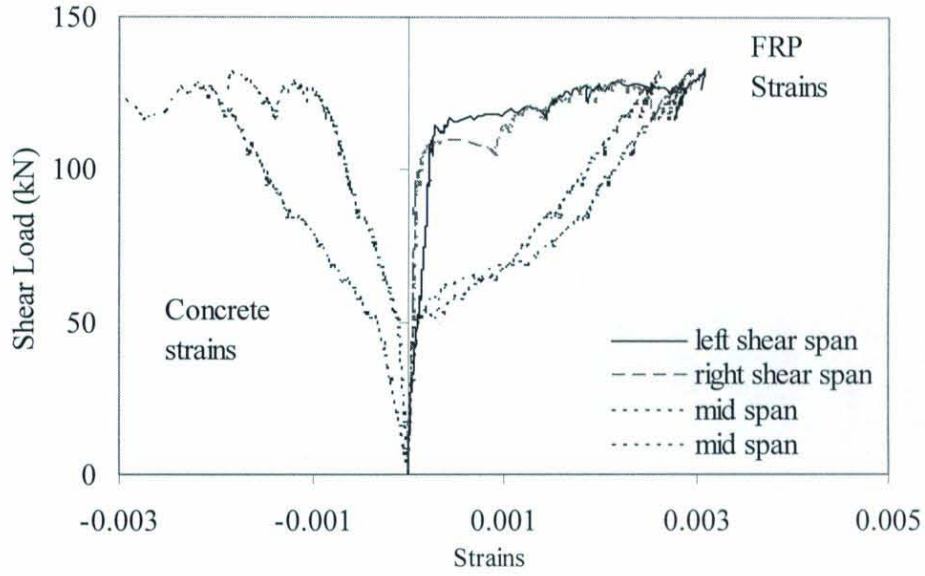

Figure C.15: Load versus strain in beam G-800

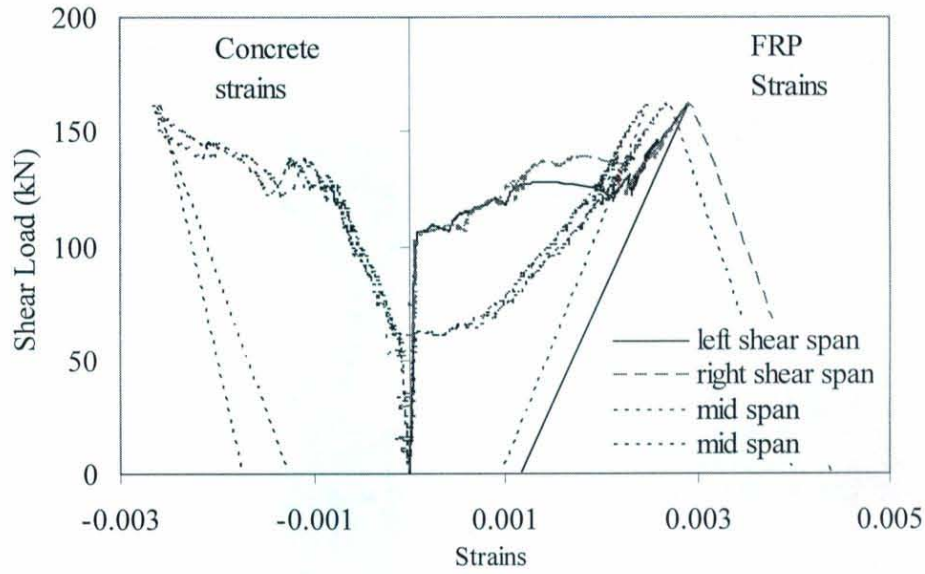

Figure C.16: Load versus strain in beam C-800

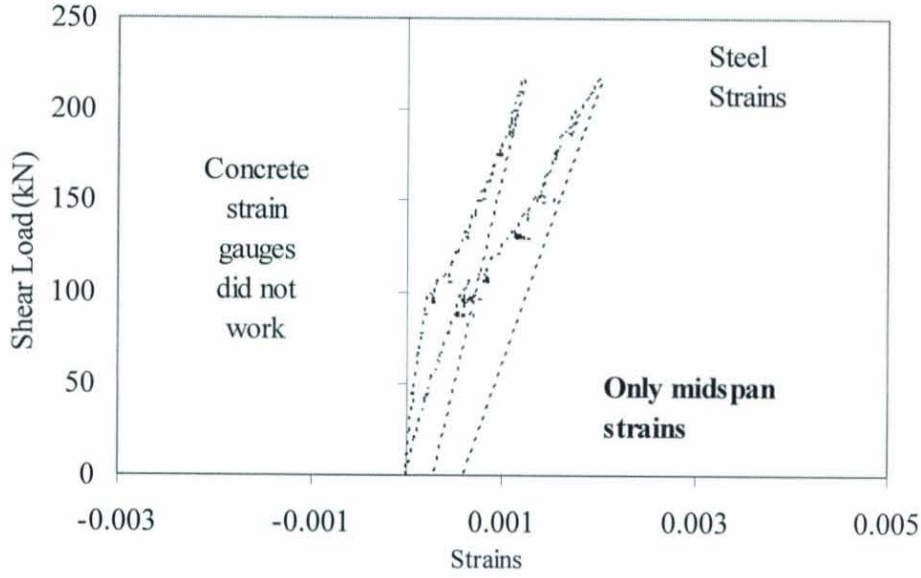

Figure C.17: Load versus strain in beam S-800

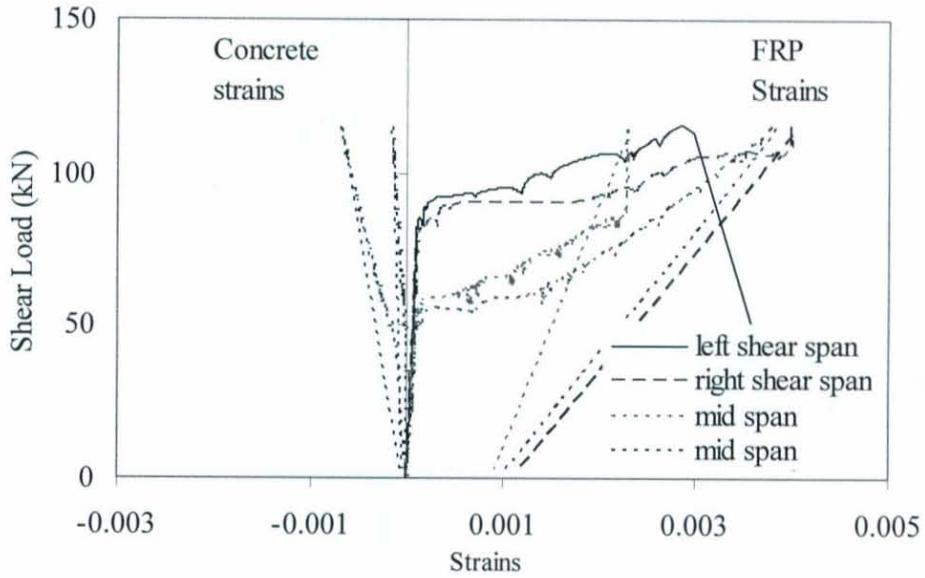

Figure C.18: Load versus strain in beam G-500-70

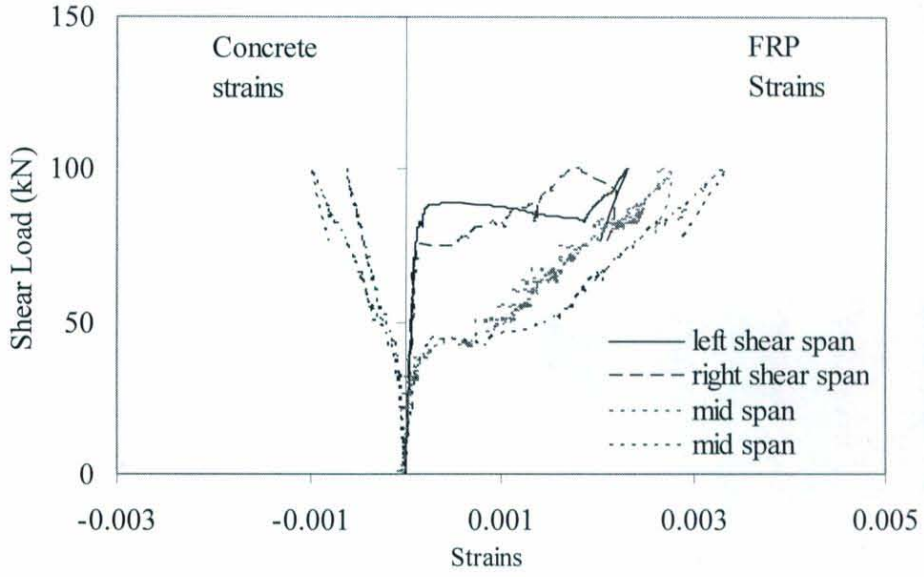

Figure C.19: Load versus strain in beam C-500-70

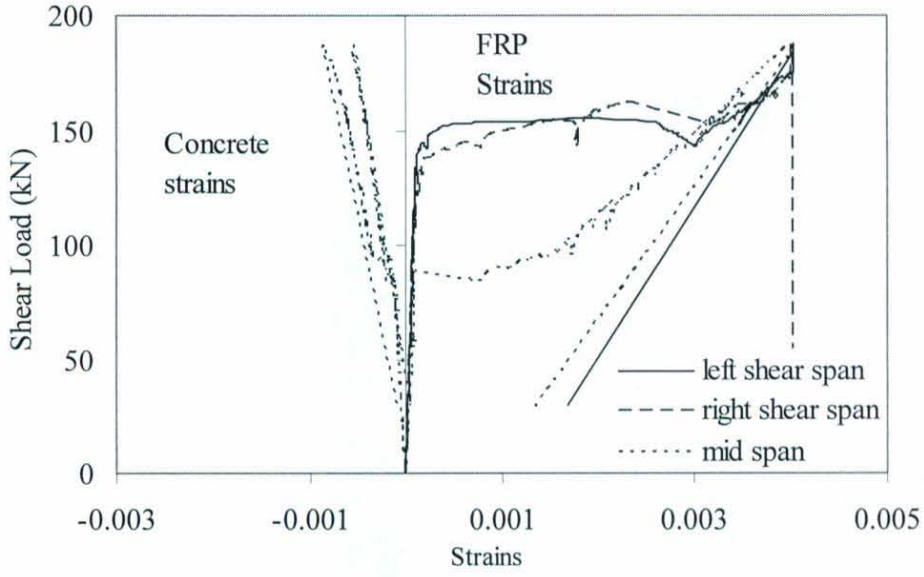

Figure C.20: Load versus strain in beam G-650-70

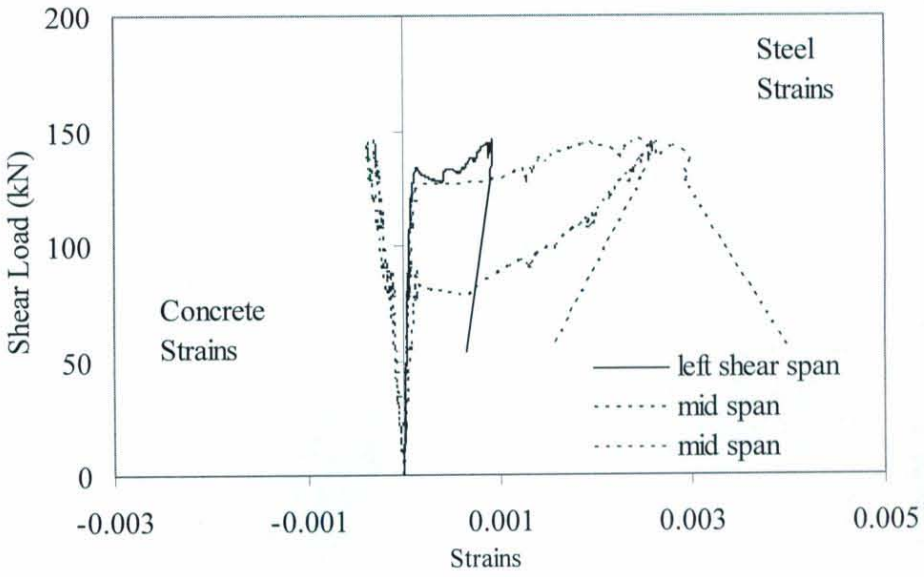

Figure C.21: Load versus strain in beam C-650-70

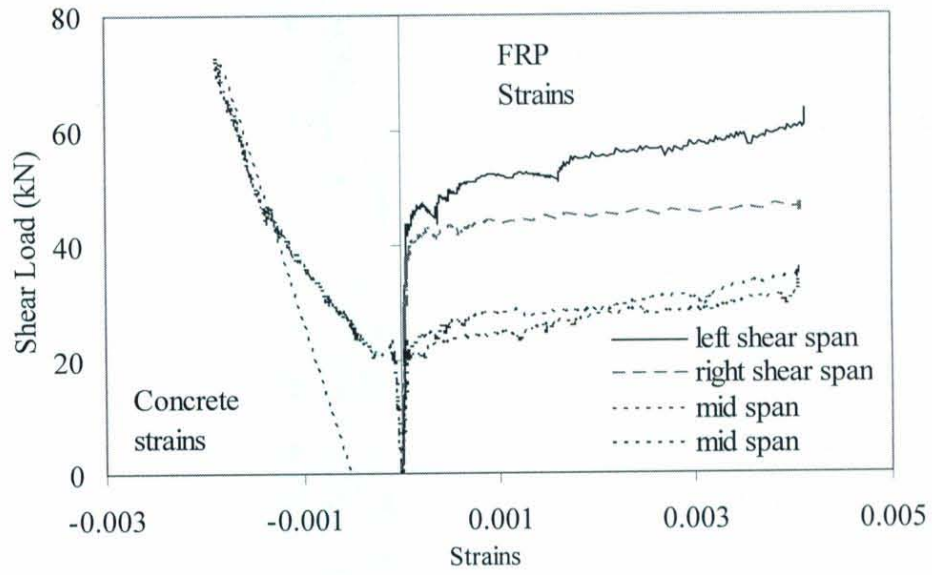

Figure C.22: Load versus strain in beam G-0.5-350

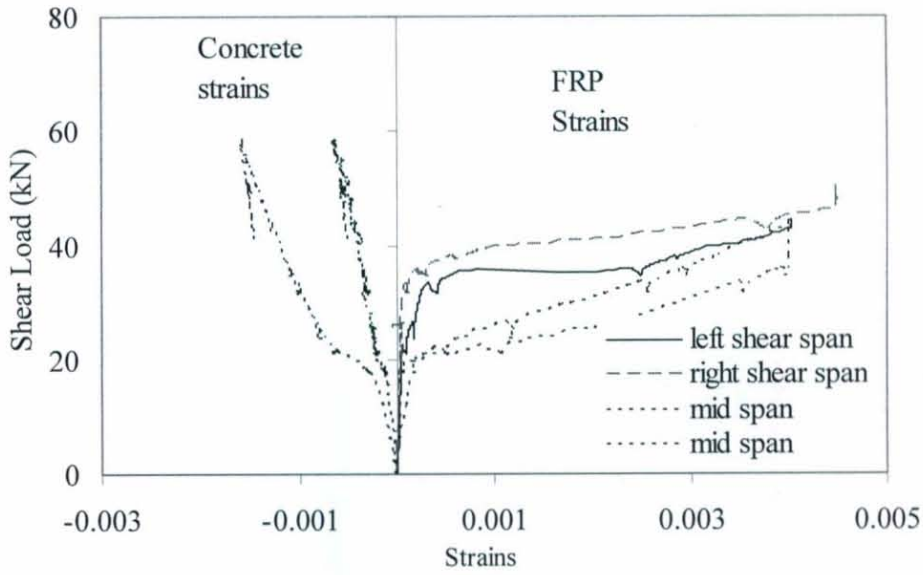

Figure C.23: Load versus strain in beam C-0.5-350

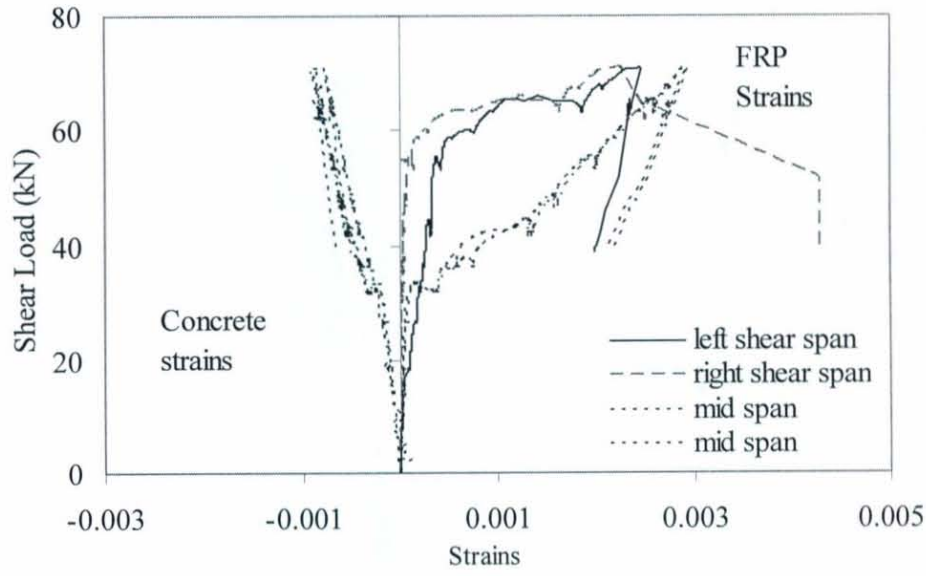

Figure C.24: Load versus strain in beam G-2.5-350

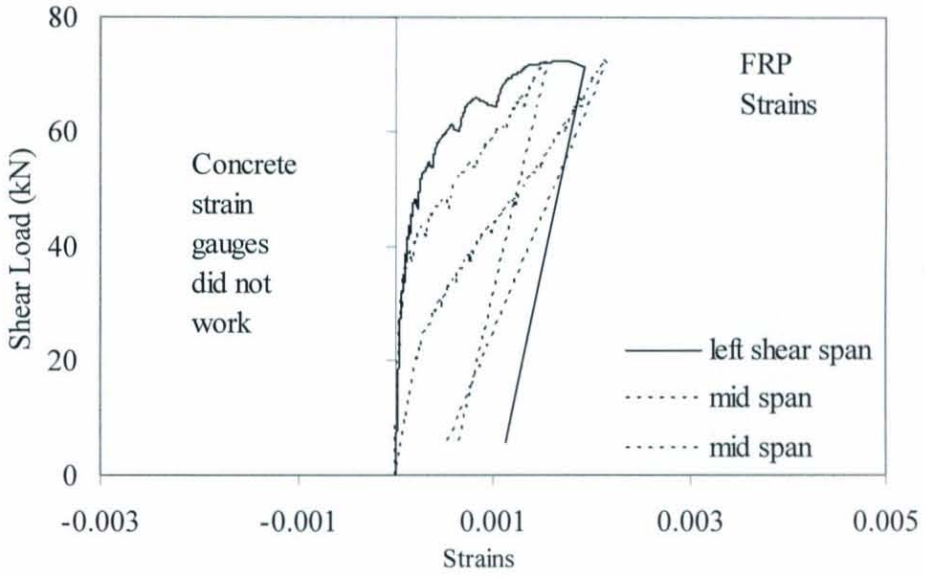

Figure C.25: Load versus strain in beam C-2.5-350

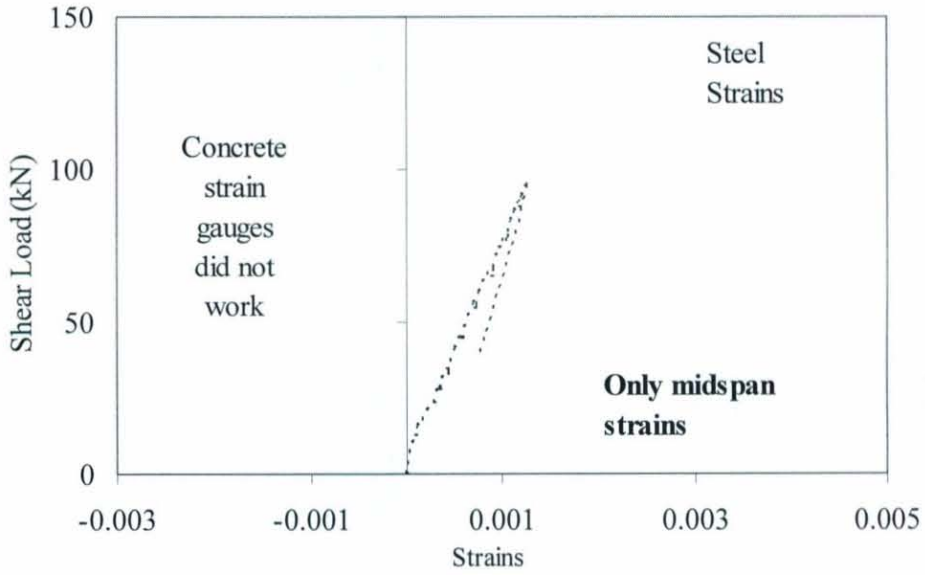

Figure C.26: Load versus strain in beam S-2.5-350

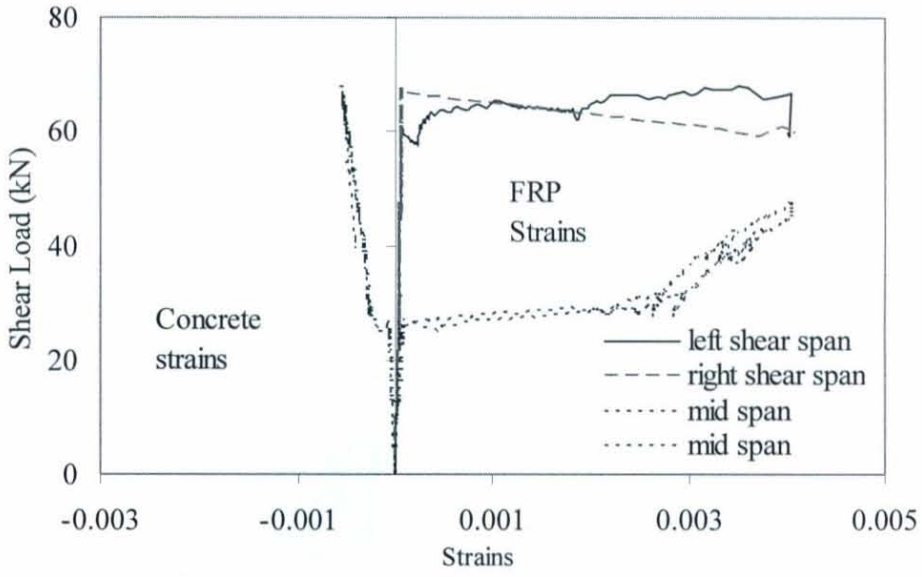

Figure C.27: Load versus strain in beam G-0.5-500

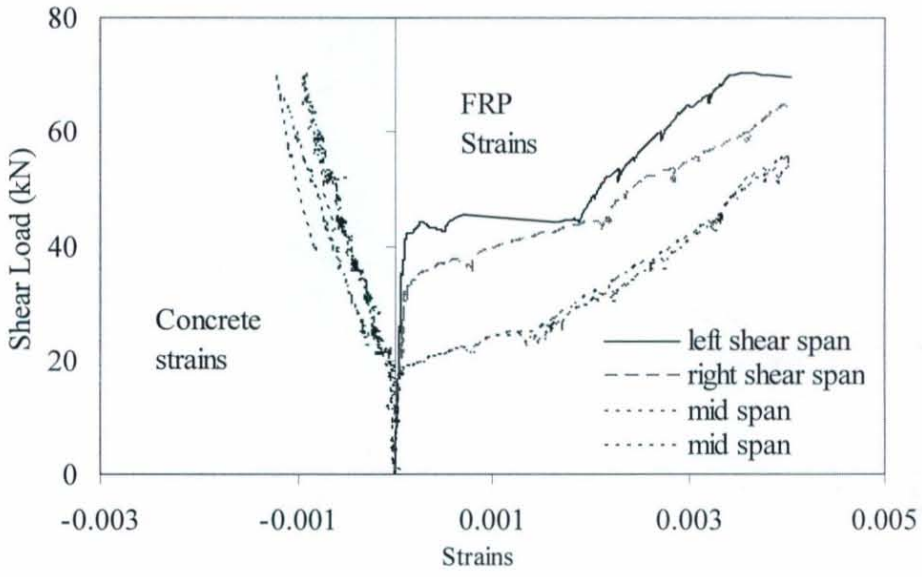

Figure C.28: Load versus strain in beam C-0.5-500

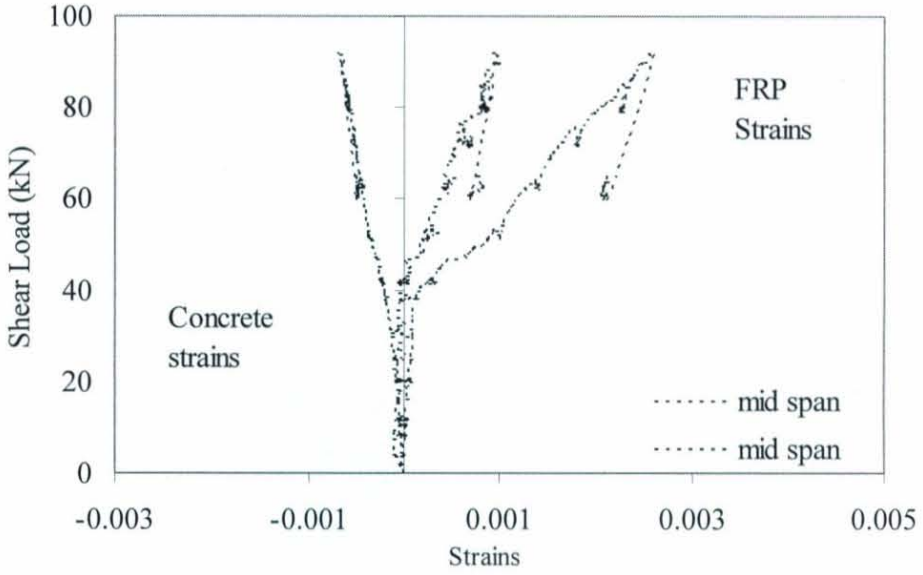

Figure C.29: Load versus strain in beam G-2.5-500

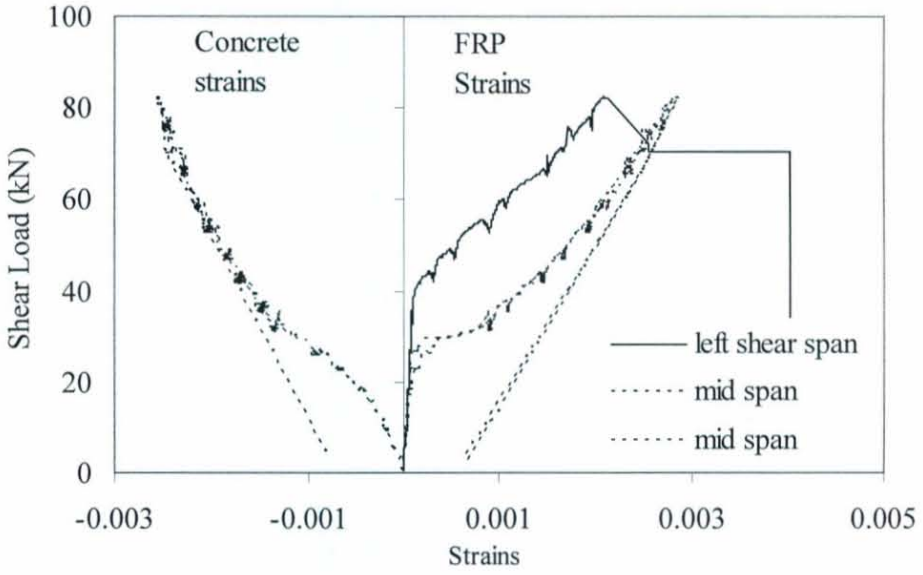

Figure C.30: Load versus strain in beam C-2.5-500

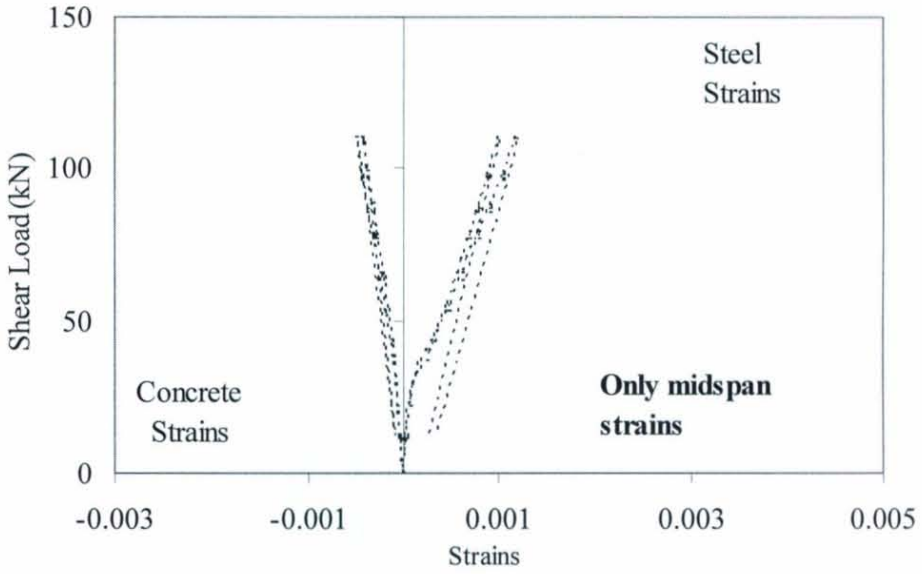

Figure C.31: Load versus strain in beam S-2.5-500

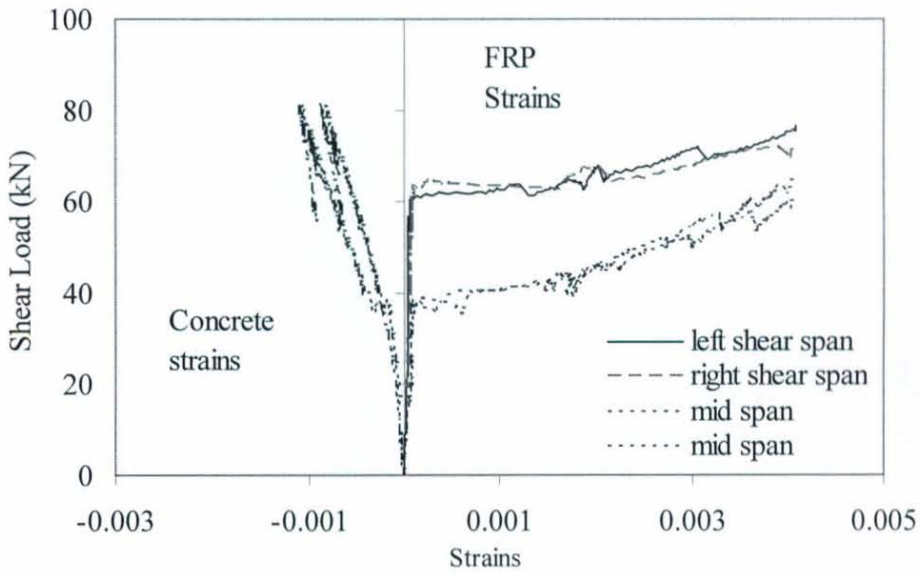

Figure C.32: Load versus strain in beam G-50

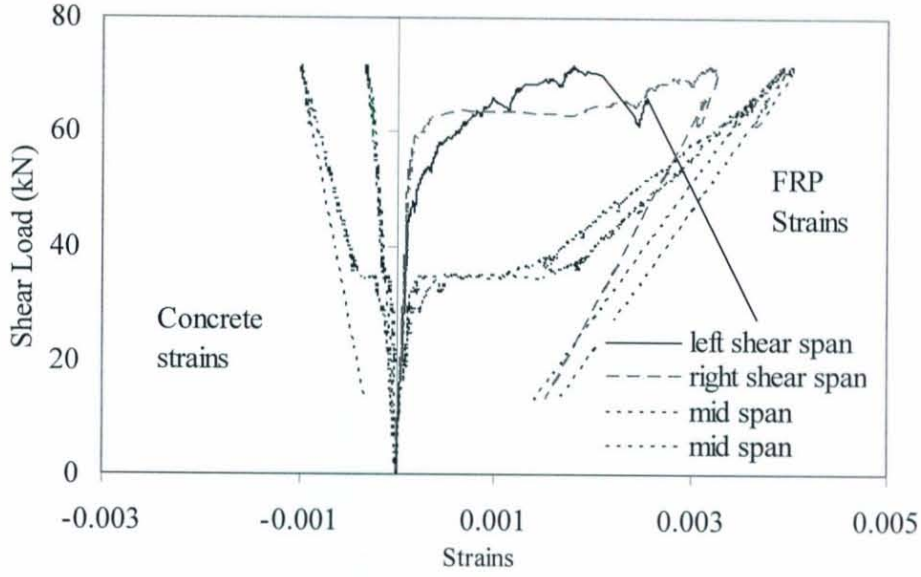

Figure C.33: Load versus strain in beam C-50

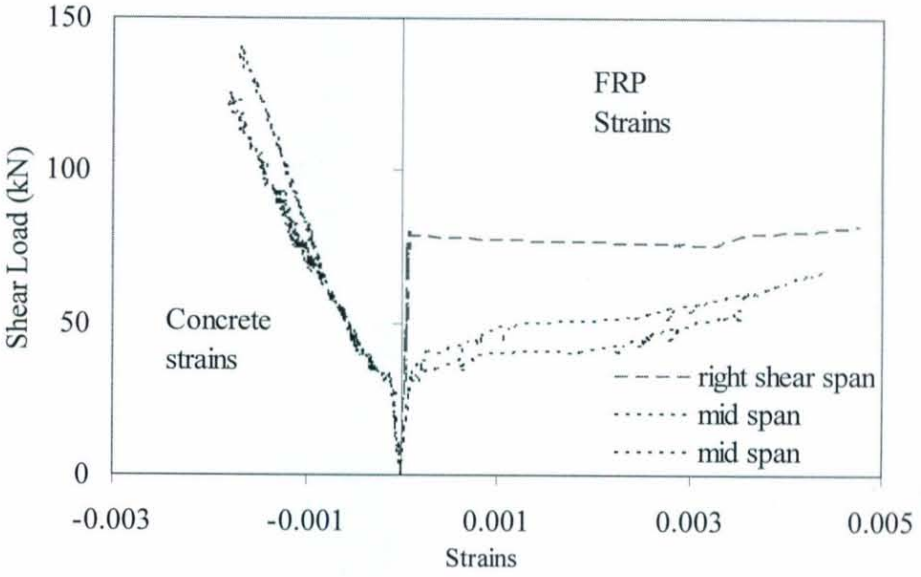

Figure C.34: Load versus strain in beam G-70

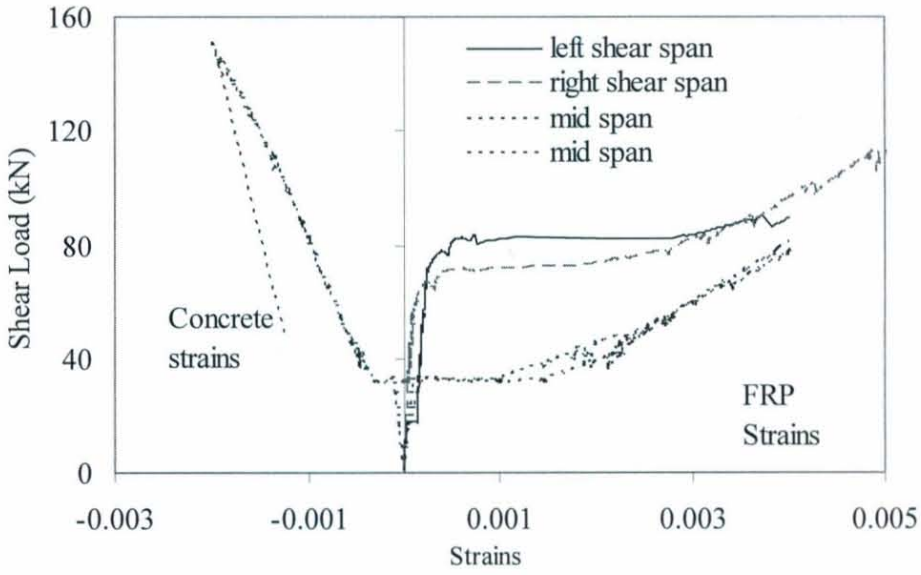

Figure C.35: Load versus strain in beam C-70